Edited by
Katarzyna **KRUKIEWICZ** Michał **MARCZYK**
Monika **BUGDOL** Sylwia **BAJKACZ**
Ziemowit **OSTROWSKI**

RECENT ADVANCES IN COMPUTATIONAL ONCOLOGY AND PERSONALIZED MEDICINE

Volume 3
CROSSING BORDERS,
CONNECTING SCIENCE

Computational Oncology
and Personalized Medicine

PRIORITY RESEARCH AREAS SILESIAN UNIVERSITY OF TECHNOLOGY

Silesian
University
of Technology

RESEARCH
UNIVERSITY
EXCELLENCE INITIATIVE

Edited by
Katarzyna KRUKIEWICZ   Michał MARCZYK
Monika BUGDOL   Sylwia BAJKACZ
Ziemowit OSTROWSKI

RECENT ADVANCES IN COMPUTATIONAL ONCOLOGY AND PERSONALIZED MEDICINE

Volume 3
CROSSING BORDERS, CONNECTING SCIENCE

The series *Recent Advances in Computational Oncology and Personalized Medicine* contains publications on research, theory, applications, and design in the field of computational oncology, personalized medicine, biomaterials and medical biotechnology, imaging informatics and telemedicine, biomechanics, analysis and drug design and public health.

The series is published within *the Excellence Initiative – Research University programme* that is implemented to increase scientific excellence and the international importance of the activities of Polish universities. As one of ten Polish universities, *the Silesian University of Technology* obtained the status of a *research university* and commenced the implementation of the programme aimed at increasing its scientific excellence and international significance.

The main objectives of the programme at *the Silesian University of Technology* are:

- Increasing recognition and visibility of the SUT, building the prestige of the University in the group of world-class universities and improving the position in renowned international rankings.
- Conducting high-quality scientific research and implementation of innovations to improve the living and health conditions of people as well as economic development.
- Ensuring high-quality education at the undergraduate and masters levels and the doctoral school, based on research and innovation.
- Supporting the scientific development of employees and PhD students.
- Increasing internationalization of science and education.

LIST OF CHAPTERS

SPIS TREŚCI

PREFACE

We present to you the third volume in our ongoing series, dedicated to the continuous exploration of recent research and practical solutions in the area of computational oncology and personalized medicine, which are the major topics in *Priority Research Area* #1 (POB1) of *the Silesian University of Technology*. Within these pages, you will find the culmination of efforts from a consortium of scientists, students, and collaborative partners from academia or the socio-economic environment. Together, they performed innovative investigations and carefully described their findings to provide valuable insights into medical science. As you read through these chapters, you'll discover that many stories are shaped in response to the practical needs expressed by medical colleagues. We warmly invite you to explore the abundant knowledge and potential that lie within these pages.

Most of the chapters represent topics related to **bioinformatics**, including medical imaging informatics (quantization of H&E stained histopathological images; analysis of bacterial cell viability through confocal microscopy), cancer-related research (expression of cytokines in colorectal cancer; clonal evolution/somatic mutations in cancers), new data processing and analysis tools (dystrophy patients stratification system; DNA sequencing reads simulator; oxford nanopore mapper), supporting the rehabilitation process (accessibility analysis of mobile rehabilitation applications and websites; games supporting rehabilitation) as well as other general applications (proliferation effect of exposure to electromagnetic field). The other group of chapters is focused on **biomodelling** (analysis of the process of heating biological tissue and its thermal damage; musculoskeletal modeling), **biomaterials engineering** (synthesis of a biodegradable and bioresorbable blood vessel scaffold), and **public health**-related problems (epidemiological studies of dengue fever and typhoid fever).

The publication of the book is one of the activities carried out by *the Silesian University of Technology* and it was published as a result of *the Excellence Initiative – Research University* programme. As one of ten Polish universities, *the Silesian University of*

Technology obtained the status of a research university and commenced the implementation of the program aimed at increasing its scientific excellence and international significance.

Editors would like to express their gratitude to the authors who have submitted their original research chapters as well as to all the reviewers for their valuable comments. Your effort has contributed to the high quality of the book that we pass on to the readers. Through this book, we want to propagate the latest achievements in computational methodologies within the scientific community. We strongly believe that the ideas and solutions presented in this series have the power to bring about new and improved tools for diagnosis, ground-breaking treatments, and advanced therapies. These innovations could support healthcare providers, ultimately leading to a better quality of life for their patients.

Sajida MARYAM[1,*], Ihtisham UL HAQ[1,2,3], Kashif RAHIM[4]

Chapter 1. MODULATION OF CYTOKINES' EXPRESSIONS IN COLORECTAL CANCER (CRC) PATIENTS IN TERTIARY CARE HOSPITALS OF PAKISTAN

1.1. Introduction

Cancer is the undifferentiated rapid growth of cells that can invade the adjoining parts of the body through a process called "metastasis" [1]. Around 600,000 new cases are diagnosed each year throughout the world [2], and in 2020 there were 10.3 million cancer deaths and 19.3 million new cancer cases [3]. Common types of cancers are lung, breast, colorectal, prostate, skin, and stomach [4]. Colorectal cancer (CRC) deaths are estimated to be 9.2% which makes it one of the leading causes of cancer deaths [3–5]. The tumorous growth in the rectum, colon, and appendix are all included in colorectal cancer, also known as large bowel cancer. For both men and women, it is the second and third most prevalent malignant condition, respectively [6]. CRC has become more prevalent in Pakistan, particularly among people over 50 [7]. According to a meta-analysis of seven different studies completed in Pakistan, the prevalence of CRC is 5% nationwide [8]. Many environmental and genetic factors contribute to the development of CRC [9]. In between 50 and 80 percent of identified cases, environmental variables have an impact on its development and 50% of colorectal cases can be attributed to dietary choices [10]. Inactivity, smoking, obesity, and low consumption of fruits and vegetables are some of its risk factors [11, 12]. Fatty acids can promote the progression of CRC [13], and it has been discovered that there is a link between obesity and colorectal cancer [14].

[1] Department of Biosciences, COMSATS University Islamabad (CUI), Islamabad 44000, Pakistan.
[2] Department of Physical Chemistry and Technology of Polymers, Silesian University of Technology, M. Strzody 9, 44-100 Gliwice, Poland.
[3] Programa de Pós-graduação em Inovação Tecnológica, Universidade Federal de Minas Gerais, Belo Horizonte, 30150-240, MG, Brazil.
[4] College of Life Science and Technology, Beijing University of Chemical Technology, Beijing, 100029, China
* Correspondence: ihaq@polsl.pl. sajida.maryam786@gmail.com.

New predictive biomarkers are required for CRC given that the disease has a poor prognosis [15, 16]. Although molecular-level diagnostics for targeted therapy for colorectal cancer are receiving more attention in research, it is still challenging to incorporate this technology into routine procedures [17]. Activated immune cells release growth factors and cytokines to regulate the inflammatory conditions in tumor tissues [18]. By accelerating metastasis and tumor growth, chronic inflammation greatly contributes to malignancies [19, 20]. Cytokine networks have a major role in the pathogenesis of colorectal cancer [21]. They are expressed by tumors with either pro- or anti-tumor characteristics [22, 23]. Many alterations have been found in cytokine profile upon CRC [24]. Variety of interleukins are involved [25, 26] with roles in tumor growth [27], invasion of cancer cells, and metastasis [28]. They may also act as biomarkers to detect cancer and predict its outcomes because they are frequently seen in blood circulation [29].

When compared to healthy individuals, CRC patients had higher serum levels of interleukin-17 (IL-17A) which is significantly correlated with tumor size [30]. The high expression of genes associated to Th17 [31] suggested that patients will have a poor prognosis for survival [32]. Interleukin-22 is another important player in the development of CRC [33]. Patients with CRC who have high serum or tissue levels of IL-22 have a poor prognosis because the IL-22 reduces the effectiveness of treatment [34]. Similarly, the level of FOXP3 is much higher in CRC tissues than in normal tissues of the colon and rectum [35] playing a prime role in cancer progression [36]. Tumor necrosis factor-stimulates invasion and epithelial-mesenchymal transitions which enhance CRC metastases [37]. Compared to normal, its expression is also noticeably greater in CRC [38,39]. Stages three and four of neoplasms exhibit higher expression than do earlier stages [38]. The risk of colorectal cancer is discovered to be connected with genetic variations in interferon-gamma (IFN-γ) [39]. Polymorphisms in genes of IL-1β also elevate the risk of colon cancer development [40]. It is a proinflammatory cytokine secreted by macrophages to propagate the inflammatory response [41, 42]. Patients with advanced colon cancer usually cannot go through surgery, therefore effective biomarkers and therapeutic targets are needed for advanced colorectal cancer [43]. This study aims to discover such cytokines in the blood serum of CRC patients in comparison to regular blood.

1.2. Experimental

1.2.1. Study Design

In this study, the expression of a genes with inflammatory cytokines in colorectal cancer was investigated through qPCR expression analysis. The extracted RNA was used to synthesize complementary DNA (cDNA). In qPCR, expression profiles of selected genes were studied using cDNA as a template. The target gene was thought to involve in the progression of gastric and colorectal cancer.

1.2.2. Sample Collection

Colorectal blood samples were collected with patient's consent from Victoria hospital, Bahawalpur and Pakistan's Institute of Medical Sciences, Islamabad after ethical approval from ethical review board. RNA was extracted manually by Trizol LS method. Nanodrop (Nanodrop™ 2000 Spectrophotometer of thermo fisher) was used to quantify RNA and stored at -20°C for further processing. All participants relevant data was tabulated such as of age, gender, region and stage.
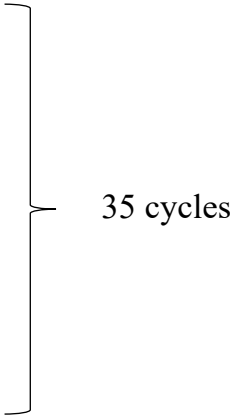
1.2.3. cDNA synthesis

cDNA synthesis is done from extracted RNA using reverse transcriptase enzyme. The first strand complementary DNA was synthesized by using kit of Thermo Fisher Scientific "RevertAid First Strand cDNA Synthesis".

1.2.4. Amplification

RNA expression of the target gene was analyzed using PCR through cDNA synthesis with set of primers. The conditions of the PCR were optimized by applying various cycles and conditions.

The following steps were performer

- Initial denaturation at 95ºC for 5 minutes

- Denaturation at 95ºC for 30 seconds

- Annealing at XºC for 30 seconds
  (According to each primer)

- Incubation of 72ºC for 45 seconds

- Final extension 10 min at 72ºC

35 cycles

For each primer, the annealing temperature of PCR was optimized to obtain appropriate annealing conditions.

1.2.5. Gel visualization and Gel Electrophoresis

To perform PCR amplification of the target genes, post amplification was performed on gel electrophoresis. 2% agarose gel was used for PCR products for which agarose to 70 ml of 1X TBE electrophoresis buffer was adding to prepared the gel and agarose was melted at high temperature for 2 minutes in microwave oven. Visualized the DNA under digitally photographed using Gel Doc imaging or UV light.

1.2.6. RT PCR

WizPure qPCR (SYBR) with ROX Dye is an optimized ready-to-use solution for real-time quantitative PCR assays.

1.2.7. Real time PCR Preparation

By using Step One qPCR system (Applied Biosystems), all real time reactions were carried out. The qPCR was performed to analyze the expression of genes in gastric and colorectal tumor versus normal cell. ß-actin was used as a reference or endogenous control. The qPCR master mix was prepared using the kit components in appropriate quantities. Appropriate quantity of cDNA template was added along with master mix and were run-in Real-time PCR system.
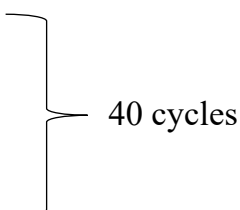
Transfer tubes into a Real-time PCR instrument and run as following:

By $2^{-\Delta\Delta CT}$ analysis method, the relative expression of *IL-22* and housekeeping gene ß-actin were calculated (Livak and Schmittgen 2001).

$$\frac{X_{Test}}{X_{Control}} = 2^{\Delta\Delta}C_T = 2(C_{T,X} - C_{T,R})_{control} - (C_{T,C} - C_{T,R})_{test} \tag{1}$$

where: X_{Test} = Value of expression of interest gene $X_{Control}$ = Expression value of reference gene e.g., ß-actin $C_{T,X}$ = Threshold cycles of gene of interest $C_{T,R}$ = Threshold cycle of the reference gene.

The PCR reaction were run on Applied Biosystems® StepOnePlus™. The qPCR steps were as follow:

- Step 1 at 95°C for 10 minutes
- Step 2 at 95 °C for 30 seconds
- Step 3 at 55 °C for 20 seconds
- Step 4 at 72 °C for 20 seconds

40 cycles

1.3. Statistical Analysis

Statistical analysis was done using OriginPro 2016 (Origin Lab, Northampton, MA). For expression analysis of data, the relative expression of the target gene *IL-22* was calculated using the endogenous control gene (ß-actin). The statistical importance was determined using either the Mann-Whitney test with a significance level of $P < 0.05$.

1.4. Results

1.4.1. Amplification of ß-actin and TNF-α

We used the Invitrogen ladder of 100 base pair (bp) to estimate the size of the product of specific gene which is 120 base pair. The bands indicate that the amplification of ß-actin (Figure 1). PCR amplification of TNF-α is done at the annealing temperature of 59°C (Figure 2).

Amplification of ß-actin
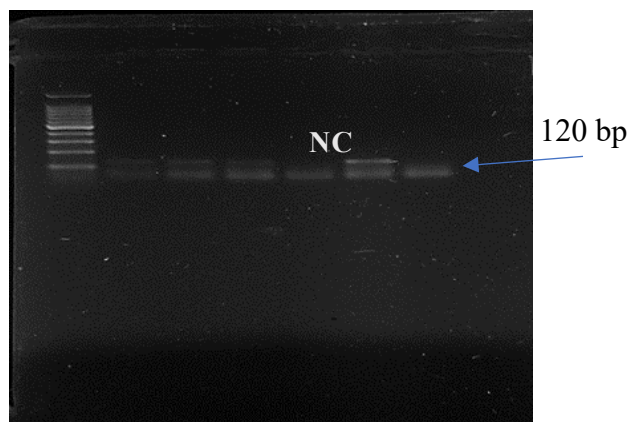
Fig. 1. Confirmatory PCR result of cDNA with ß-actin PCR product was run on 2% agarose gel for 30 minutes at 90 V and 400 mA. 5 µl PCR product was loaded in each well. As for size marker 100 bp ladder was used. NC represents the negative control for the PCR reaction. Bands were visible which indicates that amplification of gene ß-actin occurred at 120 bps size

Rys. 1. Badania PCR cDNA z ß-aktyną prowadzono na 2% żelu agarozowym przez 30 minut przy 90 V i 400 mA. Do każdej studzienki załadowano 5 µl produktu PCR. Jako marker wielkości zastosowano wzorzec 100 bp DNA Ladder. NC oznacza próbkę kontrolną-negatywną dla reakcji PCR. Widoczne prążki wskazują, że amplifikacja genu ß-aktyny zachodziła przy 120 bp

TNF-α

Fig. 2. PCR product was run on 2% agarose gel for 30 minutes at 90 V and 400 mA. 5 µl PCR product was loaded in each well. As for size marker 100 bp ladder was used. Fig shows the amplification of gene TNF-α having 217 bps size without the non-specific bindings. L5 shows amplification while NC is showing the nagative control

Rys. 2. Reakcję PCR prowadzono na 2% żelu agarozowym przez 30 minut przy 90 V i 400 mA. Do każdej studzienki załadowano 5 µl produktu PCR. Jako marker wielkości zastosowano wzorzec 100 bp DNA Ladder. Rysunek przedstawia amplifikację genów TNF-α o wiel-kości 217 bps bez niespecyficznych wiązań. L5 pokazuje amplifikację, podczas gdy NC oznacza próbkę kontrolną-negatywną

1.4.2. Amplification of IL-17 and IL1-ß

The estimated size of the *IL-17* is 156 bps for comparison we used 100 bp marker. The bands indicate that the amplification of *IL-17* in Figure 3. After the primer optimization, PCR amplification was performed at a specific annealing temperature that is 60ºC of or both tumor and control tissue samples. The bands indicate that the amplification of IL1-ß (Figure 4).

IL-17

IL1-ß
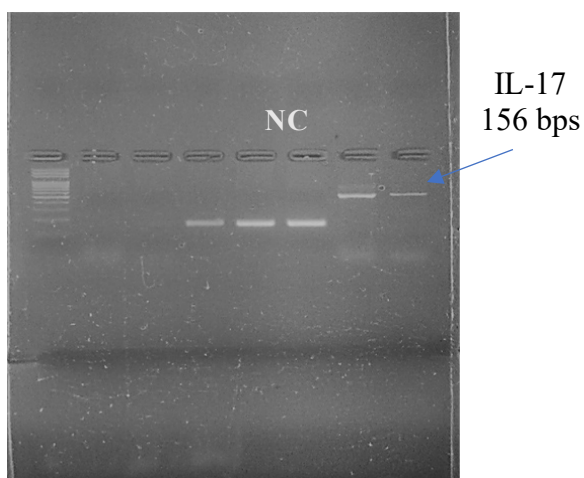
Fig. 3. PCR product was run on 2% agarose gel for 30 minutes at 90 V and 400 mA. 5 µl PCR product was loaded in each well. As for size marker 100 bp ladder was used. NC represents the negative control for the PCR reaction. The amplified PCR product of IL-17 with the size 156 bps

Rys. 3. Reakcję PCR prowadzono na 2% żelu agarozowym przez 30 minut przy 90 V i 400 mA. Do każdej studzienki załadowano 5 µl produktu PCR. Jako marker wielkości zastosowano wzorzec 100 bp DNA Ladder. NC oznacza próbkę kontrolną-negatywną dla reakcji PCR. Rysunek wskazuje amplifikowany produkt PCR IL-17 o wielkości 156 pz
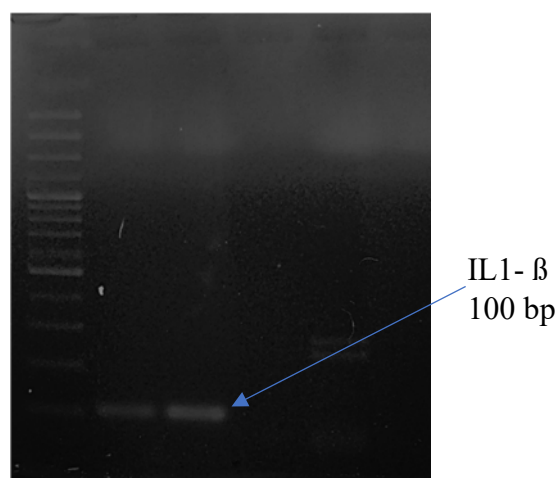
Fig. 4. PCR product was run on 2% agarose gel for 30 minutes at 90 V and 400 mA. 5 µl PCR product along with loading dye 2 µl was loaded in each well. As for size marker 100 bp ladder was used. Bands were visible which indicates that amplification of target gene IL1-ß occurred at 100 bp size

Rys. 4. Reakcję PCR prowadzono na 2% żelu agarozowym przez 30 minut przy 90 V i 400 mA. Do każdej studzienki załadowano 5 µl produktu PCR wraz z nakładającym barwnikiem 2 µl. Jako marker wielkości zastosowano wzorzec 100 bp DNA Ladder. Widoczne prążki wskazują, że amplifikacja docelowego genu IL1-β zachodziła przy wielkości 100 bp

1.4.3. Amplification of IFN-γ and TNF-α

PCR amplification was performed at of or both tumor and control tissue samples at the annealing temperature of 58°C (Figure 5). PCR amplification of TNF-α at 59°C, the gene shows clear bands of 217 bps size (Figure 7).

IFN-γ

IFN-γ
98 bps

TNF-α

TNF-α
217 bps
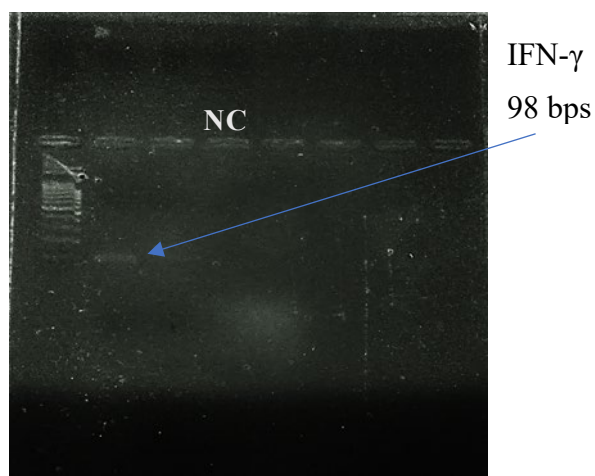
Fig. 5. PCR product was run on 2% agarose gel for 30 minutes at 90 V and 400 mA. 5 µl PCR product was loaded in each well. As for size marker 100 bp ladder was used. NC represents the negative control for the PCR reaction. The amplified PCR product of IFN-γ with the size 98 bps

Rys. 5. Reakcję PCR prowadzono na 2% żelu agarozowym przez 30 minut przy 90 V i 400 mA. Do każdej studzienki załadowano 5 µl produktu PCR. Jako marker wielkości zastosowano wzorzec 100 bp DNA Ladder. NC oznacza kontrolną próbkę negatywną dla reakcji PCR. Zaobserwowano amplifikowany produkt PCR IFN-γ o wielkości 98 bps
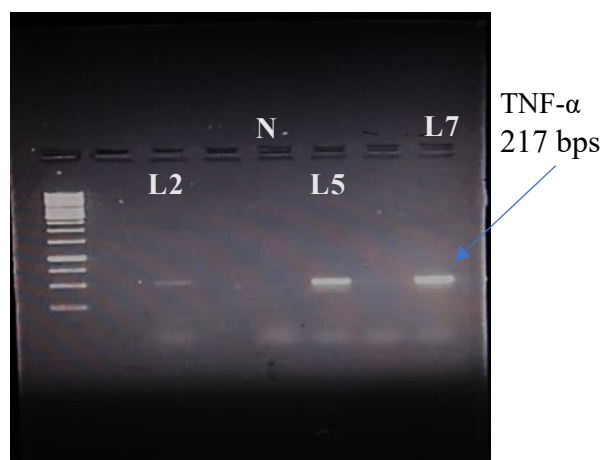
Fig. 6. PCR product was run on 2% agarose gel for 30 minutes at 90 V and 400 mA. 5 µl PCR product was loaded in each well. As for size marker 100 bp ladder was used. L2,L5 and L7 show the amplified gene while NC is negative control

Rys. 6. Reakcję PCR prowadzono na 2% żelu agarozowym przez 30 minut przy 90 V i 400 mA. Do każdej studzienki załadowano 5 µl produktu PCR. Jako marker wielkości zastosowano wzorzec 100 bp DNA Ladder. L2, L5 i L7 przedstawiają zamplifikowany gen, podczas gdy NC jest kontrolą probką negatywną

1.4.4. Amplification of FOX P3

FOX P3 was amplified at 59.5°C and the desired band size (227 bps) was obtained (Figure 7). The gradient PCR carried out at different temperatures for different genes i.e. at 60°C and 59.5°C for ß-actin and FOX P3 respectively. The amplified products are shown in Figure 8.

FOX P3
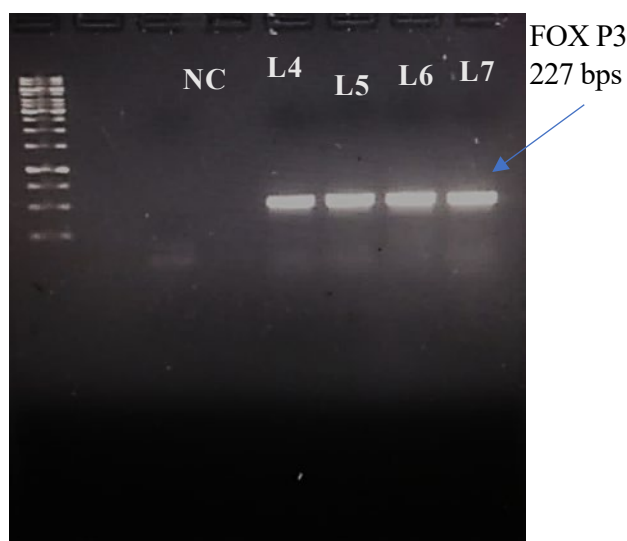
Fig. 7. PCR product was run on 2% agarose gel for 30 minutes at 90 V and 400 mA. 5 µl PCR product along with loading dye 2 µl was loaded in each well. As for size marker 100 bp ladder was used. Lane 4, 5, 6, 7 show positive samples with the amplified gene while NC is negative control

Rys. 7. Reakcję PCR prowadzono na 2% żelu agarozowym przez 30 minut przy 90 V i 400 mA. Do każdej studzienki załadowano 5 µl produktu PCR wraz z barwnikiem (2 µl). Jako marker wielkości zastosowano wzorzec 100 bp DNA Ladder. Ścieżki 4, 5, 6, 7 pokazują pozytywne próbki ze zamplifikowanym genem, podczas gdy NC jest kontrolą próbką negatywną

GRADIENT PCR
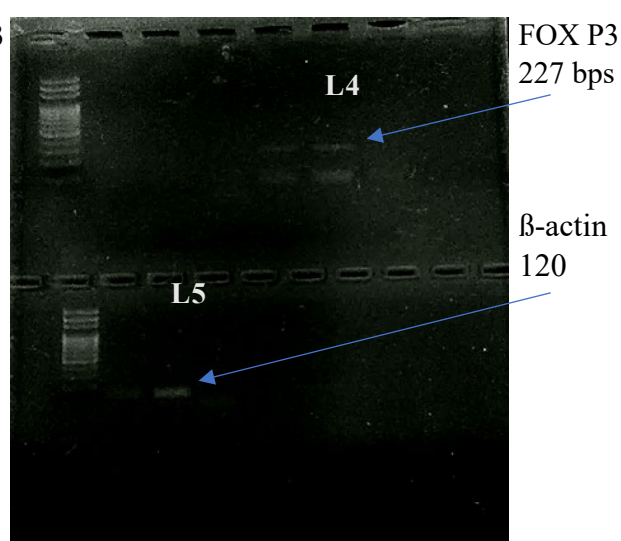
Fig. 8. PCR product was run on 2% agarose gel for 30 minutes at 90 V and 400 mA. 5 µl PCR product along with loading dye 2 µl was loaded in each well. As for size marker 100 bp ladder was used. FOX P3 with 227 bps shown in L4 while NC1 is its negative control while ß-actin with 120 bps size band is shown in L5 while NC2 is its negative control

Rys. 8. Reakcję PCR prowadzono na 2% żelu agarozowym przez 30 minut przy 90 V i 400 mA. Do każdej studzienki załadowano 5 µl produktu PCR wraz z barwnikiem (2 µl). Jako marker wielkości zastosowano wzorzec 100 bp DNA Ladder. FOX P3 z 227 bps pokazano w L4, podczas gdy NC1 jest jego kontrolą próbką negatywną. ß-aktyna z prążkiem wielkości 120 bps jest pokazana w L5, podczas gdy NC2 jest jego kontrolą próbką negatywną

1.4.5. Amplification of *IL-22*

The PCR amplification occurred at 60°C, IL-22 shows its expression as shown in Figure 9.
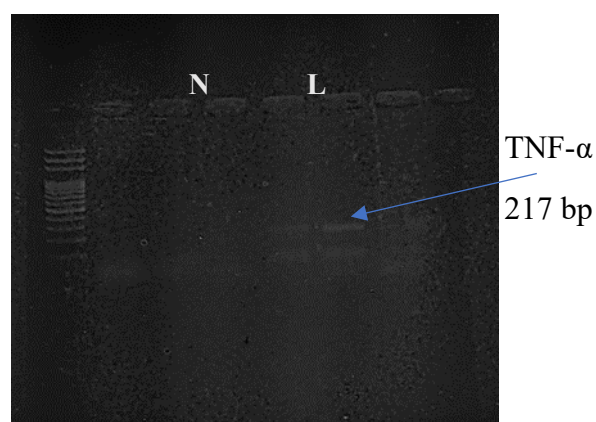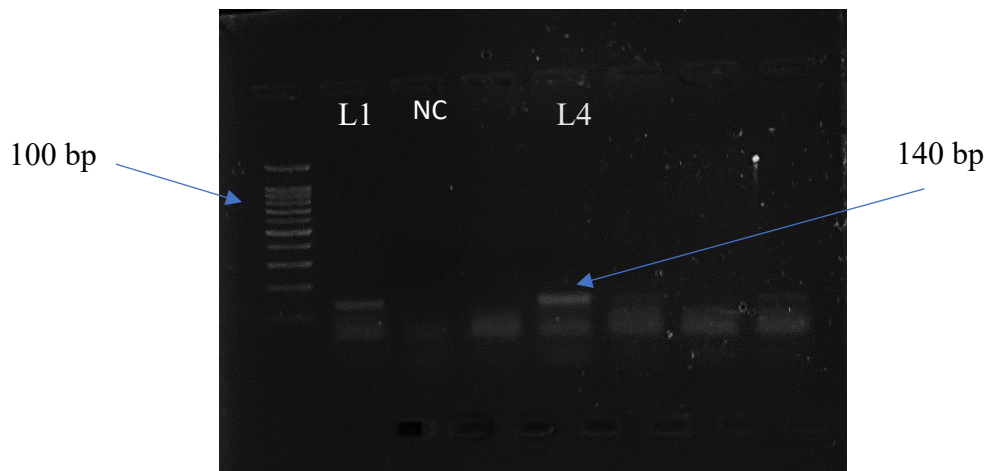
Fig. 9. PCR product was run on 2% agarose gel for 30 minutes at 90 V and 400 mA. 5 µl PCR product was loaded in each well. As for size marker 100 bp ladder was used. NC represents the negative control for the PCR reaction. L1 and L4 show 140 bps bands

Rys. 9. Reakcję PCR prowadzono na 2% żelu agarozowym przez 30 minut przy 90 V i 400 mA. Do każdej studzienki załadowano 5 µl produktu PCR. Jako marker wielkości zastosowano wzorzec 100 bp DNA Ladder. NC oznacza kontrolna próbkę negatywną dla reakcji PCR. L1 i L4 pokazują pasma 140 bps

1.4.6. Quantitative PCR

StepOne Plus™ Real Time PCR system was used. The result was determined as a ratio of relative expression level mRNA. ß-actin was used as an endogenous control. For real time assay, we used 3 technical replicates of each sample to minimize the biasness and errors that could be introduced by sample handling i.e., pipetting. Cyclic Threshold (CT) values were obtained for each sample and further normalized against the control gene (ß-actin). Relative fold changes in expression mRNA levels of *IL-22* were calculated for normal and tumor tissues.

1.4.7. Expression of *IL-22* in Colon and Gastric tumor

The expression pattern of *IL-22* mRNA, in high grade tissues of colon cancer and its normal counterparts. Our data show that relative expression levels of IL-22 gene is relatively upregulated which is significantly increase of 3-fold in mRNA levels of *IL-22* as compared to normal counterparts shown in figure 10. The significant P-value of normal and cancerous which is ≤ 0.05 are shown in Table 1 along with the standard deviation Table 2.
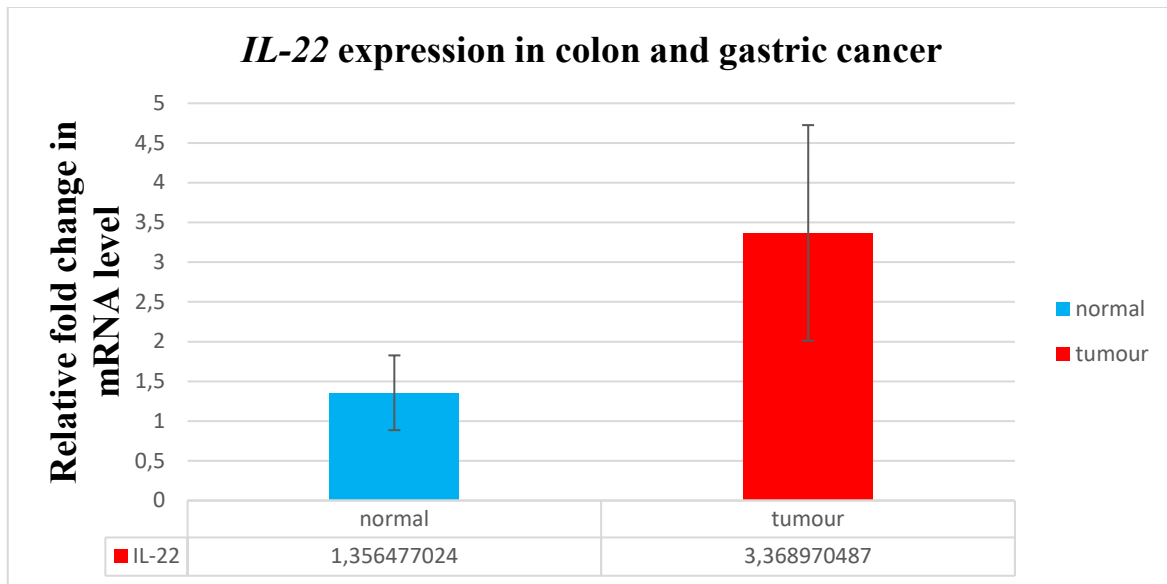
Fig. 10. Fold change expression of *IL-22* in colon and gastric cancer cases. Normal and tumor stages are indicated on x-axis and fold change mRNA expression is shown on y-axis to compare the expression of the gene with the control samples after the qPCR determination

Rys. 10. Zmiana krotności ekspresji IL-22 w przypadkach raka okrężnicy i żołądka. Etapy normalne i nowotworowe są wskazane na osi x, a krotność zmiany ekspresji mRNA jest pokazana na osi y, aby porównać ekspresję genu z próbkami kontrolnymi po określeniu qPCR

Table 1

P-value of tumor versus normal

Samples	P-Value
Tumor	0.04732836
Control	0.04732836

Table 2

Standard deviation (S.D) of tumor vs normal

Samples	Standard deviation
Tumor	1.37004959
Control	0.47046447

1.5. Discussion

The prevalence of CRC has been growing in Pakistan but, unfortunately there are no proper programs for prevention or screening [44]. Clinical techniques including colonoscopy and fecal occult blood testing have been used to screen blood, with some limitations [45–47]. Therefore, non-invasive diagnostic techniques are needed for early detection of CRC [48]. It is important to study the specific role of each cytokine in CRC development and survival as many tumorigenic cytokines are being expressed in the tissues of CRC patients [22].

In our study, statistical analysis was done using OriginPro 2016 (Origin Lab, Northampton, MA) and $P < 0.05$ was used to determine the Mann-Whitney test's significance threshold as a ratio of relative expression level mRNA. Using a Real-Time PCR technique, the relative expression of the IL-22 gene was estimated using *ß-actin* as the control gene. We observed that mRNA levels of IL-22 have increased by three times indicating the gene's relative expression levels being relatively up-regulated. Its elevated expression has already been recorded in various cancers [49] and linked to the development of colorectal/stomach cancer [50, 51]. Studies show that IL-22 is involved in the invasion of gastric cancer cells by modulating the signaling pathway of IL-22R1/AKT/MMP-9 [52]. The high expression of IL-22RA1 indicates the tumor's unfavorable prognosis [53]. An examination of IL-22 expression in human colon cancer tissue revealed that IL-22 mRNA expression was more than two times higher in the colon cancer tissue than in the adjacent normal tissues [54]. Similar findings from [55] show that it is considerably ($P < 0.05$) greater than the average. An oncogene called STAT3 controls the tumorigenic potential of IL-22 by regulating the expression of several genes involved in tumor formation [56–58].

The levels of various plasma cytokines varied significantly between CRC patients and control subjects, suggesting the possibility of differently expressed plasma cytokines as potential biomarkers for detecting the existence of CRC. We found that cytokines and interleukins (IL-17, IL1-ß, TNF-ß, IFN-ß, and FOX P3) are expressed in the patient's blood serum of the study population. These cytokines are already been reported in different populations of the world [59]. Numerous investigations have identified cytokine levels in plasma and their relationship to colorectal cancer [60].

Even with a localized tumor, interleukins are frequently identified in the bloodstream. As a result, they can serve as biomarkers to detect cancer, foretell its

effects, and manage treatment alternatives [29]. For each cytokine primer, we ran PCR amplification at a certain annealing temperature. Numerous bands of them showed their amplification in tumor samples as compared to control samples. Using a marker of 100 bp, we were able to get Interleukin 17 at a size of 156 bps. The pro-inflammatory cytokine IL-17 is up-regulated in the serum and tissues of CRC patients. Studies show that IL-17A with chemokine ligand 20 (CCL20) in serum has been found a potential diagnostic biomarker for CRC in humans [61]. Several studies have shown that IL-17 has an important role in the metastasis and prognosis of CRC [62]. It also acts as an important tumor marker in CRC patients [63] as it nurtures angiogenesis by inducting various tumorous angiogenic factors [64]. It promotes the expression and formation of other proinflammatory cytokines like IL1-ß and TNF-α [37].

Cytokine IL-17 along with TNFα collectively prompt glycolysis in CRC cells [65]. In cancer samples, we discovered amplification of the TNF-α gene with a 217-bps size. It is a crucial inflammatory cytokine in the tumor's microenvironment and promotes colon cancer invasion [66]. It also influences cancer development having an impact on CRC survival [67]. TNF-α in plasma can act as a diagnostic factor to estimate the prediction of CRC patients before other invasive tests [68]. Receptor TNF-R1 can be an optimistic biomarker of colorectal cancer playing a key role in CRC's earlier stages [69]. It regulates the gene induction of MACC1 (MET Transcriptional regulator) and displays a potential target for the treatment of CRC patients [70]. Our research revealed that the Fox P3 gene is also overexpressed at 59.5°C and has a 227-bps size. Patients with colorectal cancer have tissue with higher levels of FOXP3 than in normal [71]. Its elevated expression is related to bad prognosis in patients and is moderated by cancerous cells to progress the disease [72]. Its high level has been seen in metastasis conditions more than in patients without metastasis. It also hinders immune reaction which results in immune escape [71, 73]. Similarly, the percentage of FOXP3+Treg cells is higher in the blood of CRC patients as compared to control individuals [35].

The targeted gene of IL-1ß of 100 bp size was amplified at 58°C. Polymorphism of the IL-1β gene, accompanied by elevated levels of IL-1β has been associated with an increased risk of colon cancer development [40]. High IL-1β levels are reported in colon cancer [74, 75]. These studies have shown an association between colon IL-1β levels, the severity of IBD, and increased development and invasiveness of CRC [76]. Elevated IL-1β levels have been associated with increased colon tumor growth and invasion [77, 78]. In addition, IL-1β also inhibited the growth of xenografts *in vivo*, and may be suitable as a new therapeutic drug for CRC patients [79]. The amplified PCR product

of IFN-γ with the size 98 bps was found in our study. IFN-γ mediated by NK cells regulates IL-15 in colorectal cancer [80]. IFN-gamma leads to cell death and hinders growth [81]. The cytokine has an anti-pathogenic and immune regulatory role-playing a crucial role in organizing immune responses [82]. The control of epigenetics of the signaling pathway IFN affects tumor immunity [83].

Circulating cytokines or systemic inflammatory markers have been suggested as prognostic markers in CRC as a part of systemic inflammation [84, 85, 86]. The development and implementation of new, specific, and more sensitive biomarkers will improve diagnostic strategies soon, and allow clinicians to detect CRC cases early in the disease, thereby prognosis of thousands of patients will be improved. In this regard, more detailed research is needed on the relationship between diet, microbiota, and CRC. The upregulation of these immune cytokines can serve as an important indicator of disease progression.

1.6. Conclusion

Quantification of cytokines is still in progressing stage and there is a need to find an effective solution for the real-time identification of cytokines in vivo. In-depth study is needed to comprehend the mechanisms underlying immunological biomarkers and how they impact the onset and progression of colorectal cancer. The improvement of antitumor responses and reduction of the immune cells supporting tumor growth must be anticipated by cytokine-based cancer therapy.

Bibliography

1. Cooper G.M. (2000). The Cell: A Molecular Approach. 2nd edition. Sinauer Associates 2000. http://lib.ugent.be/catalog/ebk01:3450000000002155.

2. Liang H., Wang X.N., Wang B.G., Pan Y., Liu N., Wang D.C., Hao X.S. (2006). Prognostic factors of young patients with colon cancer after surgery. World J Gastroenterol, 12(9), 1458–1462. https://doi.org/10.3748/wjg.v12.i9.1458.

3. Maryam S., Krukiewicz K., Haq I.U., Khan A.A., Yahya G., Cavalu S. (2023). Interleukins (Cytokines) as Biomarkers in Colorectal Cancer: Progression, Detection, and Monitoring. Journal of Clinical Medicine, 12(9), 3127.

4. Bray F., Ferlay J., Soerjomataram I., Siegel R.L., Torre L.A., Jemal A. (2018). Global cancer statistics 2018: GLOBOCAN estimates of incidence and mortality worldwide for 36 cancers in 185 countries [https://doi.org/10.3322/caac.21492]. CA: A Cancer Journal for Clinicians, 68(6), 394–424. https://doi.org/https://doi.org/10.3322/caac.21492.

5. Keum N., Giovannucci E. (2019). Global burden of colorectal cancer: emerging trends, risk factors and prevention strategies. Nature Reviews Gastroenterology & Hepatology, 16. https://doi.org/10.1038/s41575-019-0189-8.

6. Nuranna L., Donny N.B., Purwoto G., Winarto H., Utami T.W., Anggraeni T.D., Peters A.A.W. (2017). Prevalence, Age Distribution, and Risk Factors of Visual Inspection With Acetic Acid-Positive From 2007 to 2011 in Jakarta. J Cancer Prev, 22(2), 103–107. https://doi.org/10.15430/jcp.2017.22.2.103.

7. Bhurgri Y., Khan T., Kayani N., Ahmad R., Usman A., Bhurgri A., Bashir I., Hasan S.H., Zaidi S. (2011). Incidence and current trends of colorectal malignancies in an unscreened, low risk Pakistan population. Asian Pac J Cancer Prev, 12(3), 703-708.

8. Idrees R., Fatima S., Abdul-Ghafar J., Raheem A., Ahmad Z. (2018). Cancer prevalence in Pakistan: meta-analysis of various published studies to determine variation in cancer figures resulting from marked population heterogeneity in different parts of the country. World J Surg Oncol, 16(1), 129. https://doi.org/10.1186/s12957-018-1429-z.

9. Williams R., White P., Nieto J., Vieira D., Francois F., Hamilton F. (2016). Colorectal Cancer in African Americans: An Update. Clin Transl Gastroenterol, 7(7), e185. https://doi.org/10.1038/ctg.2016.36.

10. Kune G.A., Bannerman S., Watson L.F. (1992). Attributable risk for diet, alcohol, and family history in the Melbourne Colorectal Cancer Study. Nutr Cancer, 18(3), 231–235. https://doi.org/10.1080/01635589209514223.

11. Botteri E., Iodice S., Bagnardi V., Raimondi S., Lowenfels A.B., Maisonneuve P. (2008). Smoking and colorectal cancer: a meta-analysis. Jama, 300(23), 2765–2778. https://doi.org/10.1001/jama.2008.839.

12. Giovannucci E. (2002). Modifiable risk factors for colon cancer. Gastroenterol Clin North Am, 31(4), 925–943. https://doi.org/10.1016/s0889-8553(02)00057-2.

13. Roynette C.E., Calder P.C., Dupertuis Y.M., Pichard C. (2004). n-3 polyunsaturated fatty acids and colon cancer prevention. Clin Nutr, 23(2), 139–151. https://doi.org/10.1016/j.clnu.2003.07.005.

14. Whitlock K., Gill R.S., Birch D.W., Karmali S. (2012). The Association between Obesity and Colorectal Cancer. Gastroenterol Res Pract, 2012, 768247. https://doi.org/10.1155/2012/768247.

15. Marventano S., Forjaz M., Grosso G., Mistretta A., Giorgianni G., Platania A., Gangi S., Basile F., Biondi A. (2013). Health related quality of life in colorectal cancer patients: state of the art. BMC Surg, 13 Suppl 2(Suppl 2), S15. https://doi.org/10.1186/1471-2482-13-s2-s15.

16. Vacante M., Borzì A.M., Basile F., Biondi A. (2018). Biomarkers in colorectal cancer: Current clinical utility and future perspectives. World J Clin Cases, 6(15), 869881. https://doi.org/10.12998/wjcc.v6.i15.869.

17. Febbo P.G., Ladanyi M., Aldape K.D., De Marzo A.M., Hammond M.E., Hayes D.F., Iafrate A.J., Kelley R.K., Marcucci G., Ogino S., Pao W., Sgroi D.C., Birkeland M.L. (2011). NCCN Task Force report: Evaluating the clinical utility of tumor markers in oncology. J Natl Compr Canc Netw, 9 Suppl 5, S1–32; quiz S33. https://doi.org/10.6004/jnccn.2011.0137.

18. Wang J., Li D., Cang H., Guo B. (2019). Crosstalk between cancer and immune cells: Role of tumor-associated macrophages in the tumor microenvironment. Cancer Med, 8(10), 4709–4721. https://doi.org/10.1002/cam4.2327.

19. Multhoff G., Molls M., Radons J. (2011). Chronic inflammation in cancer development. Front Immunol, 2, 98. https://doi.org/10.3389/fimmu.2011.00098.

20. Wu Y., Zhou B.P. (2009). Inflammation: a driving force speeds cancer metastasis. Cell Cycle, 8(20), 3267–3273. https://doi.org/10.4161/cc.8.20.9699.

21. Mager L.F., Wasmer M.H., Rau T.T., Krebs P. (2016). Cytokine-Induced Modulation of Colorectal Cancer. Front Oncol, 6, 96. https://doi.org/10.3389/fonc.2016.00096.

22. Mlecnik B., Bindea G., Angell H.K., Sasso M.S., Obenauf A.C., Fredriksen T., Lafontaine L., Bilocq A.M., Kirilovsky A., Tosolini M., Waldner M., Berger A., Fridman W.H., Rafii A., Valge-Archer V., Pages F., Speicher M.R., Galon J. (2014). Functional network pipeline reveals genetic determinants associated with in situ

lymphocyte proliferation and survival of cancer patients. Sci Transl Med, 6(228), 228ra237. https://doi.org/10.1126/scitranslmed.3007240.

23. Lee S., Margolin K. (2011). Cytokines in cancer immunotherapy. Cancers (Basel), 3(4), 3856–3893. https://doi.org/10.3390/cancers3043856.

24. Kantola T., Klintrup K., Väyrynen J.P., Vornanen J., Bloigu R., Karhu T., Herzig K.H., Näpänkangas J., Mäkelä J., Karttunen T.J., Tuomisto A., Mäkinen M.J. (2012). Stage-dependent alterations of the serum cytokine pattern in colorectal carcinoma. Br J Cancer, 107(10), 1729–1736. https://doi.org/10.1038/bjc.2012.456.

25. Li J., Huang L., Zhao H., Yan Y., Lu J. (2020). The Role of Interleukins in Colorectal Cancer. Int J Biol Sci, 16(13), 2323–2339. https://doi.org/10.7150/ijbs.46651.

26. Ning C., Li Y.Y., Wang Y., Han G.C., Wang R.X., Xiao H., Li X.Y., Hou C.M., Ma Y.F., Sheng D.S., Shen B.F., Feng J.N., Guo R.F., Li Y., Chen G.J. (2015). Complement activation promotes colitis-associated carcinogenesis through activating intestinal IL-1β/IL-17A axis. Mucosal Immunol, 8(6), 1275–1284. https://doi.org/10.1038/ mi.2015.18.

27. Hai Ping P., Feng Bo T., Li L., Nan Hui Y., Hong Z. (2016). IL-1β/NF-kb signaling promotes colorectal cancer cell growth through miR-181a/PTEN axis. Arch Biochem Biophys, 604, 20–26. https://doi.org/10.1016/j.abb.2016.06.001.

28. Zhang Y., Davis C., Shah S., Hughes D., Ryan J.C., Altomare D., Peña M.M. (2017). IL-33 promotes growth and liver metastasis of colorectal cancer in mice by remodeling the tumor microenvironment and inducing angiogenesis. Mol Carcinog, 56(1), 272–287. https://doi.org/10.1002/mc.2249.

29. Kartikasari A.E.R., Huertas C.S., Mitchell A., Plebanski M. (2021). Tumor-Induced Inflammatory Cytokines and the Emerging Diagnostic Devices for Cancer Detection and Prognosis. Front Oncol, 11, 692142. https://doi.org/10.3389/fonc.2021.692142.

30. Nemati K., Golmoghaddam H., Hosseini S.V., Ghaderi A., Doroudchi M. (2015). Interleukin-17FT7488 allele is associated with a decreased risk of colorectal cancer and tumor progression. Gene, 561(1), 88–94. https://doi.org/10.1016/j.gene.2015.02.014.

31. Tosolini M., Kirilovsky A., Mlecnik B., Fredriksen T., Mauger S., Bindea G., Berger A., Bruneval P., Fridman W.H., Pages F., Galon J. (2011). Clinical impact of different classes of infiltrating T cytotoxic and helper cells (Th1, th2, treg, th17) in patients with colorectal cancer. Cancer Res, 71(4), 1263–1271. https://doi.org/10.1158/0008-5472.can-10-2907.

32. Tseng J.Y., Yang C.Y., Liang S.C., Liu R.S., Yang S.H., Lin J.K., Chen Y.M., Wu Y.C., Jiang J.K., Lin C.H. (2014). Interleukin-17A modulates circulating tumor cells in tumor draining vein of colorectal cancers and affects metastases. Clin Cancer Res, 20(11), 2885–2897. https://doi.org/10.1158/1078-0432.ccr-13-2162.

33. Huang Y.H., Cao Y.F., Jiang Z.Y., Zhang S., Gao F. (2015). Th22 cell accumulation is associated with colorectal cancer development. World J Gastroenterol, 21(14), 4216–4224. https://doi.org/10.3748/wjg.v21.i14.4216.

34. Wu T., Wang Z., Liu Y., Mei Z., Wang G., Liang Z., Cui A., Hu X., Cui L., Yang Y., Liu C.Y. (2014). Interleukin 22 protects colorectal cancer cells from chemotherapy by activating the STAT3 pathway and inducing autocrine expression of interleukin 8. Clin Immunol, 154(2), 116–126. https://doi.org/10.1016/j.clim.2014.07.005.

35. Liu Z., Huang Q., Liu G., Dang L., Chu D., Tao K., Wang W. (2014). Presence of FOXP3(+)Treg cells is correlated with colorectal cancer progression. Int J Clin Exp Med, 7(7), 1781–1785.

36. Luo Q., Zhang S., Wei H., Pang X., Zhang H. (2015). Roles of Foxp3 in the occurrence and development of cervical cancer. Int J Clin Exp Pathol, 8(8), 8717–8730.

37. Jovanovic D.V., Di Battista J.A., Martel-Pelletier J., Jolicoeur F.C., He Y., Zhang M., Mineau F., Pelletier J.P. (1998). IL-17 stimulates the production and expression of proinflammatory cytokines, IL-beta and TNF-alpha, by human macrophages. J Immunol, 160(7), 3513–3521.

38. Al Obeed O.A., Alkhayal K.A., Al Sheikh A., Zubaidi A.M., Vaali-Mohammed M.A., Boushey R., McKerrow J.H., Abdulla M.H. (2014). Increased expression of tumor necrosis factor-α is associated with advanced colorectal cancer stages. World J Gastroenterol, 20(48), 18390–18396. https://doi.org/10.3748/wjg.v20.i48.18390.

39. Wang L., Wang Y., Song Z., Chu J., Qu X. (2015). Deficiency of interferon-gamma or its receptor promotes colorectal cancer development. J Interferon Cytokine Res, 35(4), 273–280. https://doi.org/10.1089/jir.2014.0132.

40. Gunter M.J., Canzian F., Landi S., Chanock S.J., Sinha R., Rothman N. (2006). Inflammation-related gene polymorphisms and colorectal adenoma. Cancer Epidemiol Biomarkers Prev, 15(6), 1126–1131. https://doi.org/10.1158/1055-9965.Epi-06-0042.

41. Cohen I., Rider P., Carmi Y., Braiman A., Dotan S., White M.R., Voronov E., Martin M.U., Dinarello C.A., Apte R.N. (2010). Differential release of chromatin-bound IL-1alpha discriminates between necrotic and apoptotic cell death by

the ability to induce sterile inflammation. Proc Natl Acad Sci U S A, 107(6), 2574–2579. https://doi.org/10.1073/pnas.0915018107.

42. Rider P., Carmi Y., Guttman O., Braiman A., Cohen I., Voronov E., White M.R., Dinarello C.A., Apte R.N. (2011). IL-1alpha and IL-1beta recruit different myeloid cells and promote different stages of sterile inflammation. J Immunol, 187(9), 4835–4843. https://doi.org/10.4049/jimmunol.1102048.

43. Wei X., Zhang Y., Yang Z., Sha Y., Pan Y., Chen Y., Cai L. (2020). Analysis of the role of the interleukins in colon cancer. Biological Research, 53(1), 20. https://doi.org/ 10.1186/s40659-020-00287-2.

44. Hasan F., Mahmood Shah S.M., Munaf M., Khan M.R., Marsia S., Haaris S.M., Shaikh M.H., Abdur Rahim I., Anwar M.S., Qureshi K.S., Iqbal M., Qazi S., Kasi B.A., Tahir M., Ur Rehman S.I., Fatima K. (2017). Barriers to Colorectal Cancer Screening in Pakistan. Cureus, 9(7), e1477. https://doi.org/10.7759/ cureus.1477.

45. Levin B., Lieberman D.A., McFarland B., Smith R.A., Brooks D., Andrews K.S., Dash C., Giardiello F.M., Glick S., Levin T.R., Pickhardt P., Rex D.K., Thorson A., Winawer, S.J. (2008). Screening and surveillance for the early detection of colorectal cancer and adenomatous polyps, 2008: a joint guideline from the American Cancer Society, the US Multi-Society Task Force on Colorectal Cancer, and the American College of Radiology. CA Cancer J Clin, 58(3), 130–160. https://doi.org/10.3322/ ca.2007.0018.

46. Bond J.H. (2002). Fecal occult blood test screening for colorectal cancer. Gastrointest Endosc Clin N Am, 12(1), 11–21. https://doi.org/10.1016/s1052-5157(03)00054-0

47. Pox C.P., Schmiegel W. (2010). Role of CT colonography in colorectal cancer screening: risks and benefits. Gut, 59(5), 692–700. https://doi.org/10.1136/ gut.2009.183046.

48. Mármol I., Sánchez-de-Diego C., Pradilla Dieste A., Cerrada E., Rodriguez Yoldi M.J. (2017). Colorectal Carcinoma: A General Overview and Future Perspectives in Colorectal Cancer. Int J Mol Sci, 18(1). https://doi.org/10.3390/ijms18010197.

49. Petanidis S., Anestakis D., Argyraki M., Hadzopoulou-Cladaras M., Salifoglou A. (2013). Differential expression of IL-17, 22 and 23 in the progression of colorectal cancer in patients with K-ras mutation: Ras signal inhibition and crosstalk with GM-CSF and IFN-gamma. PLoS One, 8(9), e73616. https://doi.org/10.1371/ journal.pone.0073616.

50. Kryczek I., Lin Y., Nagarsheth N., Peng D., Zhao L., Zhao E., Vatan L., Szeliga W., Dou Y., Owens S. (2014). IL-22+ CD4+ T cells promote colorectal cancer stemness

via STAT3 transcription factor activation and induction of the methyltransferase DOT1L. Immunity, 40(5), 772–784.

51. Zhuang Y., Peng L.-s., Zhao Y.-l., Shi Y., Mao X.-h., Guo G., Chen W., Liu X.-f., Zhang J.-y., Liu T. (2012). Increased intratumoral IL-22-producing CD4+ T cells and Th22 cells correlate with gastric cancer progression and predict poor patient survival. Cancer Immunology, Immunotherapy, 61(11), 1965–1975.

52. Ji Y., Yang X., Li J., Lu Z., Li X., Yu J., Li N. (2014). IL-22 promotes the migration and invasion of gastric cancer cells via IL-22R1/AKT/MMP-9 signaling. Int J Clin Exp Pathol, 7(7), 3694–3703.

53. McCuaig S., Barras D., Mann E.H., Friedrich M., Bullers S.J., Janney A., Garner L.C., Domingo E., Koelzer V.H., Delorenzi M., Tejpar S., Maughan T.S., West N.R., Powrie F. (2020). The Interleukin 22 Pathway Interacts with Mutant KRAS to Promote Poor Prognosis in Colon Cancer. Clinical Cancer Research, 26(16), 4313–4325. https://doi.org/10.1158/1078-0432.Ccr-19-1086.

54. Harrison C. (2013). IL-22: linking inflammation and cancer. Nature Reviews Drug Discovery, 12(7), 505–505. https://doi.org/10.1038/nrd4065.

55. Xi X., Hu R., Wang Q., Xu K., Yang H., Cui Z., Zhang Y., Teng M., Xia L., Chen J., Liu Y. (2021). Interleukin-22 promotes PD-L1 expression via STAT3 in colon cancer cells. Oncol Lett, 22(4), 716. https://doi.org/10.3892/ol.2021.12977.

56. Fathi N., Rashidi G., Khodadadi A., Shahi S. Sharifi S. (2018). STAT3 and apoptosis challenges in cancer. Int J Biol Macromol, 117, 993–1001. https://doi.org/10.1016/ j.ijbiomac.2018.05.121.

57. Galoczova M., Coates P., Vojtesek B. (2018). STAT3, stem cells, cancer stem cells and p63. Cellular & molecular biology letters, 23(1), 1–20.

58. Yu H., Lee H., Herrmann A., Buettner R., Jove R. (2014). Revisiting STAT3 signalling in cancer: new and unexpected biological functions. Nature Reviews Cancer, 14(11), 736–746.

59. Klampfer L. (2011). Cytokines, inflammation and colon cancer. Curr Cancer Drug Targets, 11(4), 451–464. https://doi.org/10.2174/156800911795538066.

60. Yamaguchi M., Okamura S., Yamaji T., Iwasaki M., Tsugane S., Shetty,V., Koizumi T. (2019). Plasma cytokine levels and the presence of colorectal cancer. PLoS One, 14(3), e0213602. https://doi.org/10.1371/journal.pone.0213602.

61. Wang D., Yuan W., Wang Y., Wu Q., Yang L., Chen X., Zhang Z., Yu W., Maimela N., Cao L., Wang D., Wang J., Sun Z., Liu J., Zhang Y. (2019). Serum CCL20 combined with IL-17A as early diagnostic and prognostic biomarkers for human colorectal cancer. Journal of Translational Medicine, 17. https://doi.org/10.1186/ s12967-019-2008-y.

62. Razi S., Baradaran Noveiry B., Keshavarz-Fathi M., Rezaei N. (2019). IL-17 and colorectal cancer: From carcinogenesis to treatment. Cytokine, 116, 7–12. https://doi.org/https://doi.org/10.1016/j.cyto.2018.12.021.

63. Radosavljevic G., Ljujic B., Jovanovic I., Srzentic Z., Pavlovic S., Zdravkovic N., Milovanovic M., Bankovic D., Knezevic M., Acimovic L.J., Arsenijevic N. (2010). Interleukin-17 may be a valuable serum tumor marker in patients with colorectal carcinoma. Neoplasma, 57(2), 135–144. https://doi.org/10.4149/neo_2010_02_135.

64. Numasaki M., Fukushi J., Ono M., Narula S.K., Zavodny P.J., Kudo T., Robbins P.D., Tahara H., Lotze M.T. (2003). Interleukin-17 promotes angiogenesis and tumor growth. Blood, 101(7), 2620–2627. https://doi.org/10.1182/blood-2002-05-1461.

65. Straus D.S. (2013). TNFα and IL-17 cooperatively stimulate glucose metabolism and growth factor production in human colorectal cancer cells. Mol Cancer, 12, 78. https://doi.org/10.1186/1476-4598-12-78.

66. Zhao P., Zhang Z. (2018). TNF-α promotes colon cancer cell migration and invasion by upregulating TROP-2. Oncol Lett, 15(3), 3820–3827. https://doi.org/10.3892/ol.2018.7735.

67. Stanilov N., Miteva L., Dobreva Z., Stanilova S. (2014). Colorectal cancer severity and survival in correlation with tumour necrosis factor-alpha. Biotechnol Biotechnol Equip, 28(5), 911–917. https://doi.org/10.1080/13102818.2014.965047.

68. Warsinggih, Limanu F., Labeda I., Lusikooy R., Mappincara, Faruk M. (2021). The relationship of tumor necrosis factor alpha levels in plasma toward the stage and differentiation degree in colorectal cancer. Medicina Clínica Práctica, 4, 100224. https://doi.org/10.1016/j.mcpsp.2021.100224.

69. Hosono K., Yamada E., Endo H., Takahashi H., Inamori M., Hippo Y., Nakagama H., Nakajima A. (2012). Increased tumor necrosis factor receptor 1 expression in human colorectal adenomas. World J Gastroenterol, 18(38), 5360–5368. https://doi.org/ 10.3748/wjg.v18.i38.5360.

70. Kobelt D., Zhang C., Clayton-Lucey I.A., Glauben R., Voss C., Siegmund B., Stein U. (2020). Pro-inflammatory TNF-α and IFN-γ Promote Tumor Growth and Metastasis via Induction of MACC1 [Original Research]. Frontiers in Immunology, 11. https://doi.org/10.3389/fimmu.2020.00980.

71. Liu Z., Huang Q., Liu G., Dang L., Chu D., Tao K., Wang W. (2014). Presence of FOXP3+ Treg cells is correlated with colorectal cancer progression. International journal of clinical and experimental medicine, 7(7), 1781.

72. Kim M., Grimmig T., Grimm M., Lazariotou M., Meier E., Rosenwald A., Tsaur I., Blaheta R., Heemann U., Germer C.T., Waaga-Gasser A.M., Gasser M. (2013).

Expression of Foxp3 in colorectal cancer but not in Treg cells correlates with disease progression in patients with colorectal cancer. PLOS ONE, 8(1), e53630. https://doi.org/10.1371/journal.pone.0053630.

73. Jiang L.L., Ruan L.-W. (2014). Association between FOXP3 promoter polymorphisms and cancer risk: A meta-analysis. Oncology Letters, 8(6), 2795–2799.

74. Apte R.N., Voronov E. (2002). Interleukin-1--a major pleiotropic cytokine in tumor-host interactions. Semin Cancer Biol, 12(4), 277–290. https://doi.org/10.1016/s1044-579x(02)00014-7.

75. Colasante A., Mascetra N., Brunetti M., Lattanzio G., Diodoro M., Caltagirone S., Musiani P., Aiello F.B. (1997). Transforming growth factor beta 1, interleukin-8 and interleukin-1, in non-small-cell lung tumors. Am J Respir Crit Care Med, 156(3 Pt 1), 968–973. https://doi.org/10.1164/ajrccm.156.3.9701122.

76. Voronov E., Apte R.N. (2015). IL-1 in Colon Inflammation, Colon Carcinogenesis and Invasiveness of Colon Cancer. Cancer Microenviron, 8(3), 187–200. https://doi.org/10.1007/s12307-015-0177-7.

77. Jedinak A., Dudhgaonkar S., Sliva D. (2010). Activated macrophages induce metastatic behavior of colon cancer cells. Immunobiology, 215(3), 242–249. https://doi.org/10.1016/j.imbio.2009.03.004.

78. Kaler P., Augenlicht L., Klampfer L. (2009). Macrophage-derived IL-1beta stimulates Wnt signaling and growth of colon cancer cells: a crosstalk interrupted by vitamin D3. Oncogene, 28(44), 3892–3902. https://doi.org/10.1038/onc.2009.247.

79. Chen Y., Yang Z., Deng B., Wu D., Quan Y., Min Z. (2020). Interleukin 1β/1RA axis in colorectal cancer regulates tumor invasion, proliferation and apoptosis via autophagy. Oncol Rep, 43(3), 908–918. https://doi.org/10.3892/or.2020.7475.

80. Cui F., Qu D., Sun R., Zhang M., Nan K. (2020). NK cell-produced IFN-γ regulates cell growth and apoptosis of colorectal cancer by regulating IL-15. Exp Ther Med, 19(2), 1400–1406. https://doi.org/10.3892/etm.2019.8343.

81. Razaghi A., Owens L., Heimann K. (2016). Review of the recombinant human interferon gamma as an immunotherapeutic: Impacts of production platforms and glycosylation. J Biotechnol, 240, 48–60. https://doi.org/10.1016/j.jbiotec.2016.10.022.

82. Mendoza J.L., Escalante N.K., Jude K.M., Sotolongo Bellon J., Su L., Horton T.M., Tsutsumi N., Berardinelli S.J., Haltiwanger R.S., Piehler J., Engleman E.G., Garcia K.C. (2019). Structure of the IFNγ receptor complex guides design of biased agonists. Nature, 567(7746), 56–60. https://doi.org/10.1038/s41586-019-0988-7.

83. Du W., Frankel T.L., Green M., Zou W. (2022). IFNγ signaling integrity in colorectal cancer immunity and immunotherapy. Cellular & Molecular Immunology, 19(1), 23–32. https://doi.org/10.1038/s41423-021-00735-3.

84. Diakos C.I., Charles K.A., McMillan D.C., Clarke S.J. (2014). Cancer-related inflammation and treatment effectiveness. Lancet Oncol, 15(11), e493–503. https://doi.org/ 10.1016/s1470-2045(14)70263-3.

85. Sylman J.L., Mitrugno A., Atallah M., Tormoen G.W., Shatzel J.J., Tassi Yunga S., Wagner T.H., Leppert J.T., Mallick P., McCarty O.J.T. (2018). The Predictive Value of Inflammation-Related Peripheral Blood Measurements in Cancer Staging and Prognosis. Front Oncol, 8, 78. https://doi.org/10.3389/fonc.2018.00078.

86. Turner M.D., Nedjai B., Hurst T., Pennington D.J. (2014). Cytokines and chemokines: At the crossroads of cell signalling and inflammatory disease. Biochimica et Biophysica Acta (BBA) – Molecular Cell Research, 1843(11), 2563–2582. https://doi.org/https:// doi.org/10.1016/j.bbamcr.2014.05.014.

MODULATION OF CYTOKINES' EXPRESSIONS IN COLORECTAL CANCER (CRC) PATIENTS IN TERTIARY CARE HOSPITALS OF PAKISTAN

Abstract

Cancer is a leading cause of death worldwide, accounting for nearly 10 million deaths, including 935000 colorectal cancer (CRC) cases in 2020 (WHO). One of the most prevalent forms of cancer, colorectal cancer is the second and third most common malignancy in men and women, respectively. Chronic inflammation, activated immune cells, and growth factors modulate the release of cytokines in tumor tissues. CRC has been linked, in particular, to alteration in the expression of interleukins including IL-17, IL-22, and IL-1ß. The objective of the current investigation was to identify the expression of cytokines implicated in CRC tumor development and progression. We discovered that the IL-22 gene's relative expression level was increased in CRC by three times and was consequently linked to the development of the tumor. The immune system releases these interleukins at different phases of CRC, and they can serve as biomarkers.

Jarosław GIL [1,*], Andrzej POLAŃSKI [1]

Chapter 2. MODELLING CLONAL EVOLUTION OF TUMOURS BY USING HIGH RESOLUTION STOCHASTIC SIMULATIONS

2.1. Introduction

Tumor growth, caused by accumulation of genomic somatic mutations, which disturb and eventually dysregulate cellular processes of signaling, metabolism and replication, is a complex process with various stages and modes of dynamics. Fundamental research on scenarios and mechanisms of tumor evolution, combined with observational data and biological/genetic knowledge, is of great importance for cancer research. There are many studies both theoretical and experimental devoted to characterization/observation of the process of progression of tumors. The latter ones, especially those using high throughput molecular biology assays provide quantitative background for studies on scenarios of cancer development [1-3].

Important insights to the study of dynamics of cancer evolution are given by mathematical/computational modelling tools. Mathematical models require introducing a lot of simplifying hypotheses in order to obtain interpretable conclusions. Computational stochastic simulation approaches allow for address wider range of evolution scenarios, important for explaining observational data, which are recently becoming available [3, 4]. There are several attempts to provide mathematical models able to reflect at least some properties of evolving tumor [5-7].

We present a stochastic simulation tool, based on Gillespie algorithm [8] for modelling evolution of cancer cells population. Replication process of cancer cells is affected by two types of somatic mutations occur, driver with high impact on tumor growth and passenger, assumed to have mildly deleterious effect. The elaborated algorithm allows for high resolution modelling of evolution of cancer, with

---

[1] Silesian University of Technology, Poland.
[*] Corresponding author: jaroslaw.gil@polsl.pl.

distinguishing between cancer cells and both types of somatic mutations occurring over time. It allows for confronting simulation results with experimental data concerning clonal structures of tumor cells and statistics of somatic mutations.

2.2. Scenario of evolution with driver and passenger mutations

Tumor cells evolution scenario, on which algorithm is based, consist of three possible events: cell death, cell division or cell division with mutation. Mutation types are considered as passenger (slightly deleterious effect) or driver (highly advantageous effect). When driver mutation occurs, its high effect on cell fitness is likely to create a new clone, which also have positive impact on cell division probability. Each cell in one clone have same driver mutation set. Passenger mutations provide differentiation between cells. Each passenger mutation causes mildly or no effect on fitness cell. When mutation is considered to have impact on cell fitness its accumulation in one cell increases death probability. Figure 1 describes all evolutionary events considered in algorithm construction.

Intensity of the cell division process depends on cell fitness and population size. When cell fitness is high it is more likely that cell will divide or/and mutate, on the contrary when cell fitness is low the probability of cell death is higher. Also, population size has impact on event probability. When population size is large more events occur and worse adapted cells are dying. In the course of evolution, the phenomenon of clonal interference takes place. Clonal interference is extinction of already existing clones, which are replaced by new ones. When a new clone with mean fitness of its cells emerges in the evolution it is likely that it displaces existing one ore one. The process of clonal interference is nonlinear, depends on fitness of neoplastic cells in clones as well as on clones' sizes.

The size of the whole population of cancer cells evolves according to the dynamics shaped by the mean fitness of all cancer cells. Depending on accumulated effects of deleterious and advantageous mutations acquired during evolution the cancer cells population can either increase in size, and eventually explode or decrease and extinct. Probabilities of these two scenarios depend on intensities of occurrences of driver and passenger mutations and on strengths (relative strengths) of their positive/negative selection effects.
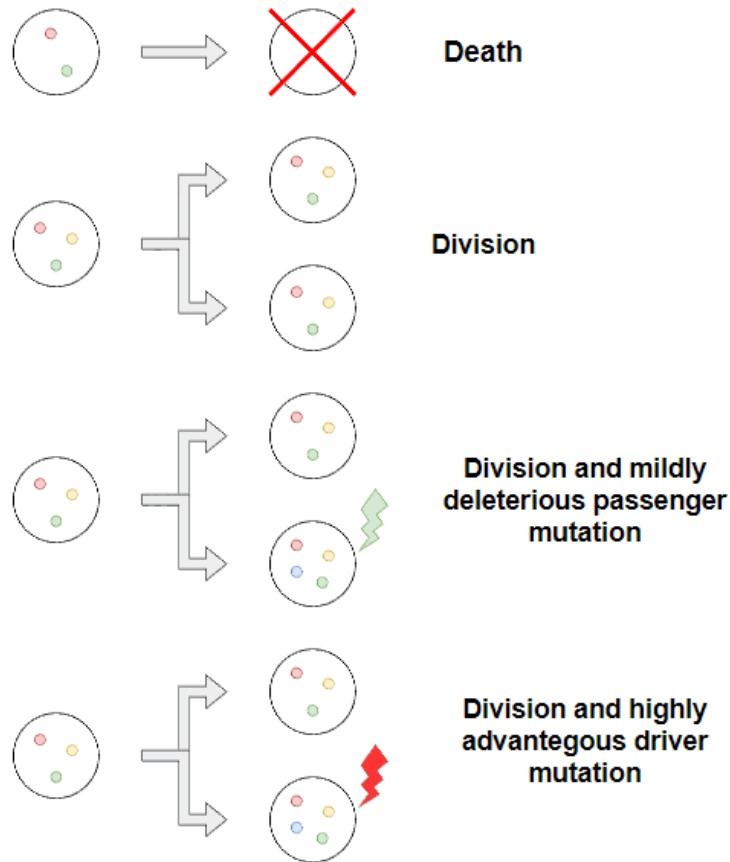
Fig. 1. Stochastic events in the evolution scenario of clonal growth of cancer
Rys. 1. Zjawiska występujące w trakcie rozwoju poopulacji komórek nowotworowych

2.2.1. Division process

Cell division probability/intensity depends on its fitness. Higher fitness provides higher chance for cell to divide. Division time can be calculated using formula (1)

$$t_{div} = random.\,exponential(1)\,/\,fitness \tag{1}$$

where division time of cell without mutations is calculated from exponential distribution. The "random.exponential(1)" notation in the above equation denotes a number generated by pseudo random generator function of exponential distribution with scale parameter equal to one. Scaling by fitness produces the variable on the left-hand side of the above equation with probability distribution adequately characterizing the process of division of cells of given fitness. Division time is inversely proportional to fitness value. In each simulation step event with event time as low as possible are considered.

2.2.2. Death process

Cell death is mostly dependent on population size. If number of cells is greater than population capacity it is more likely for cell to die. Death time can be calculated using formula (2)

$$t_{dth} = random.exponential(1) * \frac{N}{K}$$ (2)

where N denotes population size and K defines population capacity, "random.exponential(1)" has the same meaning as previously. If cells number exceeds population capacity it is more likely for cell to die than to divide.

Cell death event is considered to have bigger priority than division or division and mutation.

2.2.3. Mutation processes and its offect on fittness

Mutation can be divided into two types: passenger and driver mutation type. Passenger mutation provides cells differentiation while driver mutation provides creation of new clone. Mostly considered are events where driver mutation have mildly adventegous effect on cell fitness and passenger mutation have slightly negative effect. Cell fitness is calculated using formula (3)

$$fitness = \frac{(1 + s)^l}{(1 + f)^k}$$ (3)

where s stands for driver mutation, advantegous effect, f stand for passenger mutation deleterious effect and l and k are numbers of, respectively, driver and passenger mutations in cell.

2.2.4. Parameters of processes

In Table 1 examplary simulation parameters are presented. Driver mutation effect is considered to be quite high (about 2–5%) while passenger mutation efect should be lower (about 0.1–0.5%). Passenger mutation effect also should be considered as negative effect while driver as positive. The probabilty of mutation occurance should be respectively low for driver type and high for passenger type of mutation. As population capacity we assume the initial population size.

Table 1

Example simulation parameters
Model parameters

Mutation effect	High for driver mutation: f.e. 2%, low for passenger mutation: f.e. 0.2%
Initial population	10'000
Population capacity	10'000
Mutation probability	Low for driver mutation: f.e. 1%, high for passenger mutation: f.e. 50%
Simulation where provided till population gained about 1'000'000 cells	

Driver and passenger mutation effects and probabilities are assumed for scenario when only one kind of both types occurs. It is possible to implement more than one effect for both types to differentiate mutation kinds.

2.3. Gillespie simulation algorithm

Basing on described scenario we have elaborated appropriate version of Gillespie algorithm. We introduce modification which provides a possibility to track every mutation in population in reasonable time stamp. Modification is based on division of the whole population into clones what enables parallel computing. Each clone is composed of clone parameters: size, previous clone, driver mutation list and passenger mutation matrix. Each cell in one clone have same set of driver mutation so it is not needed to include them into cell mutation profile. The main element in clone is mutation matrix which enables tracking each mutation in every cell. Matrix rows represent clone cells and columns represents mutations. First column describes each cell fitness which is computed directly after mutation event but only for new cell. Each other column represents events of mutations existing in cell. Including mutation matrix provide possibility to copy only cells which divide or mutate without interacting with whole matrix in every simulation loop.

Each clone is updated simultaneously one cycle after another. Firstly, based on cells fitness, random variables representing time of events in the evolution, are generated according to exponential distribution. Mutation events occur only when division event happen. Mutation probabilities differ between drivers and passengers. It is possible to

implement few driver and passenger mutation types to differentiate mutation probability and effects. For each cell in clone event time is compared to simulation step – tau step. Every cell which death time is smaller is simply deleted from clone. When division time is smaller mutation flag is checked. If cell mutate type of mutation have to be considered – when driver mutation occurs new cell will create new clone, when passenger mutation occurs simply new mutation is added to mutation matrix. If cell only divide copy of that cell with no new mutation is added to mutation matrix. Block diagram of that Gillespie algorithm modification is presented on Figure 2.

After every clone update simulation time is extended by tau step and new loop is considered. Simulation end when ending condition is completed – maximum size of population is reached or simulation time exceeds assumed time.
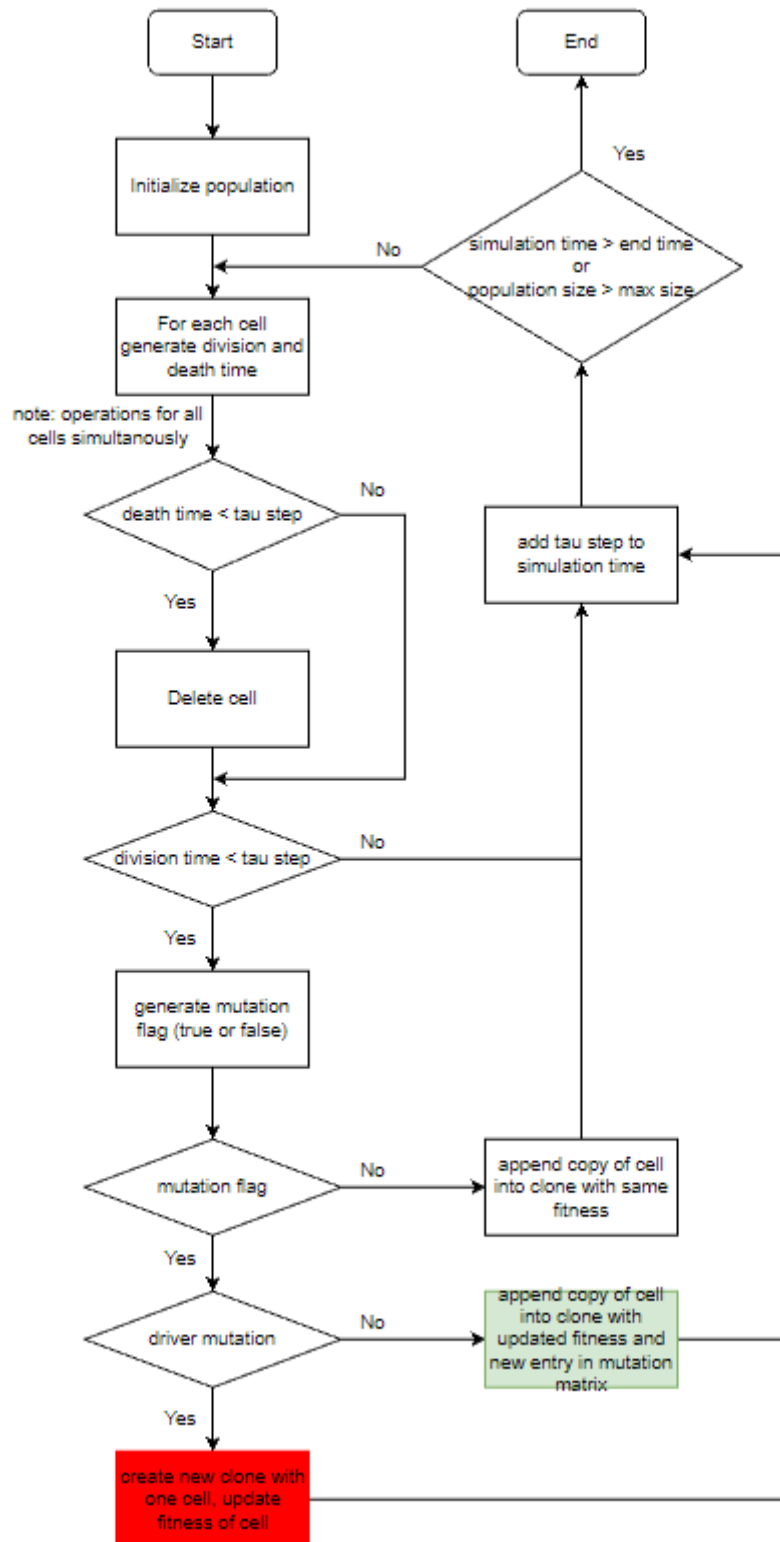
Fig. 2. Block diagram of the Gillespie simulation algorithm using parallel computing and mutation matrix

Rys. 2. Diagram blokowy algorytmu Gillespiego z wykorzystaniem obliczeń równoległych i struktury macierzy mutacji

2.4. Implementation of the mutation matrix

Table 2

Fragment of mutation matrix structure

Fitness	Pass. Mut. ID	Pass. Mut. ID	Pass. Mut. ID	Pass. Mut. ID	Pass. Mut. ID
	0	1	0	0	0
	0	0	0	1	1
	0	0	1	1	0
	1	0	0	0	0

Mutation matrix represents, in the form of binominal values, mutations presence or absence in cells. One mutation can be assigned to multiple cells and one cell can be assigned to multiple mutation. If cell contains mutation, value 1 is present in appropriate column. Because of matrix structure it can have big dimensions. To reduce memory usage that structure can be saved as sparse matrix (compressed form like map but with every ability of matrix). In python environment we are using scipy library with sparse matrix structures.

First column describes the cumulative effect of all mutation. Each driver mutation (same for every cell in clone, not present in mutation matrix) have positive effect on cell fitness. The highest fitness in clone always have cell from which clone starts progression. Each passenger mutation (all mutations in matrix) have negative effect on cell what is calculated only when parent cell mutates.

Mutation matrix application provides possibility to easily handle evolutionary events. When cell dies simply row is extracted from matrix and deleted. When cell divides, hard copy of row is appended to matrix. If cell also mutates (passenger mutation type) besides row copy, one more column is appended with value 1 in last row.

2.5. Results

High resolution stochastic simulation, implementing the idea of mutation matrix, enables tracking every mutation both separately in clones and in the whole population. Our method is able to provide information about VAF of every mutation. Mutation distribution can be viewed as VAF histogram for whole population with or without division into clones, or for one clone.

2.5.1. Clone diagrams of the evolution of cancer cells population

Basic information about clone – size and parent clone, can be used for plotting clone diagram. In Figure 3 clone size distribution along population progression has been shown. Different clones are marked by using different colors. Clone diagram provides information about dominant clone in each generation, when occurs driver mutation which have huge impact on population and how fast population is rising. The simulation end condition was about 10 times enlargement of initial population.
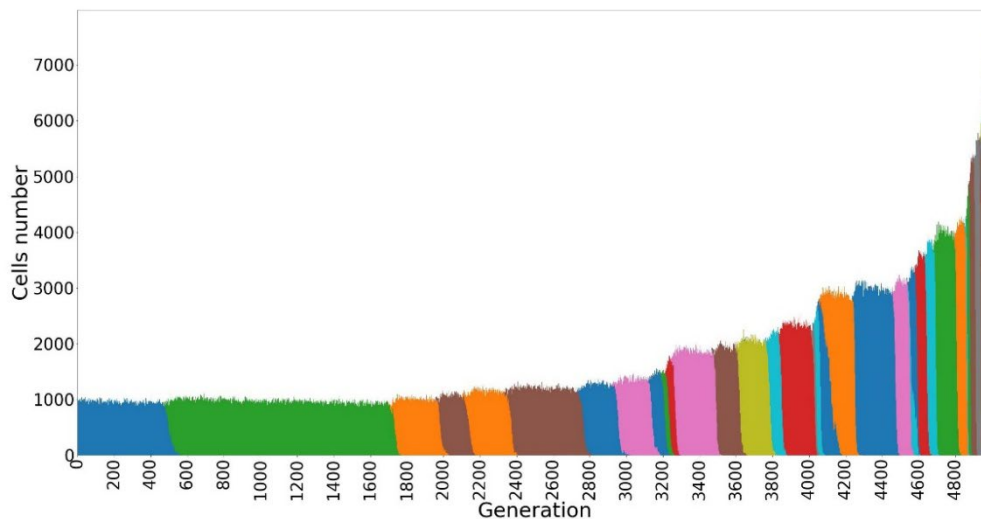
Fig. 3. Clone diagram of the evolution of cancer cells population
Rys. 3. Wykres zmian struktury klonów w trakcie ewolucji populacji

2.5.2. Evolution of variant allele frequencies (VAFs)

Due to emergence and extinction of clones, VAFs change dynamically over time. Frequencies are calculated basing on maximum cells number of interpreted groups. VAF histograms provide appropriate information to track cells differentiation and clone evolution.

2.5.3. Evolution of variant allele frequencies inside clones

In Figure 4 below we show two examples of VAF frequecies computed, separately in clones, in the course of evolution of cancer cell population. It is seen that VAFs inside

both clones are bimodal. Driver mutation, whose occurrence lead to new clones are present in all cell of the clone. All cells of the clone also contain passenger muations from the ancestral cell of the clone. In the process of evolution of the clone new passenger mutations are also generated. These passenger muations appear only in small subsets of clonal cells and therefore they correspond to low values of VAFs, concentrated on the left hand side of the chart. The above described mechanism leads to bimodality of VAF distribution shown in both charts in Figure 4.
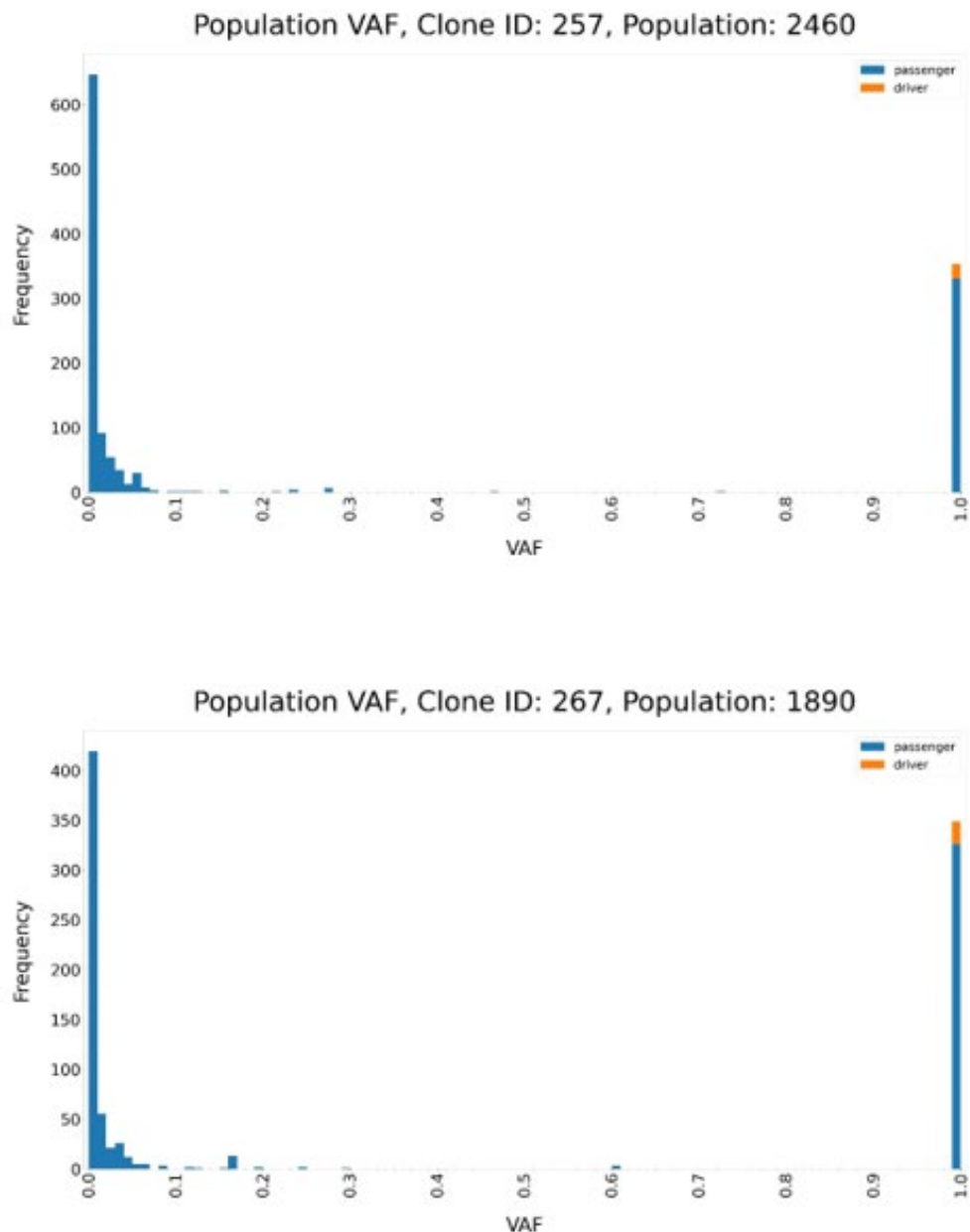
Fig. 4. VAF histograms for single clone in one generation of whole population. On chart mutation types are colored in different colors. Mutation frequency is calculated basing on only one clone cells

Rys. 4. Histogram VAF dla jednej generacji pojedynczego klonu. Na wykresie wyróżnione zostały rodzaje mutacji poprzez zastosowanie różnych kolorów. Częstotliwość mutacji obliczana jest na podstawie komórek pojedynczego klonu

2.5.4. Evolution of variant allele frequencies for the whole population

Simulated data enable also showing mutation frequencies in the whole population, as presented in Figure 4. Here the whole population of cancer cells contains two clones. Combination of all mutations in one plot results in modification of frequencies of mutations. VAFs of mutations in the whole population depend on sizes of clones and on mutations frequencies inside clones. This is seen in the plot in Figure 5. Two colors are used for showing mutations coming from two different clones. Combining VAFs of mutations of all clones in one plot results now in multimodal distribution.
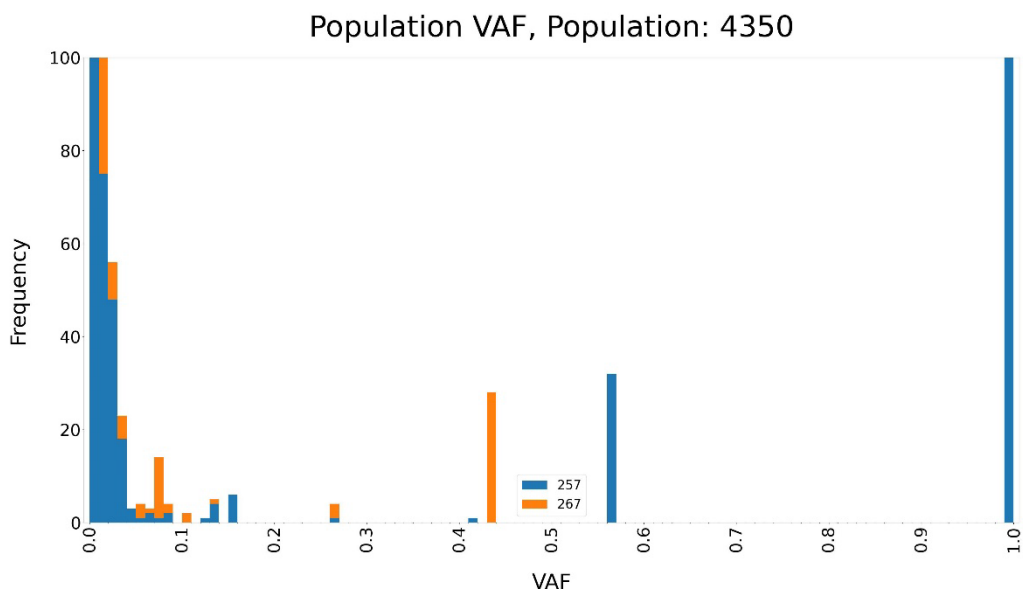
Fig. 5. VAF histogram for one generation of whole population. Each clone is presented as different color. VAF is calculated with respect to mutation frequency in all cells

Rys. 5. Histogram VAF dla jednej generacji całej populacji. Każdy klon został zaznaczony za pomocą odrębnego koloru. VAF obliczany jest na podstawie częstotliwości mutacji w odniesieniu do całej populacji

2.6. Summary and conclusion

Clonal composition of tumor is a very important determinant of its potential for malignancy transition to methstasis and predicted response to therapies. The research devoted to studying clonal structures of tumors and their relations to biological background of cancer development and clinical observations is

a wide area in computational oncology [9–13]. This scientific research area is also supported by mathematical and computational models of cancer clonal development.

We presented a high – resolution simulation system for tracing clonal evolution of tumor with interacting driver and passenger mutations. Evolution of clones when cancer cells population progresses and increases in time leads to dynamic changes of frequencies of mutations. During the evolution of separate clones distributions of VAFs (allelic frequencies) of passenger muations are biomodal, as shown in Figure 4. When distributions of VAFs are drawn for the whole cancer cells populations, as shown in Figure 5, they display multimodal shapes. These results are consistent with many observations of VAFs obtained in experimental studies [4].

Acknowledgements

Bibliography

1. Nowell P. (1976). The clonal evolution of tumor cell populations, Science 194(4260):23–28.
2. Greaves M., Maley C.C. "Clonal evolution in cancer". Nature 481.7381 (2012): 306–313.
3. Kumar S. et al. 2020, Passenger Mutations in More Than 2,500 Cancer Genomes: Overall Molecular Functional Impact and Consequences, Cell, Volume 180, Issue 5, 5 March 2020, Pages 915–927.e16 https://doi.org/10.1016/j.cell.2020.01.032.
4. Campbell P.J., Getz G., Korbel J.O., Stuart J.M., Stein L.D. The ICGC/ TCGA Pan-Cancer Analysis of Whole Genomes Consortium (2020). Pan-cancer analysis of whole genomes. Nature 578, 82–93.
5. Bozic I. et al. "Accumulation of driver and passenger mutations during tumor progression". Proceedings of the National Academy of Sciences 107.43 (2010): 18545–18550.
6. McFarland C.D. et al. "Impact of deleterious passenger mutations on cancer progression". Proceedings of the National Academy of Sciences 110.8 (2013): 2910–2915.

7. McFarland C.D., Mirny L.A., Korolev K.S. "Tug-of-war between driver and passenger mutations in cancer and other adaptive processes". Proceedings of the National Academy of Sciences 111.42 (2014): 15138–15143.

8. Gillespie D.T. (2007). Stochastic simulation of chemical kinetics. Annu. Rev. Phys. Chem., 58, 35–55.

9. Martincorena I., Campbell P.J. (2015). Somatic mutations in cancer and normal cells, Science 25 Sep 2015: Vol. 349, Issue 6255, pp. 1483–1489, DOI: 10.1126/science.aab4082.

10. Strino F. et al. (2013). TrAp: a tree approach for fingerprinting subclonal tumor composition. Nucleic Acids Res. 41(17):e165.

11. Andor N. et al. (2014). EXPANDS: expanding ploidy and allele frequency on nested subpopulations, Bioinformatics, 30(1):50–60.

12. Roth A. et al. (2014). PyClone: statistical inference of clonal population structure in cancer. Nat Methods 11(4):396–398.

13. Miller C.A. et al. (2014). SciClone: inferring clonal architecture and tracking the spatial and temporal patterns of tumor evolution. PLoS Comput Biol 10(8):e1003665.

MODELLING CLONAL EVOLUTION OF TUMOURS BY USING HIGH RESOLUTION STOCHASTIC SIMULATIONS

Abstract

Tumor growth, caused by accumulation of genomic somatic mutations, which disturb and eventually dysregulate cellular processes of signaling, metabolism and replication, is a complex process with various stages and modes of dynamics. Fundamental research on scenarios and mechanisms of tumor evolution, combined with observational data and biological/genetic knowledge, is of great importance for cancer research.

Important insights to the study of dynamics of cancer evolution are given by mathematical/computational modelling tools. Mathematical models require introducing a lot of simplifying hypotheses in order to obtain interpretable conclusions. Computational stochastic simulation approaches allow for address wider range of evolution scenarios, important for explaining observational data, which are recently becoming available.

We present a stochastic simulation tool, based on Gillespie algorithm for modelling evolution of cancer cells population. Replication process of cancer cells is affected by two types of somatic mutations, driver with high impact on tumor growth and passenger, assumed to have mildly deleterious effect. The elaborated algorithm allows for high resolution modelling of evolution of cancer, with distinguishing between cancer cells and both types of somatic mutations occurring over time. It allows for confronting simulation results with experimental data concerning clonal structures of tumor cells and statistics of somatic mutations.

Agnieszka BANAŚ[1,*], Marco SAVARESE[2], Rossella TUPLER[3], Joanna POLAŃSKA[4]

Chapter 3. TRANSCRIPTOMICS-BASED MUSCULAR DYSTROPHY PATIENT STRATIFICATION WITH THE USE OF MACHINE LEARNING

3.1. Introduction

Muscular dystrophies are a group of genetic disorders characterized by progressive muscle wasting and degeneration. There are several different types of muscular dystrophies with distinct patterns of muscle development and genetic causes. By identifying relevant features, personalized treatment strategies can be provided [1].

Over the past few years, RNA sequencing (RNA-seq) has emerged as a powerful genomic tool for the identification of genetic variants that are associated with various diseases, including rare genetic disorders like muscular dystrophies. RNA-seq is a powerful tool for unravelling the complexity of gene regulation and understanding the dynamics of RNA molecules in tissues [2].

Machine learning is a subset of artificial intelligence that focuses on developing algorithms and models capable of learning and making decisions. It has the ability to analyze complex datasets and discover hidden patterns and associations. When combined with RNA-seq, machine learning can be leveraged to develop clustering models for muscular dystrophy patient stratification, leading to improved diagnosis and treatment strategies. The aim of this study is to create a preprocessing pipeline that includes a series of steps to prepare the data for effective analysis and identifying molecular signatures.

[1] Faculty of Automatic Control, Silesian University of Technology, Gliwice, Poland.
[2] Folkhälsan Research Center, University of Helsinki.
[3] Dipartimento di Scienze Biomediche,Università degli Studi di Modena e Reggio Emilia.
[4] Department of Data Science and Engineering, Faculty of Automatic Control, Silesian University of Technology, Gliwice, Poland.
[*] Corresponding author: agniban056@student.polsl.pl.

3.2. Dataset

The dataset consists of 61,587 gene expression profiles from 197 patients with muscular dystrophies, obtained using the RNA-seq method with HiSeq4000 and NovaSeq platforms. RNA-seq is high-throughput sequencing technique used to analyze the transcriptome of an organism. It provides insight into the RNA molecules present in a biological sample, enabling the study of gene expression. It quantifies the amount of RNA molecules produced from that gene and provides valuable information about its transcriptional activity [2]. The range of expression levels in RNA-seq dataset spans several orders of magnitude, reflecting the varying levels of gene expression between different genes and patients. At the lower end of the range are genes with very low or negligible levels of expression. On the other hand, genes that are highly expressed can have expression levels that are several orders of magnitude higher.

A description of the clinical features is provided in Tables 1, 2 and 3.

Table 1

Patients phenotype

Phenotype	Number of patients
Titinopathy	63
Myopathy	32
IBM	28
Amputee control	12
CK control	7
Myopathy (HNRNPA1)	6
DMD	5
SMPX myopathy	4
FSHD	3
Actinin-2 myopathy	2
LGMD D2	1
Control cells	1
Becker	1
OPDM	1

Table 2

Patients sex

Sex	Number of patients
Male	91
Female	48
Not known	28

Table 3

Age at biopsy

Age at biopsy	Number of patients
<30	23
30 – 50	37
>50	78
Not known	29

3.3. Methods

The preprocessing pipeline in the context of machine learning refers to a series of steps and techniques applied to raw data to transform it into a format suitable for training a machine learning model. Each step in the pipeline serves a specific purpose and contributes to the overall data preparation process. The pipeline created is shown in Fig. 1.
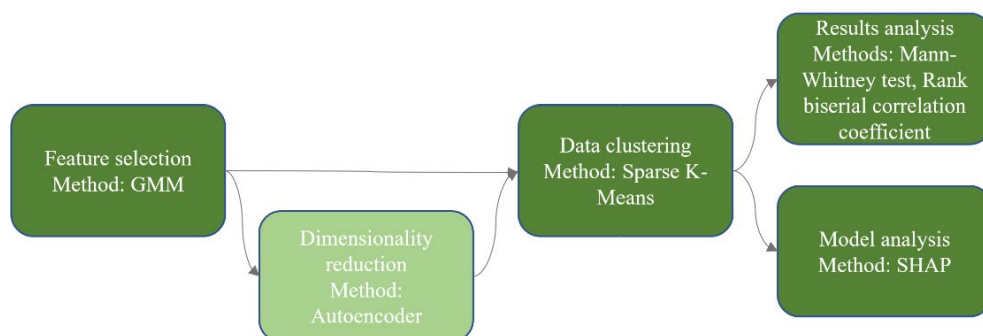
Fig. 1. Preprocesing pipeline
Rys. 1. Potok przetwarzania

3.3.1. Feature selection

The first step in a preprocessing pipeline, especially in high-dimensional datasets, is feature selection. It refers to the process of identifying the subset of features that are most relevant to the analysis. In the context of feature selection for muscular dystrophy, we decided to reject genes that are not actively expressed or have low levels of expression. Hence, the expression levels of genes were converted into binary values representing the presence or absence of gene expression. The binary heatmap depicted in Fig. 2 represents gene expression activity, where active genes are denoted by 1, and inactive genes are denoted by 0.
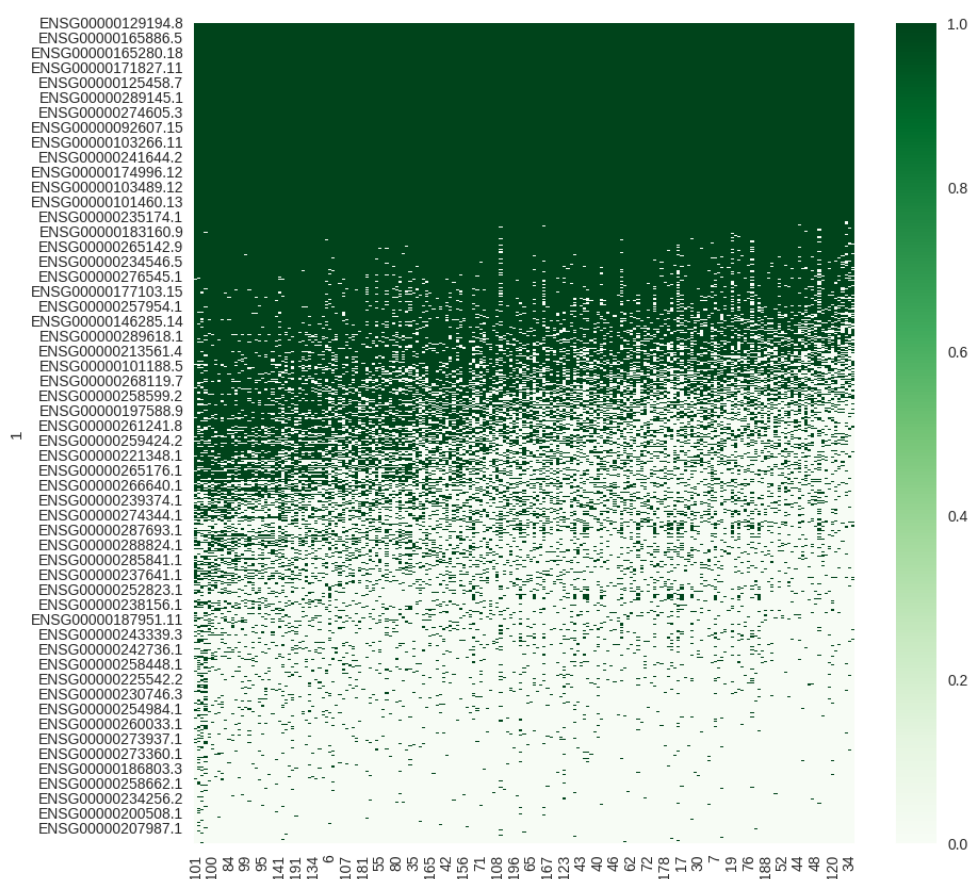
Fig. 2. Binary form of gene expression
Rys. 2. Binarna postać ekspresji genów

The Gaussian Mixture Model (GMM) was then applied to the data to reject certain components if they did not provide meaningful information. It assumes that the data points are generated from a mixture of Gaussian distributions. Determining the optimal number of components is an important step in the analysis of gene expression data. For this purpose, Bayesian Information Criterion (BIC) was used. The BIC is based on the principle of penalized likelihood, which takes into account both the likelihood of the

data given the model and a penalty term for model complexity. The GMM with the lowest BIC value is usually considered to be the optimal model. The visual representation of the GMM results is shown on Fig. 3.
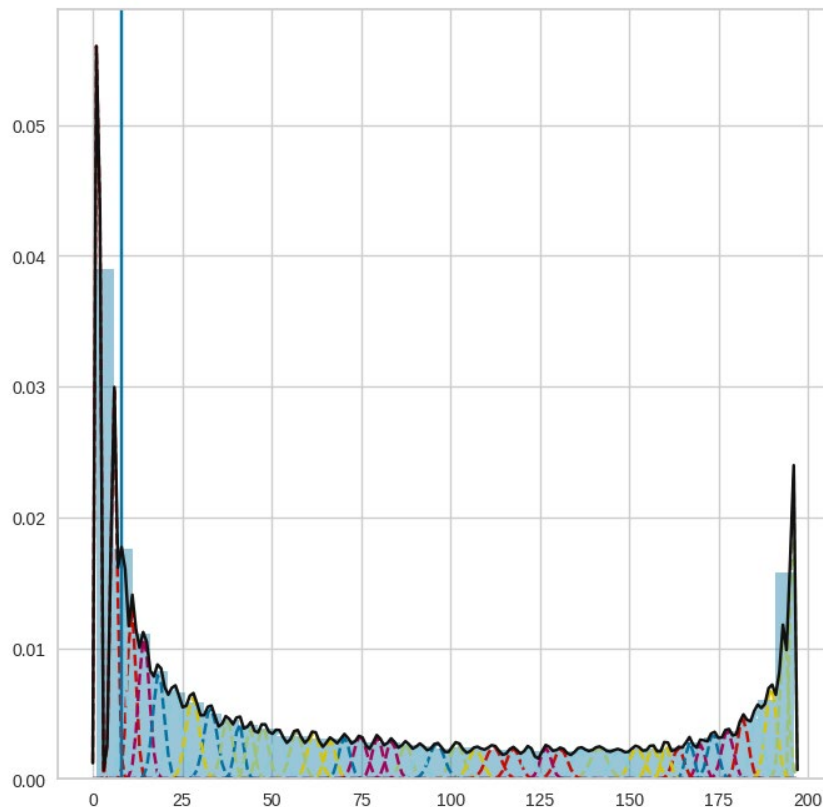
Fig. 3. GMM result
Rys. 3. Wynik działania GMM

After applying the gene rejection criteria based on low expression levels, the dataset was reduced from its original size of 61,587 genes to 32,606 genes.

3.3.2. Clustering

Determining the optimal number of clusters is a critical step in clustering analysis. The Calinski-Harabasz index and the Davies-Bouldin index were used to evaluate the clustering performance and to determine the optimal number of clusters. As the number of clusters increased, the Davies-Bouldin index increased, indicating worsened cluster separation and compactness. The highest Calinski-Harabasz index reflects a clustering solution with the most distinct clusters. Based on the indices values, it was observed that the solution with two clusters yielded the best between cluster separation and compactness within each cluster.

Clustering is a fundamental technique in unsupervised machine learning that involves grouping similar data points together based on their intrinsic characteristics. It is a process of dividing a dataset into subsets or clusters, where data points within each cluster have certain similarities and are dissimilar to data points in other clusters.

Sparse k-means involves selecting a sparse set of relevant features that contribute most to each cluster. By selecting a sparse set of features, the algorithm reduces the dimensionality of the data, which can improve accuracy and scalability compared to classical k-means [3]. The application of sparse k-means clustering to the gene expression dataset produced distinct and interpretable clustering results. UMAP (Uniform Manifold Approximation and Projection) was used for visualization purposes in the analysis of the dataset. The main UMAP principle is to find a low-dimensional representation which will preserve these neighborhoods as much as possible [4]. The using of UMAP to the patients gene expression dataset resulted in a plot on Fig. 4 that effectively captured the underlying structure and relationships of the data. The UMAP plot revealed distinct clusters representing different groups within the patient population. By applying UMAP to a dataset affected by batch effects, it is possible to visualize and potentially correct for these unwanted variations. However, the second plot provides evidence that there is no batch effect, so there is no need to apply a batch correction technique.
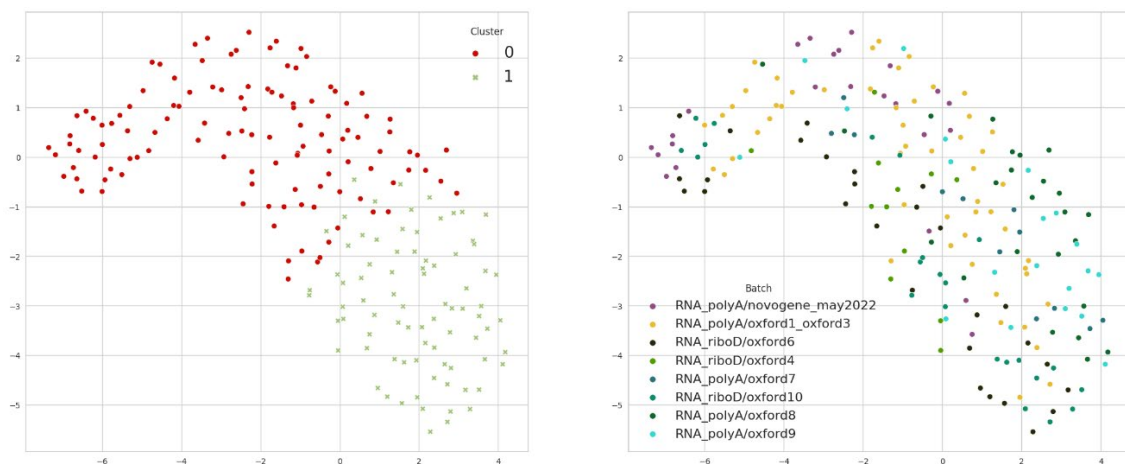
Fig. 4. UMAP visualisation
Rys. 4. Wizualizacja UMAP

The improved separation between clusters and reduced dimensionality through feature sparsity contributed to a more efficient and interpretable clustering solution.

3.3.3. Statistical analysis

To identify the most diversifying genes within specific clusters, the Mann-Whitney test was utilized. By performing the Mann-Whitney test on a feature of interest within different clusters, was determined whether the feature exhibits significant variation that distinguishes the clusters.

The Rank Biserial Correlation Coefficient can be used to assess the effect size in the context of clustering analysis. A higher absolute value of the coefficient indicates a stronger cluster separation based on the feature.

Figure 5 shows box plots illustrating the gene expression levels of of the most diversifying genes across different clusters, including MYH7, TNNI1 and ACTN2. These muscular genes play important roles in muscle contraction. Both cardiac and skeletal muscle disorders can result from a defect of MYH7 [5]. The TNNI1 gene is switched on during skeletal muscle myogenesis and is co-expressed during early stages of development [6]. ACTN2 is highly abundant in cardiac and skeletal muscle, where it plays several functional roles in the sarcomeres [7]. Each box corresponds to a different cluster and the vertical axis represents the gene expression values. The box represents the interquartile range of values within each cluster, with the median indicated by a line inside the box. By examining the box plots, we can observe variations in gene expression levels between clusters.
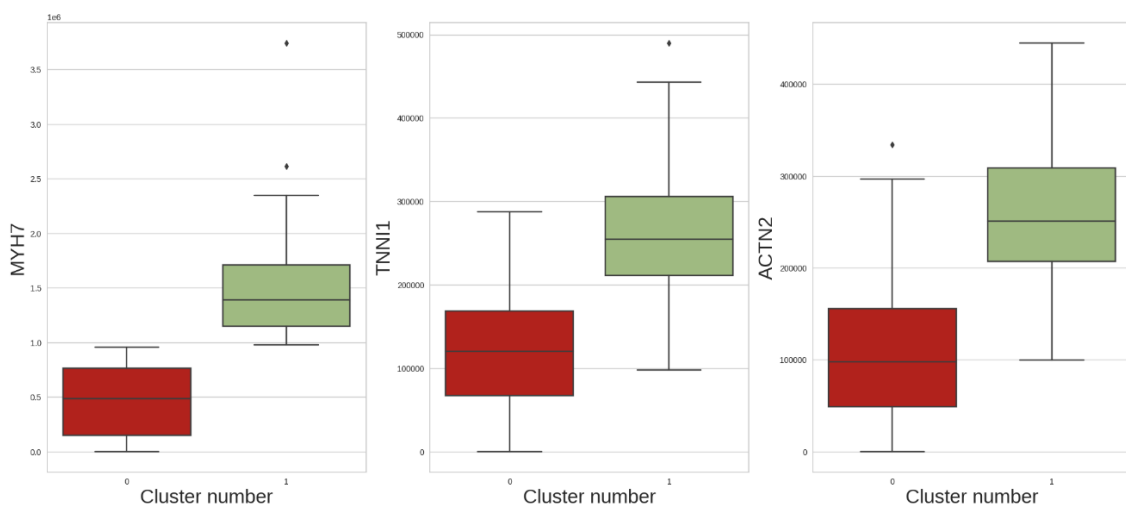
Fig. 5. Gene expression values across clusters
Rys. 5. Wartości ekspresji genów pomiędzy klastrami

3.3.4. Dimensionality reduction

Dimensionality reduction is an additional step that was included in the preprocessing pipeline to reduce the number of features in the dataset while preserving the most important information. Autoencoders were used as part of the analysis. The autoencoder neural network was trained on the dataset to learn a compressed representation of the input data. By minimizing the reconstruction error between the original input and the reconstructed output, the autoencoder effectively captured the most important features but yield a different number of clusters than what was previously determined. The analysis using the autoencoder resulted in the identification of 5 distinct clusters within the dataset which are demonstrated in Fig. 6 after UMAP transformation.
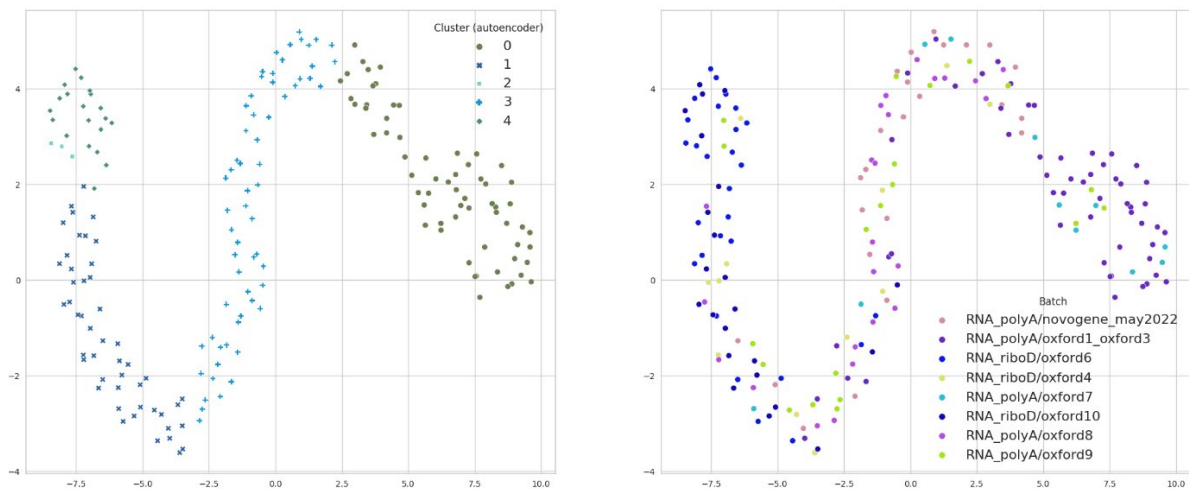
Fig. 6. UMAP space after applying the autoencoder
Rys. 6. Przestrzeń UMAP po użyciu autenkodera

The Sankey diagram shows on Fig. 7 the distribution of genes within clusters, comparing the results with and without dimensionality reduction techniques. It visually represents the flow of genes between clusters in both scenarios, highlighting any similarities in gene assignments and transitions.
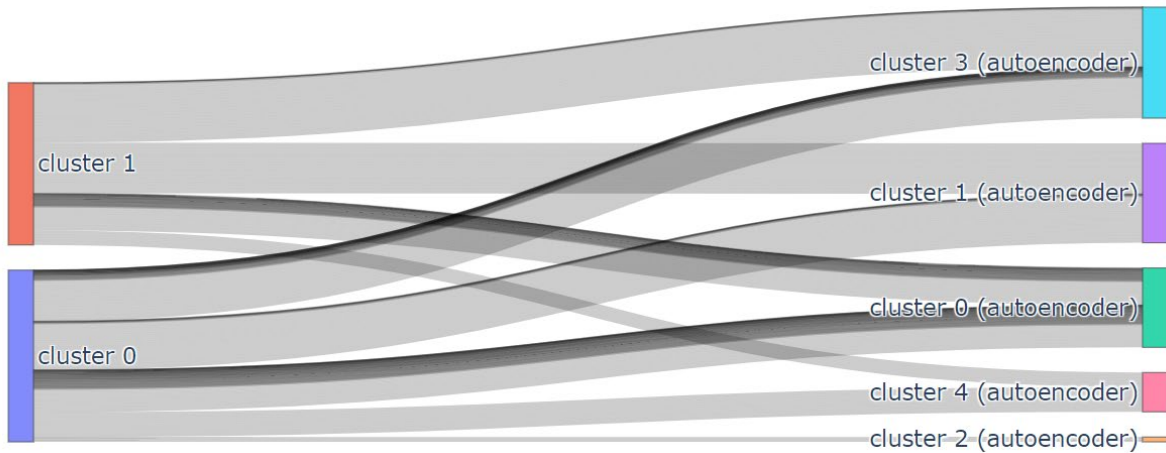
Fig. 7. Sankey diagram
Rys. 7. Diagram Sankey

3.3.5. Model analysis

Using the SHAP algorithm, we can calculate the impact of each feature on a given prediction by evaluating its contribution to the difference between the predicted outcome and the expected average prediction. SHAP (Shapley Additive exPlanations) is a model-agnostic interpretability technique used to explain the predictions of machine learning models [8]. Positive SHAP values indicate features that push the prediction towards the positive class, while negative values indicate features that push it towards the negative class. Fig. 8. Illustrates the results of the SHAP algorithm using Random Forest as the prediction model. By analyzing the SHAP values of the genes, it is possible to identify the genes that have the most significant effect on the separation of the clusters.
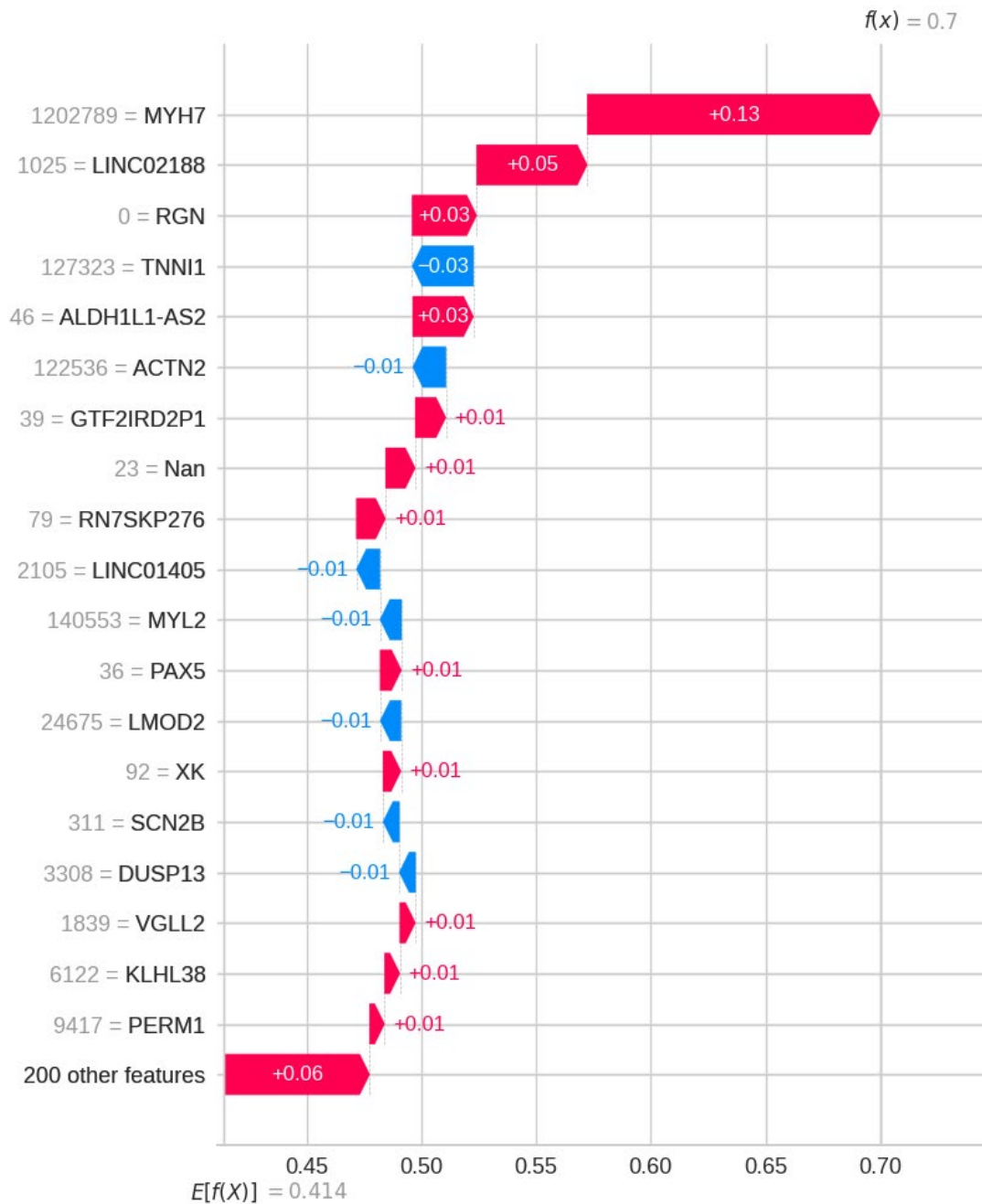
Fig. 8. SHAP
Rys. 8. SHAP

3.4. Conclusions

In conclusion, clustering analysis of the patients dataset revealed two distinct subgroups based on genetic profiles. The analysis of muscular genes revealed diverse expression patterns across different clusters. Specifically, the genes MYH7, TNNI1, or ACTN2 exhibited varying expression levels among the clusters. Further investigation

into the specific genetic mutations and biomarkers associated with each cluster could potentially lead to personalized treatment strategies and improved prognostic indicators for patients with muscular dystrophies.

Bibliography

1. Prof Alan EH Emery FRCP, The Lancet, *The muscular dystrophies* (2002) **359**:687–695.
2. Ana Conesa, Pedro Madrigal, Sonia Tarazona, David Gomez-Cabrero, Alejandra Cervera, Andrew McPherson, Michał Wojciech Szcześniak, Daniel J. Gaffney, Laura L. Elo, Xuegong Zhang, Ali Mortazavi, Genome Biology, *A survey of best practices for RNA-seq data analysis* (2016) **13**.
3. Daniela M. Witten, Robert Tibshirani, J Am Stat Assoc, *A framework for feature selection in clustering* (2010) **490**: 713–726.
4. Alex Diaz-Papkovich, Luke Anderson-Trocmé, Simon Gravel, Journal of Human Genetics, *A review of UMAP in population genetics* (2021) **66**: 85–91.
5. C. Fiorillo, G. Astrea, M. Savarese, D. Cassandrini, G. Brisca, F. Trucco, M. Pedemonte, R. Trovato, L. Ruggiero, L. Vercelli, A. D'Amico, G. Tasca, M. Pane, M. Fanin, L. Bello, P. Broda, O. Musumeci, C. Rodolico, S. Messina, G. L. Vita, M. Sframeli, S. Gibertini, L. Morandi, M. Mora, L. Maggi, A. Petrucci, R. Massa, M. Grandis, A. Toscano, E. Pegoraro, E. Mercuri, E. Bertini, T. Mongini, L. Santoro, V. Nigro, C. Minetti, F. M. Santorelli, C. Bruno on behalf of the Italian Network on Congenital Myopathies, Orphanet Journal of Rare Diseases, *MYH7-related myopathies: clinical, histopathological and imaging findings in a cohort of Italian patients* (2016) **11:** 11–91.
6. Antony J. Mullen, Paul J.R. Barton, Gene, *Structural characterization of the human fast skeletal muscle troponin I gene (TNNI2)* (2000) **242:** 313–320.
7. Marco Savarese, Johanna Palmio, Juan José Poza, Jan Weinberg, Montse Olive, Ana Maria Cobo, Anna Vihola, Per Harald Jonson, Jaakko Sarparanta, Federico García-Bragado, Jon Andoni Urtizberea, Peter Hackman, Bjarne Udd, Annals of Neurology, *Actininopathy: A new muscular dystrophy caused by ACTN2 dominant mutations* (2019) **6:** 899–906.
8. Guy Van den Broeck, Anton Maximilian Schleich, Dan Suciu, Journal of Artificial Intelligence Research, *On the Tractability of SHAP Explanations* (2022) **74:** 51–886.

TRANSCRIPTOMICS-BASED MUSCULAR DYSTROPHY PATIENT STRATIFICATION WITH THE USE OF MACHINE LEARNING

Abstract

Muscular dystrophies are a set of genetic disorders characterized by progressive muscle wasting and degeneration. Each type of muscular dystrophy is associated with specific gene mutations that have an effect on the function of the muscles. We aim to identify patient subpopulations and find their molecular signatures. The dataset consists of 61,587 RNA-Seq-based gene expression profiles from 197 patients with different muscular dystrophies. The preprocessing pipeline was created to filter noisy data that can lead to misinterpretation of the study results.

First, genetic data were transformed to present/absent form, and then the Gaussian Mixture Model of their occurrence distribution was used to identify genes with high absences. Then, the sparse K-means algorithm was applied to partition samples into clusters with Calinski-Harabasz and Davies Bouldin indices used to find the cluster number. Differences in gene expression across clusters were detected by the Mann--Whitney test and rank biserial correlation coefficient serving as effect size measure. The large effect size was observed in 219 features, mainly associated with muscular genes such as MYH7, TNNI1, or ACTN2. UMAP transformation was used to visualize results, and the 2D graph spanned over the limited feature domain was built to confirm obtained patient splitting.

Keywords: muscular dystrophy, unsupervised learning, sparse K-means, UMAP

Tomasz STRZODA[1,*], Lourdes CRUZ-GARCIA[1], Mustafa NAJIM[2],
Christophe BADIE[2], Joanna POLAŃSKA[1,*]

Chapter 4. NO-MAPPING MAPPING OF OXFORD NANOPORE LONG READS

4.1. Introduction

Understanding the DNA code has been one of mankind's most important tasks for years [1]. There are many reasons for this, such as the development of new treatments and therapies [2, 3]. The problem has led to discoveries and advances in the field of science, bringing with it various sequencing techniques and the concept of mapping (i.e. aligning reads with a reference sequence, making it possible to find where a DNA read originates [4]). Historically, sequences have not been long strings. Depending on the generation and platform, they averaged between tens and hundreds of base pairs (bp). The situation has changed slightly with Third-Generation Sequencing (TGS) for which average lengths are mostly reported in thousands of bp [5]. Among these, we can distinguish companies such as Pacific Biosciences and Oxford Nanopore Technologies differing in their approach to reading the sequence of nucleotides [6]. The latter company bases its innovative idea on nanopores, i.e. proteins placed in a membrane through which a single DNA/RNA strand passes. Based on the changes in current arising from passing a string of nucleotides, we are able to read individual letters of the sequence. Such a process is characterized by the absence of restrictions on the read length, resulting in so-called "long reads" [7].

TGS opens up new possibilities and brings with it new problems to solve. One of them is the search for a specific sequence fragment in a relatively short time.

[1] Department of Data Science and Engineering, Faculty of Automatic Control, Electronics and Computer Science, Silesian University of Technology, Gliwice, Poland.
[2] Cancer Mechanisms and Biomarkers Group, Radiation Effects Department, Radiation, Chemical & Environmental Hazards, UK Health Security Agency, Didcot, UK.
* Corresponding authors: tomasz.strzoda@polsl.pl, joanna.polanska@polsl.pl.

Such a fragment could be a specific gene that acts as a marker for a screening test that determines the dose of ionizing radiation absorbed by a person. Finding the marker itself is not an easy task and is a separate problem. Based on the literature [8, 9], it can be concluded that such a marker potentially is the FDXR gene, which was used for the present study.

Despite the ever-growing list of sequence alignment software, it still ties the task of searching for a nucleotide fragment to using a computer to search all possible read locations on a given reference, which translates into computation time. In this paper, we wanted to replace the alignment program with a machine learning model, thus narrowing down the task to searching for a specific sequence/gene. We base our idea on methods known from Natural Language Processing (NLP) [10]. Using appropriate methods, we encoded the entire sequence in a first step and then focused on the problem of narrowing our encoding to the n initial sequences and observed how this affected the efficiency of our model. In this way, we showed that it makes sense to apply NLP methods to bioinformatics tasks and how far we can move with the encoding to obtain satisfactory efficiency.

4.2. Materials and Methods

4.2.1. Data

The data consisted of Oxford Nanopore sequencing data from three repetitions of the biological experiment: A, B, C. The HT1080 cell line was used. In each repetition, the cells were exposed to a radiation dose of 10 Gy. RNA was then extracted and libraries were prepared using a direct RNA kit. Finally, six samples of epithelial cells were available, where three of them were not irradiated (Control-A, Control-B, Control-C) and another three were samples 24 hours after exposure to a 10 Gy dose (24h-A, 24h-B, 24h-C). After sequencing, 8.5 million long-read RNA sequences were obtained.

4.2.2. Data visualization

Knowing the characteristics of the data is fundamental in making further decisions. For this purpose, visualization using various plots is used, which helps humans to understand the data, detect possible errors and anomalies. In this case, to check

the distribution of read lengths of each sample, it was decided to generate a violin plot [11]. This made it possible to compare the density of the distribution and generally interpret the data.

4.2.3. Data preparation

In order to prepare the data for further use, it was decided to perform filtering to remove short reads. It was assumed that such reads could be the result of various mistakes and would not be useful for the present study. For this task, it was decided to use the Empirical Cumulative Distribution Function (ECDF) plot that was generated for each sample. By analysing the data distributions shown therein, a threshold value was chosen to ensure that the beginning of the plot line on its right-hand side was characterised by a steep slope to the horizontal axis, while at the same time not excluding too many reads from further analysis.

The final step was to divide the reads into those that could potentially belong to a given genome fragment (the FXDR gene) and those that do not. For this purpose, the minimap2 [12, 13] was used, which is responsible for matching the sequence data with the given reference sequence. This allows us to find the likely location of each read. In this case, the FDXR gene was chosen as the reference sequence.

4.2.4. Experimental design

The research was based on a machine learning model, which was responsible for determining whether or not a given sequence could potentially originate from the FDXR gene. A neural network consisting of three dense layers. The first two contained fifty neurons and ReLU activation functions, while the last contained one neuron and a sigmoid function. The training process was based on ten epochs and used Leave-One-Out Cross-Validation (LOOCV) to assess the performance of the predictive models [14]. Each time, one of the six samples was set aside as a test set, while the remaining five samples were used for training. Such a process was repeated six times, thus ensuring that each sample was used exactly once as a test set (Fig. 1).

Fig. 1. Leave-One-Out Cross-Validation for performed experiments
Rys. 1. Walidacja krzyżowa Leave-One-Out dla przeprowadzonych eksperymentów

In order to overcome the problem of converting long sequences of nucleotides into a computer-friendly form, techniques known from natural language processing (NLP) were used. Firstly, the long sequences were presented as six-letter words (k-mers) with an offset equal to one nucleotide. This means that a single word consists of two codons. Sequences of four words (four-grams) were then created and such subsets formed the final dictionary with which each long-read was encoded. The method used is called "bag-of-words" [15] and is widely applied in the field of NLP.

The present study focused on encoding n initial nucleotides and observing the impact on the final performance of machine learning models. In order to select N (the set of considered n), quartiles were calculated as one measure of the position of the observations (the string lengths). Then a certain Δ step was selected to increase the size of this set. In addition, the other end of the sequence was considered, for which the same experiment was performed. In this case, the order of nucleotides read was from right to left.

Accuracy was used as a measure of model evaluation. All long-reads belonging to the test set were encoded identically as during the model training step (same n and same end of the sequence). It is noteworthy that even for the encoding of the whole reads, the strings for the start and end of the sequence are not identical. The difference is in the order of the nucleotides: from left end to right end, or from right end to left end.

4.3. Results and discussion

4.3.1. Data visualization

Fig. 2 shows the distribution of read lengths of each sample. As can be seen, all distributions are bimodal and right-skewed. The long tail indicates a relatively small number of reads greater than 3,000 bp. The exact number of reads per sample is shown in Table 1.
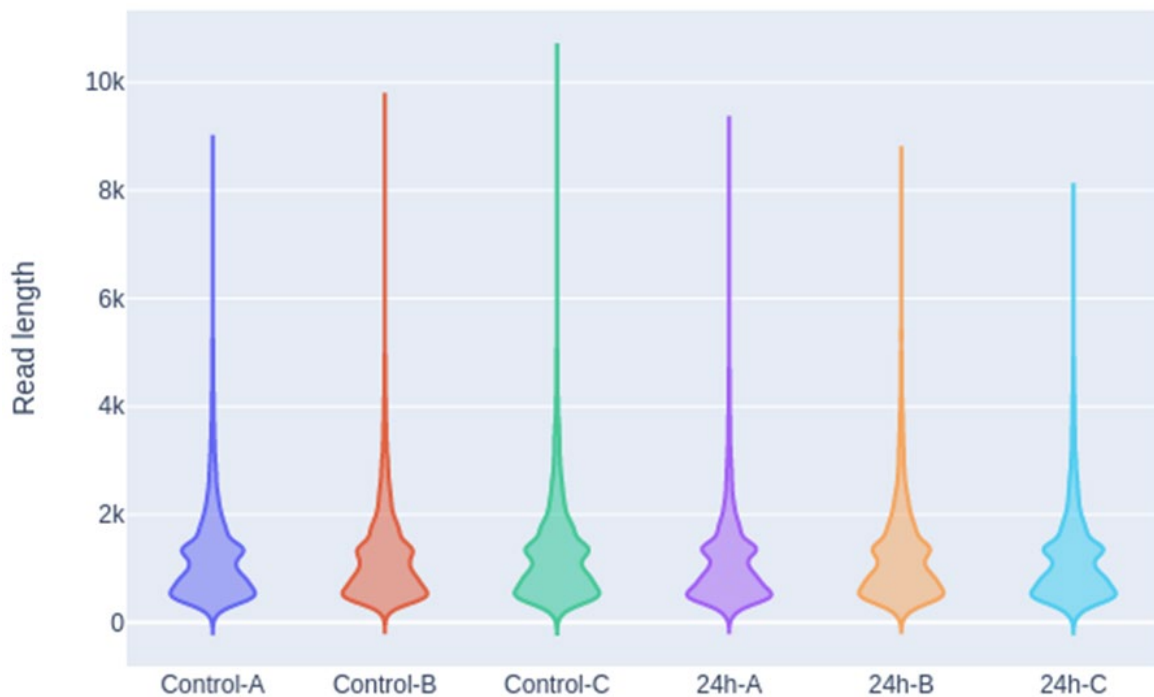
Fig. 2. Distribution of read lengths of individual samples
Rys. 2. Rozkład długości odczytów poszczególnych próbek

4.3.2. Data preparation

Plots of the empirical distribution function for the control and irradiated sample can be seen in Fig. 3. Based on these, a threshold value of 500bp was chosen. That said, all reads with a length greater than this value were not rejected. In the end, nearly 7.2 million long-reads remained. The exact numbers of long-reads per sample before and after filtering are shown in Table 1.
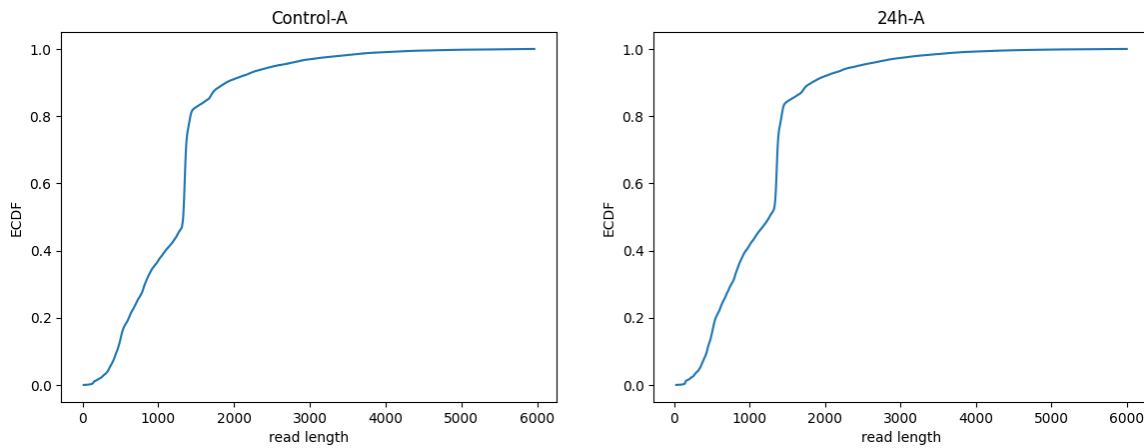
Fig. 3. Empirical cumulative distribution function plots for two samples
Rys. 3. Wykresy dystrybuanty empirycznej dla dwóch próbek

Table 1

Number of long-reads per sample

Sample	Not filtered	Filtered			
	Number of reads	Number of reads	Q1	Median	Q3
Control-A	1,232,364	1,040,293	784	1231	1692
Control-B	1,665,661	1,410,171	780	1204	1702
Control-C	1,254,760	1,069,828	802	1263	1720
24h-A	1,670,162	1,356,675	745	1146	1556
24h-B	1,859,656	1,570,158	786	1229	1721
24h-C	862,354	718,141	772	1209	1648
Total	8,544,957	7,165,266			

By performing the alignment process, the long-reads were divided into two groups. According to the aligner, the majority (7,128,352) were given the label "unmapped". This means that no potential location was found for them on the reference. The remaining reads (36,914) according to the aligner could potentially originate from the FDXR gene. Such a large difference in group sizes is as expected, because this task focused on only one among the entire set of genes.

4.3.3. Experimental design

The LOOCV approach provides a good method for validation, but involves the training of several artificial intelligence models [14]. Considering also the number of total reads (nearly 7.2 mln), which on average contain about 1,400 nucleotides and

which have to be transformed and encoded, such a process is time-consuming and complex in a memory context. Therefore, it was decided to randomly select 4,000 sequences potentially derived from the FDXR gene and 12,000 sequences unmapped to this gene during the training phase (hereinafter referred to as "approach 1"). The whole study was then repeated, but this time increasing the number of reads to 10,000 and 30,000 respectively (hereinafter referred to as "approach 2").

As mentioned earlier, the N set containing the numbers of n first encoded nucleotides was selected based on the calculated quartiles (summarised in Table 1) and the selection of a certain Δ step. That said, $N \in \{800; 1700\}$ were chosen, corresponding roughly to $Q1$ and $Q3$ of each sample. Next, the step $\Delta = 300$ was adjusted, thus obtaining the final $N \in \{200; 500; 800; 1100; 1400; 1700; \text{whole sequence}\}$.

Table 2

Model evaluation (approach 1) – accuracy with 95% confidence interval

Number of nucleotides (n)	Start of the sequence [%]	End of the sequence [%]
Whole sequence	98.31 (98.07; 98.55)	98.31 (98.13; 98.48)
1,700	96.15 (94.99; 97.31)	97.13 (96.33; 97.92)
1,400	95.59 (94.13; 97.05)	96.84 (95.85; 97.83)
1,100	94.86 (93.44; 96.28)	96.19 (94.92; 97.45)
800	93.99 (92.33; 95.65)	94.99 (93.43; 96.54)
500	92.54 (90.45; 94.63)	92.69 (90.66; 94.72)
200	90.17 (87.24; 93.09)	87.08 (83.35; 90.81)

Table 3

Model evaluation (approach 2) – accuracy with 95% confidence interval

Number of nucleotides (n)	Start of the sequence [%]	End of the sequence [%]
Whole sequence	98.58 (98.37; 98.79)	98.62 (98.50; 98.73)
1,700	96.96 (95.90; 98.02)	97.99 (97.54; 98.44)
1,400	96.67 (95.81; 97.56)	97.68 (97.04; 98.31)
1,100	96.10 (94.98; 97.22)	97.22 (96.45; 97.99)
800	95.36 (94.03; 96.69)	96.33 (95.26; 97.40)
500	94.12 (92.42; 95.81)	94.64 (93.03; 96.24)
200	91.90 (89.57; 94.22)	89.34 (85.95; 92.72)
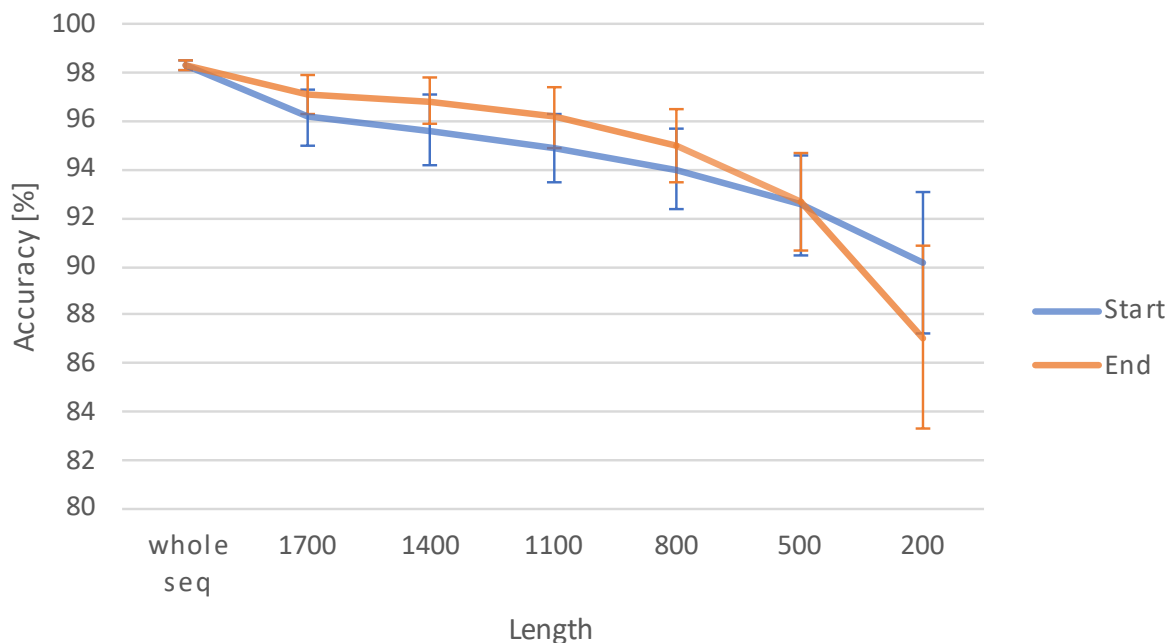
Fig. 4. Visual comparison of models' accuracies with 95% confidence intervals (approach 1)
Rys. 4. Wizualne porównanie dokładności modeli z 95% przedziałem ufności (podejście 1)
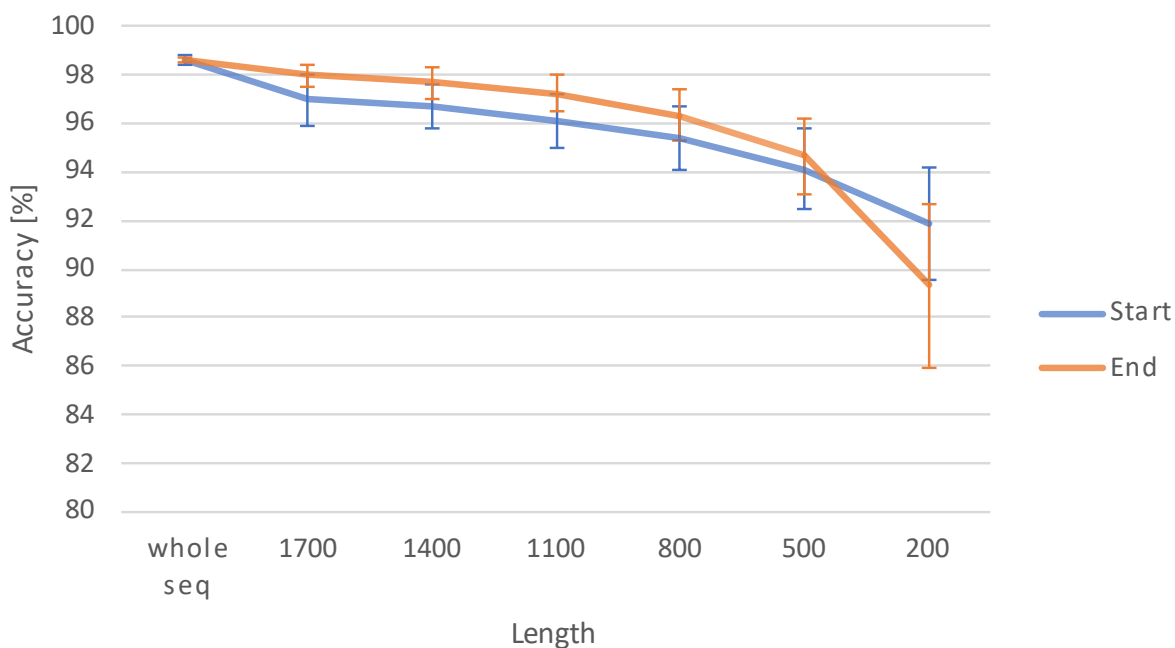
Fig. 5. Visual comparison of models' accuracies with 95% confidence intervals (approach 2)
Rys. 5. Wizualne porównanie dokładności modeli z 95% przedziałem ufności (podejście 2)

Model accuracies presented as confidence intervals with $\alpha = 95\%$ are shown in Table 2 and Table 3 for approach 1 and 2, respectively. In addition, Fig. 4 and Fig. 5 show a decrease in accuracy with a decrease in the number of n initial encoded nucleotides.

Referring to Table 3, the approach used to generate words and encode whole sequences gives a high accuracy of 98.62% thus showing the potential of applying methods known to NLP to bioinformatics. The value decreases with decreasing n of the initial nucleotides encoded and reaches a minimum value of 91.90%/89.34% for $n = 200$. In general, the second end of the sequence is more efficient, as can be seen in Fig. 5. Only in one case does the first end have a higher accuracy.

Table 2 shows that despite the training set being more than three times smaller, the accuracy of the models is marginally worse than the models trained on "approach 2". The nature of the changes remains similar, which is brilliantly shown in Fig. 4. The reduction of the training set results in faster training of the classifier, leading to a smaller dictionary size needed to encode the sequence.

1.4. Conclusions

In summary, our research shows that methods known from NLP can be successfully implemented into the analysis of Oxford Nanopore long-reads and can serve as the alternative to classical mapping approaches. Encoding a sequence in this way, training a classifier and then using it for prediction achieves an accuracy of 98.62%. The research confirmed the conjecture that encoding only the initial n nucleotides is associated with a decrease in classifier performance. For the initial 200 nucleotides, this is a decrease of up to 10% compared to encoding the whole sequence. As n decreases, the standard error increases. Such results can be satisfying when computation time is crucial.

In addition, when comparing the results of both ends of the sequence with each other, higher accuracy was obtained for the second end in almost every case. Furthermore, when comparing the results of the models trained on the two different datasets, the accuracy remains roughly similar despite more than three times fewer long-reads in approach 1.

Bibliography

1. Collins F.S., Morgan M., Patrinos A. "The Human Genome Project: lessons from large-scale biology". Science 300.5617 (2003): 286–290.
2. Boldogkői Z., et al. "Long-read sequencing–a powerful tool in viral transcriptome research". Trends in microbiology 27.7 (2019): 578–592.
3. Chen Zhiao, Xianghuo He. "Application of third-generation sequencing in cancer research". Medical Review 1.2 (2021): 150–171.
4. National Research Council. "Mapping and sequencing the human genome" (1988).
5. Kchouk Mehdi, Jean-Francois Gibrat, Mourad Elloumi. "Generations of sequencing technologies: from first to next generation". Biology and Medicine 9.3 (2017).
6. Weirather Jason L., et al. "Comprehensive comparison of Pacific Biosciences and Oxford Nanopore Technologies and their applications to transcriptome analysis". F1000Research 6 (2017).
7. Branton Daniel, David W. Deamer. Nanopore sequencing: an introduction. World Scientific, 2019.
8. Cruz-Garcia Lourdes, et al. "In vivo validation of alternative FDXR transcripts in human blood in response to ionizing radiation". International Journal of Molecular Sciences 21.21 (2020): 7851.
9. O'Brien Gráinne, et al. "FDXR is a biomarker of radiation exposure in vivo". Scientific reports 8.1 (2018): 684.
10. Ofer Dan, Nadav Brandes, Michal Linial. "The language of proteins: NLP, machine learning & protein sequences". Computational and Structural Biotechnology Journal 19 (2021): 1750–1758.
11. De Coster Wouter, et al. "NanoPack: visualizing and processing long-read sequencing data". Bioinformatics 34.15 (2018): 2666–2669.
12. Li Heng. "Minimap2: pairwise alignment for nucleotide sequences". Bioinformatics 34.18 (2018): 3094–3100.
13. Li Heng. "New strategies to improve minimap2 alignment accuracy". Bioinformatics 37.23 (2021): 4572–4574.
14. Wong Tzu-Tsung. "Performance evaluation of classification algorithms by k-fold and leave-one-out cross validation". Pattern Recognition 48.9 (2015): 2839–2846.
15. Qader Wisam A., Musa M. Ameen, Bilal I. Ahmed. "An overview of bag of words; importance, implementation, applications, and challenges". 2019 international engineering conference (IEC). IEEE, 2019.

NO-MAPPING MAPPING OF OXFORD NANOPORE LONG READS

Abstract

Sequence mapping is a time-consuming and crucial step when processing DNA-/RNA-seq data. The purpose of the study is to evaluate the effectiveness of machine learning models in replacing traditional targeted mapping for long-read sequencing data. Oxford Nanopore sequences consisted of three pairs of epithelial cell samples, where one of each pair was irradiated with 10 Gy. A total of 8.5 million long-read RNA sequences were available. Our approach proposed an alternative to classical bioinformatics solutions by using techniques known from natural language processing (NLP). At the beginning, long strings of nucleotides were expressed as base word sequences. During this research, a word length of six nucleotides and an offset of one nucleotide were used. Several sequence encoding scenarios were considered: whole sequence, first 1700 only, first 1400 only and so on until only first 200 nucleotides. In addition, the second end of the string is included. As a sequence classifier, a neural network with a dense 3-layer architecture with 50, 50 and 1 neurons, respectively, was chosen. A Leave-One-Sample-Out-Cross-Validation scheme was applied. The best results with an average accuracy of 98.62% were obtained for whole sequences, as expected. Reducing the sequence representation to 200 nucleotides resulted in a decrease to 89.34% for the same end of the sequence. These results confirmed the potential of using NLP methods in bioinformatics.

Keywords: sequencing, long reads, classification, natural language processing, oxford nanopore technology

Maciej DŁUGOSZ[1],[*]

Chapter 5. DNA SEQUENCING READS CORRECTION EVALUATION: REAL VS SIMULATED READS

5.1. Introduction

Techniques of a DNA sequencing give an opportunity to achieve a variety of scientific goals. The process typically is performed with automated machines called sequencers, resulting in a set of short DNA sequences called reads. The reads undergo a further processing, including matching them mutually in a task called *de novo* assembly to obtain long sequences called contigs. The aim is to generate the contigs possibly well-resembling sequences of the sequenced chromosomes. Another task is reads mapping, i.e. aligning them to a previously known sequence of the genome (reference genome). Mapping may be a part of workflows aiming at genetic disorders analysis, genome variants calling, identifying functional elements in genomes, and many others.

This work focuses on reads generated with Illumina sequencers, as it is one of the most popular technique. The Illumina reads are characterized by short length and relatively low amount of errors appearing in a sequencing process: some part (about a few percent, the fraction is called an error rate) of sequences symbols are incorrectly altered in reads by another ones. Such changes are called substitution errors, and are typically tens times more frequent than errors of another type, called insertions and deletions (indels). They include situations, when (typically single) symbols additionally appear in the read sequences or, respectively, they are missing. These errors tend to degrade the quality of downstream analysis. Consequently, a number of algorithms

[1] Department of Algorithmics and Software, Faculty of Automatic Control, Silesian University of Technology, Gliwice, Poland.
[*] Corresponding author: maciej.dlugosz@polsl.pl.

(correctors) aiming at detection and correction of the errors were devised. Detection can be facilitated with Phred quality scores, associated with the read symbols, however, in a step of the correction, all the algorithms utilize a data redundancy in the read. That follows, that the total length of the reads typically is significantly bigger than the length of the genome, hence one can expect, that a specified fragment of the genome is represented in multiple reads. The ratio of the lengths is called sequencing depth.

The introduction of a new corrector or performing a comparative analysis of the existing ones require choosing a correction evaluation method. One of the utilized strategies is simulating reads *in silico* and performing the correction of artificial reads. The other one is correcting reads obtained in real sequencing experiments. An emerging question concerns a concordance of these methods conclusions. In this work we focus on comparing correctors quality results obtained with three methods: two ones based on reads simulation and the one based on real reads. Our strategy is similar to the one adapted in a work [1], where it was used to evaluate correctors, however, now we observe another set of correctors, some correctors and an auxiliary assembler are of newer versions, we utilize another tool for reads simulation and obtain results for a wider range of sequencing depths. Moreover, here we consider strictly the comparison of the evaluation methods, rather than correctors evaluation.

5.2. Reads correction evaluation methods

In the literature, there are two main approaches of reads correction efficacy considered:

- direct, utilizing reads simulated with a computer by random probing a given reference genome and introducing errors; the method allows for simply comparing of corrected and erroneous reads with the original sequence and observing changes introduced by the corrector,

- indirect, utilizing reads obtained from real sequencing experiments, which are corrected and then passed as an input for another algorithms, aiming at acheiving some specific goals, as *de novo* assemblers, reads mappers or genome variant calling pipelines, and observing the results quality of such downstream processes.

5.2.1. Reads simulation methods and rationale

Utilizing simulated reads has several advantages over real ones:

- the position in the genome, where the real read originates from is not known [2],
- the period between the sequencing experiment and publishing the reads in a database can be long [2],
- a simulation allows reads with the specified characteristics to be obtained [2],
- real reads can be "contaminated" with another organisms sequences [3],
- a cost of a reads simulation is lower [3].

A simple method, based on Phred quality scores allows to simulate reads as follows. Given the reference genome and a real reads set (profile set), the sequences of the quality scores from the profile set are extracted. Then the probabilities of bases (reads symbols) substitution errors are computed by decoding the scores. Next, subsequences from the random positions of the reference genome are extracted. The subsequences are of the length equal to the profile reads, and they constitute the output reads set. Finally, the read sequences are disturbed by generating the errors with the obtained probabilities. As a result, a reads file is generated, containing the subsequences with introduced errors and accompanying quality score sequences from the profile set. The method is popular as an *ad hoc* strategy, as in [4]. In [5] it is enhanced by including different probabilities of various subtitution errors, e.g. the probability of substituting a symbol A with C is higher than with G or T.

Another approach is to engage specialized simulation tools. A group of them was presented in an overview work [6], but with no experimental veryfication. One of the tools is ART [7]. It was designed to simulate reads of a few types, including the ones from Illumina sequencers. Authors included a set of generating read models (error profiles). The profiles correspond to rather outdated versions of sequencers, nevertheless, ART allows to simply generate own error profiles based on given profile sets, hence its utilization is still adequate. Another tool, SInC [8], has a built-in model to simulate only Illumina reads of length 100 bp (base pairs). It allows to generate sequencing reads, but the tool is rather desinged to simulate genome variants, which manifest itself in the reads similarly to errors, however, they definitely are not the same. Both of them are a differences with the reference genome, but the errors differs also with the genome being sequenced. CuReSim [9] was developed to simplify a reads mappers evaluation. It has a few predefined error probability distributions, can be parametrized with real error scores and a read length, and is designed to generate reads of any type. FASTQsim [10], as the authors stated, also would be capable to simulate

reads of any techniques, as it is equipped with a tool for real reads analysis and may be parametrized with a read length, substitution probability distribution, indel length distribution, etc.

Regardless of the simulation method, the evaluation is in general similar: simulated (erroneous) reads with the errors are corrected and the resulting (corrected) reads are compared with the ones devoid of the errors (proper ones, also returned by the simulator), which allows to simply measure number of errors before and after the correction, including number of errors introduced by the corrector. The comparison may be performed in two granulation modes: in terms of single symbols (a single base error correction is treated as a success), or of entire reads (the entire read must contain just proper symbols to be successfull).

The correction measure typically is defined as

$$\text{gain} = \frac{\text{TP} - \text{FP}}{\text{TP} + \text{FN}} \tag{1}$$

where:

TP – number of symbols/reads perfectly corrected

FP – number of symbols/reads originally correct, but disrupted by the corrector

FN – number of uncorrected or miscorrected symbols/reads

The value of gain is negative, when a number of disruptions is higher than a number of effective corrections.

5.2.2. Comparison with real reads

Correctors evaluation can be performed by correcting a set of real reads and processing the output by another algorithm. In such a situation, a quality of that algorithm is measured. One of the most useful, however not straighforward method, is apdapting a *de novo* assembler. The output quality, a set of obtained contigs, typically is rated with a set of measures, i.a.: N50, NG50, NGA50, genome coverage (cov), number of missassemblies (misasm), or LGA50 values. N50 is such a contig length, that the total length of the contigs of length N50 or more constitutes half of all the contigs length. NG50 is such a contig length, that the total length of the contigs of length NG50 or more constitute a half of the entire genome. NGA50 is similar to NG50, but before rating the contigs are splitted in places of assembly errors. Genome coverage (or genome fraction) is the percentage of contig bases aligned to the reference genome, whereas number of missassemblies refers to wrong alignments of the contigs positions.

LGA50 is defined similarly to NGA50, however, it is a number of contigs rather than the length. Number of misassemblies and LGA50 indicate better results when are lower, the other ones – when higher.

5.3. Results and discussion

Table 1 contains reference genomes identifiers, whereas table 2 contains accession numbers of the real read sets used in the experiments. To simulate reads and evaluate *de novo* assembly results, we chose three model organisms: *Saccharomyces cerevisiae*, *Caenorhabditis elegans*, *Musa acuminata*. We simulated reads of various characteristics: read lengths, error rates, and sequencing depths, with two methods: Phred and ART, both based on predefined profile sets, accordant to the intended read length and error rate. The choice of the ART is motivated by possibility to generate a profile with a given profile reads set. It allows the output read characteristics to be flexibly configured with an expected length and error rate. In a context of the abovementioned arguments, the potentially competing tool for ART would be not discussed Mason 2 [2], however, due to technical problems, described in [11], we will not take it into account. Moreover, in the overview work [6] ART was stated as the best simulator.

The results were compared with a granulation of the entire reads, due to a higher usefullness of the "completely" corrected reads [12] and the reason stated in a supplementary material of [13]: a small part of Illumina reads have a huge number of errors, hence such reads can strongly affect the whole rate. Moreover, expecting the entire reads to be error-free is a stricter requirement.

The real reads evaluation was performed by assembling them with Minia [14] and achieving the aforementioned measures with Quast [15]. In experiments we have included the correctors presented in Table 3.

Table 1

Reference genomes

Organism	Genome length [Mbp]	Accession number
S. cerevisiae	11.63	GCF_000313865.2
C. elegans	102.8	GCF_000002985.6
M. acuminata	461.5	GCF_000313855.2

Table 2

Read sets accession numbers

Accession no.	Read length [bp]	Depth	Application
ERR422544	100	41	Real reads for *S. cerevisiae*
SRR543736	101	57	Real reads for *C. elegans*
ERR204808	108	16	Real reads for *M. acuminata*
DRR031158	100	–	Profile set for $p \approx 2\%$
SRR1802178	150	–	Profile set for $p \approx 2\%$
SRR065390	100	–	Profile set for $p \approx 4 - 5\%$
SRR650760	151	–	Profile set for $p \approx 4 - 5\%$

Table 3

Correction algorithms

Algorithm	Version	Paper	Algorithm	Version	Paper
RECKONER	2.0	[16]	Lighter	1.1.2	[21]
Musket	1.1	[4]	BFC	BFC-ht, version r181	[13]
RACER	–	[17]	Karect	1.0	[22]
BLESS	1.02	[18]	SAMDUDE	Uploaded 2 May, 2018	[23]
Fiona	2.4.0	[19]	CARE	2.1	[24]
Blue	1.1.3	[20]			

The reads sets were generated for two lengths (100 bp and about 150 bp), two error rates p (about 2% and 4 up to 5%) and three sequencing depths (20×, 30×, 60×), for three different-sized genomes, representing a wide range of possible reads characteristics. The real reads sets were downloaded from a public database ENA, and represent the mentioned three genomes. In a case, when a corrector has to be aparametrized with a k-mer length, we run it multiple times and chose the value resulting the best output (for simulated reads we chose the length for a sets of 20× depth).

Figures 1, 2 show, respectively, result for Phred simulation and simulation with ART. Notation LxDy means a read length x [bp] and a sequencing depth y. Gain measure values were multiplied by 100. Figures 3, 4 show results for *de novo* assembly of the real reads. As a reference, we added results for not corrected real reads, marked as (raw). With a dagger (†) we marked cases, when a corrector failed due to a timeout (more than 24 hours), with a section mark (§), when it crashed, and with an asterisk (*), when it returned a message about wrong quality scores (BLESS). For *M. acuminata* measures referring to a genome size (NG50, NGA50, LGA50), due to a low total contigs lengths, are unavailable.
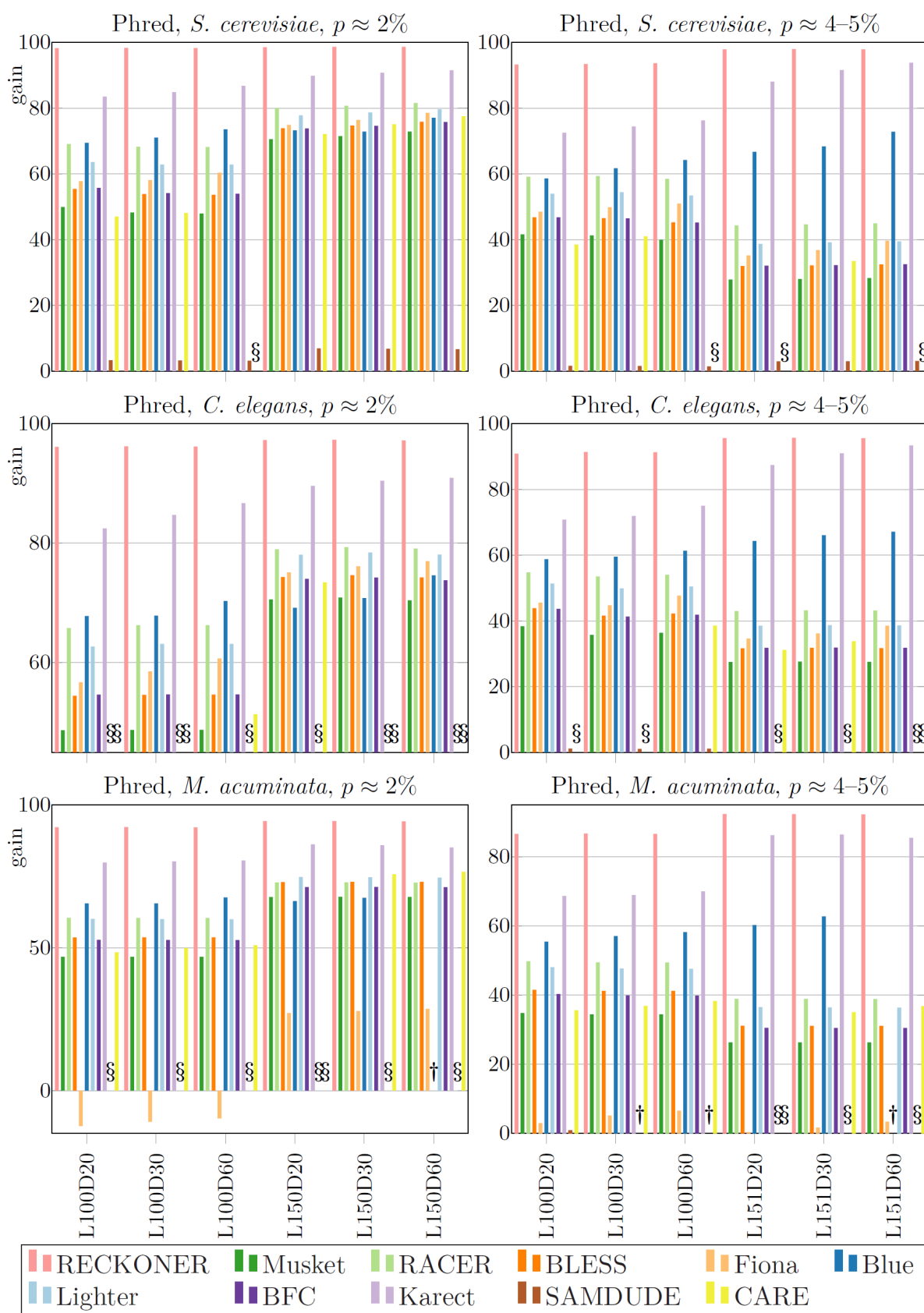
Fig. 1. Results for reads simulated with a Phred method
Rys. 1. Wyniki dla odczytów symulowanych metodą Phred
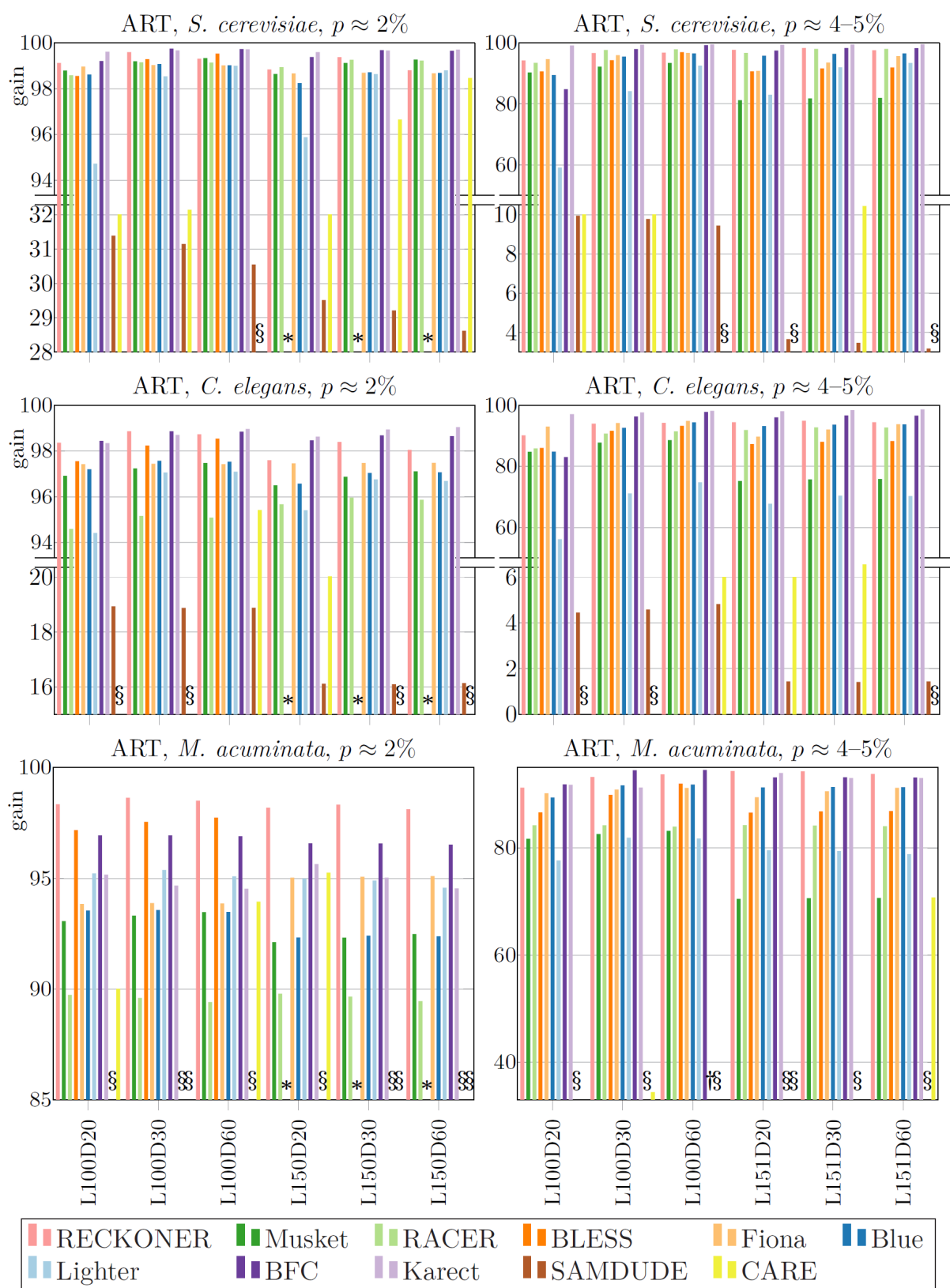
Fig. 2. Results for reads simulated with ART

Rys. 2. Wyniki dla odczytów symulowanych narzędziem ART
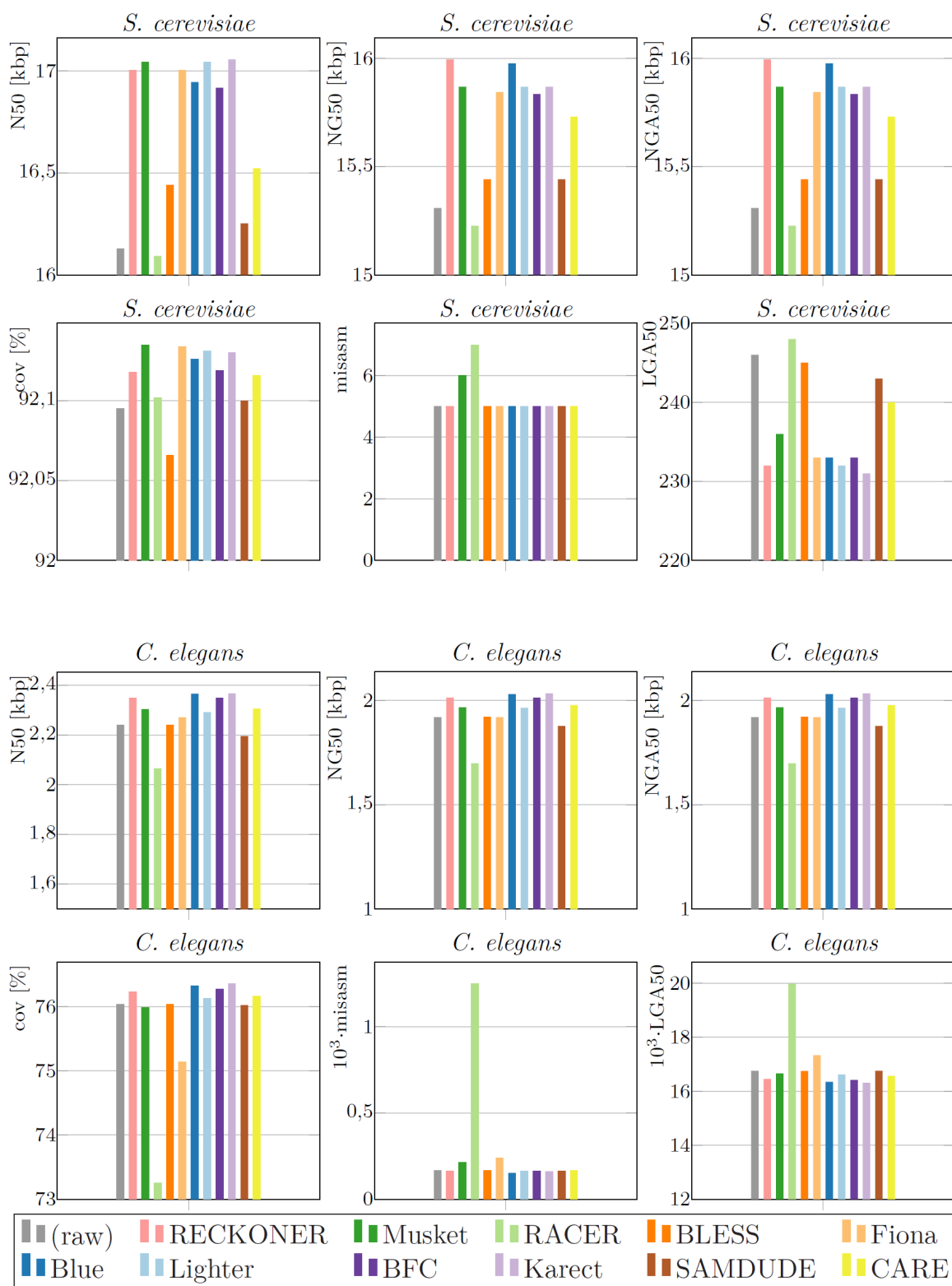
Fig. 3. Results for *de novo* assembly of the real reads
Rys. 3. Wyniki asemblacji *de novo* odczytów rzeczywistych
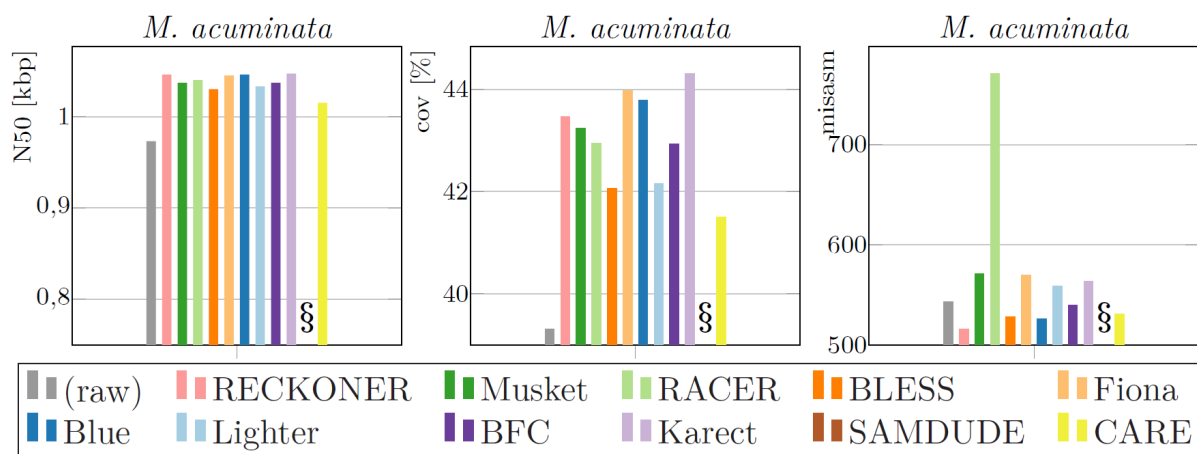
Fig. 4. Results for *de novo* assembly of the real reads (cont'd)
Rys. 4. Wyniki asemblacji *de novo* odczytów rzeczywistych (cd.)

The results for Phred simulation show, that RECKONER is extremely efficient and in most of the cases it allows to correct over 90% of erroneous reads, in some cases achieving almost 100%. Another good algorithm is Karect, and as a third appears Blue. RACER and Lighter achieve similar, average results. BLESS and BFC should be rated rather poorly, but clearly negatively outstanding algorithms are Musket, CARE and, especially, SAMDUDE. For the third genome very weak results was obtained by Fiona, which in three cases caused a general data degradation. An interesting observation is a read length impact. In the case of good-quality reads ($p \approx 2\%$) for longer reads better results were obtained. In a case of the other reads ($p \approx 4$–5%) the trend is inverted.

In the case of ART reads the general observation is that the results are more even, both between different genomes and algorithms. The correctors ranking is more varied, depending on the cases. Typically, the best is one of BFC or Karect, however, for *M. acuminata* reads Karect results are out of the top and usually the best one is RECKONER. Moderated results are obtained for BLESS and Blue. There are no cases, when Musket or Fiona are severely outstanding. The weakest algorithms are Lighter, sometimes RACER, SAMDUDE and CARE. The observed read length impact is different and more subtle. For the reads of both error rates the longer ones cause lower quality, but in some cases such phenomenon is not visible.

The relative values of *de novo* assembly evaluation, performed for the real reads corrected with different algorithms vary slightly, which is an effect of some assembler tolerance for the sequencing errors and not a straightforward transfer of the errors to the contigs quality. It seems, that the best algorithm is Karect, followed by RECKONER and Blue, however the top varies, depending on the genome and a measure. For example, for *S. cerevisiae* the top algorithms change in terms, respectively, N50 and

NG50. In general, Musket, Fiona, Lighter, BFC characterise by moderated results. The poorest algorithms are RACER, BLESS, CARE, and SAMDUDE. All of them have weak values of contigs length measures, but additionaly RACER has huge numbers of missassemblies.

To summarize, in many cases a relative and an absolute correctors qualities differ for various evaluation strategies. We will list the most visible cases. RACER achieves an average results in a case of Phred reads, rather weak for ART reads, however in a case of *de novo* assembly, the results are definitely bad. Results for BLESS are weak for the Phred and average for the ART simulated reads, but for the real ones are very poor. Fiona achieves very weak results for *M. acuminata* Phred simulated reads, but for the simulated with ART and the real ones the quality does not seem to be negative. For the Phred simulated and the real reads BFC is classified as an average algorithm, in contrast to the ones generated with ART, where it is one of the best. On the other hand, in some cases all the comparisons yielded similar conclusions. RECKONER is one of the best one in all the cases (except for the Phred reads, where it advantageously outstands), similarly to Karect. SAMDUDE and CARE in all the cases achieve weak results.

5.4. Conclusions

The experiments showed, that the correction algorithms evaluation results differ depending on the adopted strategy. A simple Phred method results are dispersed depending on the chosen corrector, probably privileging the ones accepting idealized conditions of the method. Results for the reads generated with ART are more levelled, but still does not clearly correspond to the real reads. On the other hand, the outcome for real reads undergo an impact of the addtional step of *de novo* assembly and inconsistent results for a single reads set may be obtained. Moreover, the results of the various algorithms differ just slightly.

In contrast, the comparison of methods showed, that in some cases the results are consistent. In all the strategies RECKONER and Karect are in a group of the best algorithms, while SAMDUDE and CARE almost always are the weakest, but these situations are not a clear rule. The observations give no basis to conclude, which method of simulation is more concordant with an indirect method of *de novo* assembly utilization.

Acknowledgements

Bibliography

1. M. Długosz, S. Deorowicz, RECKONER: read error corrector based on KMC, *Bioinformatics* (2017) **33(7)**:1086–1089.
2. M. Holtgrewe, Mason: a read simulator for second generation sequencing data, Technical Report FU Berlin (2010).
3. A. Shcherbina, FASTQSim: platform-independent data characterization and in silico read generation for NGS datasets, *BMC research notes* (2014) **7(1)**:1–12.
4. L. Yongchao, J. Schröder, B. Schmidt, Musket: a multistage k-mer spectrum-based error corrector for Illumina sequence data, *Bioinformatics* (2013) **29(3)**:308–315.
5. D.R. Kelley, M.C. Schatz, S.L. Salzberg, Quake: quality-aware detection and correction of sequencing errors, *Genome biology* (2010) **11(11)**:1–13.
6. M. Escalona, S. Richa, D. Posada, A comparison of tools for the simulation of genomic next-generation sequencing data, *Nature Reviews Genetics* (2016) **17(8)**:459.
7. W. Huang, L. Li, J.R. Myers, G.T. Marth, ART: a next-generation sequencing read simulator, *Bioinformatics* (2012) **28(4)**:593–594.
8. S. Pattnaik, S. Gupta, A.A. Rao, B. Panda, SInC: an accurate and fast error-model based simulator for SNPs, Indels and CNVs coupled with a read generator for short-read sequence data, *BMC bioinformatics* (2014) **15(1)**:1–9.
9. S. Caboche, C. Audebert, Y. Lemoine, D. Hot, Comparison of mapping algorithms used in high-throughput sequencing: application to Ion Torrent data, *BMC genomics* (2014) **15(1)**:1–16.
10. A. Shcherbina, FASTQSim: platform-independent data characterization and in silico read generation for NGS datasets, *BMC research notes* (2014) **7(1)**:1–12.
11. M. Długosz, S. Deorowicz, M. Kokot, Improvements in DNA Reads Correction, *International Conference on Man-Machine Interactions, October 3–6, 2017, Kraków* (2017):115–124.
12. M. Molnar, L. Ilie, Correcting illumina data, *Briefings in bioinformatics* (2015) **16(4)**:588–599.

13. H. Li, BFC: correcting Illumina sequencing errors, *Bioinformatics* (2015) **31(17)**:2885–2887.

14. R. Chikhi, G. Rizk, Space-efficient and exact de Bruijn graph representation based on a Bloom filter, *Algorithms for Molecular Biology* (2013) **8**: 1–9.

15. A. Gurevich, V. Saveliev, N. Vyahhi, G. Tesler, QUAST: quality assessment tool for genome assemblies, *Bioinformatics* (2013) **29(8)**:1072–1075.

16. M. Długosz, S. Deorowicz, Illumina reads correction – evaluation and improvements, *In Review* preprint (2023), doi:10.21203/rs.3.rs-2715541/v1.

17. L. Ilie, M. Molnar, RACER: Rapid and accurate correction of errors in reads, *Bioinformatics* (2013) **29(19)**:2490–2493.

18. Y. Heo, A. Ramachandran, W.M. Hwu, J. Ma, D. Chen, BLESS 2: accurate, memory-efficient and fast error correction method, *Bioinformatics* (2016) **32(15)**: 2369–2371.

19. M.H. Schulz, *et al.*, Fiona: a parallel and automatic strategy for read error correction, *Bioinformatics* (2014) **30(17)**:i356–i363.

20. P. Greenfield, K. Duesing, A. Papanicolaou, D.C. Bauer, Blue: correcting sequencing errors using consensus and context, *Bioinformatics* (2014) **30(19)**:2723–2732.

21. L. Song, L. Florea, B. Langmead, Lighter: fast and memory-efficient sequencing error correction without counting, *Genome biology* (2014) **15**:1–13.

22. A. Allam, P. Kalnis, V. Solovyev, Karect: accurate correction of substitution, insertion and deletion errors for next-generation sequencing data, *Bioinformatics* (2015) **31(21)**:3421–3428.

23. I. Fischer-Hwang, I. Ochoa, T. Weissman, M. Hernaez, Denoising of aligned genomic data, *Scientific reports* (2019) **9(1)**:1–11.

24. F. Kallenborn, J. Cascitti, B. Schmidt, CARE 2.0: reducing false-positive sequencing error corrections using machine learning, *BMC bioinformatics* (2022) **23(1)**:1–17.

DNA SEQUENCING READS CORRECTION EVALUATION: REAL VS SIMULATED READS

Abstract

The problem of Illumina whole genome sequencing reads correction is widely considered in the literature. Nevertheless, new correction algorithms are still introduced, requiring reliable methods of the process efficiency evaluation to be available. The methods include utilization of both reads simulated *in silico* and real ones, obtained from DNA sequencing process. The paper focuses on comparing these approaches, trying to give the answer, if a convenient reads simulation allows the correction quality to be reliably verified. We evaluated a set of correction algorithms by processing reads generated with a simple method based on a Phred scores utilization and simulated with a specialized tool. We also *de novo* assembled sets of reads obtained from real sequencing experiments, observing an impact of the correction to the contigs characteristics. Finally, a concordance of the three methods results was analyzed.

Keywords: DNA sequencing, Illumina, read error correction, reads simulation, genome assembly

Kinga GAWRON[1,2], Magdalena WĘGRZYN[1,2], Katarzyna WIAK[1,2],
Julia CIOMPERLIK[3], Sara KOCJAN[3], Małgorzata ADAMIEC-ORGANIŚCIOK[4,5],
Monika ŚMIGA-MATUSZOWICZ[6], Katarzyna KRUKIEWICZ[6,7,*],
Magdalena SKONIECZNA[4,5,*]

Chapter 6. STUDY OF THE ANGIOGENESIS PROCESS ON THE SURFACE OF BIODEGRADABLE POLYESTERS BASED ON ISOSORBIDE

6.1. Introduction

The main challenge of tissue engineering is to allow for a full restoration or repair of a damaged tissue, using a combination of chemistry, materials engineering, and molecular biology [1]. Design of multifunctional tissue scaffolds is an essential aspect of progress in tissue engineering, as a variety of health conditions requires the use of implantable biomaterials. Tissue scaffolds can be used to rebuilt body functions in different locations, e.g., skin scaffolds can facilitate wound healing, and bone scaffolds can improve bone tissue regeneration. Apart from a specialistic function, every tissue scaffold needs to enable the regenerating tissue to function properly, including its proper nutrition, for which the formation of blood vessels is necessary [2]. Therefore, the design of tissue scaffolds should take into consideration their ability to affect the formation of blood vessels. A major challenge of tissue engineering is to create a scaffold that will be

[1] Faculty of Automatic Control, Electronics And Computer Science, Silesian University of Technology, Akademicka 16, 44-100 Gliwice, Poland.
[2] Students' Scientific Society of Biotechnology at the Biotechnology Centre of the Silesian University of Technology, Krzywoustego 8, 44-100 Gliwice, Poland.
[3] Faculty of Chemistry, Silesian University of Technology, Strzody 9, 44-100 Gliwice, Poland.
[4] Department of Systems Biology and Engineering, Silesian University of Technology, Akademicka 16, 44-100 Gliwice, Poland.
[5] Biotechnology Centre, Silesian University of Technology, Krzywoustego 8, 44-100 Gliwice, Poland.
[6] Department of Physical Chemistry and Technology of Polymers, Silesian University of Technology, Strzody 9, 44-100 Gliwice, Poland.
[7] Centre for Organic and Nanohybrid Electronics, Silesian University of Technology, Konarskiego 22B, 44-100 Gliwice, Poland.
[*] Corresponding authors: mskonieczna@polsl.pl; kkrukiewicz@polsl.pl.

penetrable by the blood vessels [3]. This is why it is crucial that tissue scaffolds exhibit a porous structure, and a large surface area per scaffold volume. This allows blood vessels to passing through, to provide the transportation of cells, as well as nutrients [4].

The selection of appropriate biomaterials plays an important role in the process of developing tissue scaffolds. Of particular interest are biodegradable polymers, such as polylactide (PLA), polyglycolide (PGA), poly(lactide-*co*-glycolide) copolymer (PLGA), polycaprolactone (PCL), as well as bioactive ceramics, such as calcium triphosphate (TCP) [5]. Biomaterials can be processed with the use of different techniques to form a porous structure, that will promote angiogenesis. One of these techniques is electro-spinning, which helps to fabricate micro- and nano-fibers. This process involves pushing the polymer through an electrostatic field, which leads to the formation of a flux, which then breaks down to form fibers whose diameters can be adjusted [1]. The use of nano-fibers enables the formation of 'nano-scaffolds' that are not only lighter, but also more mechanically robust [6]. Other common methods of producing porous scaffolds include thermally induced phase separation (TIPS), or phase inversion in the solvent-insolvent system using supercritical CO_2 [7]. Phase separation methods are very sensitive to many parameters (solution concentration, polymer molecular weight, etc.), which makes it difficult to obtain a repeatable microstructure of the material [4]. Observations using a confocal fluorescence microscope are used to confirm whether cells are able to penetrate such materials. Using a confocal microscope, it is possible to visualize both, a 2D plane and a 3D structure of a biomaterial.

Angiogenesis is a process responsible for the expansion and reconstruction of the blood vessel network. It consists of two mechanisms: endothelial germination and intussusception of microvascular growth (IMG) [8]. The progression of the angiogenesis process can be monitored by the analysis of different biomarkers. For instance, vascular endothelial growth factor (VEGF) is known to induce a strong angiogenic response and lymphangiogenesis in various *in vivo* models. VEGF acts as a survival factor for endothelial cells both *in vitro* and *in vivo*, and its level determines the rate of formation of blood vessels [9]. There are several forms of VEGF proteins in the human body, for instance VEGF-A, which induces the angiogenesis process and produces arterial blood vessels, VEGF-B responsible for the development of coronary arteries, and VEGF-C and VEGF-D, thanks to which the lymphatic system develops. As all these forms have a significant impact on the angiogenesis process [10]. The process of angiogenesis can

be also studied by analyzing an expression profile of particular genes. VEGF-A expression is regulated in different tissues and conditions by a number of factors including hypoxia (e. g. via the HIF-1 pathway), other cytokines and growth factors (e. g. TGF-β), various hormones (e. g. estrogen and progesterone) and, importantly in cancer, by oncogenes and tumor suppressor genes. VEGF-A produces several different transcripts by alternative splicing; three of these, the 189, 165, and 121 amino acid forms, are thought to be of the greatest importance (mouse isoforms are one amino acid shorter). The product of VEGF-B expression is a pre-pro-protein, which in the process of post-translational processing is transformed into two isoforms, containing 167 and 186 amino acids, respectively, while VEGF-C is the product of expression of a gene located in the long arm of chromosome 4 (4q34). This factor participates in the stimulation of proliferation and migration of endothelial cells and contributes to increased vascular permeability. It also causes hyperplasia of the lymph vessels of the skin. VEGF-D stimulates the proliferation of lymphatic endothelial cells. It exhibits angiogenic properties both *in vitro* and *in vivo*. Increasing the expression of this factor in keratinocytes stimulates the formation of lymph vessels in the skin. Observations showed the presence of VEGF-D expression products also in melanocytes, fibroblasts and lung mesenchyme [12]. In addition, the angiogenesis process is regulated by the enzymes MMP-2 and MMP-9. At the same time, MMP-2 and MMP-9 may also contribute to the formation of angiogenesis inhibitors (TIMP-1, TIMP-2). The correct expression of MMPs is regulated at the level of gene transcription, translation, activation of proenzymes and by activators and tissue inhibitors (TIMPs – tissue inhibitors of metalloproteinases). Moreover, the growth factor VEGF is an important regulator of MMPs expression.

The process of angiogenesis is also related with the inflammation, since the presence of an inflammatory state induces angiogenesis. Therefore, when designing biomaterials intended to promote angiogenesis, one must pay attention to whether the same biomaterial induces inflammation. The protein IL-8 (Interleukin 8) can be used for checking whether the biomaterial induces a foreign body reaction. IL-8 is a chemotactic, and growth factor for endothelial cells. It plays an important role in tumor growth, angiogenesis and metastasis. It is correspondingly upregulated when inflammation occurs [11].

Consequently, the most effective biomaterial that will be able to serve as an efficient tissue scaffold should have a porous structure that allows cell penetration, promotes

the process of angiogenesis through the expression of appropriate genes, but at the same time prevents tissue inflammation. The main goal of our work is to develop biocompatible polyesters and to investigate their impact on the process of angiogenesis and inflammation. In our previous work [13], we have shown the synthesis of a biocompatible polyester based on poly(isosorbide sebacate) (PISEB) and poly(L-lactide-*co*-glycolide) (PLGA), as well as described the preliminary data concerning its biocompatibility. In this work, we present an in-depth analysis of its impact on the process of angiogenesis and inflammation by the analysis of microscopic images of HUVEC cells cultured on its surface.

6.2. Materials and methods

6.2.1. Materials synthesis

Poly(isosorbide sebacate) (PISEB) and poly(L-lactide-*co*-glycolide) (PLGA) were synthesized according to the previously described procedure [13]. A blend of PISEB and PLGA (1:1) was dissolved in dichloromethane and electrospun as described earlier [13].

6.2.2. Biological Characterization

The human umbilical vein endothelial cells, HUVEC (pooled donor, Lonza, Basil, Switzerland), were cultured in EGMTM-2 Endothelial Cell Growth Medium supplemented with all components from EGMTM-2 SingleQuots Supplement Pack in 75 cm^2 cell culture bottles. Once the cells reached confluency, they were removed from the culture bottle and washed with 3 mL of Dulbecco's phosphate-buffered saline, DPBS (PAN-Biotech, Aidenbach, Germany) before being treated with 3 mL of 0.25% trypsin--EDTA solution (Sigma Aldrich) for 5-10 minutes. The trypsinization was stopped by adding 6 mL of a complete culture medium. The cells were then seeded into 12-well plates at a density of 2×10^5 cells per well in a 2 mL volume of medium. After 48 hours of incubation, the cytotoxicity of the test materials was evaluated by measuring the ability of viable cells to reduce the tetrazolium dye MTT (3-[4,5-dimethylthiazol-2-yl]--2,5-diphenyltetrazolium bromide) to formazan. The cells were collected from the

12-well plates and exposed to 50 μL of MTT solution (0.05 mg/mL in phenol red- and FBS-free DMEM-F12; PAA). After 2 hours of incubation, the MTT solution was removed, and the resulting violet formazan crystals were dissolved in 400 μL of acidic isopropanol (0.05 M HCl). The absorbance of the solution was measured at 570 nm using a multi-well plate reader SYNERGY4 (BioTek Instruments, New York, NY, USA).

To conduct long-term microscopic observations, the HUVEC cells were seeded directly onto the test materials or a control polystyrene plate (Sarstedt, Numbrecht, Germany) in EGM-2 medium, supplemented with a complete Bulletkit of growth factors (Lonza). After incubating for 48 hours, the cells were live stained with Sybr Green dye (Life Technologies, Carlsbad, CA, USA) for nucleus visualization, and the signals were captured using a JuLI_FL™ apparatus (NanoEntek, Seoul, South Korea) with a magnification of 40× and collected in visible or FITC channels.

The expression of pro-angiogenic markers (IL8, VEGF, MMPs) and TIMPs was assessed by performing gene expression analysis using RT-qPCR. This analysis was conducted on both control cells and cells incubated with the tested materials for 48 h (HUVEC cell line). Following trypsinization and collection of the cells, total RNA was isolated using the phenol-chloroform extraction method with the Total RNA Isolation kit (A@A Biotechnology, Gdańsk, Poland). The efficiency of RNA isolation was measured spectrophotometrically. Gene amplification was carried out with help of commercially available kits (Real-Time 2xPCR Master Mix SYBR A; A@A Biotechnology) and a set of primers for IL8, VEGF, MMP2, MMP9, TIMP1, and TIMP2 (Genomed, Warsaw, Poland) was created with an online tool (OligoAnalyzer™ Tool, IDT, Coralville, IA, USA). The quantitative PCR reaction, preceded by reverse transcription using the NG dART RT kit (EURx, Gdańsk, Poland) was performed with the CFX96 Touch™ Real-Time PCR Detection System thermocycler (Bio-Rad, Hercules, CA, USA). Data are presented as mean ± SD, from 3 experiments, calculated with formula $R = 2^{-\Delta\Delta C_T}$ by Livak [17]. Statistical significance was calculated with a T-test and p-value < 0.05 is indicated with a star*.

The data analysis of real-time PCR reactions, as well as the control of the thermocycler and data collection, were performed using Bio-Rad's CFX Manager 3.1 software. For the obtained threshold values of Cq (Ct) determined by the software, the relative expression level of the target gene in cells was calculated compared to control cells. The 2-ΔΔCt method was used for this purpose. Measurements were conducted for a reference gene (RPL) and the target genes. This allows for the calculation of the ratio,

representing the relative increase in expression (R), based on the fluorescence intensity of the respective gene at the Cq cutoff points (Cq target and Cq reference), according to the formula.

$$R = \frac{2^{\Delta Cq\ target}}{2^{\Delta Cq\ reference}}$$

R – relative expression ratio of the gene, representing the increase in transcript quantity in the sample compared to the reference gene.

ΔCq target – the difference in threshold values (Cq) for the target gene.

ΔCq reference – the difference in threshold values (Cq) for the reference gene.

To perform confocal microscopy observations, the HUVEC cells were seeded onto the test materials, or a control polystyrene plate (Sarstedt, Numbrecht, Germany) as described above. After incubating for 48 h, the cells were stained with DAPI dye (Invitrogen™, Waltham, MA, USA) for nucleus visualization, and the signals were captured using Olympus FluoView FV1000™ confocal microscope (Olympus LS, Tokyo, Japan). In a confocal microscope, a laser is used to excite the fluorescent label present in the sample. The laser beam is concentrated to a specific point and systematically moved across the sample, scanning it in a sequential manner, line by line. DAPI stands for 4',6-diamidino-2-phenylindole, which is a fluorescent dye that specifically binds to DNA molecules. The mechanism of DAPI staining involves the intercalation of the DAPI dye molecules between the base pairs of double-stranded DNA. This binding occurs due to the affinity of DAPI for the A-T-rich regions of DNA. Once bound, DAPI molecules emit blue fluorescence when excited by ultraviolet (UV) light. DAPI undergoes approximately 20-fold enhancement of fluorescence when associated with DNA, having an excitation maximum of 358 nm and an emission maximum of 461 nm.

6.3. Results and Discussion

The biocompatibility of PLGA, PISEB, and PLGA/PISEB was assessed in the previous experiments that have been already published [13]. The MTT assay results indicated that the investigated materials were biocompatible since the relative cell viability of PISEB ($91 \pm 3\%$) and PLGA/PISEB ($91 \pm 4\%$) was only slightly lower than that of the tissue culture plastic control (100%), and comparable to that of PLGA ($94 \pm 3\%$).

The JuLI_FL™ imaging system was used to observe the visible light and green fluorescence signals emitted by the nuclei of HUVEC cells seeded on investigated polymers during 48–72 h of microscopic observation. The HUVEC cells were cultured on polystyrene plastic plates coated with collagen type IV to improve cell adhesion and vein-like morphology formation. Compared to panels stimulated with vascular endothelial growth factor (VEGF) and cultured with a complete Bulletkit of growth factors, cells on the control plates exhibited a typical tube-formation morphology during the neo-angiogenesis process (Fig. 1) [14, 15].

Fig. 1. Typical images of HUVEC cells cultured on VEGF-supplemented (w/v 0.5%) EGM-2 medium for 48 h on control polystyrene plate and tested materials: drop-casted PISEB, electrospun PLGA, and electrospun PLGA/PISEB, selected with fluorescein. Tubular shapes of the cells presented in visible light are indicated by red arrow (scale bar 500 µm; magnification 40×; JuLI_FL™ apparatus)

Rys. 1. Obrazy komórek HUVEC hodowanych na pożywce EGM-2 z dodatkiem VEGF (stężenie 0.5%) przez 48 godzin na kontrolnej płytce polistyrenowej oraz testowanych materiałach: osadzonym PISEB, elektroprzędzonym PLGA i elektroprzędzonym PLGA/PISEB, wybrane za pomocą fluoresceiny. Rurkowate kształty komórek prezentowane w świetle widzialnym wskazano czerwoną strzałką (skala 500 µm; powiększenie 40×; aparat JuLI_FL™)

Real-time qPCR reaction was performed to assess gene expression for HUVEC cell controls [13]. These cells were previously incubated with materials – PLGA, PLGA+PISEB, and PISEB for 48 hours. The ratio (relative gene expression fold change) is calculated using the formula mentioned in previous subsection – R = 2-$\Delta\Delta$Ct. As a result, the control is always determined as a value of 1.

The results (Fig. 2), which have been previously presented in [13], show that both the presence of VEGF and its absence increases the expression of the MMP2 gene. In case of TIMP2 gene, an upregulation in absence of VEGF is observed. If a similar experiment was conducted for a longer period rather than just 48 hours, it would be possible to observe more clearly how VEGF suppresses the expression of MMP2.

In the case of MMP9 and TIMP1, MMP9 is significantly overexpressed in the presence of VEGF. The situation is reversed when VEGF is not present – the expression of the TIMP1 gene outweighs the expression of MMP9. From this phenomenon, it could be concluded that angiogenesis markers are produced only in the presence of VEGF, which is the first factor initiating this process.

Similarly to MMP9, significantly higher expression of IL8 was observed after the addition of VEGF – adding VEGF to the culture medium blocked its expression. The absence of VEGF can initiate VEGF expression, so that it may undergo slight stimulation in the following days.
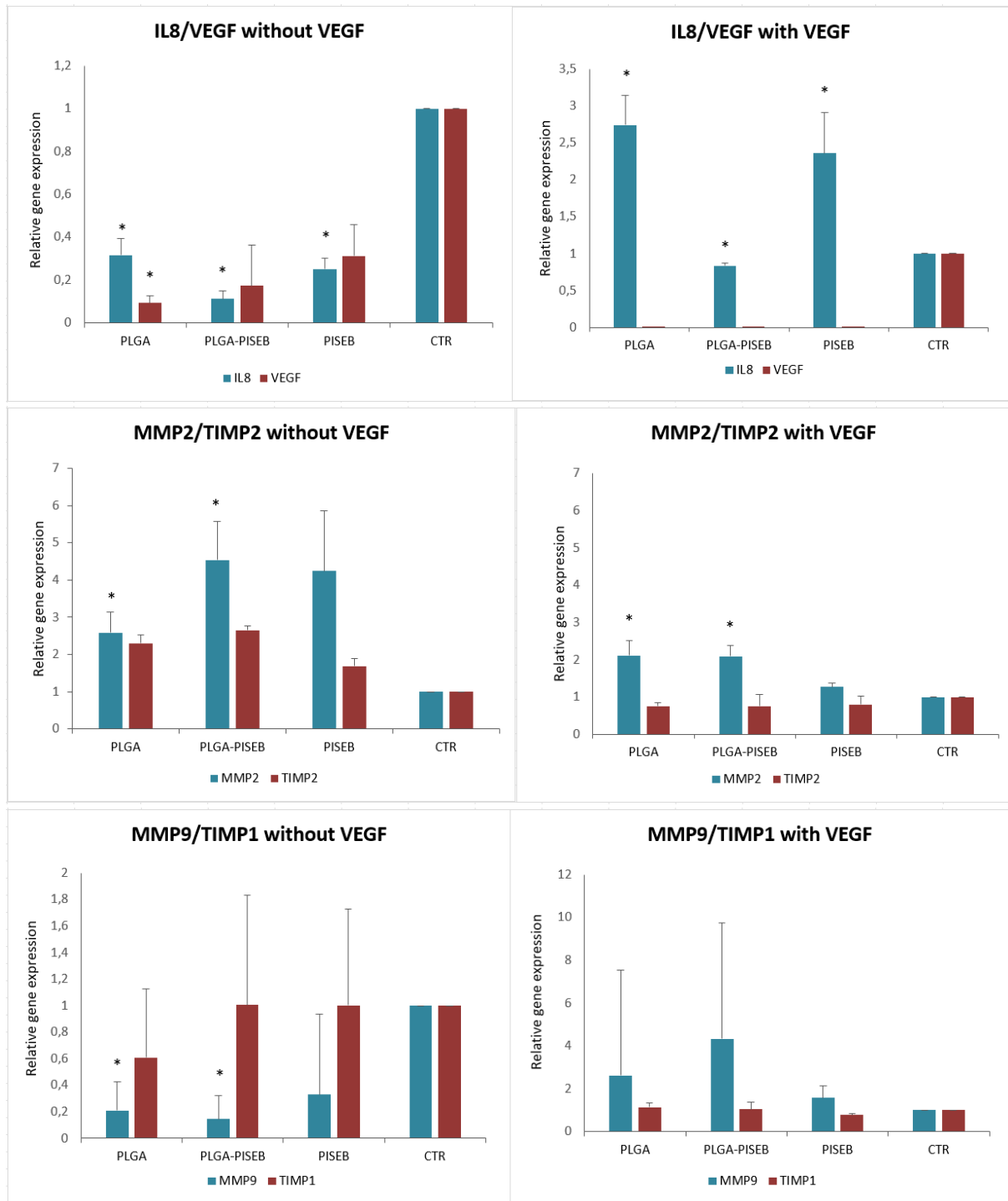
Fig. 2. Relative gene expression level, for pro-angiogenic markers: MMPs, IL8 and angiogenesis inhibitors TIMPs in HUVEC cells after 48 h of incubation on materials with, or without VEGF. Data are presented as mean ± SD from 3 experiments. Statistical significance in comparisons to controls was calculated with a Student's t-test and p-value < 0.05 is indicated with a star *

Rys. 2. Poziom względnej ekspresji genów, dla markerów pro-angiogennych: MMP, IL8 oraz inhibitorów angiogenezy TIMP, w komórkach HUVEC po 48 godzinach inkubacji na materiałach z lub bez dodatku VEGF. Dane przedstawione są, jako średnia ± SD z 3 eksperymentów. Istotność statystyczną względem kontroli policzono testem T-Studenta, gdzie wartość p przyjęto na poziomie p< 0.05 zaznaczono gwiazdką *

Observations using confocal microscopy and DAPI dye allowed for the visualization of HUVEC cell nuclei and the analysis of growth and penetration of these cells into the interior layers of the tested materials. As it can be seen in Fig. 3 and Fig. 4, the cells exhibited penetration and growth between the upper layers of the materials. However, it should be noted that the incubation lasted for 48 hours, which means that the cells did not have enough time to migrate into deeper areas of the materials. The presented images suggest that the cells showed the best growth in the case of electrospun materials such as PLGA and PLGA-PISEB, while it was poorer in the case of drop-casted PISEB material. This relationship will be analyzed in future studies.
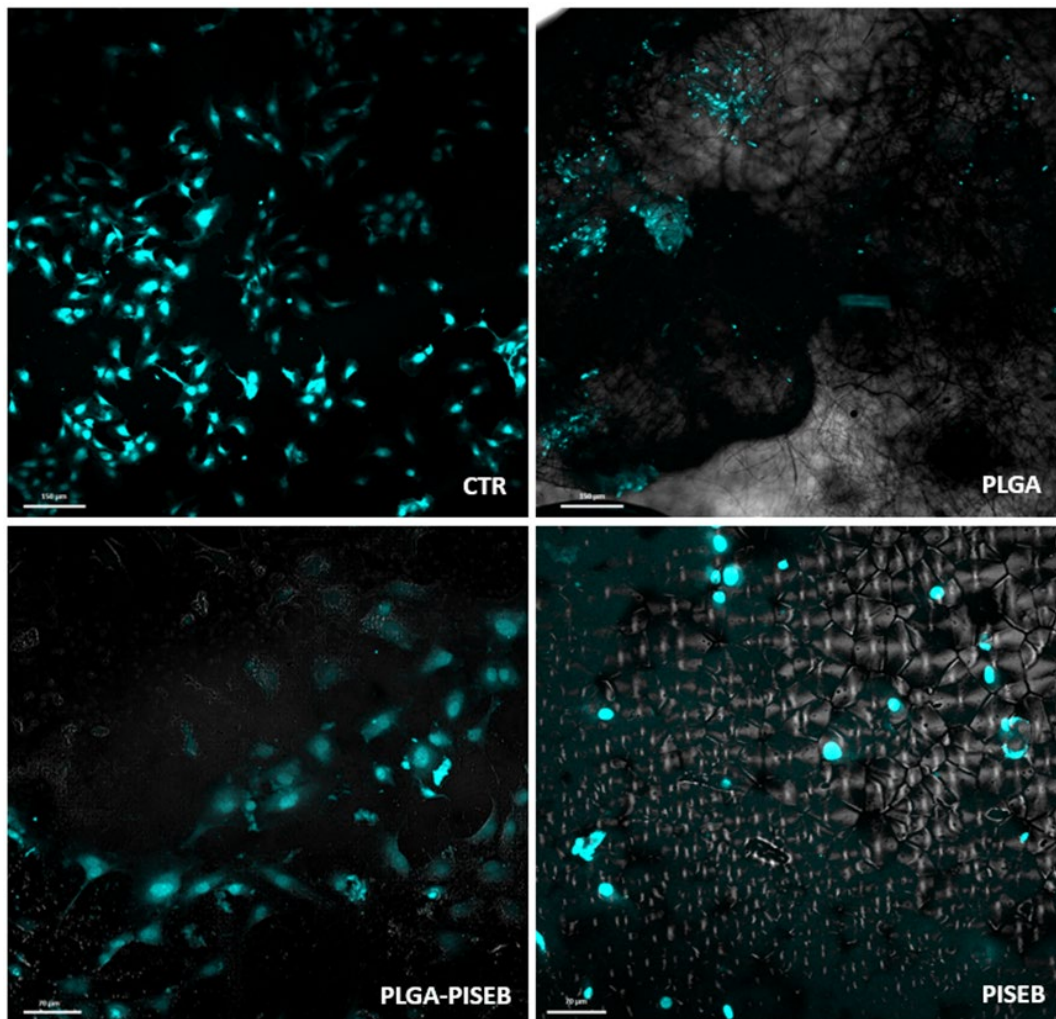
Fig. 3. Confocal images (2D) of HUVEC cells cultured on VEGF-supplemented (w/v 0.5%) EGM-2 medium for 48 h on control polystyrene plate and tested materials: drop-casted PISEB, electrospun PLGA, and electrospun PLGA/PISEB, selected with DAPI (scale bars 150 μm (top pictures), 70 μm (bottom pictures); magnification 120x, Olympus FluoView FV1000™ apparatus)

Rys. 3. Obrazy konfokalne (2D) komórek HUVEC hodowanych na pożywce EGM-2 z dodatkiem VEGF (stężenie 0,5% w/v) przez 48 godzin na kontrolowej płycie polistyrenowej oraz testowanych materiałach: osadzonym PISEB, elektroprzędzonym PLGA i elektroprzędzonym PLGA/PISEB, wybrane za pomocą barwnika DAPI (skala 150 μm – górne zdjęcia, 70 μm – dolne zdjęcia; powiększenie 120x, aparat Olympus FluoView FV1000™)

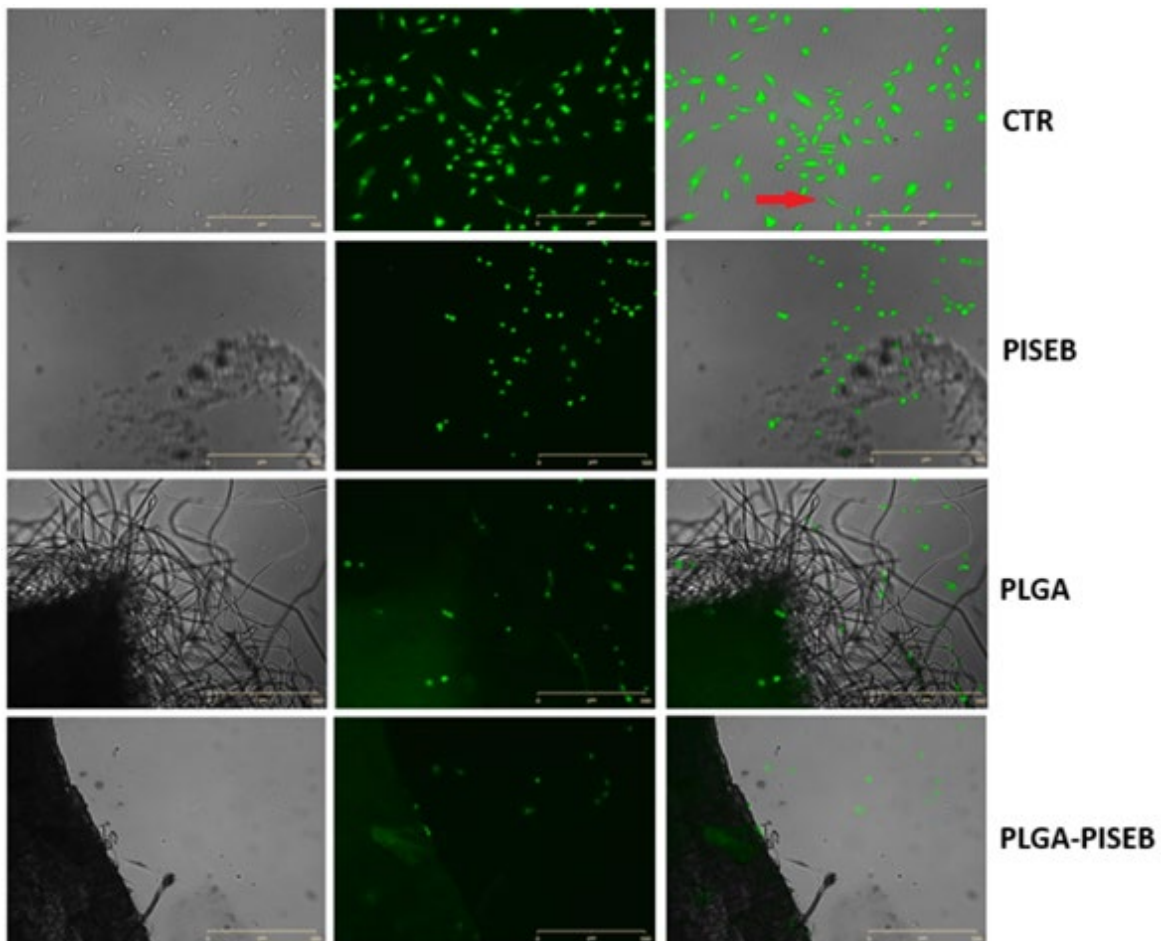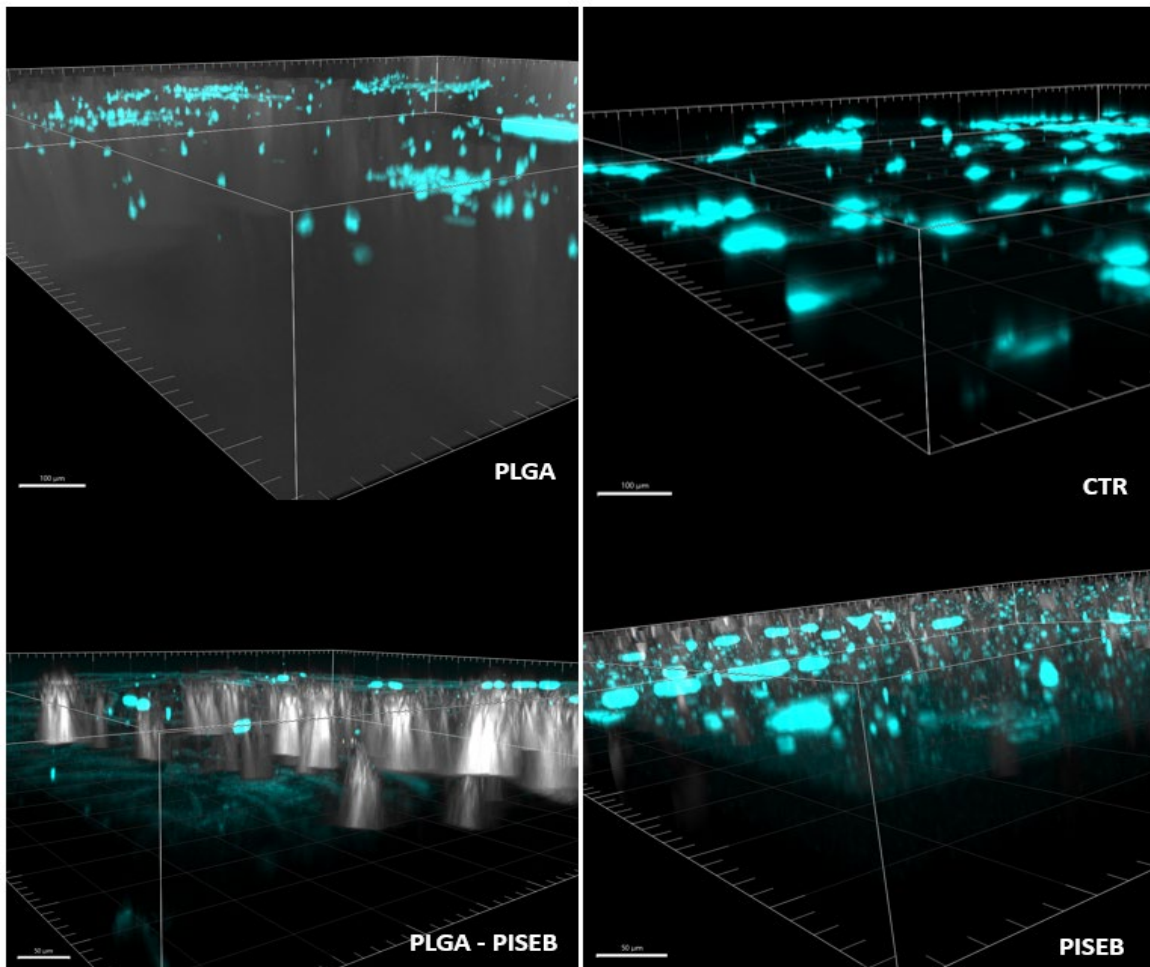Fig. 4. Confocal 3D structure images of HUVEC cells cultured on VEGF-supplemented (w/v 0.5%) EGM-2 medium for 48 h on control polystyrene plate and tested materials: drop-casted PISEB, electrospun PLGA, and electrospun PLGA/PISEB, selected with DAPI (scale bars 100 µm (top pictures), 50 µm (bottom pictures); magnification 120x, Olympus FluoView FV1000™ apparatus)

Rys. 4. Obrazy struktury konfokalnej w trzech wymiarach (3D) komórek HUVEC hodowanych na pożywce EGM-2 z dodatkiem VEGF (stężenie 0,5% w/v) przez 48 godzin na kontrolowej płycie polistyrenowej oraz testowanych materiałach: osadzonym PISEB, elektroprzędzonym PLGA i elektroprzędzonym PLGA/PISEB, wybrane za pomocą barwnika DAPI (skala 100 µm – górne zdjęcia, 50 µm – dolne zdjęcia; powiększenie 120x, aparat Olympus FluoView FV1000™)

6.4. Conclusions

In this paper, we analyzed biological properties of polymeric materials: PLGA, PISEB and PLGA/PISEB. Genotyping of HUVEC cells collected after 48 h of incubations on PISEB, PLGA and PLGA/PISEB showed a potentially pro-angiogenic expression profile. The addition of VEGF to the culture medium activated the MMPs and IL8 expression and down-regulated VEGF expression (in a negative feedback loop

for itself). Levels of MMPs were higher in all three materials than in the control group, demonstrating the pro-angiogenic properties of polymers. Long-term live microscopic observations of living cells stained with fluorescein showed cell growth both on the surface of the culture plate and on the surface of polymers with typical tubular-shapes of HUVEC cells. Microscopic observations of fixed cells stained with DAPI showed the penetration of cells only the surface part of materials - 48h incubation was not long enough for cells to penetrate the lower layers. Further research plans include long-term and 3D cell culture experiments in co-cultivation of HUVEC and Normal Human Dermal Fibroblasts (NHDF). Experiments using 3D cell cultures will aim to mimic the human tissues in body.

Acknowledgments

Bibliography

1. C. Vaquette i J.J. Cooper-White, *Increasing electrospun scaffold pore size with tailored collectors for improved cell penetration*, *Acta Biomaterialia*, t. 7, nr 6, s. 2544–2557, cze. (2011), DOI: 10.1016/j.actbio.2011.02.036.

2. J.P. Vacanti, R. Langer, *Tissue engineering: the design and fabrication of living replacement devices for surgical reconstruction and transplantation*, *The Lancet*, t. 354, s. S32–S34, lip. (1999), DOI: 10.1016/S0140-6736(99)90247-7.

3. G. Lemon, D. Howard, F.R.A.J. Rose, J.R. King, *Individual-based modelling of angiogenesis inside three-dimensional porous biomaterials*, *Biosystems*, t. 103, nr 3, s. 372–383, mar. (2011), DOI: 10.1016/j.biosystems.2010.11.009.

4. M. Dziadek, K. Cholewa-Kowalska, *Wybrane metody otrzymywania porowatych rusztowań w inżynierii tkankowej*, Acta Bio-Optica et Informatica Medica. Inżynieria Biomedyczna, Vol. 20, nr 4, s. 193–203, (2014).

5. A. Laska, B*iomateriały stosowane w inżynierii tkankowej do regeneracji tkanek*, Zeszyty Naukowe Towarzystwa Doktorantów Uniwersytetu Jagiellońskiego. Nauki Ścisłe, t. 14, s. 187, (2017).

6. S. Blonski, *I Kongres Mechaniki Polskiej*, Warszawa, 28–31 sierpnia (2007) r.

7. A. Deng i in., *Porous nanostructured poly-l-lactide scaffolds prepared by phase inversion using supercritical CO2 as a nonsolvent in the presence of ammonium bicarbonate particles*, The Journal of Supercritical Fluids, t. 77, s. 110–116, maj (2013), DOI: 10.1016/j.supflu.2013.02.020.

8. M. Mashreghi, H. Azarpara, M. R. Bazaz, A. Jafari, A. Masoudifar, H. Mirzaei, M.R. Jaafari, (2018). *Angiogenesis biomarkers and their targeting ligands as potential targets for tumor angiogenesis*. Journal of cellular physiology, 233(4), 2949–2965. https://doi.org/10.1002/jcp.26049.

9. N. Ferrara, *The role of VEGF in the regulation of physiological and pathological angiogenesis*, *EXS*, nr 94, s. 209–231, (2005), DOI: 10.1007/3-7643-7311-3-15.

10. H.F. Dvorak (2005). *Angiogenesis: update* (2005). Journal of thrombosis and haemostasis : JTH, 3(8), 1835-1842. https://doi.org/10.1111/j.1538-836.2005.01361.

11. *IL-8 Directly Enhanced Endothelial Cell Survival, Proliferation, and Matrix Metalloproteinases Production and Regulated Angiogenesis1 | The Journal of Immunology American Association of Immunologists*. https://journals.aai.org/jimmunol/article/170/6/3369/71324/IL-8-Directly-Enhanced-Endothelial-Cell-Survival.

12. M. Namiecińska, K. Marciniak, J. Nowak, *VEGF jako czynnik angiogenny, neurotrofi czny i neuroprotekcyjny*, *Postepy Hig Med Dosw*, 59(0), grudz. (2005).

13. M. Śmiga-Matuszowicz, J. Włodarczyk, M. Skorupa, D. Czerwińska-Główka, K. Fołta, M. Pastusiak, M. Adamiec-Organiściok, M. Skonieczna, R. Turczyn, M. Sobota, K. Krukiewicz, (2023). *Biodegradable Scaffolds for Vascular Regeneration Based on Electrospun Poly(L-Lactide-co-Glycolide)/Poly(Isosorbide Sebacate) Fibers*. International journal of molecular sciences, *24*(2), 1190. https://doi.org/10.3390/ijms24021190

14. S. Jin, X. Xia, J. Huang, C. Yuan, Y. Zuo, Y. Li, J. Li, *Recent advances in PLGA-based biomaterials for bone tissue regeneration*. Acta Biomater. (2021), 127, 56–79.

15. M.T. Gentile, O. Pastorino, M. Bifulco, L. Colucci-D'amato, *Huvec tube-formation assay to evaluate the impact of natural products on angiogenesis*. JoVE (2019), e58591. https://doi.org/10.3791/58591.

16. K.L. DeCicco-Skinner, G.H. Henry, C. Cataisson, T. Tabib, J.C. Gwilliam, N.J. Watson, E.M. Bullwinkle, L. Falkenburg, R.C. O'Neill, A. Morin, J.S. Wiest, *Endothelial cell tube formation assay for the in vitro study of angiogenesis*. J Vis Exp. (2014) Sep 1;(91):e51312. DOI: 10.3791/51312. PMID: 25225985; PMCID: PMC4540586.

17. K.J. Livak, T.D. Schmittgen, Analysis of relative gene expression data using real-time quantitative PCR and the 2(-Delta Delta C(T)) Method. *Methods* 2001, *25*, 402–408, DOI: 10.1006/meth.2001.1262.

STUDY OF THE ANGIOGENESIS PROCESS ON THE SURFACE OF BIODEGRADABLE SCAFFOLDS BASED ON ISOSORBIDE

Abstract

The need to regenerate blood vessels arises both in the case of congenital defects, cardiovascular diseases and accidents with accompanying hemorrhages. If the condition of blood vessels is poor, an auxiliary vascular scaffold needs to be used. The aim of our study was the synthesis of a biodegradable and bioresorbable blood vessel scaffold based on biocompatible polymers, followed by an in-depth analysis of the process of creating new blood vessels (angiogenesis). Electrospun scaffolds were made from a blend of poly(L-lactide-*co*-glycolide) (PLGA) and poly(isosorbide sebacate) (PISEB). PLGA was synthesized via a ring-opening polymerization of L-lactide and glycolide, while PISEB was synthesized via a polyesterification process. Human umbilical vein endothelial cells (HUVEC) were used for *in vitro* biological analysis. Viability of cells cultured on the obtained materials was determined by the MTT test. The process of angiogenesis was investigated by analyzing the morphology of HUVEC cells using confocal microscopy and examining the level of expression of marker genes for the angiogenesis process (MMP2, MMP9, TIMP1, TIMP2, VEGF), as well as selected biomarkers associated with inflammation (IL6, IL8). Cells collected after 48h of incubations on the surface of PLGA/PISEB scaffolds showed a potentially pro-angiogenic expression profile, as well as anti-inflammatory effects of this material.

Keywords: angiogenesis, biodegradable scaffolds, isosorbide, biocompatible polymers

Ihtisham UL HAQ[1,2,3,*], Rafi UR RAHMAN[4], Kashif RAHIM[5,*]

Chapter 7. THE EPIDEMIOLOGICAL STUDIES OF DENGUE FEVER IN KOHAT

7.1. Introduction

Dengue fever (DF) is a frequently spreading vector-borne viral infection reported throughout the world, especially in tropical and subtropical regions [1]. DF is considered a fast-spreading vector-borne infection of the 21st Century in developing countries [2]. The etiological virus of dengue fever belongs to the *Flaviviridae* family and genus flavivirus which is a single-stranded enveloped virus transmitted by the bite of female mosquitoes *Aedes aegypti* and/or *Aedes albopictus* [3]. Molecular analysis of the dengue virus reveals 4 diverse serotypes DENV-1, 2, 3, and 4 based on antigenicity [4]. Although DENV infection is asymptomatic in the majority (70%) of the cases [5] but a very small proportion (0.5 to 5%) develop severe symptoms [6]. Characteristic mild symptoms of this arboviral infection are nausea, joint pain, skin rashes, retro-orbital pain, and cough [7] while it can lead to subsequent thrombocytopenia resulting in hemorrhagic fever of severe type, and/ or a life-threatening shock [8]. Mortality rates of dengue are usually very low in the range of 1–5% [9] but it can be reduced to 1% with the proper preventive and treatment measures. Mortality rates can rise up to 26% in case of severe dengue infection [1].

Meteorological factors like temperature, rainfall, and humidity favor the circulation and persistence of DENV vectors [10–12]. In Pakistan, a dengue-like illness was first reported in 1982 in the Punjab province followed by several epidemics reported over

[1] Department of Biosciences, COMSATS University Islamabad (CUI), Islamabad 44000, Pakistan
[2] Department of Physical Chemistry and Technology of Polymers, Silesian University of Technology, M. Strzody 9, 44-100 Gliwice, Poland.
[3] Programa de Pós-graduação em Inovação Tecnológica, Universidade Federal de Minas Gerais, Belo Horizonte, 30150-240, MG, Brazil.
[4] Institute of Biomedical Sciences. University of Sao Paulo, Brazil.
[5] College of Life Science and Technology, Beijing University of Chemical Technology, Beijing, 100029, China.
* Correspondence: ihaq@polsl.pl. 2023700079@buct.edu.cn.

decades with numerous serotypes circulating in the country [13]. In Khyber Pakhtunkhwa (KPK) the first outbreak of dengue fever was reported in 2013 in district Swat with 8546 cases and 33 mortalities. Serotypes 1, 2, and 3 were prevalent among positive cases [14]. Lately, in 2017, there was another massive outbreak of DF in the provincial capital, Peshawar [15]. Several districts in KPK faced small to medium outbreaks of DF in the past few years i-e Abbottabad with 69% prevalence, Malakand with 35%, Haripur with 30%, Sawabi with 28%, and Peshawar with 21% [8] Published literature indicates that most outbreaks were reported during or after the monsoon season [16]. However, the incidence or prevalence of DF in several potentially endemic regions of the KPK province and particularly the Southern districts such as Kohat is largely unknown thus making the dengue eradication strategy ineffective.

This study was designed to figure out dengue hotspots in district Kohat by figuring out the incidence rate of the disease in two major healthcare facilities where most of the people report from all over the district.

7.2. Experimental

7.2.1. Description of the Study Area

Kohat is situated in the South of Khyber Pakhtunkhwa (KP) province of Pakistan which is one of the four provinces of the country (Fig. 9). Kohat city is the capital of the district and 4th largest city of the KP province with an area of 2,545 square kilometers (983 sq mi). The population of the district is approximately 228,779. The climate of Kohat is warm and semi-arid and the temperature rises above 37ºC after Apriland reaches 42–43ºC in June and July (Table 2).

7.2.2. Study Type and Designing

The presented explanatory and analytical study were premeditated in the Department of Biosciences, Molecular virology laboratory, COMSATS University Islamabad (CUI) and conducted in the district headquarters hospital (DHQ) Kohat and combined military hospital (CMH) Kohat, from July 2018 to November 2019. Before approaching the patients, consent was taken from the administration of the hospital. It was revealed by pilot studies that some areas of Kohat are at higher risk for dengue infection.

7.2.3. In Patient Department (IPD) Patients

Clinically positive diagnosed cases of dengue fever admitted in wards were directly observed and interviewed systematically. A pre-experienced questionnaire was used to gather the figures concerning platelets count, demographic variables, empty plot, territory portion, pond around the house (probable vector breeding site), house location, windows screening, and uncovered water containers in the house.

7.2.4. Sample Collection from Out Patient Department (OPDs) Patients

A total of 1665 suspected patients were interviewed from OPDs of both institutes. Suspected patients with the symptoms of high-grade fever from 3–5 days, severe headache, joint pain, skin rashes, shortness of breathing, and cough referred to a laboratory by physicians were taken in this study for specimen collection. A preceding approval was taken from each patient and in the case of a child, his/her guardians were consulted.

7.2.5. Sample Size and Laboratory Processing from OPD Patients

A total of 4 ml fresh blood specimen was obtained from each OPD patient in strictly sterile conditions and transferred to EDTA tubes for the detection of NS-1, IgG, and IgM antibodies using ELISA according to the guidelines of [17] (PLATELIA Bio- Rad lab, France). Samples were labeled with patient name, gender, age, region, and other useful information. The collected blood samples with data like patient name, age, date/month, gender, institute name along with other useful information were noted and samples were stored at -20°C until further use. Samples were further evaluated for centrifugation to isolate the serum. All sample reagents were liquefied at room temperature.

7.3. Lab Tests

7.3.1. Dengue Nonstructural protein 1 (NS1) Antigen

Initially, for rapid detection of NS1 (Non-structural 1 protein) NS1 antigen SD BIOLINE Dengue Duo rapid test kit was used following the manufacturer's protocol [17]. The serum of suspected patients was subjected to this method for the detection of NS1 antigen.

7.3.2. Dengue IgG/IgM

The serum was further subjected for the detection of IgM and IgG antibodies against DENV in the human serum. The isolated serum was sunk on the applicable spot on the kit along with the buffers and left for 15 minutes, the immunocomplex contacts non-mobile antibody results in the production of red purple color.

7.3.3. Demographic Profile

Consulted patients of OPD were determined demographically using a questionnaire during the time of sampling while IPD data were collected directly. Data concerning demographic and clinical information were gathered like age, signs and symptoms, residence area, month, and season of onset etc.

7.4. Data Analysis

All the results data are determined by frequency, percentage and graphical representation.

7.5. Results

From July 2018 to November 2019, a total of 1742 suspected samples were screened for detection of DENV, which revealed 453 positive patients with a percentage of 26% that comprises 319 males and 134 females' population. Most of the DENV cases reported in DHQ hospital (Table 1, Figure 1).

Table 1

Dengue infection Characteristics

Constraints		Incidence	Percentage
Institute	DHQ	286	29.21
	CMH	167	21.88
Gender	Male	285	62.91

continue table 1

Constraints		Incidence	Percentage
	Female	168	37.09
Age group	05-10	59	13
	10–20	134	29.58
	20–30	173	38.18
	30–45	87	19.24
Areas	Lachi	208	45.91
Shakardara	110	28.24	
	Hangu	79	17.43
College Town	35	7.72	
	Kaghazai	21	4.63
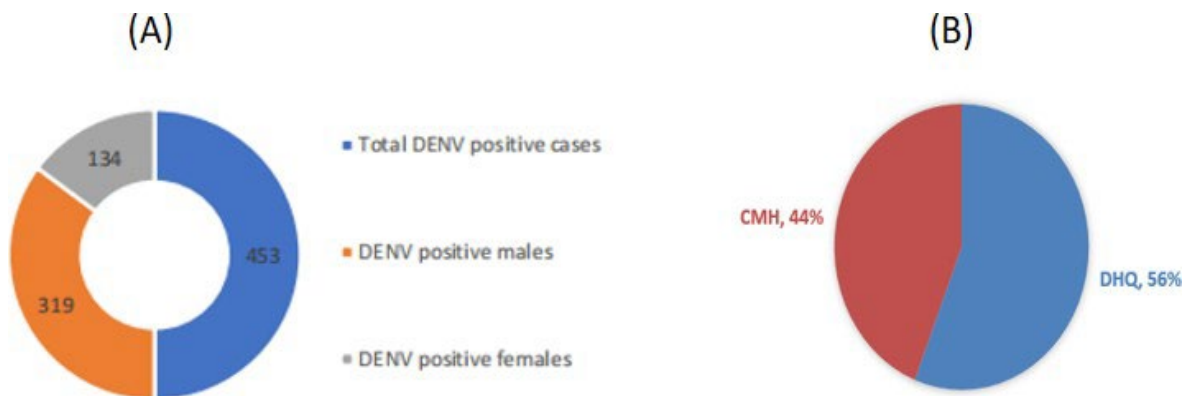
Fig. 1. The number of total cases and dengue fever positive (A). Institute-wise distribution of dengue cases (B). We can see that DHQ received more patients during the study time

Rys. 1. Liczba wszystkich przypadków gorączki denga (A). Rozkład przypadków dengi pomiędzy CMH a DHQ (B). Można zauważyć, że w DHQ odnotowano większą liczbę pacjentów

7.5.1. Laboratory markers of dengue virus infection

All of the dengue fever infected patients were found with IgG and IgM antibodies and NS1. Some patients were diagnosed with positive with IgG and IgM antibodies both. However, the incidence of IgG (47%) and IgM (27%) antibodies in infected patients were high compared to NS1 (14%) as shown in Figure 2.
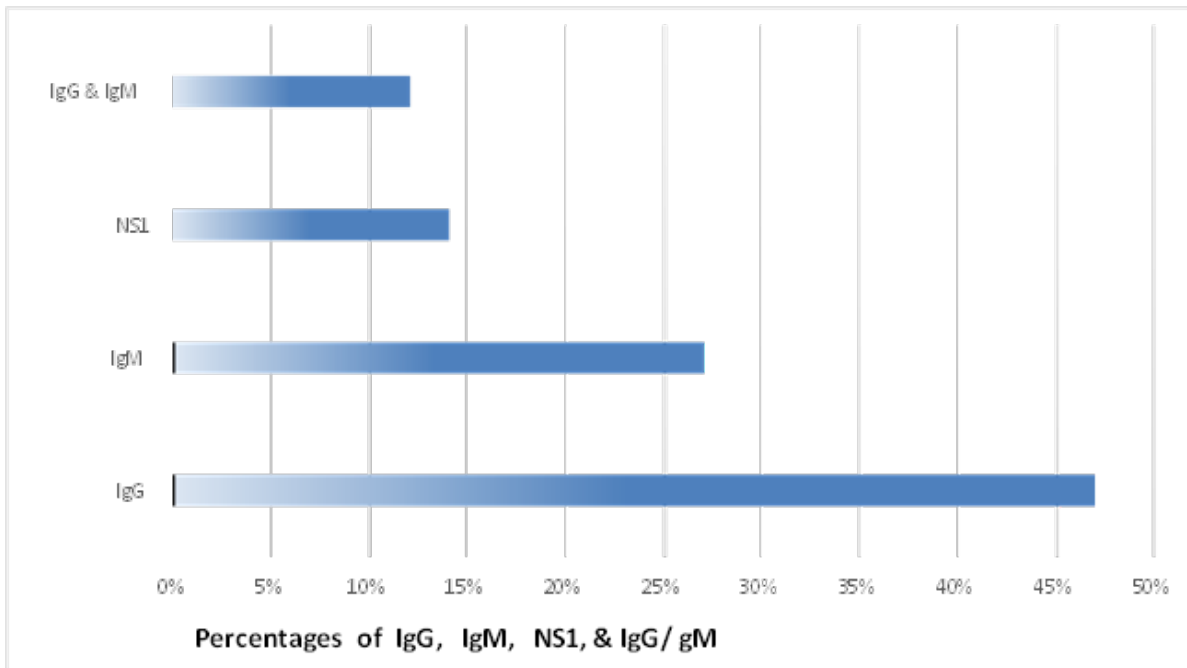
Fig. 2. Detection of DENV. It can be seen that IgG is detected in majority of the cases. Other antibodies like IgM, NS1 and others are comparatively low

Rys. 2. Detekcja DENV. IgG zostało oznaczone w większości przypadków. Inne przeciwciała takie jak IgM, NS1 oraz pozostałe odnotowane są na niskim poziomie

7.5.2. Age-Wise and Region-Based Prevalence of DENV

Results data revealed age groups 10–20 and 20–30 are more susceptible to dengue infection, the prevalence was 29.58%, 38.18% respectively. Similarly, age group 1–10 was less affected (13%) by infection while the age group 30–45 (19.24%) appeared moderately affected. (Table 1).

7.5.3. Geographical Distribution

In the existing study dengue infection mostly affected rural areas people that are living in high cultivation areas (Figure 3).
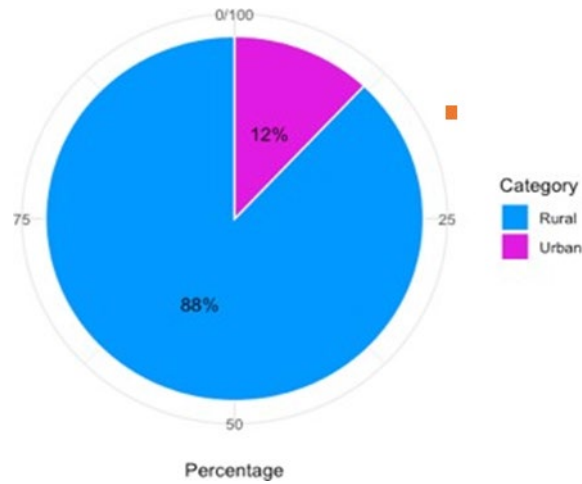
Fig. 3. Geographical Distribution of DENV. Rural regions have more DF cases compared to urban. This can be attributed to vector species distribution in urban regions and more suitable breeding places for them

Rys. 3. Geograficzny rozkład DENV, Regiony wiejskie odnotowują większą liczbę przypadkow niż regiony miejskie. Może to być związane z rozmieszczeniem gatunków-wektorów i bardziej odpowiednimi dla nich miejscami lęgowymi

7.5.4. Monthly Distribution of DENV

Data analysis revealed the incidence started in July and the highest prevalence of dengue infection was observed in October (164) (36.20%) and September 128 (28.25%). Subsequently august and July showed 82 (18.10%), and 63(13.90%) cases respectively. The percentage of infection was quite low on November 16 (3.53%) (Figure 4).
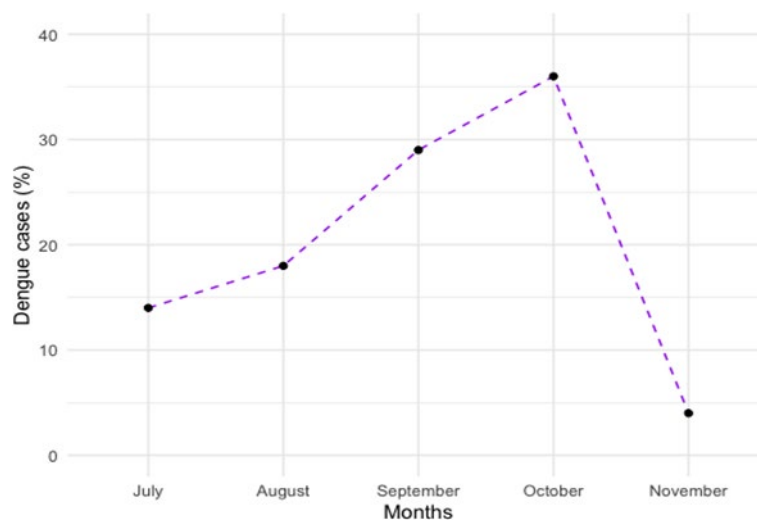
Fig. 4. Monthly prevalence of DENV infections. During the month of October, the weather remains favorable for mosquito breeding. During this month, the weather is not severe, therefore, its suites mosquito breeding

Rys. 4. Miesięczna częstość występowania zakażeń DENV. W październiku pogoda sprzyja rozmnażaniu się komarów. W tym miesiącu pogoda sprzyja rozmnażaniu się komarów

7.5.5. IPD and OPD patients of both hospitals

Among infected patients, only 77 (17%) patients were admitted to wards that were diagnosed with severe dengue infection with extreme symptoms. These pateints had low platelet count, noticeably all of the IPD patients came from Lachi and Shakaradara (cf. Figure 5).
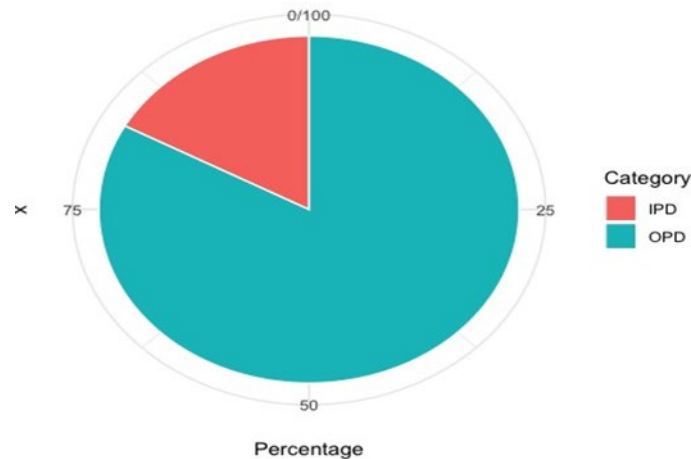
Fig. 5. Prevalence of DENV among IPD and OPD patients. OPD receives, generally more patients compared to IPD. Therefore, the incidence of DF in OPD patients is high

Rys. 5. Rozpowszechnienie DENV wśród pacjentów z IPD i OPD. OPD otrzymuje na ogół więcej pacjentów w porównaniu z IPD. Dlatego częstość występowania DF u pacjentów z OPD jest wysoka

7.5.6. Medical Records of Infected Patients

Here we present IPD patients symptomatically. All of them were observed with mild symptoms like fever, body aches, and joint pain especially in knees and shoulder joints while nausea, vomiting, and diarrhea were observed in 75% of patients, shortness in breathing (38%), and gum bleeding (7%).

7.5.7. Seasonal Deviation of Dengue Infection

The incidence rate varied with seasonal fluctuations. Monsoon sessions have a huge impact on dengue fever concerning mosquito breeding and other activities. We saw that 64.45% of cases were reported in the post-monsoon season (Figure 6).
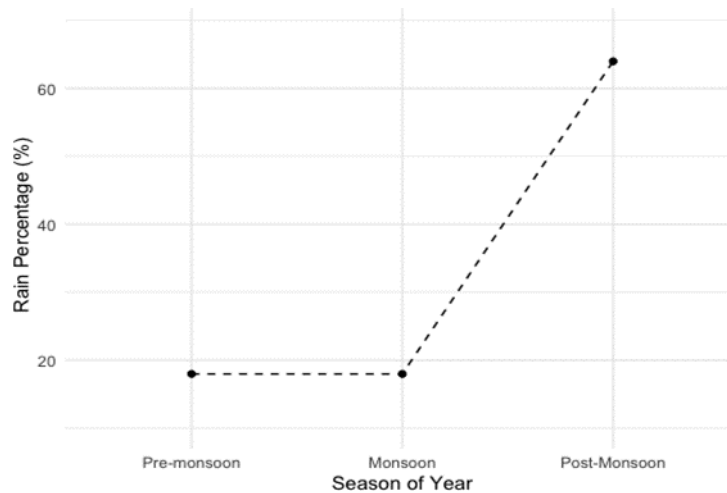
Fig. 6. Seasonal variations of dengue fever. Pakistan receives a lot of rains during monsoon, and vector breeding sites which are mainly stagnant water bodies, can be expected in great numbers post-monsoon. That is the reason why we see an exponential increase in dengue cases post-monsoon

Rys. 6. Sezonowe zmiany gorączki denga. W Pakistanie odnotowuje się wysokie opady deszcze, zwłaszcza podczas monsunów. Powstające w ten sposób stojące zbiorniki wodne są miejscem rozmanażania komarów. To jest powód, dla którego obserwujemy wykładniczy wzrost przypadków dengi po monsunie

7.5.8. Temperature Fluctuations in Kohat throughout whole year

Weather reports were scrutinized to check the impact of temperature on infection patterns. The highest temperature 44°C were reported in July month (Table 2) [17].

Table 2

Temperature of Kohat

Month	Temperature
January	09–20°C
February	11–22°C
March	11–32°C
April	21–36°C
May	31–42°C
June	37–43°C
July	33–44°C
August	30–38°C
September	29–39°C
October	26–39°C
November	16–28°C
December	15–26°C

7.5.9. Evaluation of Platelets Count

Thrombocytopenia, or low platelet count is one of the basic indicators of DENV infection. The total number of platelets decreases due to its destruction while fighting infection and the bone marrow fails to produce new [18]. Patients with severe symptoms were evaluated for platelet count (Figure 7). We can see that it was very low (20000 to 59000/μL) in the majority of the patients (50%).
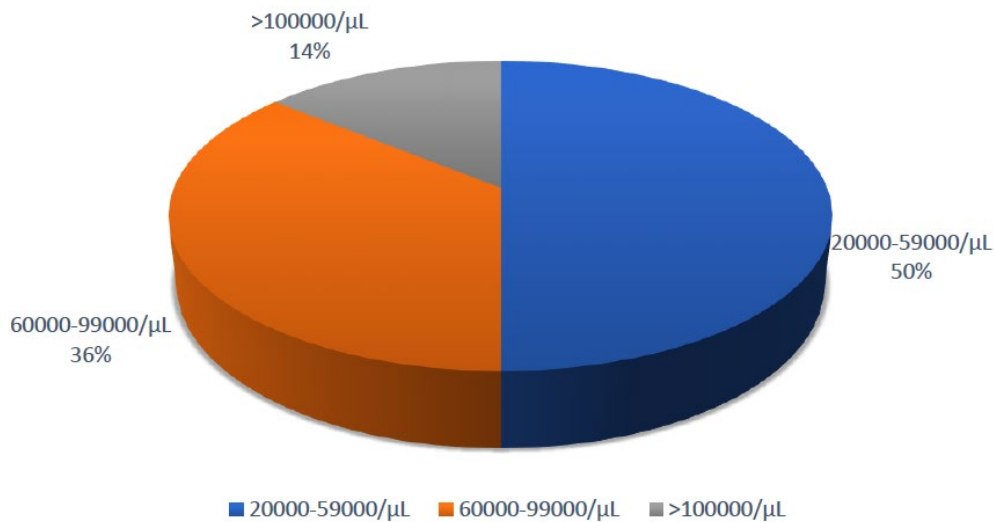
Fig. 7. Platelets count of IPD Patients. Platelets count is an important indicator of DENV infection. We can see that the majority of patients have platelets count between 20 and 59 thousand/μL

Rys. 7. Liczba płytek krwi u pacjentów z IPD. Liczba płytek krwi jest ważnym wskaźnikiem zakażenia DENV. Większość pacjentów ma liczbę płytek krwi między 20 a 59 tys./μL

7.5.10. Literacy Level of Patients

Among patients included in our study, 33% were illiterate, 25% were matric, 34% were matriculated and high school students while undergrad/graduate students were only 8%.

Fig. 8. Pakistan and its neighboring regions, study area (Kohat District) is highlighted as red and magnified. Kohat district lies in the Northwestern region of the country called Khyber Pakhtunkhwa. The map is generated with a free, open – source software qGIS (ver 3.28) (GNU General Public License), developed by the Open-Source Geospatial Foundation Project (http://qgis.org)

Rys. 8. Pakistan i sąsiednie regiony, obszar badań (dystrykt Kohat) zaznaczono na czerwono i powiększono. Dystrykt Kohat leży w północno-zachodnim regionie kraju zwanym Khyber Pakhtunkhwa. Mapa została wygenerowana za pomocą bezpłatnego oprogramowania open-source qGIS (wersja 3.28) (GNU General Public License), opracowanego przez Open-Source Geospatial Foundation Project (http://qgis.org)

7.6. Discussion

At this instant, more than 100 countries including South Asia, Africa, America, Australia, the Caribbean, Pacific Islands, and Mexico that are positioned in steamy and subtropical regions have been considered as dengue endemic countries [1]. In Asia, Pakistan is measured as a dengue-endemic country after facing certain outbreaks [19]. In 1994 the earliest case of dengue fever appeared in Karachi but frequent outbreaks started after 2000 [20]. In KPK enduring epidemics of dengue have been recorded in 2013 in different regions including Kohat. Studies on dengue fever have been conducted in multiple cities of Pakistan including KPK, but it's for the first time in Kohat. This study describes the dengue fever epidemiology, risk factors, seasonal association and medical distinctiveness to analyze the dynamics of dengue fever in the district of Kohat. Kohat is situated on the route of hilly series; mountains and hills enclosed most of its fraction and the network of 3 dams and a small river deliver water into all areas by open canals which grant adequate establishment for mosquito breeding [21]. Hilly areas favor the activities of DENV vectors like Ae. Albopictus during monsoon season in dengue-

endemic countries is reported in KPK, Pakistan as well [22]. Climatic factors like hot temperatures, heavy rainfall, and increased population have played a key role in the dengue fever expansion across the country.

The outcome of this study specified that 453 patients were diagnosed with dengue infection in a figure of 1742 subjects. The frequency of positive cases was restricted to 5 regions Lachi, Hangu, Shakardara, College town, and Kaghazai. The highest incidence was found among Lachi and Shakardara members as according to the study of S. Khan et al the water storage tanks are highly contaminated with Lachi and Shakardara [23] which are the most attractive sites for vector breeding. These are high cultivation territories and have open water channels and ponds. Meanwhile in the summer severe high rainfall; hot temperatures, and open stagnant water favor vector breeding to DENV spreading and establishment of infection [23].

In our study, we saw that males were more affected with a frequency of 62.91% while the rest were females that appeared to be less susceptible to infection, similar findings are already present in the literature [8, 24]. In a study, the percentage of males was 64% and females were 36% while in another study, the positive male was 89%. However, males are more susceptible to dengue infection as they are dependable for outer activities while female is less affected as they are restricted to the home. We also saw that rural areas are more affected by dengue infection in contrast to urban areas as rural regions are used for agriculture and cultivation and for that they need water reservoirs and supply which are usually uncovered and provide a favorable environment for DENV vector breeding, these results are in contrast with the study of Hayes et al. who reported urban areas are more susceptible as compared to rural areas [25].

Furthermore, we segregate results data into different age groups, the prevalence rate varies among different age groups, and the highest (38.18%) prevalence rate was observed in the 20–30 age group, these findings are similar to the previous studies [26]. The 10–20 age group showed the second highest prevalence (29.58%). This population is highly susceptible to dengue infection as this group people belong to school children, college students and employees mostly live outside of their homes. The age group 5–10 appeared less susceptible to infection as they lived mostly inside the home and they are safe up to some extent.

The positive cases started appearing in July, the prevalence rate was low in July and August though suddenly increased in October (36.20%) and September (28.25%) due to rainfall that favors the propagation of dengue vectors (Aedes). Similar results are present in the literature [8]. The positive patients were mostly illiterate; 45% were under Matric. Month-wise distribution of dengue infection revealed that vector-borne diseases like

dengue are strongly influenced by seasonal variations and metrological factors. Additionally, open-source water supply was identified as a risk factor for dengue infection. Considerably all the patients got DF in the summer season and only a few were recorded as positive in winter (November). In our study post-monsoon season, temperature and rainfall appeared to have more impact on the transmission of infection. According to a recent study, a temperature of more than 25°C greatly favors mosquito breeding, increasing 1°C temperature to 26°C causes the possibility of dengue transmission chances up to 1.95 times [27, 28]. In our study, (68.33%) of patients were illiterate, as they were not equipped with knowledge of prevention measures for dengue infection, this analysis shows similarity with Khanani et al, who reported illiteracy and unawareness also played an important role in the prevalence of dengue fever [29].

In the current study, high-grade fever and shivering appeared to be the main symptom observed in all patients, these observations are similar to the findings of [30] clinical signs and symptoms of suspected patients play an important role in the diagnosis and treatment of DF [31, 32]. Presently there is no antiviral drug available for dengue infection in our country; the physicians prescribe only symptomatic treatment. Controlling DENV vectors and rapid diagnosis at early stages is the precise way to reduce infection rates [33]. According to our survey in Kohat, dengue infection is diagnosed in only two institutes DHQ and CMH. The diagnostic kits should be available in endemic areas, especially during August, September, and October for the early diagnosis to control the infection timely [34]. Kohat is a populated district with poor health care settings with no dynamic inspection organization of DENV and its vectors and exclusively counting on the inactive supervision system is not enough for the whole district.

7.7. Conclusion and Suggestions

Overwhelmingly this study represents the dengue endemic areas in Kohat which are Lachi, Shakardara, and Hangu which are highly cultivated areas comprised of greenery, and open water channels that facilitate mosquito breeding and other activities. Prevention is the only way to control DENV due to the lack of proper antiviral treatment. Control strategies are required to control vector behavior, water channels, and other water reservoirs need to be covered, and the removal of dull stagnant water on priority. Furthermore, rapid diagnostic facilities need to be developed in healthcare

organizations, especially in endemic areas, and the identification of serotypes as well. Seminars and lectures need to be arranged in endemic areas for public awareness. Additionally, researchers need to improve the vaccination strategies with high efficacy.

Acknowledgments

Bibliography

1. World Health Organization, Research SPf, Diseases TiT, Diseases WHODoCoNT, Epidemic WHO, Alert P. Dengue: guidelines for diagnosis, treatment, prevention and control. (2009).
2. D.J. Gubler. Dengue, urbanization and globalization: the unholy trinity of the 21st century. Tropical medicine and health. (2011) 39:S3–S11.
3. A. Sherin. Dengue fever: a major public health concern in Pakistan. Khyber Medical University Journal. (2011) 3 :1–3.
4. M. Akram, Z. Fatima, M.A. Purdy, A. Sue, S. Saleem, I. Amin, et al. Introduction and evolution of dengue virus type 2 in Pakistan: a phylogeographic analysis. *Virology Journal* (2015) 12:1–11.
5. Q.A. Ten Bosch, H.E. Clapham, L. Lambrechts, V. Duong, P. Buchy, B.M. Althouse, et al. Contributions from the silent majority dominate dengue virus transmission. *PLoS pathogens*. (2018) 14:e1006965.
6. World Health Organization. Dengue and severe dengue. https://www.who.int/news-room/fact- sheets/detail/dengue-and-severe-dengue (2022). Accessed 06/03/2023.
7. O. Parkash, R.H. Shueb. Diagnosis of dengue infection using conventional and biosensor based techniques. Viruses. (2015) 7:5410–27.
8. S. Ali, M. Salman, M. Din, K. Khan, M. Ahmad, F.H. Khan, et al. Dengue outbreaks in Khyber Pakhtunkhwa (KPK), Pakistan in 2017: an integrated disease surveillance and response system (IDSRS)-based report. *Polish journal of microbiology.* (2019) 68:115–9.

9. S. Ranjit, N. Kissoon. Dengue hemorrhagic fever and shock syndromes. Pediatric Critical Care Medicine. (2011) 12:90–100.

10. C. Li, Y. Lu, J. Liu, X. Wu. Climate change and dengue fever transmission in China: Evidences and challenges. *Science of the Total Environment* (2018) 622:493–501.

11. J.L. Duarte, F.A. Diaz-Quijano, A.C. Batista, L.L. Giatti. Climatic variables associated with dengue incidence in a city of the Western Brazilian Amazon region. *Revista da Sociedade Brasileira de Medicina Tropical.* (2019) 52.

12. Y. Choi, C.S. Tang, L. McIver, M. Hashizume, V. Chan, R.R. Abeyasinghe, et al. Effects of weather factors on dengue fever incidence and implications for interventions in Cambodia. *BMC public health.* (2016) 16 :1–7.

13. A. Zohaib, M. Saqib, C. Beck, M. Hussain, S. Lowenski, S. Lecollinet. et al. High prevalence of West Nile virus in equines from the two provinces of Pakistan. *Epidemiology & Infection.* (2015) 143:1931–5.

14. World Health Organization. Sustaining the drive to overcome the global impact of neglected tropical diseases: second WHO report on neglected diseases. 2013.

15. J. Khan, A. Ghaffar, S.A. Khan. The changing epidemiological pattern of Dengue in Swat, Khyber Pakhtunkhwa. *PloS one*. (2018) 13: e0195706.

16. I. Rafique, M. Saqib, M.A Munir, S. Siddiqui, I.A. Malik, M.H. Rao, et al. Dengue knowledge and its management practices among physicians of major cities of Pakistan. *J Pak Med Assoc.* (2015) 65:392–6.

17. G. Lutfullah, J. Ahmed, A. Khan, H. Ihsan, J. Ahmad. Evaluation of Non-Structural Protein-1 (NS1) positive patients of 2013 dengue outbreak in Khyber Pakhtunkhwa, Pakistan. *Pakistan journal of medical sciences.* (2017) 33:172.

18. S. Das, C. Abreu, M. Harris, J. Shrader, S. Sarvepalli. Severe Thrombocytopenia Associated with Dengue Fever: An Evidence-Based Approach to Management of Thrombocytopenia. *Case Reports in Hematology*. (2022) 2022.

19. U. Raheel, M. Faheem, M.N. Riaz, N. Kanwal, F. Javed, I. Qadri. Dengue fever in the Indian subcontinent: an overview. *The Journal of Infection in Developing Countries.* (2011) 5:239–47.

20. T. Ahmad, N.A. Khan, M.M.U. Rehman, M.A. Jadoon. A story of the disease free area to high endemic. *Bull Environ Pharmacol Life Sci*. (2014) 3:1–4.

21. N. Akhtar, J. Khan, A. Khan. Dengue Outbreak in Khyber Pakhtoonkhwa, Pakistan 2013. *European Acad Res.* (2014) 1:3842–57.

22. I. Ahmad, D. Khan, R.M. Tariq, S.S. Qadri. Population dynamics of dengue vector Aedes aegypti L. in thirteen towns of Karachi, Pakistan. *International Journal of Biology and Biotechnology*. (2011) 8:637–43.

23. S. Khan, M. Shahnaz, N. Jehan, S. Rehman, M.T. Shah, I. Din. Drinking water quality and human health risk in Charsadda district, Pakistan. *Journal of cleaner production.* (2013) 60:93–101.

24. S. Fahad, L. Khan, A. Iqbal, I. Khan, A. Umar, S.H. Muneer: Institutional based prevalence and occurrence of dengue disease in capital city Peshawar of province Khyber Pakhtunkhwa (KPK), Pakistan. *Pakistan*. (2018).

25. C.G. Hayes, I.A. Phillips, J.D. Callahan, W.F. Griebenow, K.C. Hyams, S.J. Wu , et al. The epidemiology of dengue virus infection among urban, jungle, and rural populations in the Amazon region of Peru. *The American journal of tropical medicine and hygiene*. (1996) 55:459–63.

26. A.U.R. Faiz-ur-Rehman, N. ul Akbar, M. Tahir, N. Ahmad, H.Rashid, M. Waqar, et al. The Prevalence of Dengue Virus Serotypes and Dengue Cases Reported in District Peshawar.

27. S. Sang, W. Yin, P. Bi, H. Zhang, C. Wang, X. Liu, et al. Predicting local dengue transmission in Guangzhou, China, through the influence of imported cases, mosquito density and climate variability. *PloS one* (2014) 9:e102755.

28. J. Khan, I. Khan, I. Amin. A comprehensive entomological, serological and molecular study of 2013 dengue outbreak of Swat, Khyber Pakhtunkhwa, Pakistan. *PLoS One.* (2016) 11:e0147416.

29. S. Ahmad, M.A. Aziz, A. Aftab, Z. Ullah, M.I. Ahmad, A. Mustan. Epidemiology of dengue in Pakistan, present prevalence and guidelines for future control. *Int J Mosq Res.* (2017) 4:25–32.

30. B. Khalid, A. Ghaffar. Environmental risk factors and hotspot analysis of dengue distribution in Pakistan. *International journal of biometeorology*. (2015) 59:1721–46.

31. R.S. Lanciotti, C.H. Calisher, D.J. Gubler, G.J. Chang, A.V. Vorndam. Rapid detection and typing of dengue viruses from clinical samples by using reverse transcriptase- polymerase chain reaction. *Journal of clinical microbiology*. (1992) 30 3:545–51.

32. F.A. Raza, S.U. Rehman, R. Khalid, J. Ahmad, S. Ashraf, M. Iqbal, et al. Demographic and clinico-epidemiological features of dengue fever in Faisalabad, Pakistan. *PLoS One.* (2014) 9:e89868.

33. S.G. Sankar, K. Dhananjeyan, R. Paramasivan, V. Thenmozhi, B. Tyagi, S.J. Vennison. Evaluation and use of NS1 IgM antibody detection for acute dengue virus diagnosis: report from an outbreak investigation. *Clinical Microbiology and Infection*. (2012) 18:E8–E10.

34. M. Amin, A. Hussain, M. Murshed, I. Chowdhury, S. Mannan, S. Chowdhury, et al. Searo--Diagnosis of Dengue Infections by Haemagglutination Inhibition Test (HI) in Suspected Cases in Chittagong, Bangladesh. (1999).

THE EPIDEMIOLOGICAL STUDIES OF DENGUE FEVER IN KOHAT

Abstract

Dengue fever, which is emerging as a major public health problem, affects 50–100 million people annually with particular reference to developing countries. Several regionsin Pakistan have suffered severe outbreaks over the past 15 years; however, the incidence of the disease in several cities including the southern parts of the Khyber Pakhtunkhwa province is under-reported. To find out endemic regions in district Kohat, this study was conducted in two major hospitals of the region including the district headquarters hospital (DHQ) and Combined Military Hospital (CMH) from July 2018 to November 2019. The IPD patients were directly interviewed while in the case of OPD patients, blood samples were analyzed for IgG or IgM antibodies using ELISA. We examined 1742 individuals experiencing dengue-like symptoms for the presence of IgM or IgG levels. Among these, 453 (26%) individuals were positive for either IgG or IgM. The frequency of infection was higher in males 70.42% (319) compared to females 29.58% (134). Most of the cases (46%) were from the Lachi area, followed by Hangu and Kohat cities. The incidence rates varied with season with 64% of cases reported in the post-monsoon season. This study identified 3 different dengue endemic areas in district Kohat which need a dynamic surveillance system for the control of dengue fever to minimize its risk. Healthcare officials need to establish rapid diagnostic facilities in endemic areas accompanied by vector control strategies.

Keywords: Dengue, Prevalence, Kohat, DHQ, CMH, Climate, Monsoon

Ihtisham UL HAQ[1,2,3,*], Sajida MARYAM[1], Kashif RAHIM[4,*], Israr AZIZ[1]

Chapter 8. THE UPSURGE INCIDENCE OF TYPHOID FEVER UNDER THE INFLUENCE OF THE COVID-19 PANDEMIC

8.1. Introduction

The safety and security of public health are largely threatened by infectious diseases among which typhoid fever (TF) is one of the major headaches throughout the world, especially in developing countries [1]. TF is caused by *Salmonella typhi* which is rod-shaped gram-negative, highly pathogenic, and drug-resistant bacteria, its virulence is increased by the presence of a polysaccharide capsule that protects from phagocytosis [2]. The consumption of food and water contaminated with the feces of infected patient led to infection of *Salmonella typhi,* which then turn into typhoid fever and infection symptoms become apparent such as chilled fever, fatigue, headache, abdominal pain, and rash [3]. Globally, approximately, 9.9 to 24.2 million people get typhoid fever and 75,000–208,000 people lost their lives due to this life-threatening infection according to the report of the World Health Organization (WHO) [4]. Typhoid fever is very prevalent in a majority of Asian countries including Pakistan and out of 16 Asian countries, Pakistani populations are higher at risk for typhoid [5]. In Pakistan, particularly in Sindh and Khyber Pakhtunkhwa (KPK) provinces reported a high prevalence of TF, Sindh province reported 22,571 cases of typhoid from the period of November 2016 to February 2020 according to the report of the National Institute of Health (NIH). Recently, an epidemiological study of TF reported a 30% prevalence among KPK populations during 2016–17 [6].

[1] Department of Biosciences, COMSATS University Islamabad (CUI), Islamabad 44000, Pakistan.
[2] Department of Physical Chemistry and Technology of Polymers, Silesian University of Technology, M. Strzody 9, 44-100 Gliwice, Poland.
[3] Programa de Pós-graduação em Inovação Tecnológica, Universidade Federal de Minas Gerais, Belo Horizonte, 30150-240, MG, Brazil.
[4] College of Life Science and Technology, Beijing University of Chemical Technology, Beijing, 100029, China.
[*] Correspondence: ihaq@polsl.pl., sajida.maryam786@gmail.com.

However, the ongoing pandemic of COVID-19 that emerged in 2019, December [7–10] has disturbed the whole lifestyle, and disease control strategies and madeit more susceptible to secondary infections. Simultaneously, in several developing countries including Pakistan, previously overstretched healthcare infrastructure has started reporting secondary infections with COVID-19 soon after declaring a pandemic [11, 12]. Majorly, typhoid prevalence has been found to increase after the pandemic of COVID-19. In Pakistan, COVID-19 cases start spreading very quickly in May 2020, and consequently on the other hand, in the first 10 days of June, approximately 20,000 people were diagnosed with typhoid and COVID-19 infections [13]. A recent study of typhoid fever conducted in Punjab Province reported 48% from March 15 to June 15, 2020. In gender-wise distribution, the highest incidence rate was observed in males and age-wise distribution, the age group 21–40 reported the highest incidence rate of 44.5% [14]. Similarly, the NIH report presented 2,883 cases in Pakistan of TF since 12 September 2020 [15]. It's become very challenging to diagnose both infections with limited financing and healthcare resources thus, it leads to a crumpling of clinical diagnosis and management strategies [14]. The prevalence of TF has been found to increase after the COVID-19 pandemic throughout the country across various provinces such as Punjab and KP. However, while keeping in mind the abrupt cases of typhoid fever across the province this study was initiated in June 2020 and completed in November 2020 with the purpose of analysis of epidemiological studies of typhoid fever in district Kohat KPK.

8.2. Methodology

8.2.1. Description of the Study Area

Kohat is situated in the south of Khyber Pakhtunkhwa (KPK) which is one of the four provinces of Pakistan. Kohat city is the capital of the district and the 4th largest city ofthe KPK with an area of 2,545 square kilometers (983 sq mi) with a population of the district is approximately 228,779 [16]. The climate of Kohat is warm and semi-arid and the temperature rises above 37°C after April and reached 42, and 43°C in June, and July (Table 2) [17].

8.2.2. Study Type and Design

The presented epidemiological study was premeditated in the District Headquarters Hospital, Kohat Pakistan conducted from June 2020 to November 2020. Before approaching the patients, consent was taken from the hospital administration. A total of 1,165 suspected patients with the symptoms of fever, dissatisfaction headache, abdominaldiscomfort, diarrhea, malaise, and constipation referred to the laboratory by physicians were taken in this study for specimen collection. A preceding approval was taken from each patient and in the case of a child from his/her guardian according to the updated version. A pre-experienced questionnaire was used to gather information regarding their health status and issues, age, lifestyle, eating habits, and daily activities.

8.2.3. Sample Size and Laboratory Processing of Samples

A total of 4 ml fresh blood specimen was obtained from each patient in strictly sterile conditions and transferred to EDTA tubes for the detection of IgG and IgM antibodies through a typhoid test. Samples were labeled with patient name, gender,age, region, and other useful information. The collected blood samples with data like patient name, age, date/month, gender, and institute name and along with other useful information were noted and then samples were stored at -20°C until further use. In the clinical diagnosis, all the typhoid fever suspected blood samples were evaluated for the detection of IgG and IgM *Salmonella typhi*-specific antibodies by using a typhoid test comprised of dot ELISA. Typhidot strips contain immunogenic 50 kDa outer membrane protein antigen explicit for *Salmonella typhi.* The strip was kept for 10 minutes followed by centrifugation of blood to separate the serum to apply it on the sample pad. The strip comprises 3 bands IgG, IgM, and test band, appearing color on each band indicated theirresult as described by [18].

8.2.4. Data Analysis

All the results data are determined by frequency, percentage, and graphical representation.

8.3. Results

A total of 511 patients were found positive with IgG and IgM *Salmonella typhi* antibodies among 1,165 suspected patients and the infection rate was 43.86%, males reported 313 infections while females 198 (Table 1, Graph 1). In the current study, the majority (66%) of TF cases came from urban areas. (Figure 2). Results data revealed thatthe disease incidence abruptly started in June, with the highest incidence 31.50% reportedin July followed by 28.20% in June while the lowest reported in November 3.32% as shownin Figure 3. The prevalence of typhoid fever has been found significantly increased in the present study. In past, the incidence rate did not go overhead 30% but in 2020, it surpasses 44% in this study and interestingly, Lahore reported a 48% prevalence of TF in the same years as shown in Figure 4, Figure 5 and Table 2. TF transmission is highly associated with high temperature so we accessed the temperature data of Kohat from a website as shown in Table 3 [17].
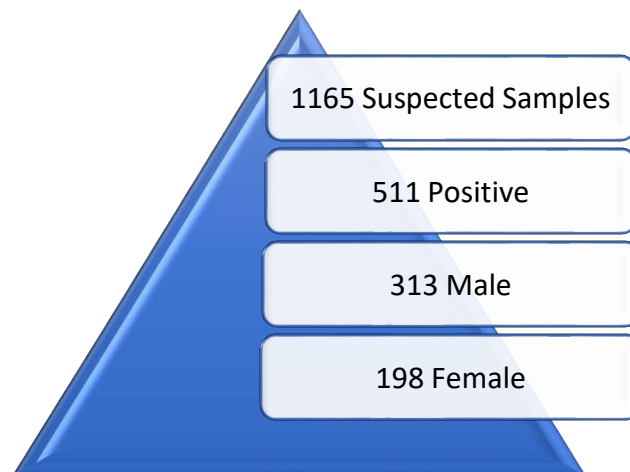
Fig. 1. Overall prevalence of typhoid fever
Rys. 1. Ogólna częstość występowania duru brzusznego

Table 1

Features of typhoid fever infection based on gender, age-wise, month,
area, and infectionhistory

Constraints	Categories	Positive cases	Percentage
Gender	Male	313	61.01
	Female	198	38.99
Age group	10–20	157	30.72
	20–30	208	40.70
	30–45	146	28.57
Areas	Uban	339	66.34
	Rral	172	33.66
Infection history	New	315	62.00
	With a history of TF	196	37.97
Months	June	144	28.18
	July	161	31.50
	Agust	93	18.19
	September	72	14.09
	October	24	4.69
	November	17	3.32
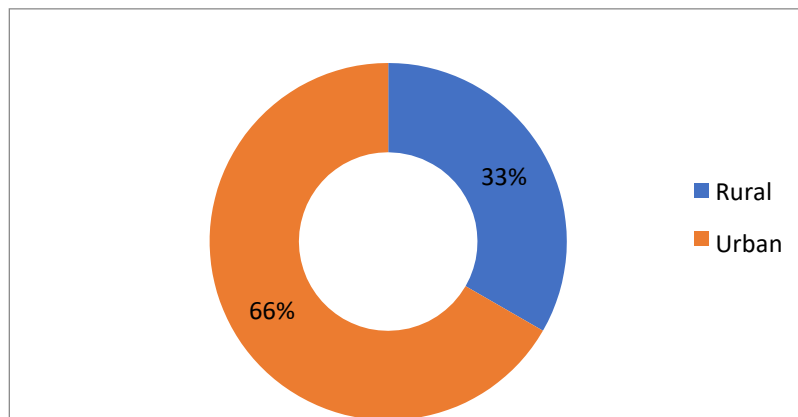
Fig. 2. Area-wise distribution of TF
Rys. 2. Rozkład występowań TF
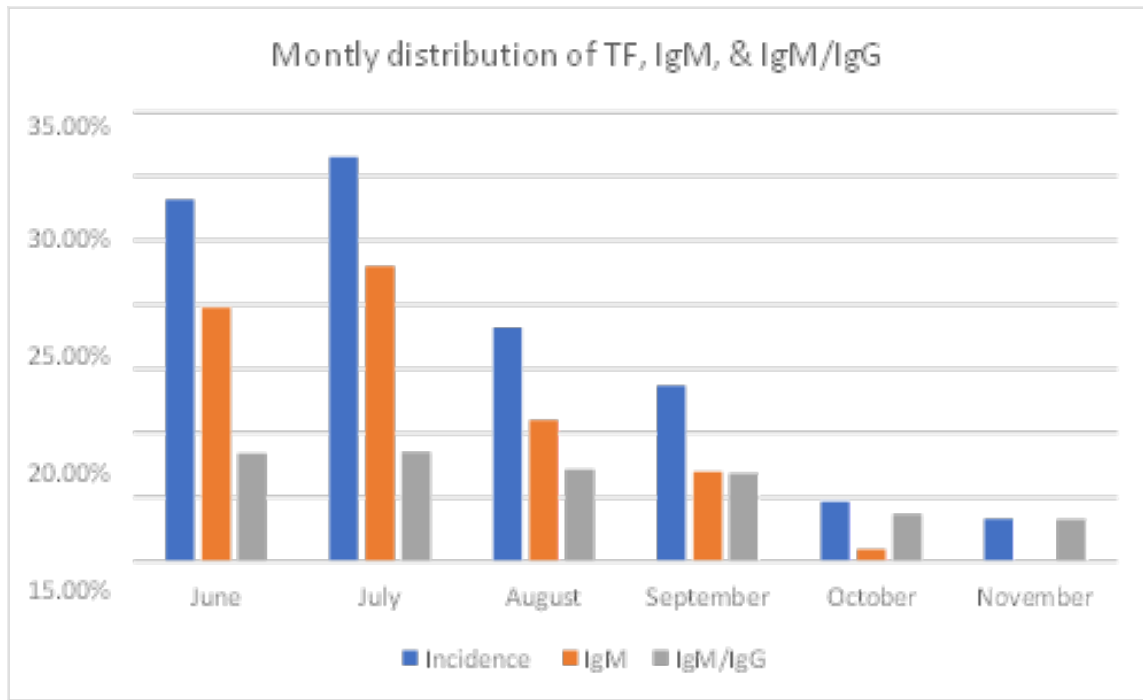
Fig. 3. Monthly distribution of TF, IgM, and IgM/IgG antibodies
Rys. 3. Miesięczny rozkład występowania TF oraz przeciwciał IgM i IgM/IgG
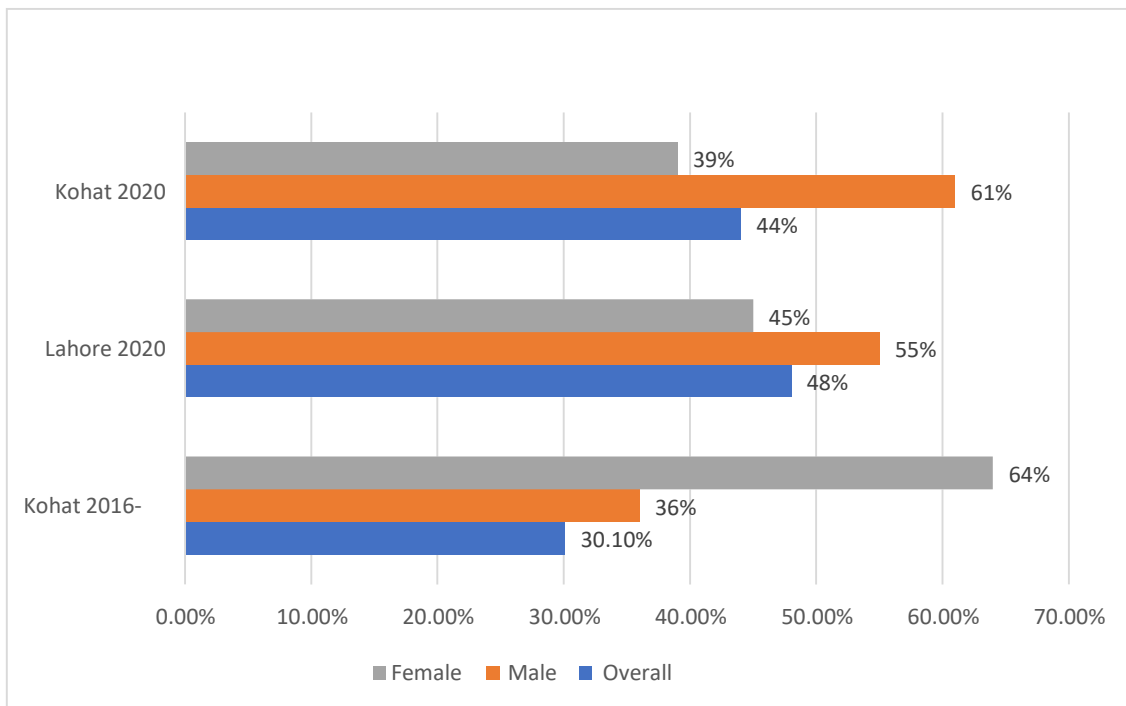
Fig. 4. Comparison of TF Prevalence with previous studies and present
Rys. 4. Porównanie występowania TF w przeszłości i obecnie
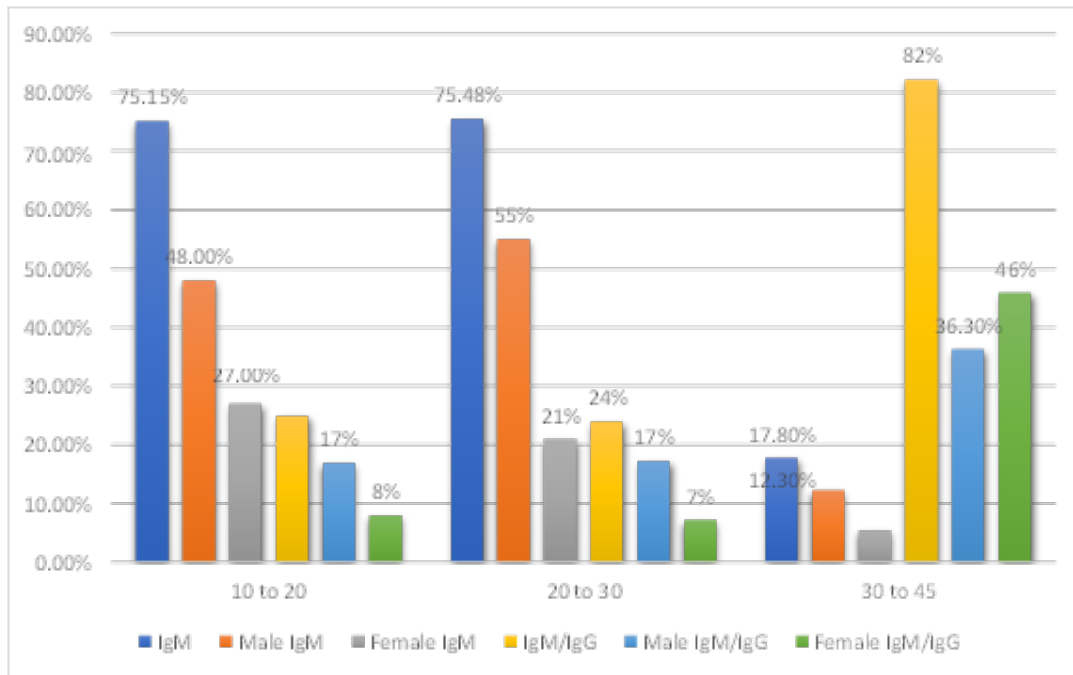
Fig. 5. The IgM and IgM/IgG antibodies prevalence among male and female patients
Rys. 5. Częstość występowania przeciwciał IgM i IgM/IgG wśród pacjentów płci męskiej i żeńskiej

Table 2

The IgM and IgM/IgG antibodies prevalence among male and female patients

Age-groups	Positive Cases	Male	Female	IgM	IgM/IgG
10–20	157	104	53	75M/43F = 118	26M/13F = 39
20–30	208	144	64	114M/43F = 157	36M/15F = 51
30–40	146	65	81	18M/8F = 26	53M/67F = 120
Total	511	313	198	301	210

Table 3

Temperature in Kohat

Months	Temperature
January	09–20°C
February	11–22°C
March	11–32°C
April	21–36°C
May	31–42°C
June	37–43°C
July	33–44°C
August	30–38°C
September	29–39°C
October	26–39°C
November	16–28°C
December	15–2°C

8.4. Discussion

Typhoid fever is a major problem in the healthcare of developing countries andis associated with high morbidities and mortalities in South-East Asian countries. Middle and lower-income countries are at higher risk for TF infection due to a lack of sanitation systems and an unhygienic environment. It is a main public health concern mainly in middle and lower-income countries including Asia. Globally, South-East Asia is the 3rd most prevalent region as most of the countries reported a high incidence of TFincluding Pakistan [19]. Currently, typhoid is considered an extensively drug-resistant infection (XDR) that infected thousands of people, recently in 2019, the first conjugate vaccine of typhoid has been familiarized by Pakistan as recommended by WHO [20]. The incidence of TF is varied as it primarily depends on the weather conditions, sporadic cases are reported throughout the year but more prevalent in summer [21–23]. The present study was led to report the updated epidemiological studies of TF. After the COVID-19 pandemic, the incidence of TF increased significantly across the province and it was stoutly recommended to report the epidemiological factors of TF to summarize the preventive and treatment strategies. The current incidence of 44% of TF has been interpreted as increased in comparison with previous studies of incidences however, it matches with the recent study conducted in Lahore in 2020 that reported a 48% incidence [6]. Incidentally, both studies reported a higher incidence in males, the current study has reported 61% at Lahore while 55% was previously reported. Our results revealed that the highest incidence was 40.70% reported in the age group 20–30, followed by 30.72% in the age group 10–20, and the age group 40–45 reported 28.57%. These figures are similar to the study of Umer Rashid and co-workers, who reported 42.33% in the age group 21–30, and 30.42% in 11–20 [6]. Similarly, Rahim et al reported a 27% incidence in the 10–20 age group [7].

The increased incidence of typhoid fever indicates the impact of COVID-19 onTF. A letter to the editor of the report characterized COVID-19 and *Salmonella typhi* co-epidemics as a real problem in Pakistan [6]. It is very difficult to report the actual prevalence of TF in the absence of an organized clinical diagnosis, sufficient sample size, and most primarily due to symptoms similar to COVID-19. Physicians face problems in the differentiation of both infections due to symptoms similarity, which is the major issue in the diagnosis of typhoid [6]. It has been reported that the prevalence of TF is high in summer and low in winter, but accidentally our study was started in June 2020 and completed in November 2020, and gradually the disease incidence starts to decline after August, and no single cases were reported in December [1]. The present

study reported a significant variation in the epidemiological studies of TF in comparison with previous studies that found deviated such as reporting of higher infection cases in urban areas. Moreover, in our study, the patients with a history of TF were fewer and the new infections reported high, which indicated that the population across the districtbecome highly susceptible to TF. It seems that TF susceptibility is increased with the ongoing pandemic of COVID-19 that affected every individual, most of the patients recovered quickly but their immune systems weakened. The weak immune system makes people more susceptible to TF in the presence of unhygienic water, food, and theenvironment. Its transmission increases due to contaminated water, poor sanitation, low hygienic environment [24], and no vaccination all these factors contributed to the susceptibility of the entire communities [25]. The transmission risk can be reduced by the implementation of preventive and treatment strategies such as providing clean waterto the public and installation of organized sanitation to dispose of the fecal material without exposure to the environment. Besides these, vaccination against typhoid in the susceptible population can play a major role in the prevention of disease that must be prioritized [25]. Timely diagnosis is necessary for parallel analysis of COVID-19 and typhoid, which is difficult in current poorly equipped healthcare facilities. COVID-19 and typhoid have become a headache for Pakistan however, the previous year Pakistan responded well to the COVID-19 pandemic and typhoid epidemics as well. The third wave of COVID-19 has started in Pakistan with alarming circumstances and concerned authorities must be determined the attenuation of the COVID-19 pandemic and typhoid epidemics.

8.5. Conclusion

Results concluded that typhoid prevalence has increased significantly in 2020 in comparison with the past studies but in parallel, various other studies of Lahore and NIH have also reported the increased prevalence of typhoid fever across the country in 2020. Interestingly, there is no significant variation of infection observed in different age groups. All the age groups revealed similar susceptibilities except the age group 20–30, which shows the highest incidence rate of 40%. Diagnostic facilities and clinical management should be improved to differentiate both infections and timely diagnosis. To combat the co-epidemics of COVID-19 and typhoid fever in the third wave of the pandemic accurate and rapid diagnosis is stoutly recommended for its better management.

Acknowledgments

Bibliography

1. A. Fusheini, S.K. Gyawu, Prevalence of Typhoid and Paratyphoid Fever in the Hohoe Municipality of the Volta Region, Ghana: A Five-Year Retrospective Trend Analysis. *Annals of Global Health.* (2020) **86**(1).

2. J. Akram, A.S. Khan, H.A. Khan, S.A. Gilani, S.J. Akram, F.J. Ahmad, R.Mehboob. Extensively drug-resistant (XDR) typhoid: evolution, prevention, and its management. *BioMed Research International*. (2020).

3. J.A. Crump. Progress in typhoid fever epidemiology. *Clin Infect Dis.* (2019) 68:S4–S9.

4. M. Antillón, J.L. Warren, F.W. Crawford, et al. The burden of typhoid fever in low- and middleincome countries: A meta-regression approach. *PLoS neglected tropical diseases.* (2017) **11**(2): 0005376.

5. M.K. Rasheed, S.S. Hasan, Z.U.D. Babar, S.I. Ahmed, "Extensively drug-resistant typhoid fever in Pakistan," *The Lancet Infectious Diseases* (2019) **19**(3): 242–243.

6. K. Rahim, I. Ul Haq, F. Hussain, W. Ashraf, A. Basit, M.M. Jalees, M.A. Gonda, M. Shuaib. The prevalence rate and epidemiological study of Typhoid fever in KhyberPakhtunkhwa, Pakistan. *Bioscience Research* (2021) **18**(1): 221–228.

7. I. Ul Haq, K. Krukiewicz, H. Tayyab, I. Khan, M. Khan, G. Yahya, S. Cavalu. Molecular Understanding of ACE-2 and HLA-Conferred Differential Susceptibility to COVID-19: Host-Directed Insights Opening New Windows in COVID-19 Therapeutics. *Journal of Clinical Medicine*. (2003). **12**(7), 2645.

8. C. Egbuna, S. Chandra, C.G. Awuchi, S. Saklan, I. Ulhaq, M. Akram, K.C. Patrick-
-Iwuanyanwu, J. Khan. Myth surrounding the FDA disapproval of 594 hydroxychloroquine sulfate and chloroquine phosphate as drugs for coronavirus disease 2019. In Coronavirus Drug Disc. Elsevier (2022) **595**, 153–168.

9. I. Ul Haq, K. Krukiewicz, G. Yahya, M. Ul Haq, S. Maryam, R.A. Mosbah, S. Saber, M. Alrouji. The breadth of bacteriophages contributing to the development of the phage-based vaccines for COVID-19: An ideal platform to design the multiplex vaccine. *International Journal of Molecular Sciences*. (2023). **24**(2), 1536.

10. S. Maryam, I. Ul Haq, G. Yahya, M. Ul Haq, A.M. Algammal, S. Saber, S. Cavalu. COVID-19 surveillance in wastewater: An epidemiological tool for the monitoring of SARS-CoV-2. *Frontiers in cellular and infection microbiology*. (2023). **12**, 978643.

11. A. Haqqi, U.A. Awan, M. Ali, M.A.N. Saqib, H. Ahmed, M.S. Afzal. COVID-19 and dengue virus co-epidemics in Pakistan: a dangerous combination for overburdened healthcare system. *J Med Virol*. (2020) 26144.

12. R. Ozaraszaras, R. Cirpin, A. Duran, et al. Influenza and COVID-19 co- infection: report of 6 cases and review of the literature. *J Med Virol.* (2020). https://doi.org/10.1002/jmv.26125.

13. B.T. Shaikh, N. Ali. COVID-19 and fiscal space for health system in Pakistan: It is time for a policy decision. *Int J Health Plann Manage*. (2020).

14. NEWS A. Doctors report increasing typhoid cases in Punjab than COVID-19. Accessed 19 June 2020. https://arynews.tv/en/doctorsreport-increasing-typhoid-cases-punjab/.

15. National Institute of Health Islamabad, Weekly field epidemiology report. https:// www.nih.org.pk/wp-content/uploads/2020/09/37-FELTP-Pakistan-Weekly-Epi demiological-Report-Sep-05-12-2020.pdf, 2020. [Accessed 13 December 2020].

16. PAKISTAN: Provinces and Major Cities. *PAKISTAN: Provinces and Major Cities*. citypopulation. de. Retrieved 4 May 2020.

17. www.accuweather.com.

18. K. Yadav, S.K. Yadav, G. Parihar. A Comparative Study of typhidot and widaltest for Rapid Diagnosis of Typhoid Fever. *Int. J. Curr. Microbiol. App. Sci (2015)*4(5): 34–38.

19. F.J. Siddiqui, F. Rabbani, R. Hasan, S.Q. Nizami, Z.A. Bhutta. Typhoid fever in children: some epidemiological considerations from Karachi, Pakistan. *International Journal of Infectious Diseases* (2006) 10(3):215–222.

20. World Health Organization. Pakistan first country to introduce new typhoid vaccine into routine immunization programme. Accessed 19 June 2020. http://www.emro.who.int/pak/pakistan-news/pakistan-first-country-tointroduce-new-typhoid-vaccine-into-routine-immunization-programme. html

21. L. Cao, S. Fu, Z. Lv, C. Tang, S. Cui, X. Li, W. Lei. West Nile virus infectionin suspected febrile typhoid cases in Xinjiang, China: West Nile virus and febrile tyhoid coinfection. *Emerging microbes & infections* (2017) 6(1): 1–4.

22. A.L. Wagner, M.Y. Mubarak, L.E. Johnson, J.M. Porth, J.E. Yousif, M.L. Boulton. Trends of vaccine-preventable diseases in Afghanistan from the Disease Early Warning System, 2009–2015. *PLoS One* (2017)12(6): e0178677.

23. H. Gu, W. Fan, K. Liu, S. Qin, X. Li, J. Jiang, Q. Jiang. Spatio-temporal variations of typhoid and paratyphoid fevers in Zhejiang Province, China from 2005 to 2015. *Scientific reports (2017)* 7(1): 5780.

24. V. Mogasale, B. Maskery, R.L. Ochiai, et al. Burden of typhoid fever in low- income and middle-income countries: a systematic, literature-based update with risk-factor adjustment. *The Lancet Global health.* (2014) 2(10): 570–580. https://doi. org/10.1016/S2214-109X(14)70301-8.

25. S. Ahmad, et al. A skeleton in the closet: The implications of COVID-19 on XDR strain of typhoid in Pakistan. *Public Health Pract* (2021) 100084.

THE UPSURGE INCIDENCE OF TYPHOID FEVER UNDER THE INFLUENCEOF THE COVID-19 PANDEMIC

Abstract

Typhoid fever is one of the most persistent bacterial infections in developing countries causes. The current study was designed to analyze the epidemiological studies of typhoid feverin the recent pandemic of COVID-19. In this study, a total of 1,165 suspected patients with typhoid symptoms were screened for typhoid. Results revealed a significant upsurge in typhoid cases. Overall, the prevalence was 44%, which is comparatively high but aligns with the recentstudies of typhoid fever reported during an ongoing pandemic. The high number of IgM antibodies in typhoid patients indicated the higher prevalence of new infections. It shows that TF susceptibility has increased with the present pandemic of COVID-19 as co-epidemics of COVID-19 and typhoid have remained a major public health issue in Pakistan. COVID-19 weakened the immune system, which makes people more susceptible to typhoid coupled with an unhygienic environment and lack of scheduled vaccination. The transmission risk can be reduced by the implementation of preventive measures such as the installation of

organized sanitation to dispose of the fecal material. Vaccination can play a major role in the prevention of typhoid. Timely diagnosis is necessary for parallel analysis of COVID-19 and typhoid, whichis difficult in poor healthcare facilities and turned into a headache for Pakistan. Such alarmingcircumstances warn the concerned authorities to develop preventive strategies for the future typhoid epidemics.

Keywords: Typhoid, COVID-19, co-epidemics, epidemiology, prevalence, Pakistan

Maria ZADOŃ[1,*], Marek JASIŃSKI[1]

Chapter 9. NUMERICAL ANALYSIS OF THE EFFECT OF TEMPERATURE ON THE PARTIAL PRESSURE OF OXYGEN IN BIOLOGICAL TISSUE

9.1. Introduction

It can be said that all kinds of life activities in living organisms are related to the presence of oxygen. Oxygen is obtained in the lungs and then transported through the circulatory system to tissues from blood in the capillaries. The oxygen content in individual tissues is not constant and may vary depending on many factors, such as the degree of activity of the body, the external conditions in which the body is located, or the presence of various substances. Oxygen deficiency is known as hypoxia [1, 2].

An increase in the temperature of biological tissue can result from a variety of causes, such as physical exertion, medical conditions, or an external heat impulse. The latter factor often leads to changes in the thermophysical parameters of the tissue and even irreversible thermal damage to the tissue. Since thermal damage is associated with damage to the blood vessel network, among other things, it can ultimately affect oxygen delivery to the tissue. An increase in temperature also causes the so-called Bohr effect of shifting to the right the oxyhemoglobin dissociation curve, a sigmoidal function, which describes the relationship between the oxygenation of hemoglobin and the partial pressure of oxygen in the blood. The oxygen dissociation curve is laboratory--determine for specific values of temperature, carbon dioxide, pH, 2,3-DPG (2,3 diphosphoglycerate), and other substances [3–7].

---

[1] Department of Computational Mechanics and Engineering, Silesian University of Technology, Gliwice, Poland.
[*] Corresponding author: maria.zadon@polsl.pl.

9.2. The effect of temperature on oxygen transport in tissue

The relationship between saturation S_{Hb}, that is, the content of oxygen in the blood (more precisely in oxyhemoglobin), and the partial pressure of oxygen in the blood P_b is described by the sigmoidal oxyhemoglobin dissociation curve (ODC) (Fig. 1). The parameter that characterizes the dissociation curve is the P_{50} pressure corresponding to 50% hemoglobin saturation. An increase in temperature causes the P_{50} value to shift to the right, which is called the right shift effect or Bohr effect [1, 6, 7]. The ODC is described by various models, among which the Hill model is the most popular [1–3].

$$S_{Hb}(P_b) = \frac{P_b^n}{P_b^n + P_{50}^n} \tag{1}$$

where n denotes the Hill coefficient that is related to the slope of the dissociation curve. For normothermia, usually $P_{50} = 26$ [mmHg] and $n = 2.7$ are assumed [1–2]. Exemplary data for these parameters, depending on temperature, are presented in Table 1. The popularity of Hill's model is mainly due to the simplicity of the model and the ease of obtaining the inverse relationship necessary for computation of the oxygen distribution model:

$$P_b(S_{Hb}) = P_{50}\left(\frac{S_{Hb}}{1 - S_{Hb}}\right)^{\frac{1}{n}} \tag{2}$$
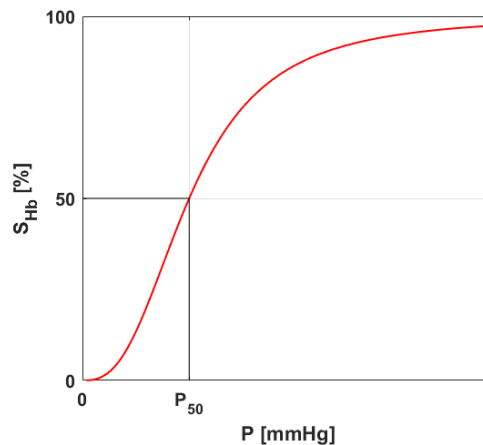
Fig. 1. Oxyhemoglobin dissociation curve
Rys. 1. Krzywa dysocjacji oksyhemoglobiny

Temperature-dependent parameters of Hill model [6]

T [°C]	23	30	37	44
P_{50} [mmHg]	12.3	17.3	27.0	35.9
n	2.39	2.35	2.57	2.45

Tissue subjected to an external heat impulse can undergo thermal damage. The basic model for determining the degree of thermal damage to tissue is the Arrhenius scheme [8–10]:

$$Arr(\mathbf{x}, t^F) = \int_0^{t^F} A \exp\left[-\frac{E}{RT(\mathbf{x},t)}\right] \mathrm{d}t \tag{3}$$

where T [K] is the temperature, R [J mol^{-1} K^{-1}] is the universal gas constant, E [J mol^{-1}] is the activation energy and A [s^{-1}] is the preexponential factor. The integral values of $Arr = 1$ and $Arr = 4.6$ correspond to a probability of 63% and 99% of cell death at a specific point $\mathbf{x}$. Both values are used as criteria for tissue necrosis.

It is obvious that tissue damage can injure the blood vessel network within it. And because the presence of blood in biological tissue is described by the perfusion coefficient, a function can be created that maps the phenomena that occur in the tissue during the increase in temperature (the initial increase in perfusion during vasodilation) and subsequent thermal damage (the decrease in perfusion resulting from rupture of the vasculature [3, 8, 11]:

$$w(Arr) = \begin{cases} \left(1 + 25\,Arr - 260\,Arr^2\right)w_0, & 0 \le Arr \le 0.1 \\ \left(1 - Arr\right)w_0, & 0.1 < Arr \le 1 \\ 0, & Arr > 1 \end{cases} \tag{4}$$

where $w(Arr)$ and w_0 denote damage-dependent and initial perfusion coefficients [s^{-1}], respectively.

Changing tissue perfusion affects parameters associated with the oxygen distribution model, e.g., blood flow rate [cm^3 s^{-1}] and blood velocity [cm s^{-1}] [12].

9.3. Govering equations

In Figure 2 the models considered in the current work are presented. On the left, the considered domain of 3D biological tissue for thermal analysis is presented. The tissue

domain is exposed to the external heat impulse at the upper Γ_0 boundary. On the right, the Krogh cylinder-based model is visible to consider oxygen transport in tissue.

As mentioned previously, in the bioheat transfer model, the presence of blood is described by a perfusion coefficient. In practice, it is determined, among other things, by knowing the number of capillaries in the cross section or the volume of the tissue (depending on the method adopted). Thus, it is also possible to determine the velocity of blood in the capillary u_b based on knowledge of the perfusion coefficient and dimensions of the capillary [4]:

$$ w = \frac{Q_b}{\pi R_t^2 L_t} = \frac{\pi R_c^2 u_b}{\pi R_t^2 L_t} \quad \rightarrow \quad u_b = w(Arr)L_t \frac{R_t^2}{R_c^2} \tag{5} $$

where Q_b [cm^3 s^{-1}] is the blood flow rate in the capillary, R_c, R_t, and L_t are the radius of the capillary radius, the tissue cylinder and length of cylinder, respectively.

This relationship was used to combine the bioheat transfer model and the oxygen distribution model. In the bioheat transfer model, points A-C have been highlighted, for which the curses of the determined parameters, including the perfusion coefficient, will be presented. For selected time steps, calculations will be carried out using the oxygen distribution model.
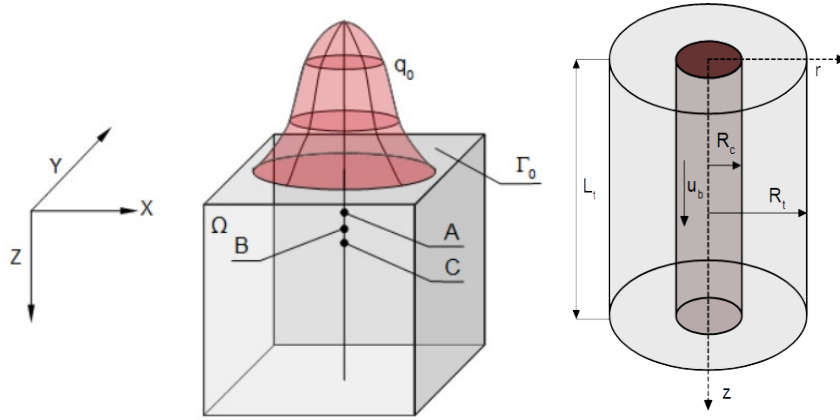
Fig. 2. Domains considered for the bioheat transfer and oxygen distribution model
Rys. 2. Obszary uwzględnione w modelu przepływu biociepła i dystrybucji tlenu

Bioheat transfer in the tissue domain Ω is described by the Pennes equation supplemented with appropriate boundary and initial conditions [8, 10, 11, 13]:

$$ \begin{aligned} &\mathbf{x} \in \Omega: \quad c\dot{T} = \nabla(\lambda \nabla T) + Q_{perf} + Q_{met} \\ &\mathbf{x} \in \Gamma_0: \quad q = q_0, \quad \text{for } t \le t_{exp}, \quad q = 0, \quad \text{for } t > t_{exp} \\ &\mathbf{x} \in \Gamma_c: \quad q = 0 \\ &t = 0: \quad T = T_{init} \end{aligned} \tag{6} $$

where λ [W m^{-1} K^{-1}] is the thermal conductivity, c [J m^{-3} K^{-1}] is the volumetric specific heat of tissue and blood, Q_{met} [W m^{-3}] is the metabolic heat source, q_0 [W m^{-2}] is the boundary heat flux, t_{exp} [s] is the exposure time while T_{init} denotes the initial distribution of temperature, and the function of internal heat sources associated with perfusion Q_{perf} is as follows [8, 10]:

$$Q_{perf}(\boldsymbol{x}, t) = c_B w [T_B - T(\boldsymbol{x}, t)] \tag{7}$$

where c_B [J m^{-3} K^{-1}] is the volumetric specific heat of the blood, T_B corresponds to the temperature of the arterial blood.

Other thermophysical parameters of the tissue may also change as a result of an increase in its temperature. In the current work, the thermal conductivity λ is assumed to be temperature-dependent (temperature in Kelvin), whereas the volumetric specific heat c is treated as dependent on the thermal conductivity [10, 14]:

$$\lambda(T) = 0.6489 + 0.0427 \, arctan[0.0252(T - 315.314)] \tag{8}$$

$$c(\lambda) = (3.385\lambda + 2.17) \cdot 10^6 \tag{9}$$

Separate equations for the radial and axial directions are applied for the Krogh cylinder model (cf. Fig. 2). For radial direction [2-4, 8, 12, 15]:

$$r \in \Omega_t : \quad K_t \frac{1}{r} \frac{d}{dr} \left(r \frac{dP_t}{dr} \right) = M_t(P_t), \quad M_t(P_t) = \frac{M_0 P_t}{P_{crit} + P_t}$$

$$r = R_c : \quad 2\pi R_c K_t \frac{dP_t}{dr} = -k(P_b - P_t) \tag{10}$$

$$r = R_t : \quad \frac{dP_t}{dr} = 0$$

where P_t [mmHg] is the partial oxygen pressure in tissue, K_t [(cm^2 s^{-1})(mol cm^{-3} mmHg^{-1})] is the Krogh diffusion coefficient, M_0 [mol cm^{-3} s^{-1}] is the oxygen demand, P_{crit} [mmHg] is the partial pressure that corresponds to half maximum oxygen consumption, k [(cm^2 s^{-1}) (mol cm^{-3} mmHg^{-1})] is the mass transfer coefficient. The component $M_t(P_t)$ is the oxygen consumption in the tissue, assumed as the Michaelis-Menten kinetics.

Along the Krogh cylinder, the partial pressure of oxygen in the capillary P_b changes, which is expressed by the following relation [8, 12]:

$$z \in \Omega_c : \quad Q_b \kappa_b \frac{d[S_{Hb}(P_b)]}{dz} = -k(P_b - P_t)$$

$$z = 0 : \quad P_b = P_{b\,inlet} \tag{11}$$

where κ_b [mol cm^{-3}$_{blood}$] is the oxygen carrying a capacity of blood at 100% saturation, while S_{Hb} is the saturation of oxyhemoglobin, determined by the adopted model of oxyhemoglobin dissociation curve (2).

9.4. Methods of solution

In the stage of numerical implementation, an explicit scheme of the finite difference method was used to solve the bioheat transfer problem and shooting method to solve the oxygen distribution tasks.

The finite difference method uses the 7-point stencil shown in Fig. 3, with corresponding definitions of differential quotients (h is the grid step) [16]

$$\left(\lambda\frac{\partial T}{\partial x}\right)_{i+0.5,j,k}^{f-1} = \lambda_{01}\frac{T_1^{f-1}-T_0^{f-1}}{h} \quad \left(\lambda\frac{\partial T}{\partial x}\right)_{i-0.5,j,k}^{f-1} = \lambda_{02}\frac{T_0^{f-1}-T_2^{f-1}}{h}$$

$$\left(\lambda\frac{\partial T}{\partial y}\right)_{i,j+0.5,k}^{f-1} = \lambda_{03}\frac{T_3^{f-1}-T_0^{f-1}}{h} \quad \left(\lambda\frac{\partial T}{\partial y}\right)_{i,j-0.5,k}^{f-1} = \lambda_{04}\frac{T_0^{f-1}-T_4^{f-1}}{h} \tag{12}$$

$$\left(\lambda\frac{\partial T}{\partial z}\right)_{i,j,k+0.5}^{f-1} = \lambda_{05}\frac{T_5^{f-1}-T_0^{f-1}}{h} \quad \left(\lambda\frac{\partial T}{\partial z}\right)_{i,j,k-0.5}^{f-1} = \lambda_{06}\frac{T_0^{f-1}-T_6^{f-1}}{h}$$

where

$$\lambda_{0e} = \frac{2\lambda_0\lambda_e}{\lambda_0 + \lambda_e}, \quad i = 1,...,6 \tag{13}$$
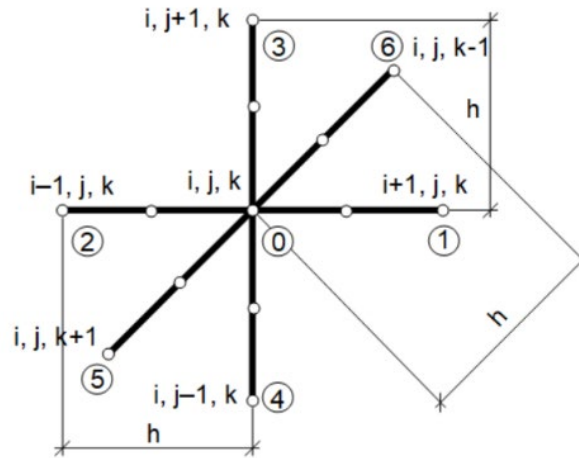
Fig. 3. 7-point stencil used in bioheat transfer problem
Rys. 3. 7-punktowa gwiazda stosowana w problemie przepływu biociepła

The idea of a shooting method is the transformation of a boundary value problem into an initial value problem (IVP). The boundary condition at the selected boundary of the domain under consideration is then used as the initial condition, while the second initial condition must be guessed. When the task is in this way, it can then be solved using one of the numerical methods for solving ODEs. The obtained value of the solution "on the second boundary" of the domain must be compared with the given boundary condition there. If the accuracy between the value of the one boundary condition and the obtained from IVP is not satisfactory, the initial value is guessed again and the problem is solved again [17, 18].

In the current work, the calculations of the shooting method were carried out in a Matlab 2022b environment. The secant method was used to determine the guess value and the fourth-order Runge-Kutta method for solving ODE [17].

9.5. Results of computations

In this work, a cube-shaped tissue domain with dimensions of $1.5 \times 1.5 \times 1.5$ cm was considered. To reduce computational complexity, only a quarter of the area was taken into account. For the FDM analysis, the domain was discretized using $76 \times 76 \times 151$ nodes. In the temperature determination, the Arrhenius injury integral and the perfusion coefficient the following data were used: $c_B = 3.9962$ [MJ m^{-3} K^{-1}], $w_0 = [0.041$ s$^{-1}]$, $Q_{met} = 245$ [W m^{-3}], $T_B = 37°C$, $q_0 = 15000$ [W m^{-2}], $t_{exp} = 30$ [s], $T_{init} = 37°C$, $A = 3.1e+98$ [s^{-1}], $E = 6.27e+5$ [J mol^{-1}], R $= 8.314$ [J mol^{-1} K^{-1}] [3, 19, 20].

The calculations for the oxygen distribution model were carried out for the following data: $R_c = 2.5$ [μm], $R_t = 25$ [μm], $L_t = 500$ [μm], $K_t = 4.1964e-14$ [(cm^2 s^{-1})(mol cm^{-3} mmHg^{-1})], $M_0 = 2.9762e-7$ [mol cm^{-3} s^{-1}], $P_{crit} = 1$ [mmHg], $k = 2.7902e-13$ [(cm^2 s^{-1})(mol cm^{-3} mmHg^{-1})], $P_{b\ inlet} = 100$ [mmHg], $\kappa_b = 8.9286e-6$ [cm$^{-3}_{blood}$], $n = 2.57$, $P_{50} = 27$ [mmHg] [3, 12]. Based on the data contained in Table 1, the following functions were assumed to describe the parameters of the oxyhemoglobin dissociation curve P_{50} and n:

$$P_{50}(T) = \begin{cases} 27, & T < 37°C \\ 1.27T - 19.99, & T \in [37°C, 44°C] \\ 35.9, & T > 44°C \end{cases} \qquad (14)$$

and

$$n(T) = \begin{cases} 2.57, & T < 37°C \\ -0.017T + 3.199, & T \in [37°C, 44°C] \\ 2.45, & T > 44°C \end{cases} \qquad (15)$$

In the first step, the task related to determining the temperature distribution, tissue damage, and damage-dependent perfusion coefficient was solved. Then the values determined in this task for the selected node were used to solve tasks related to oxygen distribution.

Figure 4 shows distribution of temperature in the domain considered for 30 s and history of temperature at selected nodes, while Figure 5 presents distribution of the Arrhenius integral and perfusion coefficients for 10, 30 and 40 s. It can be seen that the Arrhenius integral exceeds both values of the necrosis criteria, i.e., *Arr* > 1 and *Arr* > 4.6. For the perfusion coefficient, both the areas of increased perfusion, above $w_0 = 0.041$ [s^{-1}], and the area where, due to exceeding *Arr* > 1, the perfusion disappeared (cf. equation (4)) are clearly visible. Figure 6 is also related to the bioheat transfer analysis and presents history of the Arrhenius integral and the perfusion coefficient at the selected nodes.

For the analysis of oxygen distribution, point B (cf. Fig. 2) was selected.
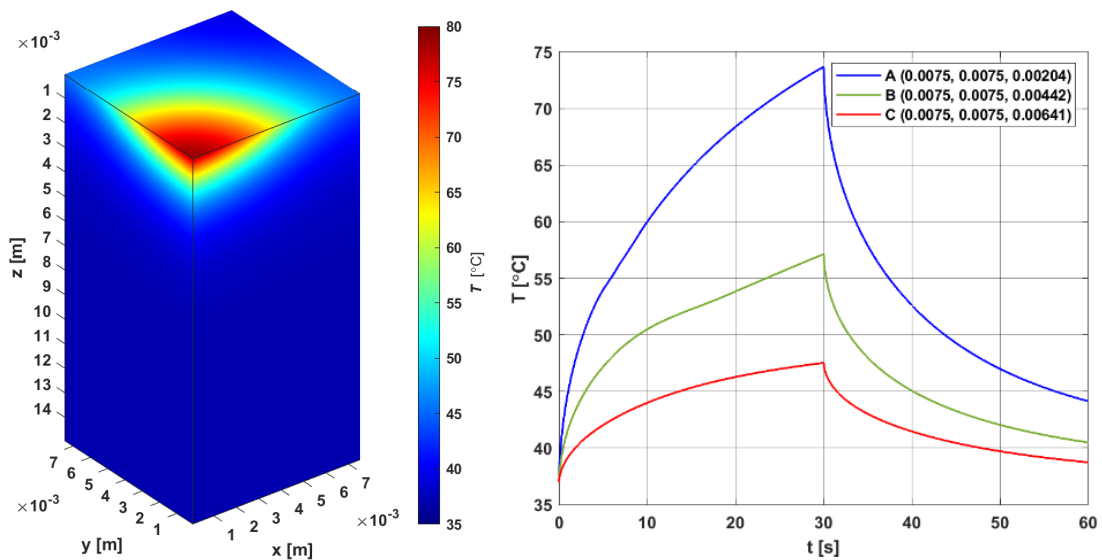
Fig. 4. Distribution of temperature for 30 s and history of temperature at selected nodes
Rys. 4. Rozkład temperatury dla 30 s oraz historia temperatury w wybranych węzłach
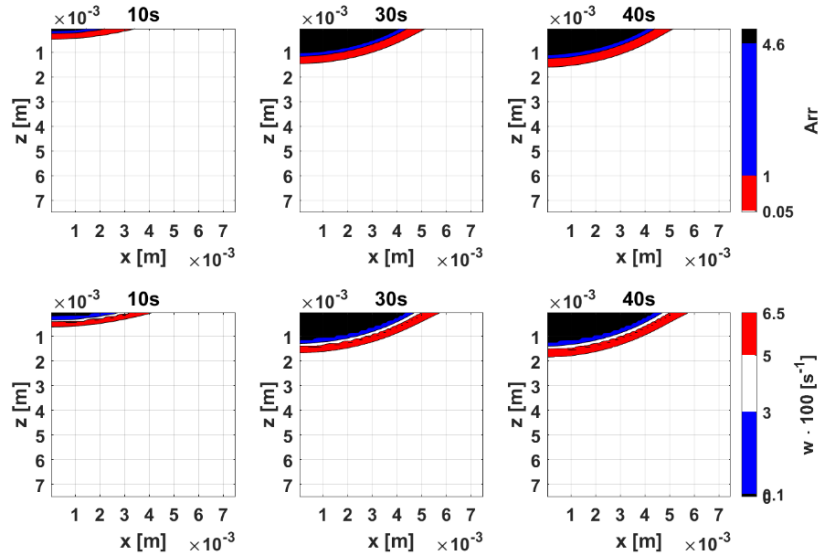
Fig. 5. Distribution of the Arrhenius integral and perfusion coefficient for 10, 30 and 40 s
Rys. 5. Rozkład całki Arrheniusa i współczynnika perfuzji dla 10, 30 i 40 s

Based on the history of the perfusion coefficient and equation (5) the blood velocity in the capillary u_b was calculated for selected time steps: 0, 10,…, 60 s. The following variants of simulation were conducted:

- variant 1: constant u_b, variable P_{50} and n,
- variant 2: variable u_b, constant P_{50} and n,
- variant 3: variable u_b, variable P_{50} and n.
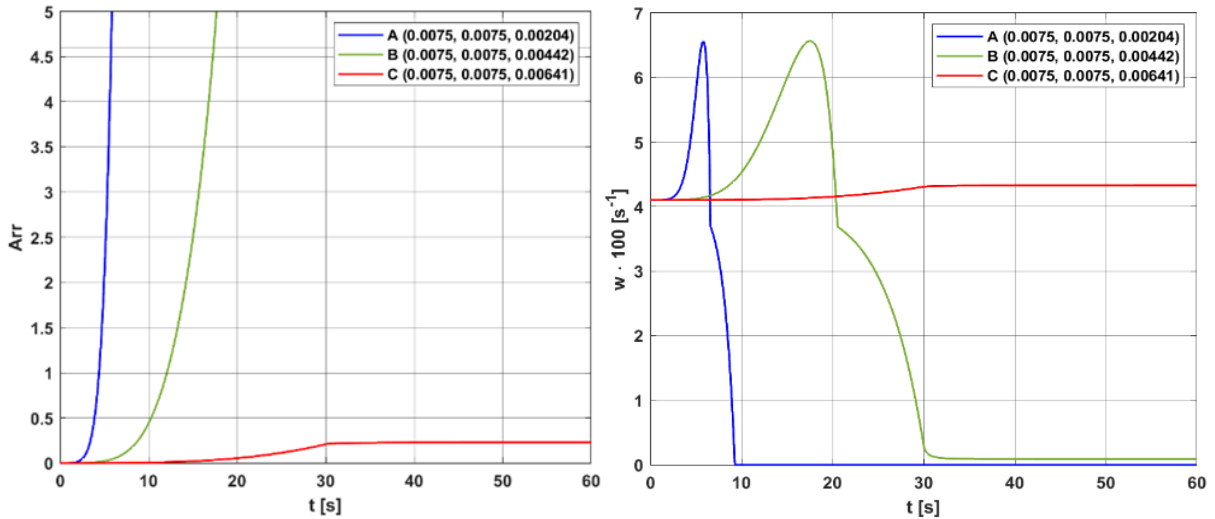
Fig. 6. History of Arrhenius integral and perfusion coefficient at selected nodes
Rys. 6. Historia całki Arrheniusa i współczynnika perfuzji w wybranych węzłach

The assumption of the constant parameter values means that their values for $t = 0$ are used (i.e. associated with $T_{init} = 37°C$, $w = w_0 = 0.041$ [s^{-1}]), while the variable parameters are related to u_b estimated on the basis of equation (5) and/or P_{50} and

n estimated on the basis of equations (14) and (15). The variant with constant u_b and constant Hill curve parameters was not considered because it corresponds to the simulations for $t = 0$, for each of the calculation variants. As is visible, the hypoxia phenomenon, that is, a drop in the partial pressure of oxygen in the capillary to zero before the end of the capillary, occurs only for variants 2 and 3.
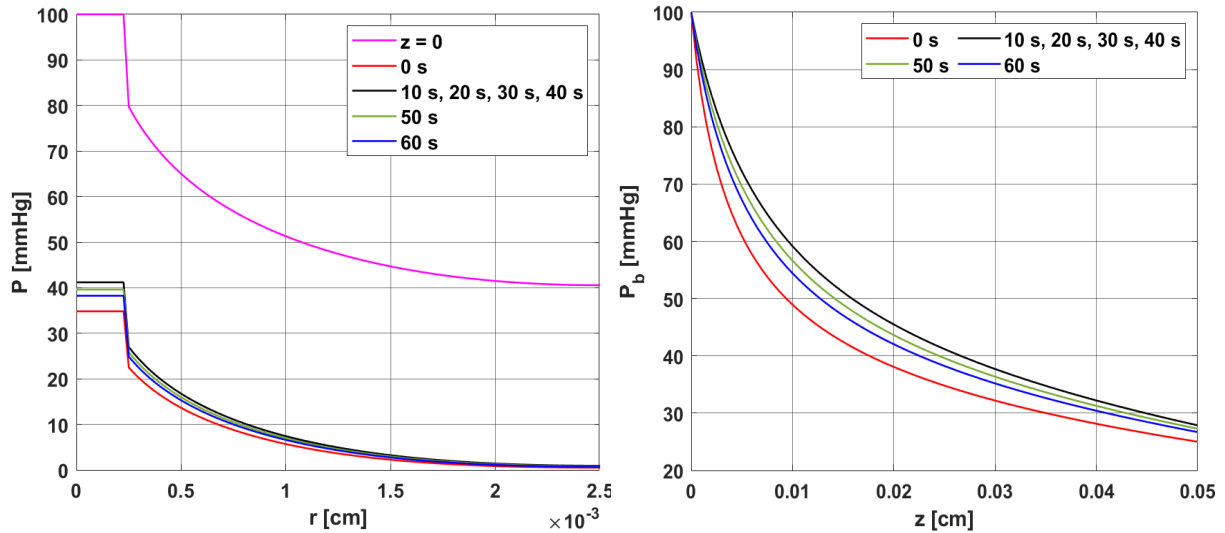
Fig. 7. Distribution of partial pressure in radial and axial directions in variant 1 (constant u_b, variable P_{50} and n)

Rys. 7. Rozkład ciśnienia parcjalnego w kierunku promieniowym i osiowym dla wariantu 1 (stałe u_b, zmienne P_{50} i n)
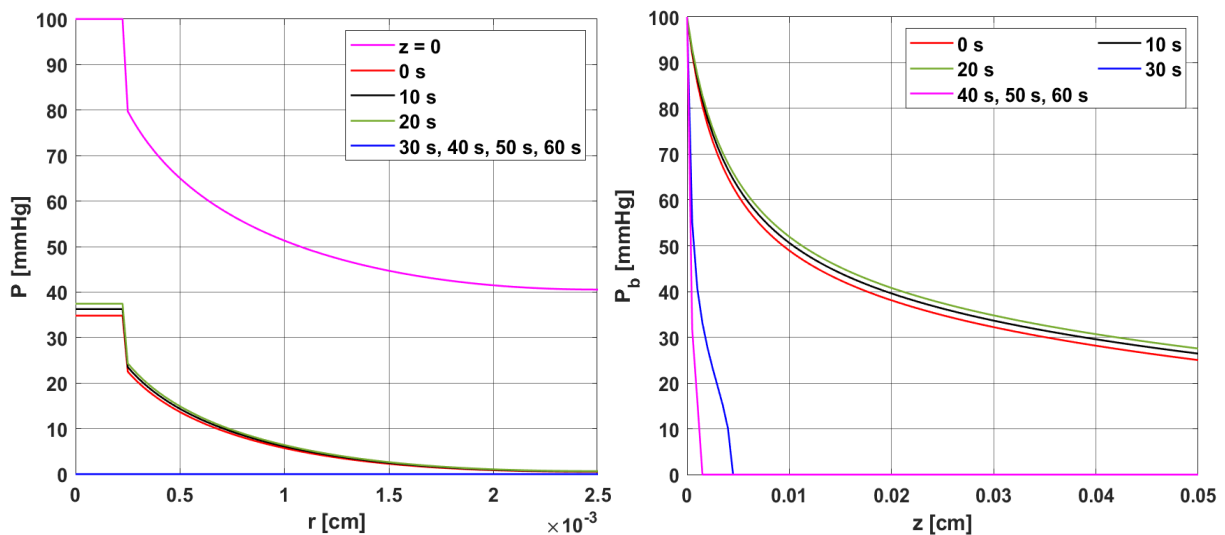
Fig. 8. Distribution of partial pressure in radial and axial directions in variant 2 (variable u_b, constant $P50$ and n)

Rys. 8. Rozkład ciśnienia parcjalnego w kierunku promieniowym i osiowym dla wariantu 2 (zmienne u_b, stałe $P50$ i n)
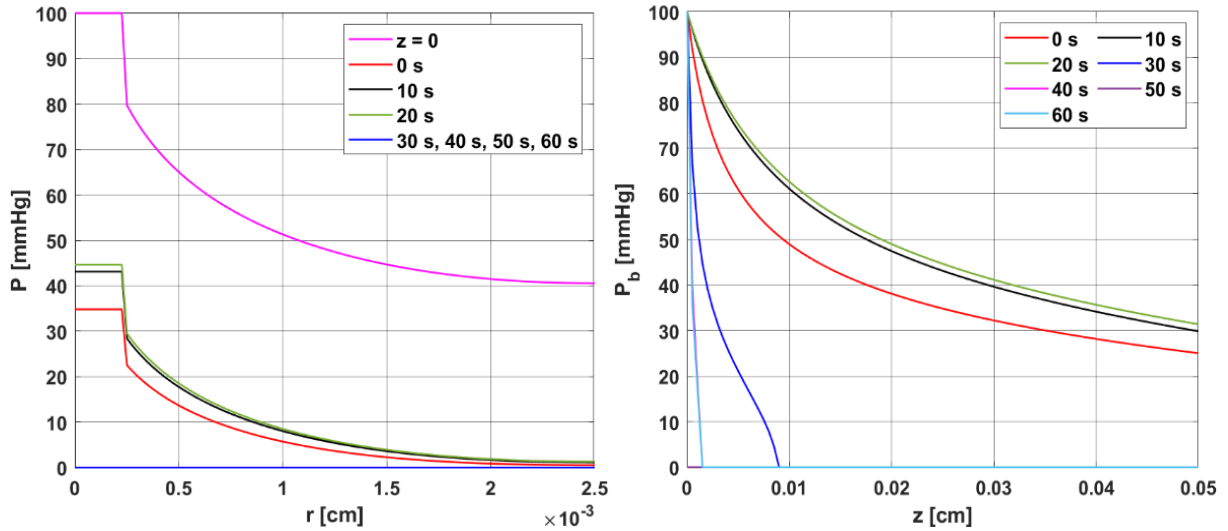
Fig. 9. Distribution of partial pressure in radial and axial directions in variant 3 (variable u_b, P_{50} and n)
Rys. 9. Rozkład ciśnienia parcjalnego w kierunku promieniowym i osiowym dla wariantu 3 (zmienne u_b, P_{50} i n)

9.6. Conclusions

The simulation cases show that the appearance of the hypoxia phenomenon was mainly influenced by the change in blood velocity resulting from the value of the perfusion coefficient value. The latter was closely related to thermal tissue damage through function (4). A drop in the perfusion value causes a simultaneous decrease in blood velocity. The effect of dependence of Hill curve parameters on temperature causes an increase in pressure with increasing temperature. In situations such as those of variant 3, it can counteract the occurrence of hypoxia.

It should be pointed out that many of the parameters used in the simulations were assumed to be constant values, e.g. $P_{b\ inlet}$. Thermal damage can cause changes at different levels of the vascular network, so this value should also be accepted as related to tissue damage. It is also worth noting that part of the function (4) is defined in connection with dilatation of the blood vessels ($0.1 < Arr \leq 1$), which in the model related to temperature distribution and determining the degree of tissue damage means an increase in perfusion, while in the oxygen distribution model it could mean a change in diameter of the capillary R_c.

The overall model presented shows that the phenomenon of thermal damage is complex, not limited to one type of phenomena. In addition, there are suggestions in the literature about the effect of oxygen on some kind of reversal of the thermal damage phenomenon, which may be important, especially when modeling various types of

therapies in which the temperatures used are not high. Attempts have been made to account for this phenomenon by attaching an additional component to the Arrhenius integral [9].

Bibliography

1. D. Goldman, Theoretical models of microvascular oxygen transport to tissue, *Microcirculation*, (2008) **15**(8): 795–811.
2. A.S. Popel, Theory of oxygen transport to tissue, *Critical Reviews in Biomedical Engineering*, (1989) **17**(3): 257–321.
3. M. Jasiński, Numerical analysis of the temperature impact to the oxygen distribution in the biological tissue, *Journal of Applied Mathematics and Computational Mechanics*, (2020) **19**(3): 17–28.
4. B.C. Fry, T.K. Roy, T.W. Secomb, Capillary recruitment in a theoretical model for blood flow regulation in heterogeneous microvessel networks, *Physiological Reports*, (2013) **1**(3): e00050.
5. T.W. Secomb, J.P. Alberding, R. Hsu, M.W. Dewhirst, A.R. Pries, Angiogenesis: An adaptive dynamic biological patterning problem, *PLoS Computational Biology*, (2013) **9**(3): e1002983.
6. M.P. Hlastala, R.D. Woodson, B. Wranne, Influence of temperature on hemoglobin-ligand interaction in whole blood, *Journal of Applied Physiology*, (1977) **43**(3): 545–550.
7. M. Castaing, M. Sinet, Temperature and oxygenation of human blood at constant total CO2 content, *Pflugers Archiv, European Journal of Physiology*, (1980) **386**(2): 135–140.
8. M. Jasiński, Numerical analysis of thermal damage and oxygen distribution in laser irradiated tissue, *Journal of Applied Mathematics and Computational Mechanics*, (2022) **21**(2): 51–62.
9. L.A. Dombrovsky, Laser-induced thermal treatment of superficial human tumors: An advanced heating strategy and non-Arrhenius law for living tissues, *Frontiers in Thermal Engineering*, (2022) **1**: 807083.
10. J.T. Oden, K.R. Diller, C. Bajaj, J.C. Browne, J. Hazle, I. Babuška, J. Bass, L. Biduat, L. Demkowicz, A. Elliott, Y. Feng, D. Fuentes, S. Prudhomme, M.N. Rylander, R.J. Stafford, Y. Zhang, Dynamic data-driven finite element models for laser treatment of cancer, *Numerical Methods for Partial Differential Equations*, (2007) **23**(4): 904–922.

11. J.P. Abraham, E.M. Sparrow, A thermal-ablation bioheat model including liquid-to-vapor phase change, pressure- and necrosis-dependent perfusion, and moisture-dependent properties, *International Journal of Heat and Mass Transfer*, (2007) **50**(13-14): 2537–2544.

12. B.J. McGuire, T.W. Secomb, A theoretical model for oxygen transport in skeletal muscle under conditions of high oxygen demand, *Journal of Applied Physiology*, (2001) **91**(5): 2255–2265.

13. B. Mochnacki, M. Ciesielski, Sensitivity of transient temperature field in domain of forearm insulated by protective clothing with respect to perturbations of external boundary heat flux, *Bulletin of the Polish Academy of Sciences: Technical Sciences*, (2016) **64**(3): 591–598.

14. G. Hamilton, Investigations of the thermal properties of human and animal tissues, Ph. D. Thesis, University of Glasgow, UK, (1998).

15. Y. He, M. Shirazaki, H. Liu, R. Himeno, Z. Sun, A numerical coupling model to analyze the blood flow, temperature, and oxygen transport in human breast tumor under laser irradiation, *Computers in Biology and Medicine*, (2006) **36**(12): 1336–1350.

16. E. Majchrzak, B. Mochnacki, Dual-phase lag equation. Stability conditions of a numerical algorithm based on the explicit scheme of the finite difference method, *Journal of Applied Mathematics and Computational Mechanics*, (2016) **15**(3): 89–96.

17. A.Ü. Keskin, Boundary Value Problems for Engineers, Springer International Publishing, Heidelberg, (2019).

18. B.S. Attili, M.I. Syam, Efficient shooting method for solving two point boundary value problems, *Chaos, Solitons & Fractals*, (2008) **35**(5): 895–903.

19. E. Majchrzak, L. Turchan, M. Jasiński, Identification of laser intensity assuring the destruction of target region of biological tissue using the gradient method and generalized dual-phase lag equation, *Iranian Journal of Science and Technology – Transactions of Mechanical Engineering*, (2019) **43**: 539–548.

20. M. Jasiński, M. Zadoń, Mathematical modeling of the phenomena that occur in a biological tissue containing a photosensitizer, *Journal of Applied Mathematics and Computational Mechanics*, (2023) **21**(4): 40–51.

NUMERICAL ANALYSIS OF THE EFFECT OF TEMPERATURE ON THE PARTIAL PRESSURE OF OXYGEN IN BIOLOGICAL TISSUE

Abstract

The impact of an external heat pulse causes an increase in the tissue's temperature, resulting in a change in the tissue's thermophysical parameters and even irreversible thermal damage to the tissue. Damage to the blood vessel system can also affect oxygen delivery to the tissue. An increase in temperature causes the so-called Bohr effect, which affects the oxyhemoglobin dissociation curve describing the relationship between the oxygenation of hemoglobin and the partial pressure of oxygen in the blood. The work concerns the numerical analysis of the process of heating biological tissue and its thermal damage under the influence of an external heat impulse. The analysis is based on the bioheat transport equation in Pennes form. Using the Arrhenius scheme, the degree of thermal damage to the tissue is estimated, and, tissue parameters are treated as temperature-or damage-dependent. A model based on the Krogh cylinder concept was used to analyze changes in oxygen distribution in the capillary vessel and surrounding tissue. A Hill model was used to describe the oxyhemoglobin dissociation curve. Variable values of the parameters of dissociation curve and the blood velocity in the capillary were considered. The oxygen distribution model is linked to the thermal model through the relationship between the blood velocity in the capillary and the perfusion coefficient. In the stage of numerical realization, the finite difference method and the shooting method were used.

Keywords: bioheat transfer, tissue thermal damage, oxygen transport, finite difference method, shooting method

Patryk DĄBKOWSKI[1], Joanna POLAŃSKA[1,*]

Chapter 10. INTELLIGENT SELF-ADAPTIVE H&E-STAINED TISSUE SCAN QUANTISATION

10.1. Introduction

Tumour-infiltrating lymphocytes (TILs) can effectively indicate the immune risk [1] as they provide information about the organism's response to the cancer cells, which play a significant role in therapy or treatment selection. The score representing TIL's concentration relates to patient survival [2]. To obtain necessary information about tissue structure and cell spatial distribution in the collected specimen, samples are stained with hematoxylin and eosin (HE) to selectively colour cancer cells, blood cells, and fibres in a specific way that enables their identification. Analysing such preparations by doctors or specialists is highly time-consuming and challenging, and obtaining precise results is difficult. Unsupervised machine learning methods must be adopted to extract the crucial diagnostic information from H&E-stained tissue scans efficiently. We propose a three-stage modular pipeline for automated tissue detection on HE-stained scans, staining quantisation and image segmentation and demonstrate its properties using the exemplary breast cancer tissue scans from the TCGA database.

[1] Department of Data Science and Engineering, Faculty of Automatic Control, Silesian University of Technology, Gliwice, Poland.
[*] Corresponding author: joanna.polanska@polsl.pl.

10.2. Materials and Methods

10.2.1. Data

Images are scans of breasts tissues cancer, as the example in Fig.1, saved in TIFF format and of a substantial spatial resolution, containing millions of pixels and 400 + GB volume. They are considered Big Data and need to develop suited and intelligent solutions that avoid increasing computational costs. Data come from TCGA (The Cancer Genome Atlas) database and contain over thousand images of breast cancer H&E stained scans.
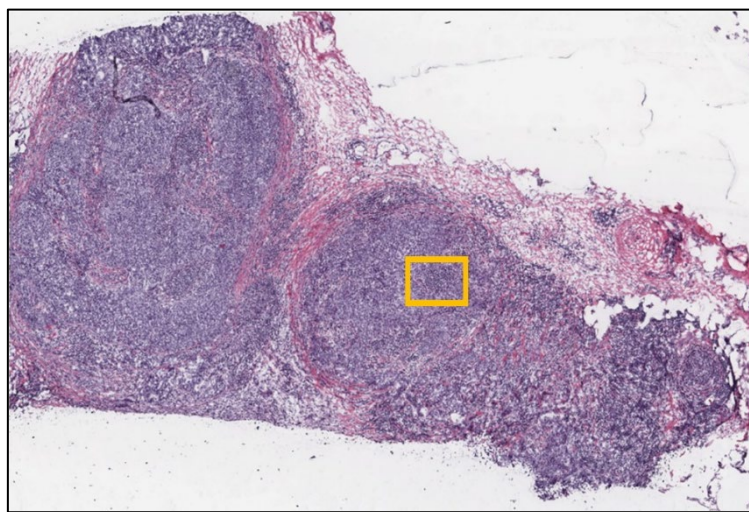
Fig. 1. Exemplary tissue scan with the zoom region marked as yellow box
Rys. 1. Przykładowy skan wycinka tkankowego z obszarem zainteresowania oznaczonym ramką w kolorze żółtym

10.2.2. Tissue mask detection

Among the various image segmentation methods available, the aim was to choose an approach that would effectively separate the tissue region from a relatively homogeneous background. The most popular watershed segmentation algorithm was discarded through experimental trials as it led to over-segmentation for complex images. The reasons for rejecting the watershed segmentation algorithm were also low computational efficiency, the need for calculations performed on each pixel, and the large number of hyperparameters that impede code automation and task universality.
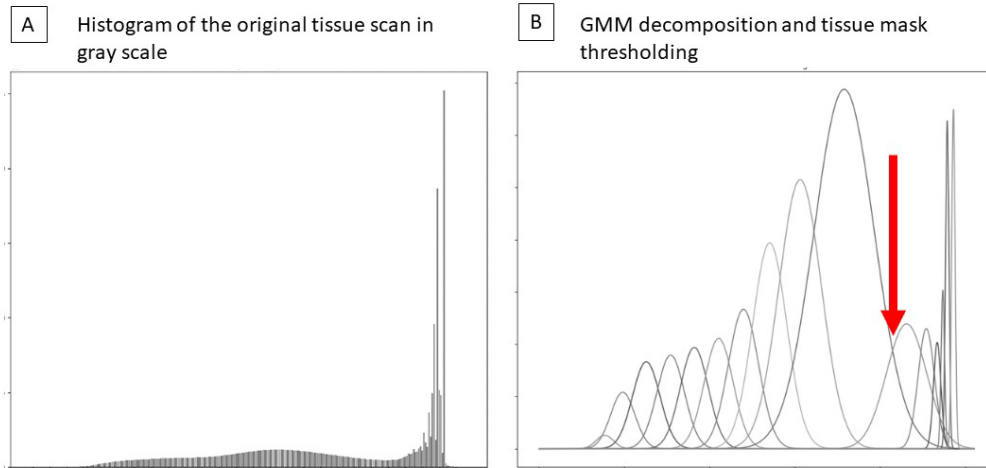
Fig. 2. Grayscale histogram (A) and its GMM decomposition (B) for the exemplary tissue scan
Rys. 2. Histogram w kolorach szarości (A) i jego dekompozycja do mieszaniny rozkładów normalnych
(B) dla przykładowego skanu wycinka tkankowego

Segmentation based a threshold usage obtained from the analysis of the grayscale image's histogram's envelope allowed us to reduce computationally expensive iterative operations on each pixel. The selection of the threshold point was performed through histogram analysis using the Gaussian Mixture Model (GMM) decomposition (Fig. 2) [3]. The GMM-type algorithm can be applied to segment the image histogram and determine the threshold for thresholding mask segmentation. The signal frequency distribution is modelled as a Gaussian mixture following the formula:

$$f(x_n) = \sum_{k=1}^{K} \alpha_k f_k(x_n, \mu_k, \sigma_k) \tag{1}$$

where K stands for the number of Gaussian components in the model, the coefficients α_k that sum up to 1 are the weights of the individual component with means μ_k and standard deviations σ_k. Dempster's expectation-maximisation algorithm is used to estimate the model parameters. Let us define the term *envelope,* which refers to a curve resulting from the sum of Gaussian components in the obtained model (Fig. 3). Additionally, we define a set of potential thresholds similarly as it is done for GMM-based classification problems. The crosspoints between consecutive GMM components are considered candidate greyscale image segmentation thresholds, and the first one after the dominating Gaussian component is chosen (as value 211 in the exemplary envelope in Fig. 2B – red arrow – and Fig. 3).
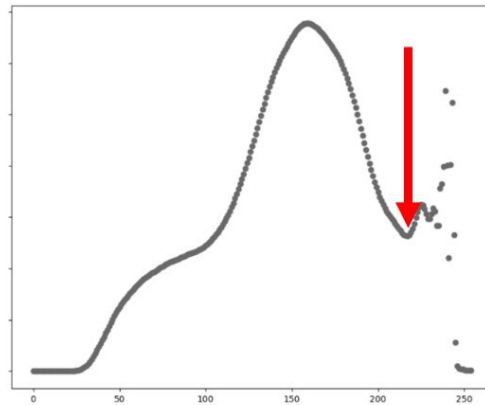
Fig. 3. GMM envelope for the exemplary scan
Rys. 3. Obwiednia modelu mieszanin rozkładów normalnych dla przykładowego skanu wycinka
      tkankowego

The number of Gaussian components is determined by the Bayesian Information Criterion (BIC). The criterion is conceptually defined as the model probability expressed through Bayes' theorem for model M and dataset y, where P(M|y) represents the marginal likelihood function:

$$P(M_i|y_1, \cdots, y_n) = \frac{P(y_1, \cdots, y_n|M_i)}{P(y_1, \cdots, y_n)} P(M_i) \tag{2}$$

Pixels with colour values above the chosen threshold are considered background, while the remaining ones constitute the tissue mask. To guarantee mask spatial homogeneity, the standard morphological operations as dilation and erosion are applied.

10.2.3. Staining quantisation

Quantisation is the process of reducing the number of signal or data values. This reduction can be helpful in data compression, denoising, standardisation, and extracting crucial and relevant information. Colour images can contain millions of unique colours, making it difficult for algorithms to effectively select features and make predictions or classifications with the desired accuracy.
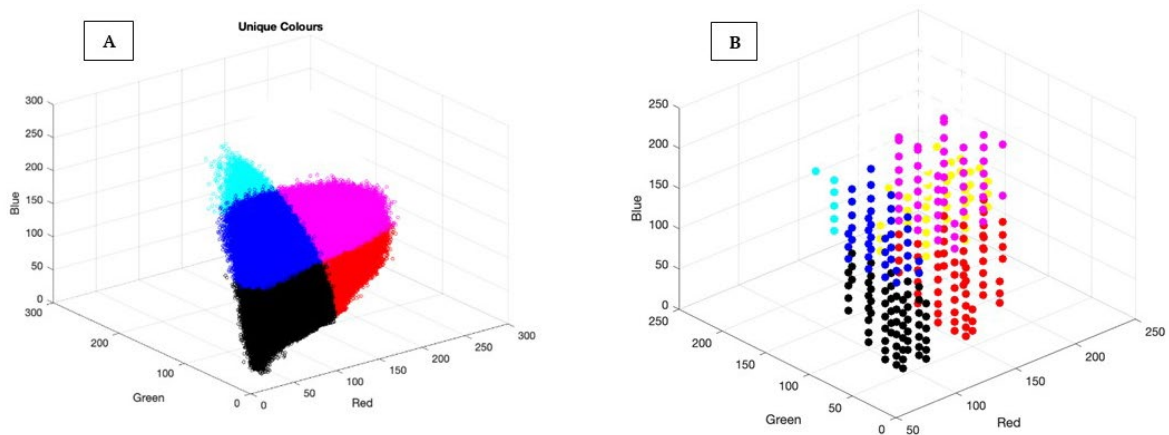
Fig. 4. (A) Unique colours of the original image (B) Unique colours of the quantised image in expanded RGB space (eRGB)

Rys. 4. (A) Unikatowe kolory oryginalnego skanu (B) Unikatowe kolory dla obrazu po wstępnej kwantyzacji barw w rozszerzonej przestrzeni RGB (eRGB)

Therefore, minimising the loss of information and the number of unique colours through colour reduction can be essential for identifying tumour-infiltrating lymphocytes. In our method, quantisation was achieved by utilising Gaussian Mixture Models for each RGB channel's histogram separately. Gaussian distributions are calculated based on the analysis of these histograms and with the Bayesian Information Criterion (BIC) to determine the number of components. The new colour values for each pixel are defined by their relation to RGB-specific Gaussian components. We propose to use a colour projection method that translates H&E stained colour images into new expanded colour space. New colour space is dynamic and defined by GMM components identified per each RGB channel. The final colour vector is of Mx1 dimension, where M denotes the total of GMM components from all RGB channels. The new colour feature value is 1 if GMM-based classifier assigns the pixel to the respective RGB channel specific GMM component, otherwise is equal to 0. Instead of 3D colour space we get the expanded M-dimensional space with 0/1 values only. That dimensionality expanding and colour coding let us distinguish colours and features that could not be distinguished in RGB space.

10.2.4. Image segmentation

The final step involves image segmentation performed in the expanded colour domain via pixel grouping according to their colour in the expanded colour domain. Clustering is done by the K-means++ algorithm, first introduced in [4]. The method is based on iterative fitting data into a static and predefined number of groups represented

by the mean of each group, aiming to minimise the error of data fitting. The K-Means++ variant ensures more evenly distributed and distant initial centroids. As a result, the algorithm is less prone to convergence to local minima, which helps achieve better cluster quality. The properly chosen initial in K-means++ results in faster convergence and a reduction of the number of iterations required to achieve convergence. Dimensionality expanding and colour quantisation let us effectively spread the colour values into distinguishable groups. The number of K-means clusters is defined by the Calinski and Harabasz score. Finally, the obtained colour clusters are represented by a static colour palette, which aims to standardise the obtained results, enabling more effective analysis of the scans by doctors. The kNN algorithm is applied to identify palette colours for each cluster. The reference palette is represented in Fig. 5.
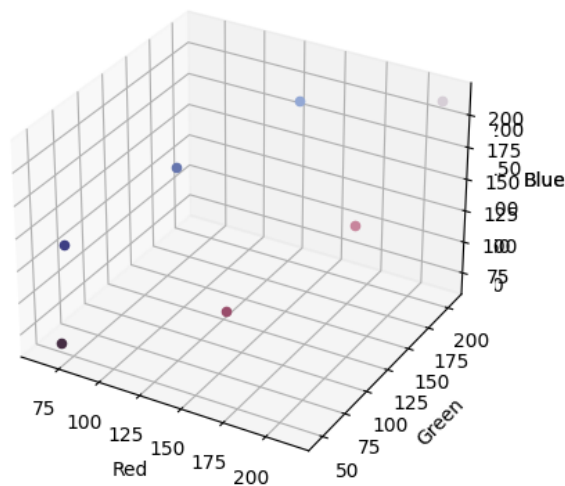
Fig. 5. The final reference colour palette in RGB space
Rys. 5. Ostateczna paleta pseudobarw klastrów przedstawiona w przestrzeni RGB

The resulting pipeline is presented in Fig. 6. It effectively utilises machine learning techniques for the segmentation, quantisation, and clustering of histopathological images stained with the H&E method.

Fig. 6. The image processing pipeline
Rys. 6. Proponowany potok przetwarzania obrazów

10.3. Results

The developed pipeline has been applied to a diverse set of images from the TCGA dataset, and the proposed method proves to be successful in extracting principal features important for TIL scoring. The developed tissue region segmentation method provides an accurate and precise binary mask, as presented in Fig. 7A.
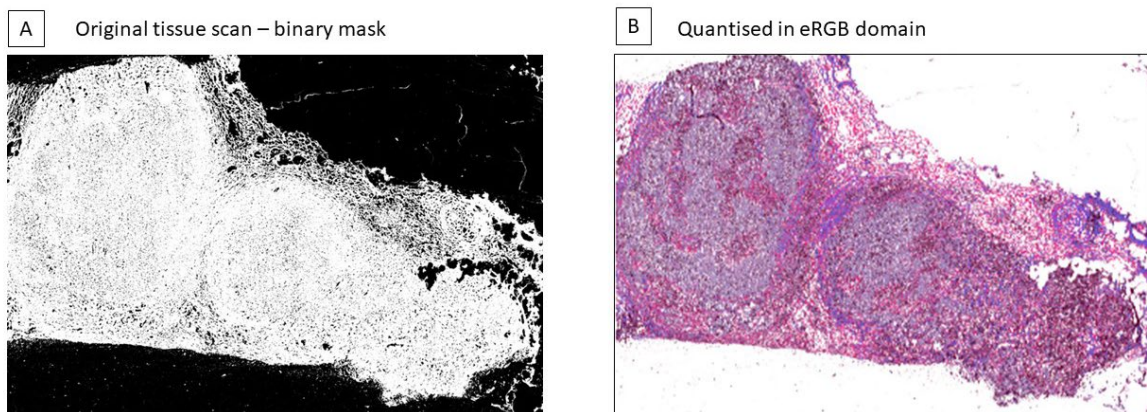
Fig. 7. Segmentation mask (panel A) and quantisation result (panel B) for the exemplary tissue scan from Fig. 1
Rys. 7. Binarna maska wycinka tkankowego (panel A) oraz wyniki kwantyzacji barw (panel B) dla przykładowego skanu wycinka tkankowego z Rys. 1

The number of unique colours in the exemplary image from Fig. 1 was 1,152,408. The applied colour quantisation method resulted in the reduction to 730 unique colours, and K-means clustering ended up with seven tissue segments (as shown in Fig. 7B and Fig. 8). The details of the cell neighbourhood are presented in Fig. 9, where one can easily distinguish the cell nucleus and cytoplasm. The preservation of this information in the process of image segmentation is essential from the point of view of the TILS index value assessment.
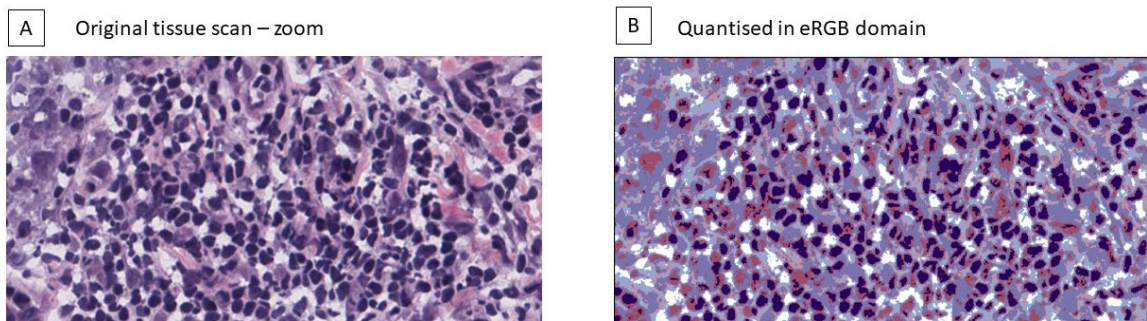
Fig. 8. Image segmentation for the zoom of the exemplary tissue scan from Fig. 1
Rys. 8. Wynik segmentacji obrazu dla wybranego regionu zainteresowania z przykładowego skanu wycinka tkankowego przedstawinego na Rys. 1
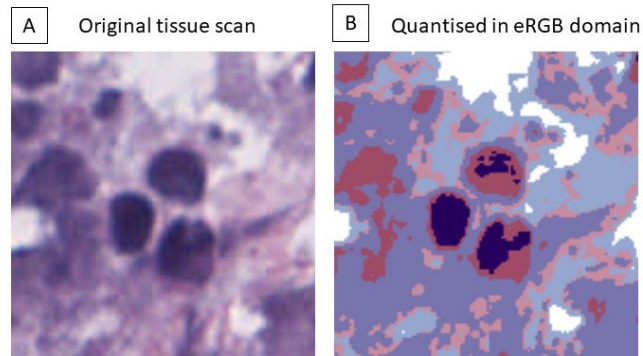
Fig. 9. Details of the original (panel A) and segmented (panel B) tissue region
Rys. 9. Szczegóły wybranego fragmentu tkanki: oryginalny obraz (panel A) i po segmentacji (panel B)

To investigate the importance of the RGB colour domain expansion, a similar image segmentation pipeline using the K-means clustering algorithm and the number of clusters set based on the analysis performed in expanded RGB (eRGB) was applied to the image represented in RGB colour space. Figure 10 presents the results of tissue region segmentation without (panel B) and with colour domain expansion (panel C). One can notice that quantisation without domain expansion provides a lower quality of the compressed images, where cells are inseparable. That phenomenon is not observed in the second case (panel C).
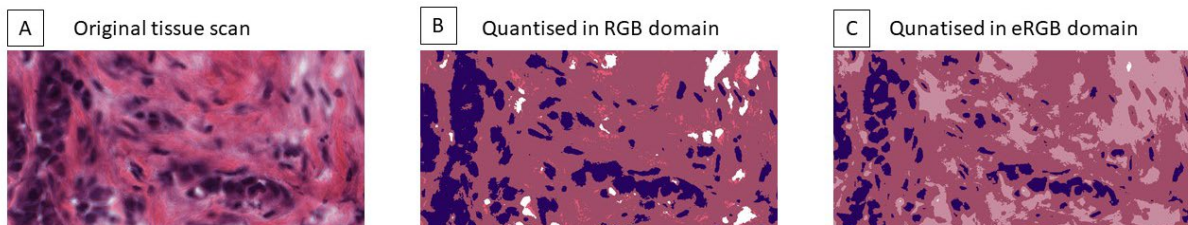
Fig. 10. Zoom of the original (panel A) and segmented tissue regions done without (panel B) and with (panel C) expansion of the colour space
Rys. 10. Szczegóły wybranego fragmentu oryginalnego skanu (panel A) i po segmentacji wykonanej bez (panel B) oraz z (panel C) proponowanym rozszerzeniem przestrzeni barw

10.4. Conclusions

We have shown that it is possible to perform fast and effective H&E-stained tissue scan segmentation by using the expanded RGB colour domain combined with the classical K-means approach. As the staining quantisation and standardisation are crucial either for cell identification as well as for further Deep Learning TIL score estimation, the above-developed image preprocessing pipeline should be a required step

in data analysis schema. For a more comprehensive exploration, we defer further discussion on the topic of effectively determining the number of clusters and estimation of TILs score to future research endeavours.

Bibliography

1. H.J. Wanebo, P.P. Rosen, T. Thaler, J.A. Urban, H.F. Oettgen. Immunobiology of operable breast cancer: an assessment of biologic risk by immunoparameters. Ann Surg. 1976 Sep;184(3):258–67. DOI: 10.1097/00000658-197609000-00003. PMID: 962394; PMCID: PMC1344377.
2. A. Suwalska, L. Zientek, J. Polanska, M. Marczyk. Quantifying Spatial Heterogeneity of Tumor-Infiltrating Lymphocytes to Predict Survival of Individual Cancer Patients. Journal of Personalized Medicine, 12(7):1113, 2022.
3. A. Polanski, M. Marczyk, M. Pietrowska, P. Widlak, J. Polanska. Signal Partitioning Algorithm for Highly Efficient Gaussian Mixture Modeling in Mass Spectrometry. PLOS ONE, 10(7), 2015.
4. R. Ostrovsky, Y. Rabani, L.J. Schulman, C. Swamy, "The Effectiveness of Lloyd-Type Methods for the k-Means Problem", 2006 47th Annual IEEE Symposium on Foundations of Computer Science (FOCS'06), Berkeley, CA, USA, 2006, pp. 165–176, DOI: 10.1109/FOCS.2006.75.

INTELLIGENT SELF-ADAPTIVE H&E-STAINED TISSUE SCAN QUANTISATION

Abstract

H&E-stained tissue scans are widely used to estimate the tumour-infiltrating lymphocyte score, serving as an essential prediction factor in cancer treatment. The proportion and location of the lymphocytes can determine the organism's response. However, this analysis is a demanding and time-consuming task. The support of machine learning approaches is crucial for achieving complete and precise estimates. Existing computer-aided methods allow image segmentation and lymphocyte identification by supervised and unsupervised learning methods. Although still, the obtained results are unsatisfactory and sensitive to different stain concentrations. We present a three-stage, modular self-adaptive image quantisation pipeline which uses

statistical modelling and clustering techniques. DL-based TILS regression models can then efficiently analyse the quantified images. At first, RGB colour channels are analysed independently. The channel-specific colour quantisation is based on the Gaussian Mixture Model of its intensity histogram. Then, the k-means pixel grouping is done, with the variance ratio criterion applied to set the number of clusters. The proposed quantisation reduces the number of unique colours from millions to 330,000 and afterwards to ~700 in the exemplary image without any apparent loss of quality or detail. The K-means grouping detected seven main tissue subtypes, which concord with the biological structure of a given tissue. The apriori set of pseudocolours is assigned to each cluster.

Keywords: H&E tissue stained scans, image processing, segmentation, colour quantisation, clustering, unsupervised machine learning

Wiktoria WOJNAROWSKA[1, 2,*]

Chapter 11. ESTIMATION OF HIP JOINT LOADS DURING WALKING USING MUSCULOSKELETAL MODELING

11.1. Introduction

Research that examines the biomechanics of the joint has substantial clinical and economic implications for the understanding and prevention of hip diseases. In particular, the hip joint is a subject of great interest due to its vital role in preserving human posture and mobility, and its susceptibility to degenerative conditions [1]. Knowledge of the loads on the hip joint during gait is an important aspect of musculoskeletal research, as it provides information on the mechanics of human movement and facilitates the development of effective treatments for musculoskeletal diseases. However, currently there is no straightforward approach to accurately determine hip joint loads, except through in vivo measurement of contact forces with the use of telemetric implants [2, 3]. Unfortunately, this method can only be implemented by joint replacement surgery, making it invasive. Therefore, a wider implementation of such technologies is currently not possible.

An alternative method for estimating joint contact forces is musculoskeletal modeling. These methods involve the construction of a mathematical model of the musculoskeletal system, which incorporates information on the anatomy and mechanics of the joint, as well as surrounding muscle and ligaments. This model can then be used to simulate walking movements, allowing for the estimation of joint loads and the evaluation of various factors that can influence these loads, such as gait speed, stride length, and body weight (BW). The non-invasive nature of musculoskeletal modeling allows for force calculation with reduced risks and expenses compared to the in vivo

---

[1] Doctoral School at the Rzeszów University of Technology, Rzeszów, Poland.
[2] Department of Physics and Medical Engineering, Faculty of Mathematics and Physics, Rzeszów University of Technology, Rzeszów, Poland.
* Corresponding author: wwojnarowska@prz.edu.pl.

measurement of contact forces using telemetric implants. Due to its ability to simulate complex movements and evaluate various loading scenarios, musculoskeletal modeling is a powerful tool [4].

Currently, computer software is gaining popularity for modeling the musculoskeletal system to simulate bone-muscle-joint interactions during movements and estimate joint reaction forces. In recent years, musculoskeletal modeling software packages that rely on graphical user interfaces (GUI), such as SIMM [5], OpenSim [6], and AnyBody [7], have become increasingly popular. These packages have simplified the simulation processes and facilitate the development and distribution of new models [8]. To represent the simulated system as closely as possible to reality, the musculoskeletal models should be validated [9]. In order to validate musculoskeletal models, it is essential to compare the results of subject-specific simulations with the experimental in vivo data of the corresponding subject.

One of the commonly applied applications of musculoskeletal modeling is the estimation of the hip joint reaction force (HJF) during different activities [4, 8, 10]. For the development of efficient treatments for musculoskeletal disorders such as osteoarthritis, accurate calculation of HJFs is essential. By providing information on the mechanics of joint loading, musculoskeletal modeling can be beneficial in the development of interventions that target specific loading situations and lower the risk of joint degeneration. Furthermore, the use of musculoskeletal modeling in the estimation of joint loads can provide valuable information for designing prostheses and various assistive devices, as well as for improving rehabilitation regimens.

In general, the prediction of HJF during walking using musculoskeletal modeling is a fascinating area of research that has the potential to have a significant impact on biomechanics, orthopedics, and rehabilitation disciplines. In addition, musculoskeletal modeling can be applied to the design of devices that interact with the human body. These can include equipment such as bicycles, shoes, exoskeletons, training equipment, or orthoses, as demonstrated by Zhou et al. [11], who optimized a shoulder orthosis. Musculoskeletal modeling can provide a more comprehensive understanding of biomechanics and therefore lead to the development of new treatments and interventions for musculoskeletal disorders, ultimately improving the quality of life for those affected.

The purpose of this study was to use the available model to calculate the reaction forces of the hip and evaluate these results.

11.2. Material and Methods

The study used a combination of experimental data and musculoskeletal modeling to estimate HJF during walking. The estimated HJFs were then compared with the in vivo measurements obtained by the use of an instrumented endoprosthesis to evaluate the results.

11.2.1. Experimental data

The experimental data used in the current study were obtained from the publicly available Orthoload database [12]. The data set used in this study was from a single male subject of 61 years, who had a body weight of 75 kg and a height of 172 cm (file 'h2r_150811_2_100'). The subject suffered from osteoarthritis and underwent total hip arthroplasty (THA). This dataset consisted of level-walking kinematic data captured using an optical motion capture system (VICON Metrics, Oxford, UK), force plate data (AMTI, Watertown, USA), and in vivo HJF measurements obtained using an instrumented prosthesis [13].

11.2.2. Musculoskeletal Modeling

Among the range of available musculoskeletal modeling software, AnyBody software (AnyBody Technology, Denmark) was selected, which is a commercial tool, providing a comprehensive musculoskeletal model of the whole body through the AnyBody Managed Model Repository (AMMR). For the analyzes, AnyBody software v.7 with lower extremity musculoskeletal model (AMMR, v.2.4.3) was used [14]. The model consists of the legs and the trunk, which included the head, thorax, and lumbar spine (Fig. 1). The legs are based on cadaver data from the Twente Lower Extremity Model [15].

Fig. 1. Musculoskeletal model from AnyBody modeling software with marker set
Rys. 1. Model mięśniowo-szkieletowy dostępny w programie AnyBody modeling z zestawem markerów

The first step of simulation was to specifically-adaped model, which means that it was scaled to match overall anthropometrics and marker data. A patient-specific scaled model, individual joint angles, and force plate data were used as input for the next part of the simulation. To compute joint kinematics, a kinematic analysis was conducted on the basis of the marker trajectories. Subsequently, inverse dynamics analysis was performed to calculate the required muscle activation and forces, as well as the resulting joint moments. Among other things, the components of the force acting on the hip were obtained during the simulation.

11.2.3. Processing of calculated data

After conducting simulations, three reaction force components that act on the left hip joint were chosen for exportation. Subsequently, the data was imported into EXCEL for processing. To ensure comparability, all forces were normalized by the subject's body weight, which was determined to be 75 kg.

The magnitude of the resultant force was calculated based on the three selected components. The resultant force was determined by taking the square root of the sum of the squares of these components. Subsequently, the time-dependent patterns for component forces and the resultant force during the stance phase were plotted, including both calculated and experimentally obtained data.

11.2.4. Comparison with the in vivo measurements

The precision of the predicted HJF and the validation of the simulation results were assessed by comparing the simulated HJF with the in vivo HJF. Comparison was made by visual inspection. Furthermore, the performance of the musculoskeletal model in predicting in vivo hip contact forces was evaluated numerically by computing in the EXCEL software two error metrics as follows:

- Root mean square error (RSME) as a percentage of body weight (%BW), as a global measure of the goodness of the fit. RSME was calculated in the stance phase for the anteroposterior, mediolateral, and vertical components, as well as for the total HJF.
- Pearson's correlation coefficient (R) between the measured and predicted HJFs for the three components of the HJF and the resulting HJF during the entire stance phase. Significance of the correlation was tested with a significance level of 0.05.

Furthermore, the calculated maximum peak value of hip contact force was compared with the results of other studies that used mathematical models to calculate hip contact forces during walking, in order to evaluate the accuracy and reliability of the current model.

11.3. Results and Discussion

The primary objective of this study was to estimate the HJF during walking using a musculoskeletal model and subsequently to evaluate the precision of the calculated forces. Calculations were made only for walking, which is the most reported daily activity. The described data were used for the calculations and the HJFs in stance phase were calculated. Figure 1 shows the model predicted and measured in vivo component hip contact forces and resulting force.
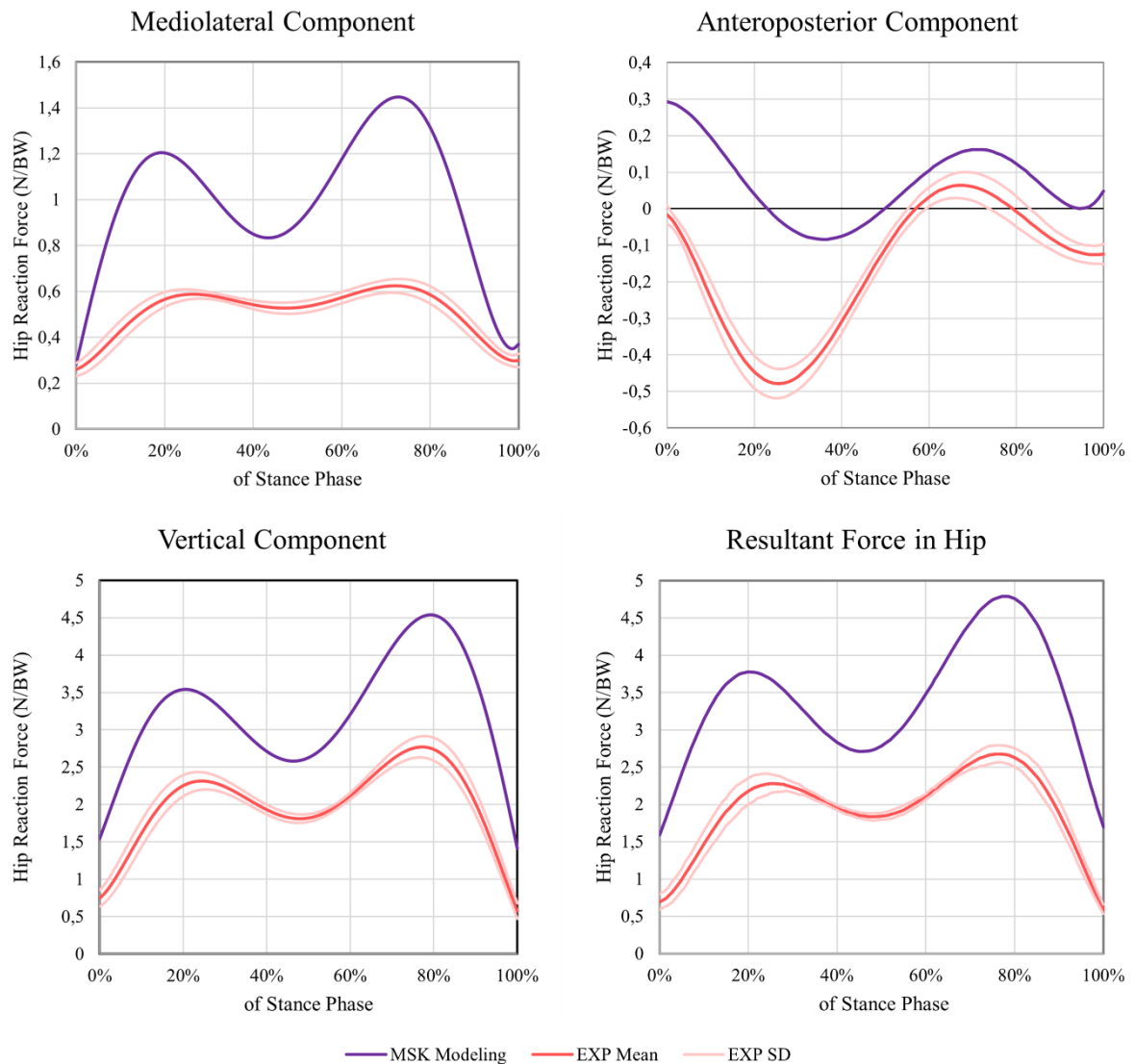
Fig. 2. Measured and predicted hip contact forces in the stance phase of walking
Rys. 2. Zmierzone i przewidywane siły kontaktowe w stawie biodrowym podczas fazy podporowej chodu

The HJF calculated and measured during walking exhibit similar patterns during the stance phase. This suggests that the computational model used in the study captures the general characteristics of hip joint forces during walking. In general, visual analysis indicates that the computational model utilized in this study has the ability to predict the contact forces in the hip joint during walking with a reasonable level of precision. However, there are discrepancies between the magnitudes of the calculated and measured HJF values. The calculated HJF values exhibit a higher magnitude compared to the corresponding measured values. The discrepancies between the magnitudes of the calculated and measured HJF values may arise from limitations of the computational model or measurement errors associated with the instrumented prosthesis.

The maximum resultant force calculated by musculoskeletal modeling is 43.7% higher than the measured in vivo value. This suggests that the model may overestimate the forces acting on the hip joint during walking. This difference may be due to various factors such as measurement error, variability in human anatomy, and differences in modeling assumptions. Typically, a difference of less than 10% between measured and calculated values is considered acceptable in biomechanics research [5]. Studies using instrumented implants have shown that the maximum hip joint reaction forces during normal gait typically range from 2.5 to 3.5 times body weight. However, depending on the condition of the subject, the maximum peak HJFs during gait can reach 4.9 times body weight [2, 16]. Based on these values, the calculated maximum peak resultant force of 4.79 times body weight falls within the range reported in the literature. However, it is at the higher end of the range. It is worth noting that different studies can report slightly different values depending on the methodology and assumptions used, as well as the characteristics of the subject and gait conditions.

The maximum peak value of the resultant force calculated in this study was compared with the results of other works that have used musculoskeletal modeling to estimate hip joint forces during walking. Figure 2 presents a comparison of the results obtained in this study with the maximum peak force values (in Newtons per BW) reported in the selected research.
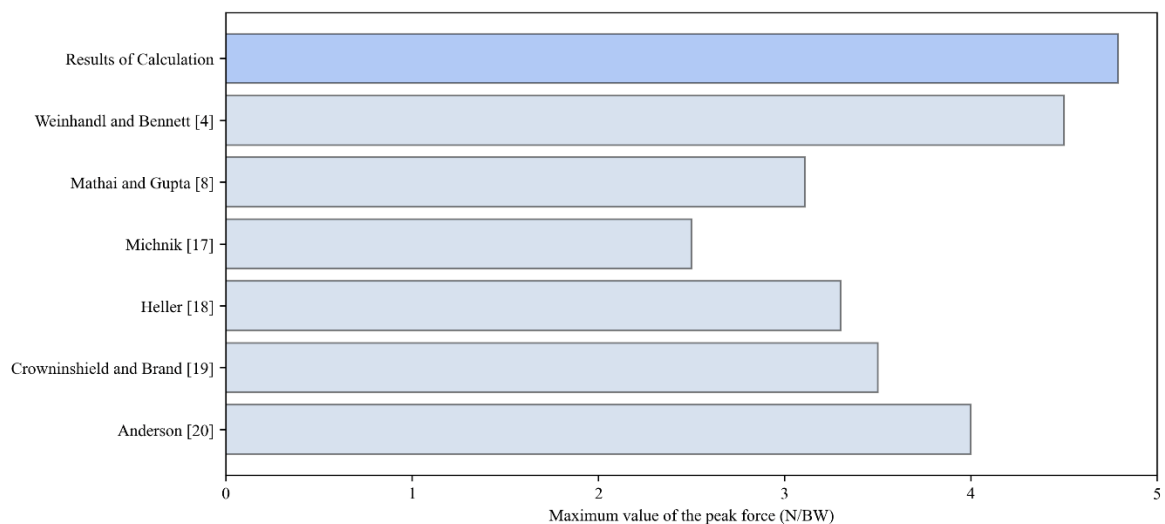
Fig. 3. Comparison of the maximum contact forces of the hip during walking determined by mathematical models

Rys. 3. Porównanie maksymalnych wartości sił reakcji w stawach podczas chodu wyznaczone za pomocą modeli matematycznych

Comparing the maximum peak value of the calculated resultant force with peak values from other works using musculoskeletal modeling for calculations, it can be seen

that the peak value of the contact force at the hip during gait calculated in this study is higher than in the other works, with the exception of the work of Weinhandl and Bennett [4], where the maximum value was similar. Differences in results may be due to different modeling assumptions.

Further evaluation of the calculated results included a quantitative assessment, which required calculation of selected error metrics, including the correlation coefficient and the RSME. In statistical analysis, the correlation coefficient represents the degree of concordance between the observed and predicted values, while the RSME is a measure of the accuracy of the prediction. Together, these metrics are used to evaluate the degree of agreement and the quality of the fit between the model predictions and the measured values. The correlation of the HJFs from the musculoskeletal model with the measured values of the HJFs is presented in Table 1, as well as the RSME (in % of the BW).

Table 4

Comparison of error metrics

Parameters	Force Components			Resultant Force
	Vertical	Med-Lat	Ant-Post	
R	0.92	0.89	0.56	0.89
RSME	126.83	52.83	27.54	151.31

The Pearson's correlation coefficient values suggest a strong positive linear correlation between the measured and predicted HJF values in the stance phase for the anteroposterior and vertical components, as well as the resultant force. However, the correlation coefficient for the anteroposterior component of the hip joint contact force was only 0.56, suggesting a weaker positive linear relationship between the measured and predicted values for this component. This may indicate that the model is less accurate in predicting this component of the hip joint contact force during walking, and further improvements may be necessary to improve the accuracy of the model for this component. Overall, these values suggest that the musculoskeletal model is performing well in predicting the in vivo hip contact forces during walking.

The RSME values are quite high, ranging from 27.54% to 151.31%. These values indicate a large percentage error between the predicted and actual reaction force values of the computational model, suggesting potential inaccuracies in capturing the complex dynamics of the hip joint during movement. When comparing the RSME value for the resultant force with the range of RSME values reported in the studies by Weinhandl and Bennett [4] and Mathai and Gupta [8], the 150% value is considerably higher, indicating

a wordpoorer accuracy of the model in predicting hip joint forces. This suggests that further refinements may be necessary to improve the accuracy and reliability of the current model.

In general, the calculated hip contact forces in this study were found to be significantly higher than the measured values and data from the previously reported literature. This discrepancy may suggest the need to improve the accuracy of the musculoskeletal model or reconsider the assumptions and input parameters used in the calculations.

11.4. Summary

Estimation of hip joint loads during walking is a critical aspect of musculoskeletal research with significant clinical and economic implications for the prevention and understanding of hip diseases. Invasive techniques, such as telemetric implants, can accurately measure contact forces; however, these techniques are costly and risky. Musculoskeletal modeling, which involves constructing a mathematical model of the musculoskeletal system and simulating walking movements, offers a non-invasive alternative for estimating joint loads. This study used a combination of experimental data and musculoskeletal modeling to estimate the contact forces in the hip during walking. Computational models proved to be valuable tools for predicting contact forces in a human joint, but validation through comparison with experimental data is essential for their accuracy.

The HJFs during walking were successfully estimated and the results were validated using in vivo measurements obtained by the use of an instrumented endoprosthesis. It was found positive correlation between the calculated and measurement data, suggesting potential of the model to predict reaction forces accurately. However, the RSME values suggest the need for further refinement or adjustments to achieve a higher level of precision in predicting the reaction forces of the hip joint. Therefore, further analysis is necessary to identify potential sources of error and refine the model.

The use of musculoskeletal modeling for the estimation of joint loads provides valuable information for the design of prostheses, various assistive devices, and rehabilitation regimens. This research highlights the potential of musculoskeletal modeling as a powerful tool to understand the biomechanics of human movement,

develop effective treatments for musculoskeletal diseases, and improve the quality of life of those affected. In general, musculoskeletal modeling is a valuable tool for estimating hip joint reaction forces during daily activities.

Bibliography

1. A. Wareńczak, P. Lisiński, Does total hip replacement impact on postural stability?, *BMC Musculoskeletal Disorders* (2019) **20(1)**:229.

2. G. Bergmann, G. Deuretzbacher, M. Heller, F. Graichen, A. Rohlmann, J. Strauss, G.N. Duda, Hip contact forces and gait patterns from routine activities, *Journal of Biomechanics* (2001) **30(7)**:859–871.

3. I. Kutzner, A. Richter, K. Gordt, J. Dymke, P. Damm, G.N. Duda, R. Günzl, G. Bergmann, Does aquatic exercise reduce hip and knee joint loading? In vivo load measurements with instrumented implants, *PLoS One* (2017) **12(3)**:e0171972.

4. J.T. Weinhandl, H.J. Bennett, Musculoskeletal model choice influences hip joint load estimations during gait, *Journal of Biomechanics* (2019) **91**:124–132.

5. S.L. Delp, J.P. Loan, M.G. Hoy, F.E. Zajac, E.L. Topp, J.M. Rosen, An interactive graphics-based model of the lower extremity to study orthopaedic surgical procedures, *IEEE Transactions on Biomedical Engineering* (1990) **37(8)**:757–767.

6. S.L. Delp, F.C. Anderson, A.S. Arnold, P. Loan, A. Habib, C.T. John, E. Guendelman, D.G. Thelen, *IEEE Transactions on Biomedical Engineering* (2007) **54(11)**:1940–1950.

7. M. Damsgaard, J. Rasmussen, S.T. Christensen, E. Surma, M. de Zee, Analysis of musculoskeletal systems in the AnyBody Modeling System, *Simulation Modelling Practice and Theory* (2006) **14(8)**:1100–1111.

8. B. Mathai, S. Gupta, Numerical predictions of hip joint and muscle forces during daily activities:A comparison of musculoskeletal models, *Proceedings of the Institution of Mechanical Engineers; Part H: Journal of Engineering Medicine* (2019) **233(6)**:636–647.

9. T. Bassani, E. Stucovitz, Z. Qian, M. Briguglio, F. Galbusera, Validation of the AnyBody full body musculoskeletal model in computing lumbar spine loads at L4L5 level, *Journal of Biomechanics* (2017) **58**:89–96.

10. P. Amiri, A.M.J. Bull, Prediction of in vivo hip contact forces during common activities of daily living using a segment-based musculoskeletal model, *Frontiers in Bioengineering and Biotechnology* (2022) **10**:995279.

11. L. Zhou, S. Bai, M.S. Andersen, J. Rasmussen, Modeling and design of a spring-loaded, cable-driven, wearable exoskeleton for the upper extremity, *Modeling, Identification and Control* (2015) **36(3)**:167–177.

12. G. Bergmann (ed.), Charité Universitaetsmedizin Berlin (2016) *OrthoLoad*: 'h2r_150811_2_100' retrieved from http://www.OrthoLoad.com, 20 March, 2023.

13. P. Damm, F. Graichen, A. Rohlmann, A. Bender, G. Bergmann, Total hip joint prosthesis for in vivo measurement of forces and moments, *Medical Engineering & Physics* (2010) **32(1)**:95–100.

14. M.E. Lund, S. Tørholm, D.S. Chander, B. Engelund, The AnyBody Managed Model Repository (AMMR) (2.4.3), *Zenodo* (2023): https://doi.org/10.5281/zenodo.7572879.

15. M.D. Klein Horsman, H.F.J.M. Koopman, F.C.T. van der Helm, L. Poliacu Prosé, H.E.J. Veeger, Morphological muscle and joint parameters for musculoskeletal modelling of the lower extremity, *Clinical Biomechanics* (2007) **22(2)**:239–247.

16. G. Bergmann, F. Graichen, A. Rohlmann, Hip joint loading during walking and running, measured in two patients, *Journal of Biomechanics* (1993) **26(6)**:969–990.

17. R. Michnik, Badania modelowe i doświadczalne chodu człowieka w aspekcie procesu jego rehabilitacji, Wydawnictwo Naukowe Instytutu Technologii Eksploatacji – PIB, Radom 2013.

18. M.O. Heller, G. Bergmann, G. Deuretzbacher, L. Dürselen, M. Pohl, L. Claes, N.P. Hass, G.N. Duda, Musculo-skeletal loading conditions at the hip during walking and stair climbing, *Journal of Biomechanics* (2001) **34(7)**:883–893.

19. R.D. Crowninshield, R.A. Brand, A physiologically based criterion of muscle force prediction in locomotion, *Journal of Biomechanics* (1981) **14(11)**:793–801.

20. F.C. Anderson, M.G. Pandy, Static and dynamic optimization solutions for gait are practically equivalent, *Journal of Biomechanics* (2001) **34(2)**:153–161.

ESTIMATION OF HIP JOINT LOADS DURING WALKING USING MUSCULOSKELETAL MODELING

Abstract

Reliable data on the condition of the musculoskeletal loading of a human joint during daily activities is critical to understanding the mechanics of human locomotion. Currently, the only way to measure joint forces in vivo is by implanting an instrumented prosthesis in patients undergoing total joint replacement. However, this is an invasive

method and cannot be performed for all people. Particularly in individuals in whom joint replacement is not necessary, this is not recommended. An alternative means to human movement analysis is musculoskeletal modeling, which uses various musculoskeletal models. In this study, the AnyBody Modeling system model was used for musculoskeletal modeling. The model was customized for one subject based on subject-specific anthropometric data and then used to simulate walking using motion capture data from the OrthoLoad public database. The estimated loadings were compared to the in vivo measurements.

The results showed that the model has the potential to accurately predict reaction forces. However, compared to previous studies, the estimated HJFs were quite high. Estimated forces can be used to develop personalized interventions for gait disorders and also as boundary conditions to develop numerical models of anatomical structures. Furthermore, it can be used to advance our understanding of the mechanics of human locomotion. In summary, musculoskeletal modeling provides a powerful tool for estimating hip joint reaction forces during daily activities.

Keywords: Musculoskeletal simulations, Inverse dynamics, Hip Joint Forces, AnyBody Modeling, Human locomotion, Hip biomechanics

Marcel OCHOCKI[1], Robert CICHOROWSKI[1], Barbara ILNICKA[1],
Marta PROCHOTA[1], Olga KOCIKOWSKA[2,3,*], Marek BAJTOŠ[4,5],
Klaudia HARGAŠOVÁ[6], Roman RADIL[4], Ladislav JANOUŠEK[4],
Sebastian STUDENT[2,7,*]

Chapter 12. EFFECT OF A WEEK-LONG EXPOSURE OF INTERMITTED LOW ELECTROMAGNETIC FIELD ON PROLIFERATION POTENTIAL OF HUMAN CELLS

12.1. Introduction

The rapid development of technologies present in everyday life in the last 30 years has resulted in the appearance of many electronic devices in households and workplaces. As a consequence, current-operated devices generate an electromagnetic field (EMF) which has become one of the environmental factors affecting living organisms and has also become subject of environmental monitoring. Workers who spend most of their time in close proximity to wiring are exposed to the constant presence of extremely low-frequency electromagnetic field (ELF-EMF) of approximately 50–60 Hz due to the frequency in electrical sockets [1]. Non-ionizing electromagnetic field interactions with biological objects at various levels have lately become a fast-growing research area but it has been the subject of public concern for many years [2]. Questions regarding its possible health risks are even more frequent and this particular area remains unclear, especially regarding long-term radiation. A couple of studies confirmed that ELF-EMF

[1] Department of Data Science and Engineering, Faculty of Automatic Control, Silesian University of Technology, Gliwice, Poland.
[2] Department of Systems Biology and Engineering, Faculty of Automatic Control, Electronics and Computer Science, Silesian University of Technology, Gliwice, Poland.
[3] Department of Physiology, Faculty of Medical Sciences, Silesian University of Medicine, Katowice, Poland.
[4] Department of Electromagnetic and Biomedical Engineering, Faculty of Electric Engineering and Information Technology, University of Žilina, Žilina, Slovakia.
[5] Department of Electrical, Computer and Energy Engineering, University of Colorado Boulder, Boulder, USA.
[6] ASTAR Spółka z o.o., Bielsko-Biała, Poland.
[7] Biotechnology Center, Silesian University of Technology, Gliwice, Poland.
* Corresponding author: sebastian.student@polsl.pl.

may be a potentially genotoxic and cytotoxic factor [3, 4], thus the main goal of this project was to verify if a week-long exposure has influence on human cells. This experiment models a typical week of workers' exposure to ELF-EMF with a frequency of 50 Hz with consideration of a two-day weekend break.

12.1.1. Physics of EMF

According to the classical electrodynamic theory an electromagnetic field is combination of electrical and magnetic field, which propagates in a certain medium. Properties of electromagnetic fields depend on many factors like their source, frequency, propagation medium etc. The method of electromagnetic fields generation depends on their properties and applications. Generally, any current flow through the conductive wire generates electromagnetic field. In this case, it is necessary to obtain higher magnetic field than electrical field by coil. According to Faraday's law of induction – a current flowing through the coil's wires generates magnetic flux proportional to the flowing current, the proportional coefficient is coil's induction. In general assumption, a coil is linear electrical element, so the output magnetic flux is similar to the input. Magnetic flux divided by surface represents magnetic flux density which is also named the B-field (1). It is described by following formula [5]:

$$B = \frac{LI}{S} \tag{1}$$

Where:
L – value of coil inductance [H]
I – value of current flowing through the coil [A]
S – surface area crossed by magnetic flux [m^2]
B – value of magnetic flux density (B-field) [T]

12.1.2. Influence of ELF-EMF on human cells

Last thirty years of research provided ambiguous claims about EMF impact on cells condition [5]. Depending on frequency, exposure time or type of electromagnetic wave used in experiment as well as type of cells tested, carcinogenic, proliferative and antiproliferative effects were distinguished. Several studies established a connection between ELF magnetic field exposure and leukemia and brain tumors [6] while others discarded such influence [7]. The possible carcinogenic influence caused by increase in

the oxidative stress in cells exposed to ELF-EMF was also shown in studies [8]. Contrarily another study showed possible anti-carcinogenic effect of ELF-EMF exposure on melanoma cells caused by downregulation of human endogenous retroviruses (HERVs) genes therefore neutralizing them [9].

In contrast to possible negative influence on human cells, electromagnetic field is commonly used in orthopedic treatments as a tissue's regeneration stimulating factor [10]. In the case of osteoblast-like cells, the proliferation-enhancing effect of ELF-EMF is confirmed [11]. The influence of the electromagnetic field on the efficiency of wound healing has been studied, but also in this regard the results of various research groups are contradictory. More recent studies focused on reducing inflammation after skin exposure to ELF-EMF and confirmed the possible alleviation of the irradiated area by contributing to the reduction of pro-inflammatory cytokines [12].

Clinical trial conducted in the Department of Biochemistry, University of Cambridge based on ELF-EMF classification as a possible harmful factor didn't provide significant evidence of such influence, but highlighted the fact that small changes in genes expression can exert significant effects on health [13]. Meta-analysis that focused on damage of mammalian cells exposed to electromagnetic field clarified the importance of including various genotoxicity endpoints in the assessment of DNA damage in the future studies [5]. Depending on the examined tissue and the type of cells exposed to ELF-EMF, the effect on their condition differs, which is why it is important to analyze a variety of cell lines under different irradiation conditions.

12.2. Materials and methods

12.2.1. Cell culture and cultivation

To determine the proliferation efficiency a clonogenic assay was performed with 5 samples each for control (CTRL), sham (SHAM), i.e. samples subjected to the same conditions as treated ones but with the turned off coil and treated groups (EMF) of HeLa GFP H2B cell line. Cells were seeded onto cell dishes ($\varnothing$ 3.5 cm) in the final concentration of 1700 cells per milliliter and incubated in a final volume of 2 ml Dulbecco's Modified Eagle Medium (DMEM/Ham's F12), supplemented with 7.5% Fetal Bovine Serum (FBS) in 5% CO_2 at 37°C. Control and sham samples were incubated under normal conditions, with SHAM (according to common practice an

inactive procedure to mimic experimental conditions) samples incubated inside unpowered coil. Test samples were additionally irradiated (frequency: 50 Hz, magnetic flux density: 85 µT) for 6 hours per day for 5 days and 2 days without irradiation afterwards as to model a worker's week of exposure to EMF irradiation.

12.2.2. Coil, irradiation system

The irradiation system was set up so that it would enable us to perform CTRL, SHAM and EMF tests at the same time (Figure 1). The set up for SHAM experiments consisted of an unconnected coil (L_{Sham}). The set up for EMF samples consisted of a generator connected to coil (L_{EMF}) via ammeter. The generator allowed us to choose the voltage of 3.6 mV, sinusoidal wave and the frequency of 50 Hz as an output signal. The ammeter connected between generator and coil shows value of current flowing through the coil. The coils were located inside incubator so that coil generating electromagnetic filed would not affect SHAM and CTRL samples.
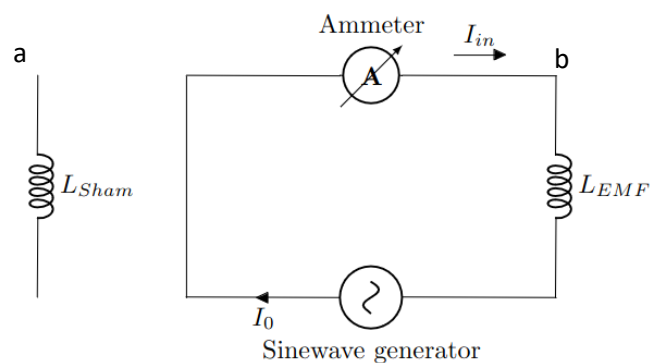
Fig. 1. Schemes of sham system (a) and irradiation system (b)
Rys. 1. Schemat układu dla próby pozornej (a) i układu dla próby badawczej (b) wpływ promieniowania

12.2.3. Clonogenic assay

After appropriate incubation of all samples (CTRL in normal conditions for 7 days, SHAM in unpowered coil in normal conditions for 7 days and EMF in treated conditions for 5 days and normal conditions of 2 days) were fixed with 96% EtOH, then washed with ddH2O. To enhance the visibility of formed colonies, samples were incubated in 0.2% crystal violet solution to obtain an intensive colour. After, dishes were twice quickly washed with ddH2O. All images of culture dishes with colonies were taken with

the use of G-BOX XT4 from SynGene and its software. Procurement of images after staining has been performed with visible light and white background. Colonies were then counted manually excluding abortive and merged ones.

To determine the performance of cells proliferation after ELF-EMF treatment both Proliferation Efficiency (PE, as a number of full-sizes colonies and seeded cell ratio) and Survival Fraction (SF, as a non-treated and treated samples PE ratio) factors have been used.

12.3. Statistical analysis

To determine the occurrence of differences in proliferation efficiency, non-parametric Kruskal-Wallis and Wilcoxon tests have been used. Analysis was prepared for 0.05 alpha significant levels.

12.4. Results and discussion

12.4.1. Clonogenic results
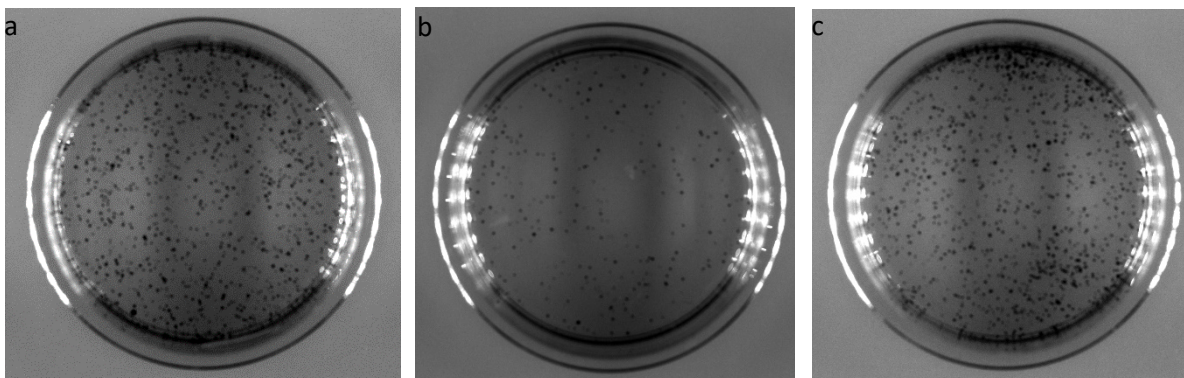
Fig. 2a. SHAM 2b. EMF 2c. CTRL plates with stained colonies
Rys. 2a. Płytka SHAM 2b. Płytka EMF 2c. Płytka CTRL z wybarwionymi koloniami

Table 1

Colonies counted for each experimental set

SET	SHAM	EMF	CTRL
1	382	279	348
2	598	222	603
3	325	392	405
4	532	369	396
5	591	567	699

Although data suggests (Table 1) fewer colonies in treated samples (EMF) (Figure 2b) compared to non-treated ones (SHAM and CTRL) (Figure 2a and Figure 2c) the results of Kruskal-Wallis' test show no significant differences in proliferation efficiency exist between any of the analyzed groups (Figure 3). When treated samples were compared to control and sham groups individually, Wilcoxon test resulted in p-values equal to 0.15 and 0.22 respectively. Moreover, there were no differences between ratio of PE from treated samples to PE of either control or sham samples (Figure 4). However, it is observed that nearly for all analyzed samples PE values for EMF samples are less than in the control and sham groups.
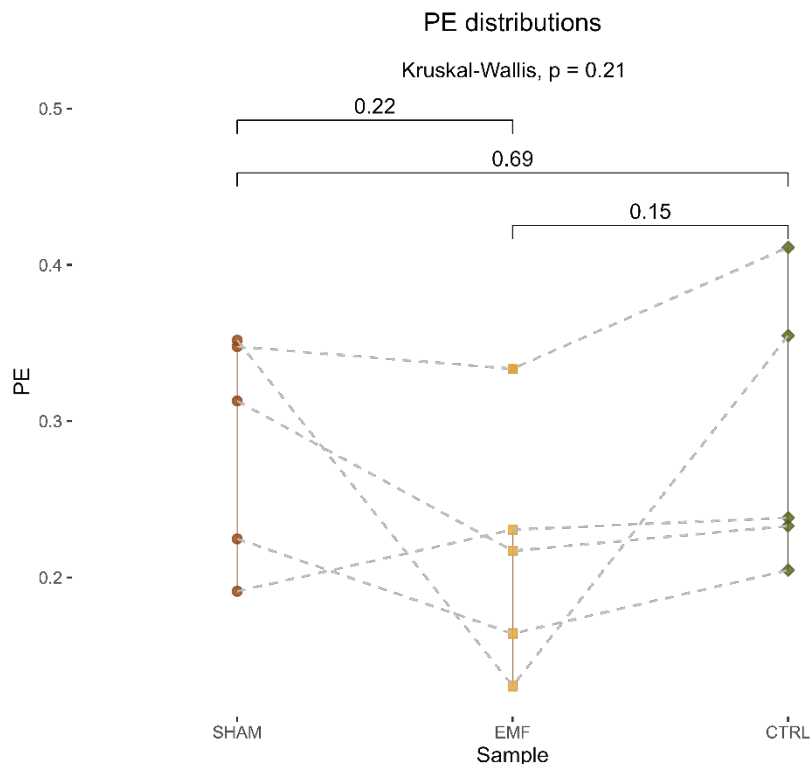
Fig. 3. Comparison of PE values between sham, treated with EMF and control samples. Results of Kruskal-Wallis and Wilcoxon tests. Dashed lines connect the linked samples. The Upper and lower quartiles are marked with the vertical lines

Rys. 3. Porównanie wartości PE pomiędzy próbami pozorną, badaną i kontrolną. Wyniki testów Kruskala-Wallisa i Wilcoxona. Przerywanymi liniami zaznaczono odpowiadające sobie próby. Górne i dolne kwartyle oznaczono za pomocą pionowych linii
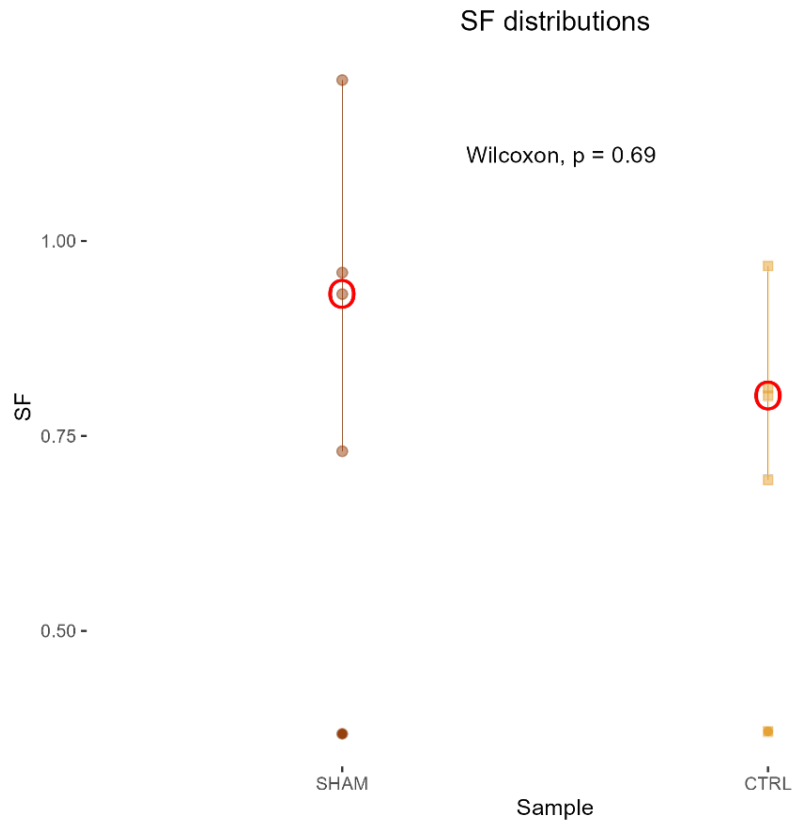
Fig. 4. Comparison of SF values between sham and control as a non-treated sample. Results of Wilcoxon test. The Upper and lower quartiles are marked with the vertical lines. Red circles represent each group medians.

Rys. 4. Porównanie wartości SF pomiędzy próbami kontrolnymi i pozornymi. Wyniki testu Wilcoxona. Pionowymi liniami zaznaczone zostały górne i dolne kwartyle. Czerwonymi okręgami oznaczono mediany.

12.5. Conclusions

The main results of this work show that one week-long exposure of ELF-EMF has no statistically significant impact on HeLa cells proliferation. However, it has been shown that samples treated with EMF irradiation are characterized with lower PE ratio values, thus those results might be correlated with conclusion provided by Kirschenlohr et al. [14] that non-significant changes in cell function caused by tested factor, yet difficult to observe, may carry health consequences in the future. Therefore, it can be supposed that the impact of ELF-EMF may be a potential risk factor for cells condition. Moreover, there were statistical differences between proliferation efficiency between control samples and those which were incubated in sham conditions, which was also verified by statistical analysis of surviving fractions. Future studies should take into

account the conclusions received so far and not only monitor the impact of ELF-EMF with different parameters at different times on different cell lines, but also check multiple endpoints that may be more sensitive to those slight changes.

12.6. Funding

Acknowledgments

Bibliography

1. Commission Regulation (EU) 2017/1485 of 2 August 2017 establishing a guideline on electricity transmission system operation (OJ L 220, 25.8.2017, pp. 1–120).
2. W.K. Stevens, Scientists Debate Health Hazards of Electromagnetic Fields, *New York Times* (1989) **07.11(C):**1
3. C.T. Mihai, P. Rotinberg, F. Brinza, et al., Extremely low-frequency electromagnetic fields cause DNA strand breaks in normal cells., J Environ Health Sci Engineer (2014) **12**:15.
4. S. Ivancsits, E. Diem, A. Pilger, H.W. Rüdiger, O. Jahn, Induction of DNA strand breaks by intermittent exposure to extremely-low-frequency electromagnetic fields in human diploid fibroblasts. *Mutation research* (2002) , **519(1–2):**1–13.
5. P. Vijayalaxmi, T.J. Prihoda, Genetic damage in mammalian somatic cells exposed to extremely low frequency electro-magnetic fields: A meta-analysis of data from 87 publications (1990–2007), *International Journal of Radiation Biology* (2009), **85(3)**:196–213.
6. E.M. Purcell, D.J. Morin. Electricity and Magnetism. *Cambridge Univ. Press*, p. 364.

7. C.D'Angelo, E. Costantini, M.A. Kamal, M. Reale, Experimental model for ELF-EMF exposure: Concern for human health, *Saudi Journal of Biological Sciences* (2015), **22(1)**:75–84.

8. N. Leitgeb, Comparative health risk assessment of electromagnetic fields, *Wien Med Wochenschr* (2011), **161**:251–262.

9. R. J. Bułdak, R. Polaniak, Ł. Bułdak, K. Żwirska-Korczala, M. Skonieczna, A. Monsiol, E. Birkner, Short-term exposure to 50 Hz ELF-EMF alters the cisplatin-induced oxidative response in AT478 murine squamous cell carcinoma cells, *Bioelectromagnetics* (2012), **33(8)**:641–651.

10. Y. Wei, H. Xiaolin, S. Tao, Effects of Extremely Low-Frequency-Pulsed Electromagnetic Field on Different-Derived Osteoblast-Like Cells, *Electromagnetic Biology and Medicine* (2008), **27(3)**:298–311.

11. C.L. Ross, M. Siriwardane, G. Almeida-Porada, C.D. Porada, P. Brink, G. J. Christ, B.S. Harrison, The effect of low-frequency electromagnetic field on human bone marrow stem/progenitor cell differentiation, *Stem Cell Research* (2015), **15(1):** 96–108.

12. M. Pesce, A. Patruno, L. Speranza, M. Reale, Extremely low frequency electromagnetic field and wound healing: implication of cytokines as biological mediators, *European Cytokine Network* (2013), **24(1**):1–10

13. A. Karimi, F. Ghadiri-Moghaddam, M. Valipour, Y. Yahyavi, Effects of prolonged exposure to ELF-EMF on HERVs expression in human melanoma cells, *Mol Biol Res Commun*. (2022), **11(2)**:67–71.

14. H. Kirschenlohr, P. Ellis, R. Hesketh, J. Metcalfe, Gene Expression Profiles in White Blood Cells of Volunteers Exposed to a 50 Hz Electromagnetic Field, *Radiation Research* (2012), **178(3)**:138–149.

EFFECT OF A WEEK-LONG EXPOSURE OF INTERMITTED LOW ELECTROMAGNETIC FIELD ON PROLIFERATION POTENTIAL OF HUMAN CELLS

Abstract

Extremely low frequency electromagnetic field (ELF-EMF) is generated among others by power lines and electrical devices; therefore, most people are exposed to its effects each day. This experiment models a typical week of workers' exposure to ELF-EMF with consideration of a two-day weekend break and analyzes its effect on human cells. Determination of proliferation potential was performed on HeLa cells with intermittent ELF-EMF of 50 Hz generated by a coil particularly measured for this experiment. Cytotoxicity was examined by a clonogenic assay that permits to inspect the ability of formation clonogenic colonies by tested cells. For this purpose, cells were cultivated in three groups: control one (cultivated in normal conditions), sham one (cultivated in an unwired coil in normal conditions) and exposed one (cultivated for 5 days in conditions of intermittent irradiation followed by two days of relaxation). To analyze the experiment's results appropriate devices and statistical tools have been used.

Keywords: electromagnetic field, HeLa cells, cancer, proliferation, cytotoxicity

Oskar TOKARCZYK[1], Robert CICHOROWSKI[1], Krzysztof JANIK[1],
Weronika LOSA[1], Marta PROCHOTA[1], Tomasz ŻYTECKI[1],
Divine Yufetar SHYNTUM[2], Alicja STAŚCZAK[1,2,*], Sebastian ŻABCZYŃSKI[3],
Dariusz CHOIŃSKI[1], Sebastian STUDENT[1,2]

Chapter 13. AUTOMATIC SYSTEM FOR BACTERIAL CELL VIABILITY ANALYSIS OF CONFOCAL MICROSCOPY IMAGES

13.1. Introduction

In recent years, light-emitting diodes (LEDs) have become increasingly popular in the field of research because of their diverse capabilities, including their small size and low energy consumption [1], which make them ideal for use in sterilisation systems. One of the most widely used applications of LEDs is in the field of ultraviolet radiation, specifically UVC irradiation. UVC radiation is a type of ultraviolet wavelength of radiation with a 100 to 280 nm. It is known for its mutagenic effect on microorganisms such as viruses or bacteria [2, 3], which causes damage to their DNA and prevents them from reproducing. This makes UVC irradiation a highly effective tool for sterilisation purposes. When applied to a surface or object, UVC radiation can penetrate the cell walls of microorganisms, disrupting their genetic material and rendering them inactive or dead. The COVID-19 pandemic has drawn increased attention to the use of UVC irradiation for sterilisation purposes. The SARS-CoV-2 virus, which causes COVID-19, is highly contagious and can survive on surfaces for extended periods of time, making it a significant challenge in preventing transmission. However, studies have shown that UVC irradiation can be effective in eliminating the virus on surfaces and in the air.

[1] Faculty of Automatic Control, Electronics and Computer Science, Silesian University of Technology, Gliwice, 44-100, Poland.
[2] Biotechnology Center, Silesian University of Technology, Gliwice, 44-100 Gliwice, Poland.
[3] Environmental Biotechnology Department, Faculty of Energy and Environmental Engineering Silesian University of Technology, Gliwice, 44-100 Gliwice, Poland.
* Corresponding author: alicja.stasczak@polsl.pl.

In fact, several hospitals and healthcare facilities have begun using UVC irradiation systems as part of their infection prevention measures for COVID-19. These systems are used to sterilise patient rooms, waiting areas, and equipment, and have been shown to be effective in reducing the risk of transmission. UVC irradiation is also being explored as a potential method to sterilise personal protective equipment (PPE) used by healthcare workers. Due to shortages of PPE during the pandemic, finding ways to safely and effectively sterilise and reuse PPE has become a critical issue. While UVC irradiation has shown promise as a tool for combating COVID-19, it is important to note that it is not a substitute for other measures of infection control, such as social distancing and hand hygiene. However, when used in combination with these measures, UVC irradiation can be a powerful tool to reduce the spread of the virus and achieve sterile conditions in a wide range of applications. To determine the effectiveness of UVC irradiation, authors conducted an experiment in which bacterial cells were exposed to UVC irradiation for a fixed period of time in an isolated space and the survival rate of the bacteria was evaluated. The assessment of bacterial survival is a crucial step in many experiments, but it can be a time-consuming and tedious process, prone to measurement error when performed manually by visual assessment of microscopic images by the researcher. Automated methods for assessing bacterial survival rates are much more efficient and can greatly reduce the chances of measurement errors, while also enabling the analysis of a much larger number of samples. To address this challenge, researchers have developed a computer program that can accurately identify dye signals in confocal microscope images and then automatically count the number of live and dead bacterial cells in the sample. This automated process can significantly reduce the time and effort required to assess bacterial survival rates, making it easier for researchers to obtain accurate and reproducible results.

13.2. Materials and methods

In the experiment, a workstation which can be seen in Fig. 1, equipped with a UVC lamp, a nebuliser was used to spread bacteria. After irradiation, fluorescent markers and a confocal microscope were used for taking images. The UVC lamp emitted ultraviolet radiation in the range of 100 to 280 nm, which was found to be highly effective in killing bacterial cells. The nebuliser was used to evenly spread the bacterial cells across the surface of the sample, ensuring that all cells were exposed to UVC

irradiation. Fluorescent markers were used to identify and differentiate between live and dead bacterial cells, and a confocal microscope was used to capture high-resolution images of the bacterial cells.

13.2.1. Equipment and reagents

Custom-made chamber with nebulisation system, UVC lamp composed of six LiteON LTPL-G35UVC275GM UV light emitting diodes and LEDiL VIOLET-12X1 lenses, fluorescent markers kit: LIVE/DEAD® BacLightTM Bacterial Viability Kit, microscope slides, coverslips, Eppendorf and confocal microscope.
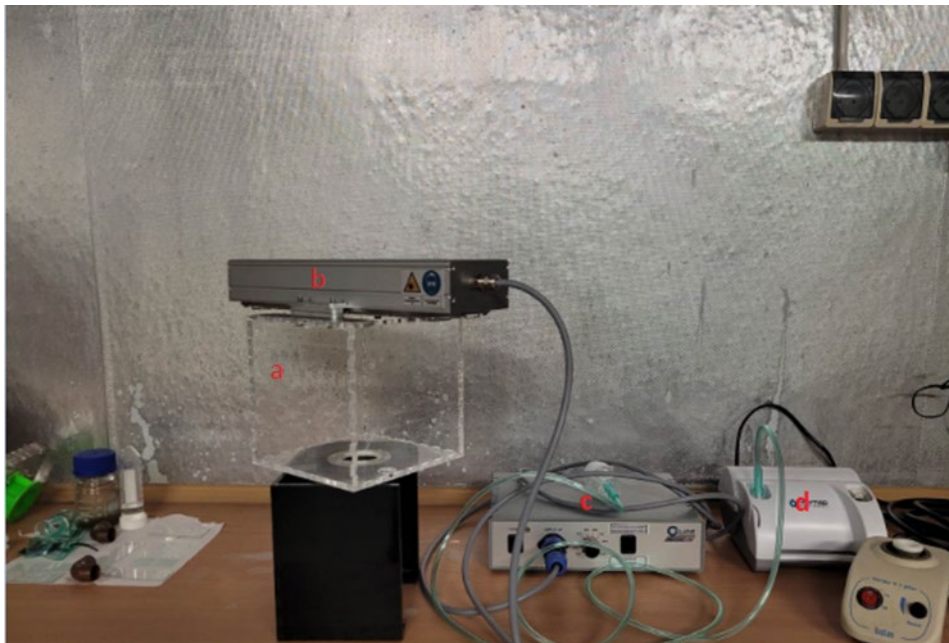
Fig. 1. Bacteria irradiation station equipped with sample chamber (a), UV lamp (b), controller to control lamp power (c), and nebuliser to distribute bacteria in chamber (d)

Rys. 1. Stanowisko do napromieniania bakterii wyposażone w komorę na próbki (a), lampę UV (b), sterownik do sterowania mocą lampy (c) oraz nebulizator do rozprowadzania bakterii w komorze (d)

13.2.2. Fluorescent markers kit

The fluorescent markers used in the experiment were the LIVE/DEAD® BacLightTM Bacterial Viability Kit. They enable dead bacteria to be distinguished from live bacteria for a wide range of strains such as *Bacillus cereus*, *B. subtilis*, *Clostridium perfringens*, *Escherichia coli*, *Klebsiella pneumoniae*, *Micrococcus luteus*, *Mycobacterium phlei*, *Pseudomonas aeruginosa*, *P. syringae*, *Salmonella oranienburg*, *Serratia marcescens*, *Shigella sonnei*, *Staphylococcus aureus* and *Streptococcus*

pyogenes. The LIVE/DEAD BacLight Bacterial Viability Kits utilise mixtures of two solutions: SYTO® 9 green-fluorescent nucleic acid stain and red-fluorescent nucleic acid stain, propidium iodide. These stains differ in their spectral characteristics and ability to penetrate healthy bacterial cells. When used alone, the SYTO 9 stain generally labels all bacteria in a population – those with intact membranes and those with damaged membranes. In contrast, propidium iodide penetrates only bacteria with damaged membranes, causing a reduction in the fluorescence of the SYTO 9 stain when both dyes are present. Thus, with an appropriate mixture of the SYTO 9 and propidium iodide stains, bacteria with intact cell membranes stain fluorescent green, whereas bacteria with damaged membranes stain fluorescent red [4].

13.2.3. Methodology of the experiment

At the beginning the functioning of the UV lamp was verified with a UVC sensor. The reads from the sensor showed that the lamp was operating in the UV. Before starting the experiment, the dye solution was prepared. To do this, a sterile 1.5 ml Eppendorf tube was carefully wrapped in aluminium foil to limit the availability of light, since the dyes decompose when exposed to light. The tube was then added 1 ml of PBS, along with 3 µl of green fluorescent dye and 3 µl of fluorescent red dye. The first step of the experiment was to prepare the bacteria slides. Five millilitres of activated sludge solution was added to the nebuliser from a large bioreactor located at the Silesian University of Technology. The nebuliser tip was placed in a copper tube that led to a container made of transparent plastic with lined basal slides on the bottom. After the nebuliser was switched on, the bacteria were sprayed for 2.5 minutes and then the UV lamp was immediately turned on. During operation, the lamp and chamber were wrapped in aluminium foil to shield the equipment operators from UVC radiation. The irradiations were carried out in 2 cohorts. In the first cohort, bacteria were exposed to UVC for 7 minutes, 3.5 minutes and 1 minute and in the second cohort, bacteria were exposed for 15 minutes, 10 minutes and 7 minutes, respectively. Three plates were exposed at a time in each group and control plates with bacteria that were not exposed were also left in each cohort. After removal from the chamber, 40 µl of the previously prepared fluorescent dye solution described above was added to the slides and coverslips were applied. The slides prepared in this way were incubated in the dark for 60 minutes. After incubation time, the slides were observed on an Olympus FV3000 confocal fluorescent microscope. Example results can be seen in Fig. 2.
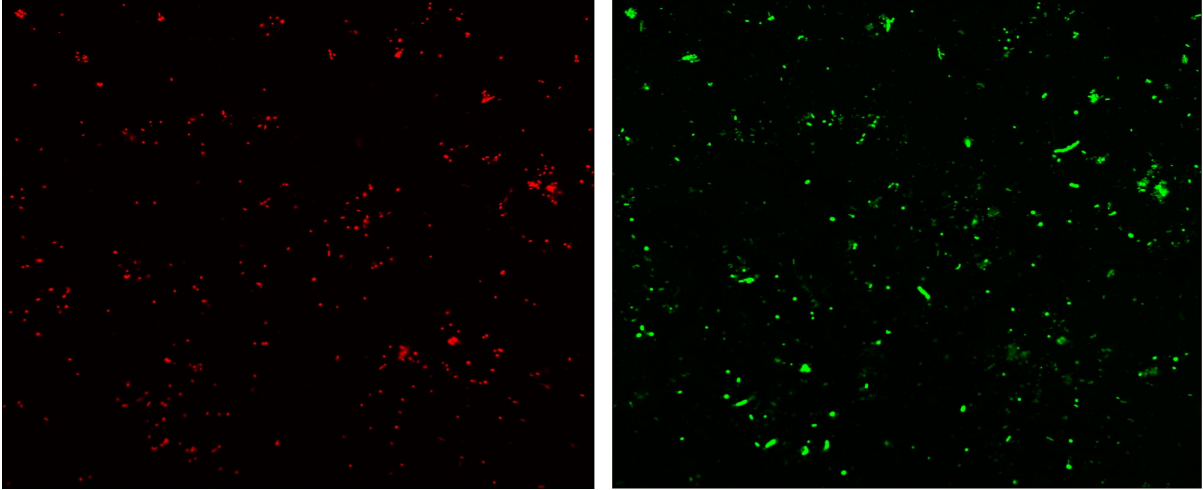
Fig. 2. Sample images obtained through microscopic observations using 60x magnification using oil immersion. Bacteria exposed to UVC irradiation for 10 minutes (green colour stains live cells, red only dead cells)

Rys. 2. Obrazy próbek uzyskane w wyniku obserwacji mikroskopowych przy użyciu powiększenia 60x z zastosowaniem immersji olejowej. Bakterie wystawione na działanie promieniowania UVC przez 10 minut (kolor zielony barwi żywe komórki, czerwony martwe komórki)

13.2.4. Exposure time formula

The formula of exposure time was derived from the lamp parameters [5] and information about the sufficient energy density to eradicate the entire population of microorganisms. To model the exposure time, the work of Kheyradish A. and Mohseni M. [6] was used to properly calculate the illumination angles. The formula is as follows:

$$t = \frac{U}{\eta \cdot P} \cdot \frac{h^2 tan^3 \alpha}{\sqrt{1+tan^2\alpha-1}} [s] \tag{1}$$

where:
U – value of sufficient energy density to eradicate the whole microorganisms population [J/m^2]

P – power of single diode [W/Sr]

η – single diode efficiency [%]

h – distance between the diode and the exposure surface [m]

α – exposure angle [°]

t – exposure time [s]

With six LiteON LTPL-G35UVC275GM UV light emitting diodes and a LEDiL VIOLET-12X1 lens, the energy density was 40 mJ/cm^2 and, according to the above formula (1) and at the maximum lamp power setting, the exposure time is approximately 15 minutes.

13.3. Data analysis

To analyse the data obtained, in order to avoid measurement errors and tedious counting of cells by hand, it was decided to create a computer programme. The raw microscope images contain three channels. Two of them contain pixels coloured in one colour. The "green channel" only contains live bacteria, and the "red" only dead bacteria. Sometimes there are common pixels/bacteria between the channels. This is due to the imperfectly selected proportions of dyes in the live/dead set. In the further part of the text "Green cells" mean cells in the modified green channel of the image, i.e. alive and dead, and "Red cells" mean cells in the red channel of the image, i.e. dead, this terminology is used because of the fact how the algorithm works and to be easier to understand for reader. The algorithm summarises all pixels from green channel and red channel in "Green cells" channel and then artefacts resulting from bad proportions of dyes can be cleared.

Cell detection software was developed as a plugin for Fiji / ImageJ2, allowing users to process cell viability data for a single image or an entire directory. The graphic user interface allows the user to change the parameters of the algorithm, which allows for more precise data analysis. The plugin can be easily installed in the same way as other imageJ2 plugins. After receiving the input data, depending on the method, the algorithm is performed once or many times, counting the number of cells. It consists of several steps. First, it separates channels (colours) of the input image and gets the green and red channels. Then it modifies channels (merging/deleting pixels), all cells should be in the green channel and only dead cells in the red channel. After this Gaussian filter is used to blur the channels, the channels are binarized using the Otsu method. Finally, blobs/spots (cells) are created in both channels. To analyse the results, the numbers of red and green cells were calculated. The output of the algorithm consists of images with detected cells as can be seen in Fig. 3 and a text file with the number of cells detected.
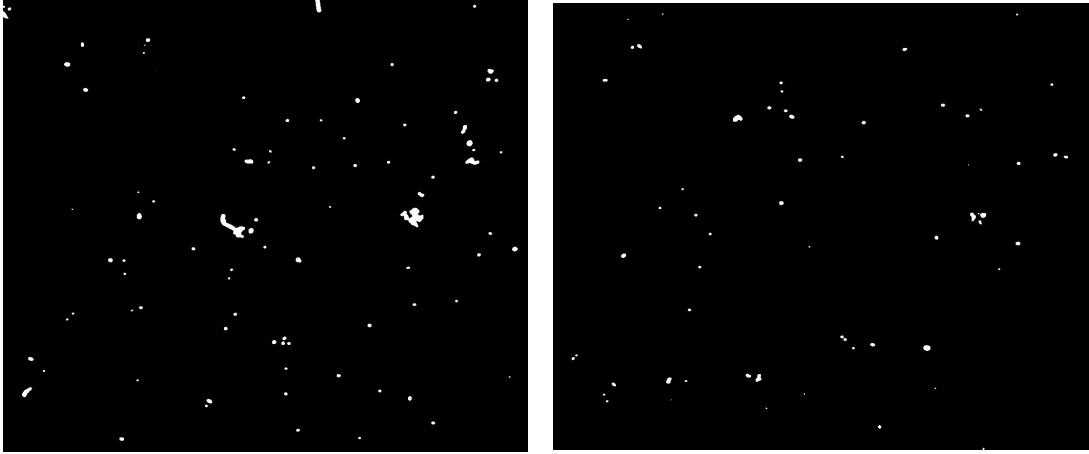
Fig. 3. Example images obtained using the algorithm
Rys. 3. Przykładowe obrazy uzyskane za pomocą algorytmu

The percent of living cells is determined as the difference between the green and red cell numbers, divided by the number of green cells. It can be defined as:

$$\text{LIVE CELLS} = \left(\frac{GREEN\ CELLS\ - RED\ CELLS}{GREEN\ CELLS}\right) \cdot 100\% \tag{2}$$

where:
GREEN CELLS – all live and dead bacterial cells
RED CELLS – dead bacterial cells
LIVE CELLS – living bacterial cells

The result of these calculations (2) is the viability of bacterial cells, making it possible to produce cross-sectional data showing the effectiveness of the UVC lamp at different exposure times.

13.4. Results and Discussion

The effect of UVC radiation on bacterial cells has been checked using a computer algorithm created, there is a correlation between exposure time and cell viability.

13.4.1. UVC Irradiation

As we can see in Table 1, there is a clear correlation between the viability of bacterial cells and the duration of their UVC irradiation. Low rate of living bacteria with no exposure time is due to the old age of the bacterial culture from which the sample was

taken. From Pearson's correlation coefficient, we know that the value of R is: -0.9548. This is a strong negative correlation. As shown in Fig. 5. below, cells irradiated for 15 minutes show almost 75% less viability than unexposed cells. The study confirmed that the minimum irradiation time to reduce bacterial viability by more than 50% of the bacterial mass is 7 minutes. The results of the studies conducted on the UVC lamp suggest that this method of disinfection is effective in eliminating bacteria, provided it is applied for the right amount of time. Finding the optimal irradiation time is key to achieving the best sterilisation results.

Table 1

Bacterial viability depending on irradiation time

Incubation time [min]	0	1	3.5	7	10	15
Bacterial viability [%]	53.13	46.87	37.04	23.27	21.35	19.35
Standard dev. (σ) [%]	1.64	1.73	1.12	0.4	0.8	0.9
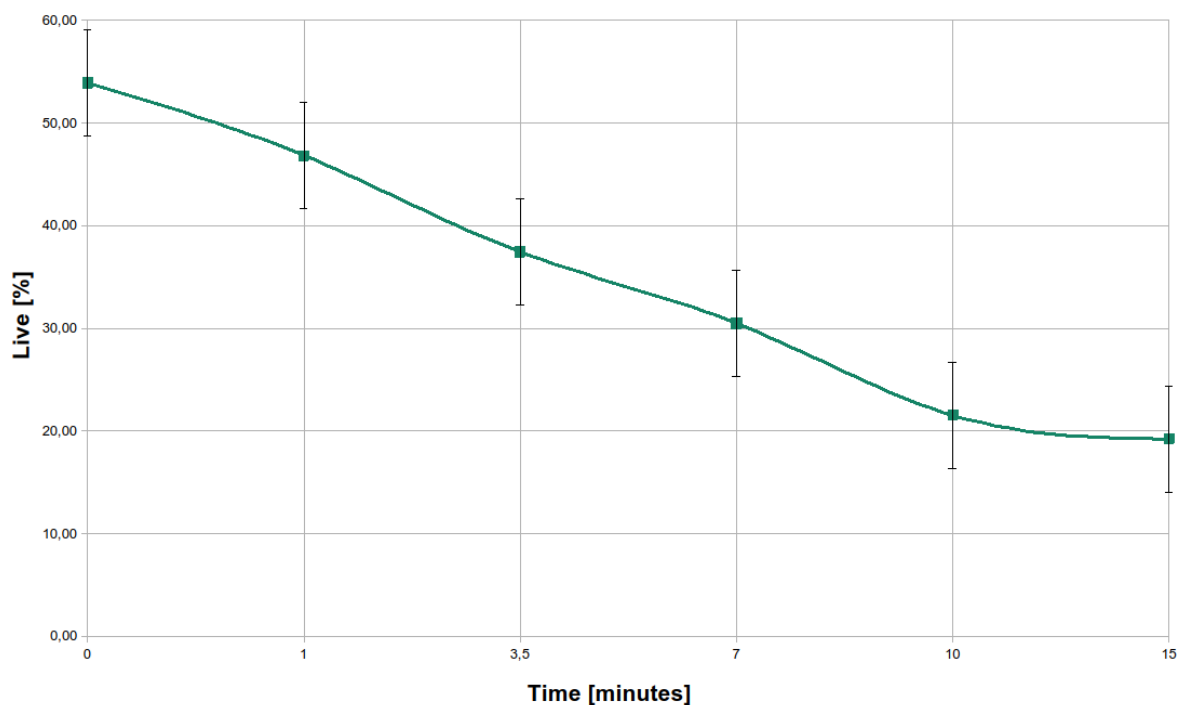
Fig. 5. Bacterial mortality depending on irradiation time
Rys. 5. Śmiertelność bakterii w zależności od czasu napromieniania

The experiment showed that there is a correlation between irradiation time and the viability of the bacteria, however, as can be seen in Table 1, 19% of the bacteria remained alive, so it can be concluded that longer irradiation times would have to be used for such sterilisation to be fully effective. The automated method of assessing bacterial survival provided accurate and reproducible results. These findings are expected to have significant implications for the development of new sterilisation methods and for the use of LEDs in a wide range of applications. More research in this area is needed to explore the potential of UVC irradiation and automated bacterial survival assessment methods in other areas of research and industry.

13.4.2. Algorithm

An algorithm has been successfully created that, on the basis of captured images, distinguishes and quantifies live and dead cells obtained after irradiation. In addition, a relationship has been demonstrated between the time of irradiation and the number of dead cells, which confirms the negative impact of UVC exposure on the bacteria tested. The study has also shown the need to exercise caution and follow safety guidelines when using UVC lamps due to their potentially harmful effects on living organisms. The plug-in was created with the implementation of the algorithm, which will be extended with new possibilities in the future. In addition, we would like to introduce additional functionalities, such as removing elements that are not a point of interest (e.g. inorganic objects that may have been coloured by a fluorescent pigment). We plan to perform additional stages of data processing using standard image processing methods or using neural networks. Once we consider a plugin stable, we will make it publicly available under the "GNU GPL" version 3 licence.

Bibliography

1. K. Song, M. Mohseni, F. Taghipour, Application of ultraviolet light-emitting diodes (UV-LEDs) for water disinfection: A review. Water Research, 94, 341–349. DOI:10.1016/j.watres.2016.03.003.
2. D.-K. Kim, D.-H. Kang, UVC LED Irradiation Effectively Inactivates Aerosolized Viruses, Bacteria, and Fungi in a Chamber-Type Air Disinfection System. Applied and Environmental Microbiology, 84(17). DOI:10.1128/aem.00944-18.
3. L. Eisenlöffel, T. Reutter, M. Horn, S. Schlegel, U. Truyen, S. Speck, Impact of UVC-sustained recirculating air filtration on airborne bacteria and dust in a pig facility. PloS one, 14(11), e0225047.
4. LIVE/DEAD® BacLight Bacterial Viability Kits Product Information 15-July-2004.
5. https://www.ledil.com/product-card/?product=FN17810_VIOLET-12X1-RS.
6. A. Kheyrandish, F. Taghipour, M. Mohseni, UV-LED radiation modeling and its applications in UV dose determination for water treatment, *Journal of Photochemistry and Photobiology A:Chemistry* 352 (2018) 113–121.

AUTOMATIC SYSTEM FOR BACTERIAL CELL VIABILITY ANALYSIS CONFOCAL MICROSCOPY IMAGES

Abstract

Electroluminescent diodes have gained popularity in the research field due to their wide potential, including their small size, which facilitates their application in sterilisation systems. Ultraviolet radiation with a wavelength from 100 to 280 nm (UVC) is characterised by mutagenic effects against microorganisms. In the above project, the effect of UVC radiation on bacteria contained in the nebulized activated sludge solution from the bioreactor. The methodology focuses on a self-constructed chamber system that allows for the isolation of the tested space. A nebulised solution consisting of activated sludge is aerosolised in the chamber, and exposed to UVC electroluminescent diodes for selected times A software was developed to visualise the power density dependence of UVC radiation. The effect of radiation was verified by evaluating the viability of bacteria using the viability kit. An algorithm has been successfully created that, based on captured images, distinguishes and quantifies live and dead cells obtained after irradiation. A relationship between the time of irradiation and the number of dead

cells has been demonstrated, which confirms the negative impact of UVC exposure on the tested bacteria. The results show that UVC radiation negatively affects bacterial cells, and the automatic system for detecting dead cells as well as live cells works properly. The automatic system we have developed fulfils its purpose and can serve as a commercial tool.

Keywords: UVC, ultraviolet radiation, viability, live and dead cells, algorithm, automatic system, irradiation

Krzysztof DOBOSZ[1,*], Aleksandra MUSIAŁ[1]

Chapter 14. PROVIDING ACCESSIBILITY IN THE REHABILITATION MOBILE GAME

14.1. Introduction

The rehabilitation of people with cognitive deficits, due to the ageing population in Europe, is a major challenge. The number of elderly people continues to increase, and one of the consequences is an increase in stroke cases. According to [1], the number of stroke-related hospitalizations in Poland is constantly increasing (2019 – 14241 patients, 2020 – 14536 patients, 2021 – almost 14985 patients). The duration of hospital neurological rehabilitation after brain stroke is between 6 and 16 weeks [2]. After returning home, patients often continue rehabilitation, sometimes individually.

Taking the above into account, there is no doubt that tools are needed to support the effective therapy and rehabilitation of neurological patients. At the same time, let us remember that neurological patients often have motor and often visual deficits in addition to cognitive disabilities. Therefore, it is also important that the tools are developed in such a way as to ensure accessibility for users with different special needs. At the same time, the tools should be common enough so that the person being rehabilitated can also practice on their own wherever they are. Therefore, rehabilitation tools can take the form of mobile applications that can be used on smartphones.

The aim of the study was to analyse how to make a rehabilitation tool in the form of a mobile game accessible to people with cognitive deficits. By analysing the state of art, existing solutions and guidelines, a prototype rehabilitation tool was developed and its accessibility was assessed against other similar applications.

---

[1] Department of Algorithmics and Software, Faculty of Automatic Control, Electronics and Computer Science, Silesian University of Technology, Gliwice, Poland.
* Corresponding author: krzysztof.dobosz@polsl.pl.

14.2. Related work

Personalized medicine is used in the field of treatment of neurological disorders [3]. However, due to the variety of possible deficits resulting from e.g. a brain stroke, we should focus on the individual characteristics of each patient [4]. Therefore, it is important to match the forms of rehabilitation to individual deficits, which can bring more benefits. The positive impact of personalized therapy is also confirmed by clinical trials [5]. Effective therapy of neurological patients can also be achieved using solutions based on virtual reality. Such solutions can help in the rehabilitation of the motor and cognitive functions [6, 7]. However, it should be remembered that rehabilitation exercises can also be realized at home using common devices. This is where smartphones can be very useful. Mobile devices provide a number of solutions that make them better suited for use by people with disabilities than, for example, desktop computers, which often require the provision of specially adapted hardware. In addition, smartphones have a small size and the ability to operate without charging. Therefore, there are great candidates to become a target group of devices to support the development of applications for people with disabilities [8]. Touchscreens have great potential to enhance and speed up navigation on a mobile device due to their ability to recognise various gestures. In addition to existing screen readers or applied commands, further techniques are emerging to improve the use of smartphones by defining a customised set of gestures [9], where each gesture is assigned a function. It is also important to be aware of any options provided by mobile operating systems so that the application under development does not interfere, but works with them.

14.3. Mobile games accessibility

14.3.1. Embedded mechanisms

Mobile devices have many built-in mechanisms that are helpful in daily use by people with disabilities. Every mobile application developer should be aware of the built-in facilitation that mobile devices provide, as some of these eliminate the need to implement some user interaction requirements. In special cases, the developer does not need to include additional code to ensure full accessibility for people with special needs. Smartphones' built-in facilitation mechanisms include [10]:

- Screen reader – gives audible descriptions of the text and images on your screen,
- Font size – allows the user to change a font size of the text on the screen,
- Display – the user can choose to turn on High Contrast Text, Dark Theme, Color Inversion, or Color Correction to make everything more visible.
- Magnification – the user can pinch with two fingers on the screen to adjust the magnification,
- Lookout – relies on computer vision to recognize an object or text, then describes it to the user,
- Voice access – users can provide spoken commands to do everything from opening apps to typing messages to placing a call,
- Voice input – allows users with physical or visual impairments to type text messages, emails, and other notes by saying the words out loud,
- Live transcribe – provides real-time speech-to-text captions in many languages, and many common sounds like applause or laughter, for people who are deaf or hard of hearing,
- Switch access – allows users to navigate their phones with a designated "switch" like a keyboard key or mouse button instead of tapping,
- Sound notifications – alerts users when it hears sounds like fire alarms, doorbells, crying babies, and more.

Developing software for mobile devices, dedicated to the disabled group, requires familiarization with all the functionality that smartphones or tablets offer. Useful features include Speech-To-Text and Text-To-Speech mechanisms, a built-in gyroscope and accelerometer, vibration, volume up and down buttons, and support for multiple touchscreen gestures. In mobile applications, all of these features can be used to prepare an alternative control method.

14.3.2. Game accessibility

The awareness of mobile application developers is growing every year. The number of people with disabilities who speak publicly about their limitations and aspects of their lives that could be made accessible to them with the use of appropriate assistive technologies is also increasing [11]. Thanks to the collaboration of IT teams and people with disabilities, many applications and ways of adapting software to inclusivity have been developed.

There are a few standard and simple rules that can and should be applied to any game or mobile application without much effort. All over the world, associations have been set up to collect information on the limitations that exist and together with a group of people with disabilities, to explore ways of eliminating them. Thanks to the cooperation of many specialists and university representatives, accessibility guidelines for game developers have been prepared [12]. In Poland, the Poznan Gamers Guild Association has been active on this topic for many years and has also made its guidelines available [13]. However, one of the most important issues is simplifying the application interface to the bare minimum [14]. We should also note that sound games are starting to become increasingly popular [15, 16]. They take advantage of auditory acuity in people with other sensory impairments and also allow them to exercise their imagination based on the sounds they hear.

Cognitive disorders refer to problems with, among other things, memory, attention and information processing. Board games are often part of cognitive rehabilitation for patients with neurological problems. Among the widely available materials on the development of accessible mobile applications, you can find separate guidelines addressed directly to developers of mobile games. Paper [17] specifies the field of research for card games. The authors of the article [18] also undertook an analysis of recommendations for board games. There are also wider interpretations and refinements of existing recommendations [19].

14.3.3. Accessibility guidelines

The Memory game, although often using cards, is classified as a board game because of the need to use a flat surface, e.g. a table, to lay out all the guessing pieces. From a set of approximately 120 accessibility guidelines [12], we selected only those that are closely related to mobile board games and are intended for players with cognitive disabilities. These guidelines are collected in three levels: *basic*, *intermediate* and *advanced*. These levels are based on a balance of three elements: reach (number of people who benefit), impact (the difference made to those people), value (cost to implement). The set of *basic* guidelines contains:

- Allow the game to be started without the need to navigate through multiple levels of menus.
- Use an easily readable default font size.
- Use simple clear language.

- Use simple clear text formatting.
- Include interactive tutorials.
- Allow players to progress through text prompts at their own pace.
- Avoid flickering images and repetitive patterns.
- Offer a wide choice of difficulty levels.

Intermediate guidelines are as follows:

- Include contextual in-game help/guidance/tips.
- Indicate/allow a reminder of current objectives or controls during gameplay.
- Include a means of practicing without failure, such as a practice level or sandbox mode.
- Ensure no essential information (especially instructions) is conveyed by text alone, reinforce with visuals and/or speech.
- Give a clear indication that interactive elements are interactive.
- Provide an option to turn off/hide background movement.
- Provide separate volume controls or mutes for effects, speech and background/ music.
- Ensure sound/music choices for each key objects/events are distinct from each other.
- Allow difficulty level to be altered during gameplay, either through settings or adaptive difficulty.

Advanced guidelines include:

- Allow all narrative and instructions to be replayed.
- Provide an option to turn off/hide all non-interactive elements.

The set of analysed guidelines was enlarged, keeping in mind that the deficits that often accompany cognitive disabilities are motor deficits (due to paresis after strokes) and visual deficits (due to the often old age of neurological patients). Due to possible motor deficits, the following *basic* guidelines were selected:

- Ensure controls are as simple as possible, or provide a simpler alternative.
- Ensure interactive elements/virtual controls are large and well spaced, particularly on small or touch screens.
- Include a toggle/slider for any haptics.

Intermediate guidelines:

- Make interactive elements that require accuracy (eg. cursor/touch controlled menu options) stationary.
- Ensure that all key actions can be carried out by digital controls (pad/keys/presses), with more complex input (eg. analogue, speech, gesture) not required.

- Include an option to adjust the game speed.
- Allow interfaces to be resized.

And two *advanced* guidelines:

- Allow play in both portrait and landscape.
- Include a cool-down period (post acceptance delay) of 0.5 second between inputs.

Taking into account accessibility for visually impaired users requires the implementation of additional guidelines. Set of basic guidelines covers:

- Use an easily readable default font size.
- Ensure interactive elements/virtual controls are large and well spaced, particularly on small or touch screens.
- Use simple clear text formatting.
- Provide high contrast between text/UI and background.
- Ensure no essential information is conveyed by a colour alone.

The set of *intermediate* guidelines includes:

- Provide volume controls or mutes for sound.
- Ensure sound/music choices for key objects/events are distinct from each other.
- Allow interface to be resized.
- Provide an option to turn off/hide non-interactive elements.
- Ensure screen reader support for mobile devices.

Advanced guidelines include:

- Provide pre-recorded voiceovers for all text, including menus and installers.
- Ensure that all key actions can be carried out by voice commands.
- Use distinct sound/music design for all objects and events.

Some guidelines are similar, for different categories of deficits. However, during the study we decide not to merge them, because the application of each guideline group will be analysed separately.

14.4. Methodology

Testing the accessibility of a mobile application can be achieved through various methods. An approach proposed by those working on the Android operating system is to identify four ways of verifying applications [20]: manual testing, the use of dedicated tools, automated testing and testing with people with disabilities. Our study focused on

manual testing, using a screen reader mechanism and the Switch Access application. The next step will be to use the Accessibility Scanner tool to test contrast.

According to the guidelines in WCAG 2.2 (Web Content Accessibility Guidelines) [21], the minimum contrast ratio (AA level) is at least: 3.0 for large text, 4.5 for small text. The enhanced contrast ratio (AAA) is a minimum of 4.5 for large text and 7.0 for small text respectively, where the border between small and large text is 24 pixels.

Then we will propose our own *AccessibleMemory* game, in which we will try to implement as many guidelines as possible. We will compare it with other simple board games: those with the highest number of downloads, and those for which the authors have declared accessibility in the description. Each application will be verified to meet the guidelines for mobile board games for people with cognitive, motor and visual deficits, according to the guidelines indicated in the previous chapter.

In an article [22] on inclusive gaming in relation to cognitive disorders, it was proposed that the accessibility index should count as the sum of the guidelines met. However, in order to obtain a normalised accessibility ratio, the sum of implemented guidelines must be divided by the sum of all guidelines. The overall accessibility ratio *AR* will be calculated using a formula that takes into account the weighting of each level of the guidelines:

$$AR = \frac{a_b \sum g_{bi} + a_i \sum g_{ii} + a_a \sum g_{ai}}{a_b \sum g_b + a_i \sum g_i + a_a \sum g_a} \tag{1}$$

where:

g_{bi}– number of implemented guidelines at *basic* level

g_{ii}– number of implemented guidelines at *intermediate* level

g_{ai}– number of implemented guidelines at *advanced* level

g_b– number of all guidelines at *basic* level

g_i– number of all guidelines at *intermediate* level

g_a– number of all guidelines at *advanced* level

a_b– weight of guidelines at *basic* level

a_i– weight of guidelines at *intermediate* level

a_a– weight of guidelines at *advanced* level

We noticed that the *basic* level guidelines had a fundamental impact on the accessibility of the application, hence they were given the greatest weight ($a_b = 4$). They are extended by *intermediate* level guidelines ($a_i = 2$). The guidelines from the *advanced* ($a_a = 1$.) level have the least impact on the overall assessment related to the widest possible accessibility.

14.5. Prototype of the mobile rehabilitation tool

The author's task was to develop a fully accessible Memory mobile game. Note: the rehabilitation game was developed without prior knowledge of the selected guidelines. In this way, it was possible to later identify the elements that caused the most problems for the developers. The tool developed for cognitive rehabilitation is called *AccessibleMemory*. Figure 1 shows the main screen, the choice of difficulty level and the help screen. In addition to the rules of the game, the help screen also provides information on the available ways to move around the board. It also explains the number of cards in each difficulty level. Five levels are available: very easy (2x2 board), easy (2x3 board), medium (2x4 board), difficult (3x4 board) and professional (4x5 board).
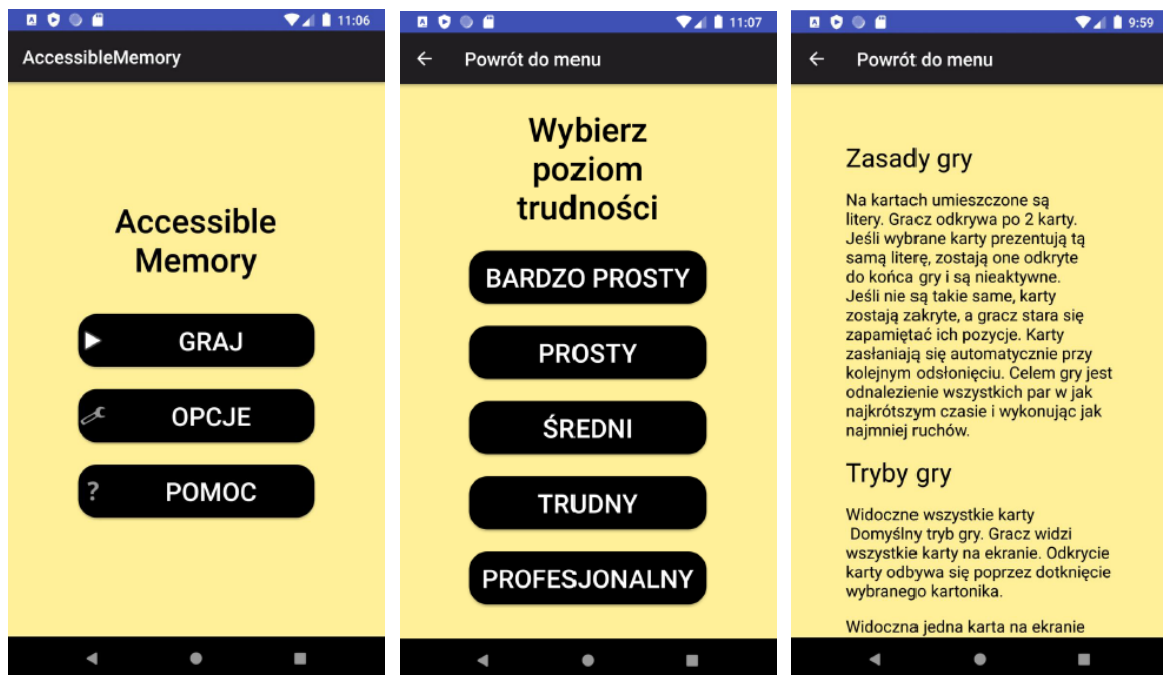
Fig. 1. *AccessibleMemory*: main screen, difficulty level screen, help screen
Rys. 1. *AccessibleMemory*: ekran główny, ekran poziomów trudności, ekran pomocy

Figure 2 shows the options panel and the two modes of presentation of the card board. The options panel (Figure 2) is divided into two sections. The top section refers to general settings. The first option is to enable sounds, while the second allows the user to change the gameplay mode. *AccessibleMemory* uses two modes to present the board. By default, the user sees all the cards on the screen (classical view). In the case of blind users and a system-enabled screen reader, they can explore the board with the cards by moving over them with a pointer, such as a finger. The second mode is related to the

presentation of only one card on the screen. It is dedicated to users with severe visual deficits who do not wish to use the support of the system screen reader. When the single card view is selected, additional settings become available. The first is to enable vibration when the user wants to move beyond the edge of the board. The second allows the user to change the control from swiping to changing the position of the smartphone.
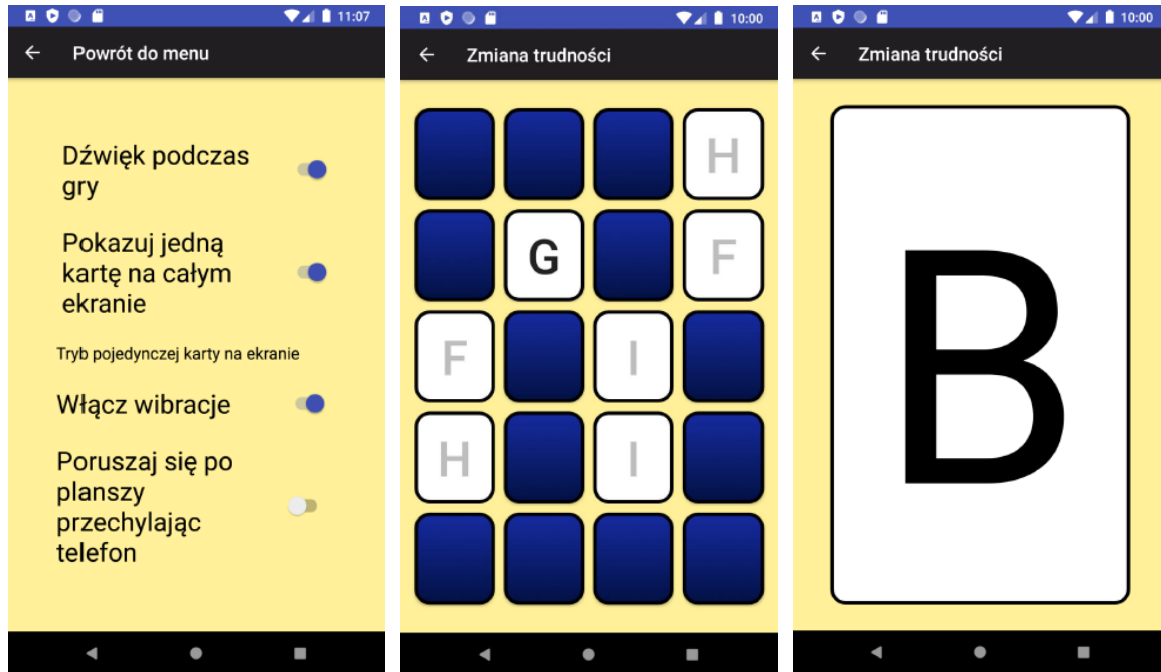
Fig. 2. *AccessibleMemory*: option screen, classical view, single card view
Rys. 2. *AccessibleMemory*: ekran opcji, widok klasyczny, widok pojedynczej karty

14.6. Results and discussion

After the prototype was developed, it proceeded to evaluate it against other simple board games. For the research purposes of this work, three games from the Google Play store with the largest number of downloads and with the highest ratings were selected:

- *Checkers Online* (100M+ downloads, rating 4.5)[1].
- *Backgammon* (10M+ downloads, rating 4.4)[2].
- *Mills* (1M+ downloads, rating 4.8)[3].

---

[1] https://play.google.com/store/apps/details?id=pl.lukok.draughts
[2] https://play.google.com/store/apps/details?id=uk.co.aifactory.backgammonfree
[3] https://play.google.com/store/apps/details?id=com.donkeycat.mill

The authors of these games have not declared accessibility. The selected set was extended with three accessible mobile applications. However, this time, there was little choice among the board games with declared accessibility. Selected applications include:

- *Accessible Memory* (100+ downloads, rating 4.3) – the application allows two forms of gameplay: traditional (i.e. using a touch screen) or accessible – with an external switch (Switch Access option)[4]; in our assessment we will call it Memory I.
- *Accessible Memory Trial* (1K+ downloads, rating 3.8) – description contains the information that applications is fully accessible for Talkback users; all provided functions of the game are accessible for blind and visually impaired users[5]; in our assessment we will call it Memory II.
- *Chessback* (10K+ downloads, rating 4.0) – blind and partially sighted chess players have been identified as a target group.[6]

It should be noted that no information about accessibility for users with cognitive deficits was found in the description of any application. The study included six selected applications and a proposed prototype solution. It was verified that each of the guidelines selected for mobile board games was implemented. Then the accessibility ratio was calculated according to equation (1). A comparison of the results (AR value) obtained for each of the applications assessed and the set of guidelines is shown in Figure 3.
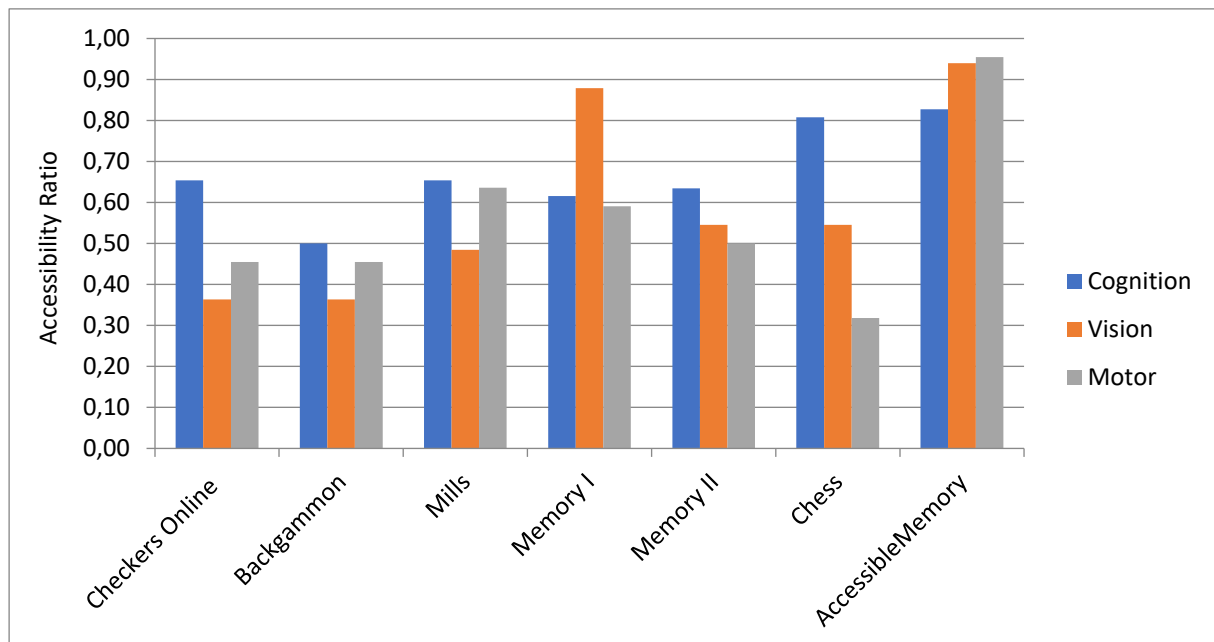
Fig. 3. Comparison of calculated Accessibility Ratio (AR) values
Rys. 3. Porównanie obliczonych wartości Współczynnika Dostępności (AR)

---

[4] https://play.google.com/store/apps/details?id=com.mouse4all.memory
[5] https://play.google.com/store/apps/details?id=hu.gersoft.accessiblememory
[6] https://play.google.com/store/apps/details?id=vnspeak.android.chess

The results for the number of implemented guidelines in games without an accessibility declaration (*Checkers Online, Backgammon, Mills*) were surprisingly positive. As expected, none of the advanced level recommendations were included, while every game contained at least one intermediate suggestion implemented. However, it should be noted that, despite a relatively high AF value of 0.5 to 0.65, none of them use an easily readable default font size, iterative tutorials, reminders or practicing without failure, which for users rehabilitating cognitive function is a major shortcoming. The degree of implementation of the other requirements (guidelines for visual and motor disabilities) for these applications also oscillates around a value of 0.5.

When analysing the applications declaring accessibility (*Memory I, Memory II, ChechBack*), it was found that they implement some of the recommendations from the advanced level. It is noticeable that the implementation of the guidelines for cognitive deficits in the case of Chess and the guidelines for visual deficits in the case of Memory I is correct. However, this does not change the fact that, despite a little better performance, the results are not satisfactory. Applications claiming accessibility still have deficiencies in the implementation of the guidelines, even at a basic level.

The *AccessibleMemory* rehabilitation game developed best implements recommendations for visual and motor impairments (value around 0.95). Some advanced level guidelines were omitted, but all recommendations of the basic and intermediate levels were implemented. However, for cognitive guidelines the AF value is only 0.83. Unfortunately, of the cognitive guidelines, four were not included: interactive tutorials, contextual in-game help/tips, practice level, repetitive instructions.

14.7. Conclusions

Although the topic of accessibility in mobile games and applications is not unknown, however, there are still many software developers who overlook the needs of people with disabilities. However, accessibility is very important, especially for people with disabilities who want to use them for rehabilitation purposes. Hence, there is a need to prepare sets of accessibility guidelines for mobile applications with a well-defined purpose. Note that even the developer's awareness of the need for accessibility did not allow all the guidelines selected to be included. Attempts to ensure general accessibility may not be sufficient when we need, for example, a specific rehabilitation tool to exercise cognitive functions for neurological patients. Moreover, even for cognitive

rehabilitation, a set of guidelines will be a little different for short-term memory exercises, another for attention or language fluency exercises. We therefore conclude that there is a need to define sets of accessibility guidelines for a certain group of mobile app applications and then disseminate them. Then evaluating the apps, using the proposed accessibility factor, will lead to an effective selection for specific rehabilitation exercises. Finally, we indicated a general need to prepare sets of accessibility guidelines for mobile applications with a well-defined goal, e.g. games for cognitive rehabilitation.

Bibliography

1. E-zdrowie. Liczba hospitalizacji związanych z udarem mózgu. https://ezdrowie. gov.pl/9157, [accessed: 10 April, 2023].

2. Narodowy Fundusz Zdrowia. Rehabilitacja lecznicza. https://www.nfz.gov.pl/dla-pacjenta/informacje-o-swiadczeniach/informacje-o-pozostalych-swiadczeniach/ [accessed: 10 April, 2023].

3. M. Semprini, M. Laffranchi, V. Sanguineti, L. Avanzino, R. De Icco, L. De Michieli, M. Chiappalone, Technological Approaches for Neurorehabilitation: From Robotic Devices to Brain Stimulation and Beyond, *Frontiers in Neurology* (2018) **9**:212.

4. J. Zielińska, Sprofilowana i spersonalizowana terapia pobudzana (sterowana) danymi, *Niepełnosprawność – zagadnienia, problemy, rozwiązania* (2017) **23**:132–148.

5. A. Stasieńko, I. Sarzyńska-Długosz, Zastosowanie rzeczywistości wirtualnej w rehabilitacji neurologicznej, *Postępy Rehabilitacji* (2016) **4**:67–75.

6. RehaCom, https://www.treningmozgu.pl/doc/metody/katalog_rehacom.pdf, [accessed: 20 April, 2023].

7. CogniPlus, https://cognific.pl/produkt/cogniplus/, [accessed: 20 April, 2023].

8. K. Dobosz, Designing mobile applications for visually impaired people. *Visually Impaired: Assistive Technologies, Challenges and Coping Strategies* (2016) 103–126.

9. S. Kane, J. Bigham, J.O Wobbrock. Slide rule: making mobile touch screens accessible to blind people using multi-touch interaction techniques. *Proceedings of the 10th international ACM SIGACCESS conference on Computers and accessibility* (2008) 73–80.

10. B. Nelson, 25 Smartphone Accessibility Settings You Need to Know About, https://www.rd.com/article/accessibility-settings, [accessed: 20 April, 2023].

11. B. Yuan, E. Folmer, F. Harris. Game accessibility: a survey. *Universal Access in the information Society* (2011) **10(1)**:81–100.

12. Game accessibility guidelines. http://gameaccessibilityguidelines.com, [accessed: 10 April, 2023].

13. Dostępność gier wskazówki dla twórców gier. https://gildiagraczy.pl/wp-content/uploads/2019/04/Dostepnosc-gier-wskazowki-dla-tworcow-gier.pdf, [accessed: 10 April, 2023].

14. K. Dobosz, J. Ptak. How to control a mobile game. *15ᵗʰ International Conference on Computers Helping People with Special Needs, Proceedings Part I* (2016) 523–529.

15. O.T. Borges, M. de Borba Campos. "I'm blind, can i play?" recommendations for the development of audiogames. *International Conference on Universal Access in Human-Computer Interaction, Springer* (2017) 351–365.

16. G. Johnson, S. Kane. Game changer: Accessible audio and tactile guidance for board and card games. *Proceedings of the 17th International Web for All Conference*, New York, NY, USA (2020) 1–12.

17. K. Dobosz, A. Adamczyk. Accessibility of mobile card games. *17ᵗʰ International Conference on Computers Helping People with Special Needs, Proceedings, Part I* (2020) 217–224.

18. M. Heron, P. Belford, H. Reid, M. Crabb. Eighteen months of meeple like us: An exploration into the state of board game accessibility. *The Computer Games Journal* (2018) **7(2)**:75–95.

19. G. Mahardhika, A. Kurniawardhani, D. Yolhanda. Mobile games interaction design for people with visual impairment using participatory design approach. *IOP Conference Series: Materials Science and Engineering* (2019) 482:12–39.

20. Test your app's accessibility. https://developer.android.com/guide/topics/ui/accessibility/testing, [accessed: 10 March 2023].

21. Web Content Accessibility Guidelines (WCAG) 2.2, https://www.w3.org/TR/WCAG22/#contrast-minimum, [accessed: 10 March 2023].

22. A. Jaramillo-Alcázar, S. Luján-Mora, L. Salvador-Ullauri. Inclusive education: Mobile serious games for people with cognitive disabilities. *Enfoque UTE* (2018) **9(1)**:53–66.

PROVIDING ACCESSIBILITY IN THE REHABILITATION MOBILE GAME

Abstract

In the article, we presented how to ensure accessibility for the mobile rehabilitation application. First, we demonstrated the need to develop mobile applications that can act as rehabilitation tools for neurological patients. We then listed a number of accessibility mechanisms provided by modern mobile operating systems. As a next step, we looked at accessibility in mobile games and proposed three sets of guidelines for accessibility for people with cognitive, motor and visual disabilities. Then we proposed our own rehabilitation application and compared its accessibility with similar applications with the highest number of downloads and three more for which the authors declared availability. For the assessment, we recommend a new method of calculating the accessibility ratio.

Keywords: cognitive impairment, rehabilitation, accessibility, mobile application, card game

Ewa LACH[1,*], Iwona CHUCHNOWSKA[2], Adam BEDNORZ[3,4], Iwona BENEK[4,5], Adam KRUCZKOWSKI[1], Maria FILIPEK[2], Bartłomiej SZEWCZYK[2], Agnieszka BONCZEK[5]

Chapter 15. SERIOUS GAME FOR PERSONALISED REHABILITATION OF THE COGNITIVE FUNCTIONS OF THE ELDERLY

15.1. Introduction

Current demographic forecasts predict an increase in life expectancy and a significant increase in the elderly population which will result in an increase in health problems in society [1]. To address the challenges of an ageing population, research and policy planning worldwide are focused on ensuring a better quality of life for older people and reducing the burden on the traditional healthcare systems. This has started a trend in healthcare to go from curative to preventive care. More emphasis has been placed on preventing or delaying the onset or progression of diseases by promoting a healthy lifestyle [2–4] and seniors' monitoring [5–8]. Cognitive functions are a set of processes thanks to which we receive information from the environment and notice the relations between them. Cognitive decline with age is inevitable, but the extent to which it occurs and the rate at which it occurs varies from person to person [14]. In general, however, the symptoms of age-related cognitive decline (ARCD) include: decreased psychomotor speed, memory and learning disorders, visual-spatial disorders, diminished spatial orientation, language disorders, executive function disorders, slower inductive reasoning, and slower problem-solving. The development of effective interventions that could maintain levels of cognitive functioning and delay cognitive and

[1] Faculty of Automatic Control, Electronics and Computer Science, Silesian University of Technology, Silesian Gliwice, Poland.
[2] Faculty of Biomedical Engineering, Silesian University of Technology, Silesian Gliwice, Poland.
[3] Szpital Geriatryczny im. Jana Pawła II, Katowice, Poland.
[4] Institute of Psychology, Humanitas Academy, Sosnowiec, Poland
[5] Faculty of Architecture, Silesian University of Technology, Gliwice, Poland.
[*] Corresponding author: ewa.lach@polsl.pl.

functional decline is critical in the field of public health. In recent years, interest in cognitive remediation techniques in the elderly has increased. Cognitive treatment to enhance cognitive functions is studied in the elderly with ARCD, mild cognitive impairment (MCI), early stages dementia (Alzheimer's disease (AD) and vascular dementia (VaD)), brain damage or disease (stroke, brain tumours, traumatic brain injury, etc.) [9, 10, 13]. There are cognitive function assessment tools for classifying various types of cognitive impairments (e.g. the Mini-Mental Status Exam (MMSE) [11]). Usually, however, they require professional medical personnel to perform the tests and a long testing time. With the accelerating development of technologies, many smart devices are used to evaluate and enhance the fitness of the elderly. In recent years, it has been common to use serious games (SG) characteristics to design cognitive function training games. SG does not take entertainment as the primary goal but is used to achieve learning purposes. Research showed that SG training could improve the players' cognition, coordination, behavioural, and psychological symptoms [10]. Computer-based tools can also be used as one of the primary screening tools for the cognitive function of the elderly [11–13]. There are also studies concerning the relationship between fitness and cognition. The research results suggest that fitness training can enhance cognition [14]. Also, reduced balance ability due to ageing has been reported to be associated with cognitive functions and slowing central information processing speed [15].

The aim of this work is to evaluate the SG supporting the process of rehabilitation of cognitive functions of the elderly while activating them to move by introducing motion control of the application. The presented tool uses automatic adjustment of game levels to personalise the difficulty of tasks performed by players. The authors present preliminary tests carried out with the participation of seniors aged 70–79.

15.2. Serious game "Catch me!"

15.2.1. Aim of the game

The created serious game supports the rehabilitation of the cognitive functions of a broad group of elderly with cognitive impairment. Additionally, the game activates older people to move by using a motion control of application (upper limbs movement). By playing, the elderly can maintain (or even improve) their cognitive and physical

functioning levels and delay psychophysical decline. The proposed game can help the elderly with ARCD, MCI, early stages dementia, brain damage or disease. The requirements for the player are the ability to manoeuvre the upper limbs, the basic ability to process visual data and the basic ability to analyse information. The authors did not impose a position on the user during the game. Standing is recommended but not required to add to the physical intensity of the game. Users are allowed to sit while playing.

15.2.2. Game description

During the game, players are supposed to recognise collectable/non-collectable objects appearing on the game scene and select collectable while ignoring non-collectable (Fig. 1a). Selecting an object consists of keeping your hand on the object for a specific time. The game uses the Azure Kinect 3D's depth camera to recognise the player's motion for game control and seniors' behaviour monitoring.

The game scene has a console with six holes, from which three-dimensional objects slide out in random order. At the moment, 38 objects belonging to 4 categories have been prepared: sports, food, dishes, and electronics. At the beginning of the game, the category of objects is randomly selected, and the player is informed what kind of objects to collect. Items belonging to a given category are set as collectable, belonging to the other three categories – non-collectable. Additionally, one more game level, "Very Easy", has been added, where the player selects the green cuboids and skips the red cuboids. This level was added for people who have problems with recognising categories.
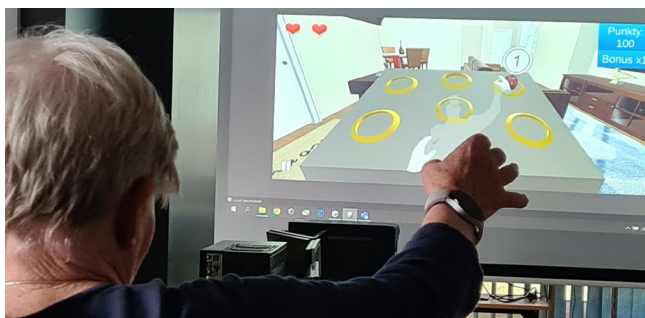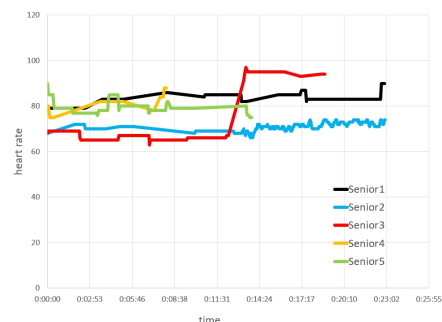
(a)   (b)

Fig. 1. Testing of the game "Catch me!" (a) and seniors' heart rate during gameplay (b)
Rys. 1. Testowanie gry „Złap mnie!" (a) i tętno seniorów odnotowane w trakcie rozgrywki

For each correct choice, the player receives points multiplied by the bonus value for a series of correct selections. If the player does not get a newly appearing collectable object, the bonus value is reset to 1. When the player selects another correct object, the bonus value is increased by 1 (at most to 5). For example, after collecting all four collectable objects that appeared in succession, the bonus value is 4. If the player chooses a non-collectable object, they lose one heart. At the beginning of the game, the player gets three hearts. The player also loses one heart if they fail to select ten correct objects in a row. The game ends when a player loses all three hearts or when the assigned time limit (10 minutes) is reached. Information about the time remaining to the end of the game appears for the last 60 seconds. Thanks to this, the user cannot feel time pressure for most of the test and can focus on the task.

The player starts the game on one of five difficulty levels of their choice: "Very Easy", "Easy", "Medium", "Hard", and "Very Hard". In the first level, there are only two types of objects: green cuboids – collectable, and red cuboids – non-collectable. Three-dimensional objects from the four presented categories appear on the next levels. The levels differ in: the number of collectable and non-collectable objects, the frequency of appearance of collectable and non-collectable objects, the interval between the appearance of successive objects, the time the objects stay on the scene to be selected, the time needed to select an object (holding your hand over the object). As the game progresses, the difficulty level is automatically lowered when the player loses a heart. Once a certain number of points are earned, the player is upgraded to a higher difficulty level.

15.2.3. Technology and tools

Microsoft's Azure Kinect 3D device is applied for tracking and capturing movements with a 3D vision sensor and artificial intelligence algorithms. The device maps depth using structured light, performing real-time calculations. Azure Kinect SDK is a set of development tools that enable image processing, detection of the position and movement of the user's skeleton and body, and speech recognition. The following SDKs of the Azure Kinect DK development environment were used in the project:

- Sensor SDK for low-level sensor and device access.
- Body Tracking SDK for tracking bodies in 3D – providing body segmentation and access to an anatomically correct skeleton for any part or entire body within the

camera's field of view. In the game, the position and rotation of each user's joint in relation to the device are obtained, as well as information, in the form of an image on pixels assigned to a detected body.

The following project tasks are accomplished with the captured data:

- Motion control of virtual 3D objects simulating the body segments of the character. The joints of the character's skeleton (e.g. right or left hand) are assigned to three-dimensional objects in the virtual scene. As a result, the object representing the joint on the screen moves in a manner similar to the selected segment of the user's body. To properly control a given virtual object, it is assigned boundaries that limit the movement of the 3D object. These limits are mapped to the minimum and maximum deviation of the base joint from the control joint defined for each simulated segment (e.g., right hand base joint can be right shoulder, steering joint – right wrist). Controlling a virtual body segment boils down to detecting collisions of this object with other 3D objects of the virtual scene and responding to collision events.

- Measuring the distance of the player from the device.
  Four possible outcomes are defined: too close, too far, perfect, and undetected. The distance is measured from the position of the character's pelvis to the camera.

- Monitoring and recording the motion of players during the game.
  When checking the collision of simulated body segments with objects in the virtual scene, information about each joint (its name, position and rotation relative to the device's camera) is recorded.

Unity game engine was used as the development environment. It allows the creation of interactive 2D and 3D games and other interactive experiences such as virtual reality (VR) and augmented reality (AR) applications. Unity provides a comprehensive set of tools and features that facilitate the entire game development process. The C# language enables developers to write custom code to implement game mechanics, behaviour, and interactions.

15.2.4. Rehabilitation tool for the elderly.

As part of the project, the requirements and limitations of the elderly, as the target recipient of the project, were identified. The limitations of seniors have been divided into physical, cognitive and social. The following physical and cognitive limitations (L) have been addressed in the design of the game (G):

- L: Auditory limitations including impaired hearing, the occurrence of tinnitus, and the occurrence of speech understanding disorders in noise.

  G: Sound effects have been abandoned in the game, assuming that players will have the basic ability to process visual data, and sound information can be distracting and disorientating.

- L: Greater fatigue, an impaired adaptation of the circulatory system to the increased effort as well as disorders of the balance apparatus and occurrence of dizziness.

  G: Standing is recommended but not required to increase the physical intensity of the game. Users can sit while playing.

- L: Motion limitations including reduced overall mobility, reduced range of motion, reduced level of orientation in determining the position of individual parts of the body, and weaker eye-hand coordination.

  G: The game encourages the movement of the upper limbs, testing the range of motion by selecting objects in various areas of the console and practising eye-hand coordination by mapping the player's hand movement on the screen.

- L: After a stroke the hemispatial neglect syndrome may occur, belonging to the category of neuropsychological disorders of attention, manifested by the failure to notice objects on one side of the patient's body.

  G: The game allows detection of the disorder by observing the player's reaction to objects appearing on one side only.

- L: Cognitive limitations including decreased psychomotor speed, memory and learning disorders, visual-spatial disorders, diminished spatial orientation, language disorders, executive function disorders, slower inductive reasoning, and slower problem-solving.

  G: Operation of the game includes: slower, subdued game mechanics, a limited number of stimuli, and the amount of information provided by the game and only the necessary functionalities.

Following cognitive impairments have been identified as those that can be remedied in the proposed game:

- a short-term episodic memory disorder,
- learning disorder,
- executive functions disorder,
- attention and concentration disorder.

It is accomplished by remembering by the player the category of objects to collect, distinguishing objects, reacting appropriately to the appearance of the "correct" objects

and ignoring the "wrong" ones. Moving the limbs to select an object requires the player to analyse information, decide on further actions and perform a specific activity. All this must be done within a limited time.

It is important to remember that older people are not a homogeneous group but are characterised by diverse skills, needs and limitations. Because of that, it is necessary to personalise the game's difficulty. Five game levels are defined in the game, requiring different cognitive abilities. In addition, as the difficulty level increases, the time needed for the player's reaction decreases, which is associated with greater physical demands. At the beginning of the game, the player determines his skill level by selecting the corresponding game level. However, the player may not know his level or make a mistake when choosing. In this situation, the level increases or decreases based on the player's performance. In addition, it is possible to make small changes to the game's difficulty level by fine-tuning parameters within a given level (e.g. increasing the number of collectable objects) without changing the level while observing the ongoing results of the players.

In order to be able to tune the game to the player, provide the player with a game summary and analyse the results obtained to evaluate the player or group of players, it is necessary to implement an appropriate monitoring system within the game. During the game, players' behaviour and results are monitored and saved in external files. For our project, the following data was selected for recording:

- Motion data.

  During the game, when checking for collisions of simulated body segments with objects in a virtual scene, information about each joint is recorded (its name, position and rotation relative to the device's camera).

- Gameplay data.

  During the game, information about the selected objects is recorded: the name and category of the object, whether it was collectable or not, from which hole in the console it slid out, and how many points the player got for it. Information about the player's difficulty level, level change, bonus reset and heart loss is also recorded. During the recorded events, information about the current number of hearts and the number of points scored by the player is also saved. For each recorded event, the time of the event is logged.

The recorded data allows the analysis of the quality of the game parameters and the physical and intellectual condition of the players. Collecting the above data for each player in subsequent periods allows the diagnosis of deterioration or improvement in the players' health. Based on the saved data, it is possible to reconstruct the player's

movements and their analysis (e.g. range of mobility of selected joints). We can determine the speed at which the players analyse information and their reaction time. We can assess the state of the player's cognitive functions.

15.3. Game evaluation

15.3.1. Game design process

The development of the game was an iterative, user-centred process carried out by an interdisciplinary team of supervisors and students of the Faculty of Automatic Control, Electronics and Computer Science, the Faculty of Biomedical Engineering, and the Faculty of Architecture of the Silesian University of Technology, supported by external medical experts from Geriatric Hospital in Katowice and volunteer seniors. The project was carried out in three phases. The objective of the first phase was to develop a prototype solution based on consultations with seniors, medical personnel and literature studies. During the second phase, the solution was iteratively tested with project participants (aged 19–20) to identify universal problems limiting the quality of the game and issues with player behaviour monitoring. Consultations with seniors and medical personnel were also conducted. Both expert knowledge and lessons learned from testing were used to refine the solution. In the third phase, the game was tested by seniors. The prototype game was developed as the result of the project "PBL as part of the program Excellence Initiative – Research University" titled "The use of artificial intelligence sensors in the rehabilitation of the cognitive functions of the elderly". The prototype was then tested and refined as part of the project "PBL as part of the program Excellence Initiative – Research University" titled "Testing the possibilities, limitations and preferences of seniors when using modern IT tools".

(a) (b)
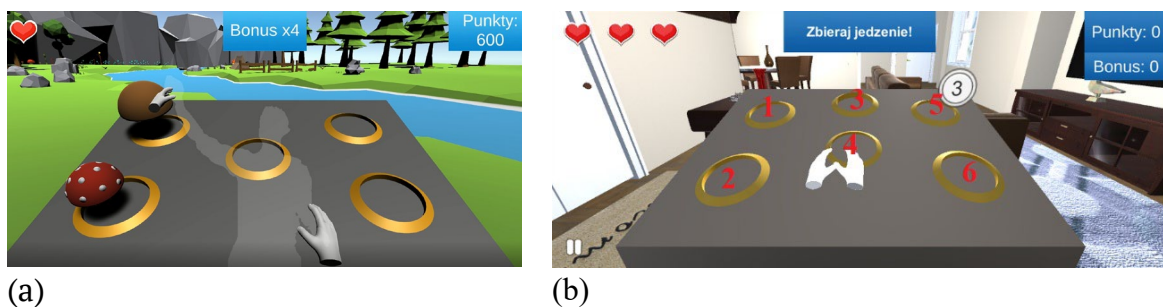
Fig. 2. A screen of prototype game (a) and game after changes with numbered console holes (b)
Rys. 2. Ekran prototypu gry (a) i gry po zmianach z ponumerowanymi otworami konsoli (b)

The first phase resulted in the development of a prototype game [13]. During phase two of the design process following problems (P) were identified and addressed (A):

- P: The camera motion in the main menu is disorienting (too fast) and distracting.
  A: Camera motion in the main menu has been significantly slowed down, and the background has been simplified to provide less distraction from option buttons.
- P: In the game prototype, the scene background and collectable objects could cause additional confusion for the urban elderly due to it being a foreign environment: a rocky forest area with forest objects (Fig. 2a).
  A: In response, the background was changed to an apartment and items from the life of seniors (e.g. dishes) or commonly recognisable items (e.g. laptop, boxing glove) were chosen for selection (Fig. 2b).
- P: Determining the difficulty of a level based on the category of selected objects is problematic because it depends on the player's knowledge and experience.
  A: The category of objects is determined randomly at the beginning of each game, providing variety without imposing level difficulty.
- P: Lack of a reaction to not selecting a large number of collectable objects.
  A: The player loses one heart if he fails to select eight correct objects in a row.
- P: Difficulty levels do not take players' response time into account.
  A: The levels differ in the interval between the appearance of successive objects, the time the objects stay on the scene to be selected, and the time needed to select an object.
- P: The number of non-collectable objects is constant for all difficulty levels.
  A: The levels differ in the number and frequency of appearance of non-collectable objects.
- P: The collision boxes defining the selection areas of the selected objects are too small – they do not cover the whole objects.
  A: The collision boxes cover the whole objects.
- P: The lack of a time limit for a single game makes it difficult to compare games (e.g. whether the game was finished due to physical fatigue or boredom).
  A: A time limit (10 minutes) has been set for a single game.
- P: Gameplay data is saved after the game ends, which summarises the game but does not allow monitoring of the player's behaviour during the game.
  A: Player and game events are recorded during the game.
- P: There is no adjustment to the player's skill once the game level is selected.
  A: The difficulty level is automatically decreased or increased depending on the player's performance.

The second phase resulted in refining the game, which volunteer seniors then tested in the third phase. The results were compared with the results of tests carried out by young people (aged 19–20) and young people in a suit simulating old age.

15.3.2. Game testing process

The project's third phase included the process of initial testing of the game with the participation of volunteer seniors. During the tests, additional tools were used to evaluate the game:

- Surveying.
  The survey concerns the feelings of seniors after participating in the testing process. It asks about the overall impression of the game and the degree of its transparency (distinguishability of objects, level of complexity of the rules). In addition, it also tries to determine the degree of usefulness of the created application in the rehabilitation process.
- Smartwatch Samsung Galaxy Watch 4.
  Information on the senior's heart rate can significantly expand our knowledge of the senior's physical condition during the gameplay. The heartbeat becomes faster when people are active, excited, or scared and drops when they are resting, calm, or comfortable. Furthermore, heart rate depends on a person's age and overall health. Therefore, a "normal" heart rate varies from person to person, but for most healthy adult women and men, resting heart rates (when they are at rest and their heart is pumping the lowest amount of blood to supply the oxygen their body needs) range from 60 to 100 BPM (beats per minute). The rate at which the heart beats when it is working its hardest is a maximum heart rate and can be roughly calculated from a person's age (that is, 220-age).
  Smartwatches and fitness bands measure heart rate by scanning blood flow near a wrist with green LED lights paired with light-sensitive photodiodes that illuminate the skin and measure changes in light absorption. Smartwatches are less accurate than professional medical equipment. However, they can be close and let an individual monitor their heart rate while walking, running, cycling, or exercising.
- Suit simulating old age.
  The age-simulating suit was used to compare the performance of seniors with young people (students) wearing it. The suit is designed to simulate the physical limitations of the elderly. It consists of a set of weights and restraint straps placed on the chest, neck, elbows, wrists, knees, and feet, respectively. In order to fully exploit the

potential of the suit, the students climbed the stairs several times after putting it on, which caused them to feel tired, thus increasing the effect simulated by the costume.

The testing process involved five seniors (3 women, 2 men) aged 70 – 79 in good physical and mental health and two students (woman, man) aged 19 – 20 wearing a suit simulating old age and without a suit. All participants except one (senior1) were right-handed. All tests were held standing, 3–5 meters from the Azure Kinect camera. Each game started with a "Medium" level, which progressively changed depending on the player's skills. The seniors and students were informed about the tools used in the study and its purpose. After all information was provided, the seniors and students agreed to participate in the study.

15.3.3. Results

Table 1 presents a comparison of the results of seniors (s), students (st), and students wearing age suit (sts). The following average values for a single game were compared: the number of hearts lost (ht), the number of collected objects (no), the hole with the most frequently selected objects (hb), the hole with the least frequently selected objects (hw), game time in seconds (gt), average heart rate (hr), absolute rise in heart rate (hri).

Table 1

Game testing results

	s1	s2	s3	s4	s5	st1	st2	sts1	sts2
ht	3.0	2.7	3.0	3.0	2.0	0.0	0.0	2.0	1.0
no	18.0	54.0	13.5	21.0	34.5	68.0	68.0	62.5	60.5
hb	2	6	4	6	4	3	4	6	2
hw	6	1	5	1	2	2	1	3	3
gt	269.0	403.0	210.0	353.0	452	576.0	577.0	591.0	582.0
hr	84.0	70.8	74.7	80.9	79.5	117.0	108.0	115.0	141.0
hri	12.0	6.0	35.0	10.0	15.0	5.0	2.0	6.0	3.0

Elderly people are more likely to lose hearts than young people. According to the observations made during the measurements, most hearts were lost due to not collecting "good" objects. Losing hearts by collecting "bad" objects was very rare. During most games, seniors lost three hearts, which resulted in a premature end to the game. It was noticed that young people, after wearing a suit simulating old age, showed a greater tendency to lose hearts. During the game, a change in the difficulty level for players could be observed. Seniors moved primarily to the "Easy" level and students to the "Hard" level.

The console hole that was selected the least often was located at the top, on the left side of the console, while the most often, the respondents chose holes numbered 4 and 6 (Fig. 2b). The exception was senior1 (left-handed), who preferred hole numbered 2, and least often selected objects from hole number 6.

Figure 1a presents values of the heart rate of seniors during the gameplay. Playing the game in each case resulted in an increase in the measured heart rate, wherein in most cases, this increase in seniors was higher than in students. Surveys at the end of the tests indicate that seniors did not perceive the gameplay as "tiring". As the main problems during the game, seniors indicated keeping their hands steady over the object for the recommended time (to select it) and difficulty coordinating hand movement with their virtual counterparts. Students did not report problems with keeping their hands in one position or with the coordination of virtual hands. However, after wearing a suit simulating old age, they indicated increased difficulty in the above activities. The difficulty level of the presented game was described as easy by 40% and moderate by the rest of the surveyed seniors.

When asked about possible improvements to the game, seniors indicated, in particular, the change of virtual hands to more precisely synchronise the position of the selected object and the hand.

All the surveyed seniors stated that if they had the opportunity, they would use a form of rehabilitation using modern technologies. Each of them would also recommend this type of rehabilitation to their friends.

15.3.4. Discussion

When analysing the obtained results, one should be aware of the limitations resulting from the small group of participants and that the participants represent seniors with mild ARCD. Further testing is needed, especially among people with more apparent cognitive disorders, to assess the cognitive aspect of the game in more precision. The current results are primarily about the game's physical demands (this is evident by the fact that seniors could easily recognise "good" objects). Conducted tests still allow for an initial evaluation of the game from the point of view of older people.

Seniors have a higher tendency to end the game by losing hearts than by the time allotted. The fact that the students could compensate for its effect after wearing the suit simulating old age, and as a result – persevere until the end of the game indicates the deterioration of hand-eye coordination and the ability to adapt it with age. In addition,

it may indicate that the players' results are influenced by non-physical aspects, such as attention and concentration, and the speed of analysing information, which are not affected by the suit. Seniors' difficulty levels indicate the need to lower the game difficulty for all programmed levels to allow older people to move between more difficulty levels, not just the easiest.

The preference for collecting objects appearing in the lower holes may prove the deterioration of motor skills and the difficulty in keeping the arms raised stably, which could be slightly noticed during the tests of students in the age suit.

The elderly did not perceive the game as "tiring", and at the same time, their physiological parameters recorded during the game suggested increased physical activity (increased heart rate). The game engaged seniors to an appropriate degree in terms of motion, forcing users to exercise. At the same time, the elements of gamification meant that it was not perceived as "intrusive" but motivating and even entertaining.

15.4. Conclusion

In this paper, we presented a serious game for elderly people supporting cognitive rehabilitation, using motion control of cognitive tasks to motivate older people to move. The game was initially evaluated by seniors aged 70–79. The results of the tests indicate that the game allows to determine the psychophysical skills of the elderly by activating them to perform cognitive and physical tasks. Monitoring players' behaviour and results makes it possible to personalise tasks to players' skills. The conducted research showed, however, the need for less effort in the physical aspect of the game, particularly reducing the time needed to select objects. It is also necessary to conduct additional research with seniors showing more signs of cognitive disorder to refine the cognitive tasks of the game.

Bibliography

1. United Nations Department of Economic and Social Affairs, World Population Prospects 2019, *Highlights. Multimedia Library* (2019). Available online: https://population.un.org/wpp/Publications/Files/WPP2019/Highlights.pdf.

2. Y. Netz, M.-J. Wu, B.J. Becker, G. Tenenbaum, Physical Activity and Psychological Well-Being in Advanced Age: A Meta-Analysis of Intervention Studies, *Psychol. Aging* (2005) **20**: 272–284.

3. T.D. Robbins, S.N. Lim Choi Keung, T.N. Arvanitis, E-health for active ageing; A systematic review, *Maturitas* (2018) **114**: 34–40.

4. M. Cabrita, H. op den Akker, M. Tabak, H.J. Hermens, M.M.R.Vollenbroek-Hutten, Persuasive technology to support active and healthy ageing: An exploration of past, present, and future, *J. Biomed. Inform.* (2018) **84**: 17–30.

5. D.J. Cook, M. Schmitter-Edgecombe, L. Jönsson, A.V. Morant, Technology-Enabled Assessment of Functional Health, *IEEE Rev. Biomed. Eng.* (2019) **12**: 319–332.

6. R.M. Brouillette, H. Foil, S. Fontenot, A. Correro, R. Allen, C.K. Martin, A.J. Bruce-Keller, J.N. Keller, Feasibility, Reliability, and Validity of a Smartphone Based Application for the Assessment of Cognitive Function in the Elderly, *PLoS ONE* (2013) **8**.

7. L. Dasenbrock, A. Heinks, M. Schwenk, J.M. Bauer, Technology-based measurements for screening, monitoring and preventing frailty, *Z Gerontol Geriat* (2016) **49**: 581–595.

8. E. Lach, A. Szewczenko, I. Chuchnowska, N. Bursiewicz, I. Benek, S. Widzisz--Pronobis, D. Bal, K. Elsner, M. Sanigórska, M. Sutor, J. Włodarz, The Problem of Monitoring the Psycho-Physical Condition of Seniors during Proposed Activities in Urban Space, *Sensors* (2023) **23(3)**: 1602.

9. I. Sharma, J. Srivastava, A. Kumar, R. Sharma, Cognitive remediation therapy for older adults, *J Geriatr Ment Health* (2016) **3**: 57–65.

10. H.M. Gavelin, A. Lampit, H. Hallock, J. Sabatés, A. Bahar-Fuchs, Cognition-Oriented Treatments for Older Adults: a Systematic Overview of Systematic Reviews, *Neuropsychol Rev.* (2020), **30(2)**: 167–193.

11. Ch. Lin, T. Mao, Ch. Huang, A Novel Game-Based Intelligent Test for Detecting Elderly Cognitive Function Impairment, *Computational and Mathematical Methods in Medicine* (2021).

12. E. Lach, I. Benek, A. Bednorz, The application of virtual reality for cognitive functions' diagnosis of the geriatric hospital's patients, *ICERI 2020* (2020) 3756–3760.

13. E. Lach, I. Chuchnowska I. Benek, A. Bonczek, Ł. Kubicki, M. Piątek, A. Kościecha, B. Gordon, M. Nerwiński, Rehabilitation of cognitive functions of the elderly with the use of depth sensors-the preliminary results, *Innovations in Biomedical Engineering, Springer* (2023), accepted for printing.

14. A.F. Kramer , L. Bherer, S.J. Colcombe, W. Dong, W.T. Greenough, Environmental influences on cognitive and brain plasticity during ageing, *J Gerontol A Biol Sci Med Sci.* (2004) **59(9)**: 940–957.
15. I. Ayed, A. Ghazel, A. Jaume-i-Capó, G. Moya-Alcover, J. Varona, P. Martínez-Bueso, Feasibility of Kinect-Based Games for Balance Rehabilitation: A Case Study, *Journal of Healthcare Engineering* (2018).

SERIOUS GAME FOR PERSONALISED REHABILITATION OF THE COGNITIVE FUNCTIONS OF THE ELDERLY

Abstract

The world's population is ageing rapidly, putting a heavy strain on traditional healthcare systems. Developing effective interventions that can maintain the functioning of older people and delay their decline is critical for public health. The aim of this work is to evaluate a serious game supporting the process of rehabilitation of cognitive functions of the elderly while activating them to move by introducing motion control of the application. The presented tool uses automatic adjustment of game levels to personalise the difficulty of tasks performed by players. The authors present preliminary tests carried out with the participation of seniors aged 70–79.

Keywords: cognitive function rehabilitation, elderly, serious game, depth camera

Krzysztof DOBOSZ[1,*], Benedykt WASZKIEWICZ[1]

Chapter 16. PERSONALIZED ASSESSMENT OF WEB CONTENT ACCESSIBILITY FOR PEOPLE WITH SPECIAL NEEDS

16.1. Introduction

Nowadays, we are increasingly obliged to use websites and Internet applications to deal with official, financial and professional matters. This trend was intensified during the COVID-19 pandemic, which led many companies and public institutions to enable communication via the Internet. A consequence of the introduction of Internet-based solutions may be that it is more difficult for people who are excluded because of their disability to access information. The most technically excluded people are the elderly. This is a group at risk of all kinds of impairments (e.g. eyesight, hearing) [1]. Of course, there is also a large group of other people who, due to problems related to various types of disabilities, are excluded because of technological limitations or software shortcomings. Although accessibility at first sight seems to benefit mainly people with disabilities, it also brings many advantages to the rest of the users [16], because the environmental influence can also cause accessibility problems [9]. A way of verifying the usability [10] of websites for a person with special needs could be a personalized accessibility assessment.

At present, tools for automatic web accessibility analysis treat the assessment in a general way, examining compliance with all possible WCAG guidelines. However, the accessibility problem is often personal. Therefore, even a very high overall accessibility score obtained with any of the existing tools does not necessarily mean that a web application or a website is accessible to a user with specific special needs.

The main website for all patients in Poland is *www.pacjent.gov.pl*. It will be used to find an answer for research question: *How to make a personalized website accessibility*

[1] Department of Algorithmics and Software, Faculty of Automatic Control, Electronics and Computer Science, Silesian University of Technology, Gliwice, Poland.
* Corresponding author: krzysztof.dobosz@polsl.pl.

assessment for patients with special needs? To find the answer, we will first try to identify the accessibility needs of the user-patient looking for information on the Internet. We will then propose a method for calculating the accessibility factor. Finally, we will consider whether to apply it to the results of an automated or manual audit.

16.2. Web content accessibility

This article focuses on worldwide guidelines for web content accessibility. However, it is important to note that accessibility is a wide topic, so it is important to mention equally important documents describing accessibility guidelines for web browsers and the software used to create them. These include:

- key components of Internet accessibility [20],
- description of the guidelines for the accessibility of user programs [21],
- description of the guidelines for the accessibility of authoring tools [22].

Accessibility assessments are carried out through a variety of approaches, each with specific benefits. These approaches include automated checking by specific tools, manual validations by accessibility experts and empirical evaluations [8].

16.2.1. Accessibility guidelines

The Web Content Accessibility Guidelines (WCAG) is a part of a series of web accessibility guidelines published by the Web Accessibility Initiative (WAI) of the World Wide Web Consortium (W3C), the main international standards organization for the Internet. They are a set of recommendations for making Web content more accessible, primarily for people with disabilities. The requirements described in WCAG 1.0 included the provision of alternatives to visual and auditory content, guarantees of contextual information, orientation and features to navigate the site using assistive technologies supporting people with disabilities [4].

The W3C received a lot of feedback indicating the need to update the guidelines to improve them, to make them more understandable to a wide audience, easier to implement, and more precisely formulated to be easier to test [17]. As a consequence, WCAG 2.0 was created, ensuring that relevant information can be found for both technical and non-technical audiences [23]. The document is organized into four layers:

- *principles* – provide the foundation for Web accessibility: *perceivable*, *operable*, *understandable*, and *robust*,
- *guidelines* – define the basic goals that authors should work toward in order to make content more accessible to users with different disabilities,
- *success criteria* – defined for each guideline and are measurable, and can be used to define the non-functional requirements of a website or web application,
- *sufficient and advisory techniques* – documented for each guideline and success criteria that are informative. The advisory techniques go beyond what is required and allow the authors to better address the guidelines.

WCAG 2.0 consists of *success criteria*, written as testable statements, independent of technology. In addition, it has general information on the interpretation of these criteria, described in separate documents, in order to make the guidelines easier to understand. This feature of the document has facilitated error reporting by automated audit tools, making them common [19].

Despite significant improvements in the approach to the topic of digital accessibility, WCAG 2.0 did not cover all the potential problems that people with disabilities could encounter [5]. For this reason, an update of the standard to version 2.1 was released in June 2018 [6]. In comparison to the previous edition, new success criteria were added for users with cognitive or learning disabilities, users with low vision and disabilities that cause difficulties in using mobile devices. In January 2023, W3C announced draft recommendations for WCAG 2.2 [24]. This new version extends WCAG 2.1 by adding new success criteria, definitions to support them, and guidelines to organize the additions. So far, it has not been approved.

16.2.2. Manual audits

Manual audits examine the structure of the website and its functionality. Tests carried out using assistive software help to show possible problems of people with disabilities using a website. Experts familiar with the problems encountered by disabled users perform audits using checklists [25]. Manual audits use tools that find errors and present them to the auditor. In many cases, these are also the tools used to carry out automated audits. The use of these programs allows experts, among other things, to quickly detect errors related to missing alternative text for hyperlinks or images, which would be very time-consuming without these tools. However, not all checkpoints may be accepted immediately, and some cases may require multiple tests to be accepted for an audit. An expert, based on his knowledge and skills, can also notice errors not detected by programs for automatic website analysis for accessibility.

Informal experiential techniques are also included in manual evaluation. In this case, the evaluation is based on the use of an interface in such a way that the sensory, motor or cognitive capabilities of the auditor are reduced. Then, scenarios of independent exploration of the site and use of its functionality are performed, and information on what was successful and what was not, is noted. Such tests can also be carried out by people with disabilities, using a 'think-aloud' protocol to verify the achievement of the intended action [2]. Through such tests, it is possible to gain a better understanding of disabled people's problems and their expectations of the site.

16.2.3. Automated audits

Automated audits are performed by special tools to analyse a website for accessibility (examples are given in Table 1). They evaluate a website based on the success criteria set out in the WCAG document. Some solutions allow for the evaluation of a single page, while others evaluate the entire content of a website. Accessibility can be examined at every step of a website's development: from design, implementation, deployment and maintenance. For this reason, various quality control solutions have been developed for designers, developers, project managers and auditors evaluating the final state of a product. Unfortunately, in some cases, the various tools may provide inaccurate results. Among other reasons, for this reason it is not advisable to use only automated tools to assess the quality of a website, but they can help with manual review [15].

There has been debate for many years on how to measure web accessibility [3]. Many studies report that web accessibility auditing tools do not cover all the success criteria defined in the WCAG. However, many of them refer to version 1.0 or 2.0 [4, 7, 19]. At the same time, many of these papers highlight the still small amount of research in that area. Taking into account the dynamics of the development of Internet technologies and the growing interest in the subject of accessibility, it is worth conducting more and more research in this area. It should also be noted that many projects from around ten years ago on accessibility evaluation tools have been abandoned. There has been a change in the W3C Consortium's approach regarding the WCAG, allowing for easier testing of success criteria [14] and new solutions have been developed. Automated audits provide a quick and easy way to obtain a report on a given web site. They often do not require the intervention of an auditor. They are therefore affordable in economic terms and are suitable for analysing a large number of websites in real time [18].

16.2.4. Tools for accessibility analysis

The tools selected for the analysis were pre-verified. The possibility of automatically auditing a website based on the criteria defined in WCAG was checked, as well as the possibility of saving the resulting report in a form that can be later processed. Tools allowing only interactive website analysis, without the possibility of a full audit and report saving, were excluded. The tools selected were not limited to free solutions. In the case of commercial applications, free trial periods were used to analyse and collect reports of pre-selected websites for examination. The selection of tools was guided by a list prepared by the W3C Consortium containing set of 167 tools [26]. The set of tools being the result of review is shown in Table 1.

Table 1

Overview of selected analysis tools

Name	Type	Revised guidelines	Subpage analysis	Form of report
Lighthouse[1]	web app, command line app, web browser extension, NodeJS module	WCAG 2.1	no	CSV JSON
Axe DevTools[2]	web browser extension	WCAG 2.0 (A, AA) WCAG 2.1 (A, AA)	no	JSON
Axe Core[3]	NodeJS module	WCAG 2.0 (A, AA) WCAG 2.1 (A, AA)	no	JSON
WAVE Web Accessibility Evaluation Tool[4]	application interface	WCAG 2.1	no	JSON
Tenon[5]	Internet platform	WCAG 2.0, 2.1	no	CSV
Ace IT[6]	Internet platform	WCAG 2.1	yes	CSV XLSX
Domain Accessibility Audit[7]	opensource web app	WCAG 2.0 (A, AA) WCAG 2.1 (A, AA)	yes	JSON

---

[1] https://developers.google.com/web/tools/lighthouse
[2] https://www.deque.com/axe/devtools/
[3] https://github.com/dequelabs/axe-core
[4] https://wave.webaim.org/
[5] https://tenon.io/
[6] https://ace.useit.se/
[7] https://github.com/MSU-NatSci/DomainAccessibilityAudit

Name	Type	Revised guidelines	Subpage analysis	Form of report
IBM Equal Access Accessibility Checker[8]	web browser extension, NodeJS module	WCAG 2.0 (A, AA) WCAG 2.1 (A, AA)	no	CSV JSON
Accessibility Insights for Web[9]	web browser extension	WCAG 2.1	no	HTML

16.3. Medical Classifications

16.3.1. International Classification of Diseases

The International Classification of Diseases (ICD) is a widely use diagnostic tool. It is used for health management, clinical purposes and epidemiology. The ICD is maintained by the World Health Organisation (WHO). The ICD was originally designed as a healthcare classification system, providing a system of diagnosis codes to classify diseases and a wide range of symptoms, abnormal test results or even social circumstances and external causes of injury or illness. The document contains an accepted worldwide system of categories to which disease entities have been assigned according to established criteria. It consists of twenty-one chapters containing classification groups identified by a three-character identifier, which are further subdivided into four-character subcategories [13].

The ICD is still being developed, detailing the diseases already defined and including new ones. The latest – eleventh revision of the International Classification of Diseases (ICD-11), is almost five times as big as its previous version. In our research we only show that appropriate WCAG mappings to the ICD are possible, so we have stayed with references to the ICD-10.

---

[8] https://www.ibm.com/able/toolkit/tools/#verify
[9] https://accessibilityinsights.io/

16.3.2. International Classification of Functioning, Disability and Health

The International Classification of Functioning, Disability and Health, known more commonly as ICF, is a classification of health and health-related domains [12]. The structure of the ICF is based on the following components: functions and physique, activity and involvement in a life situation. In addition, it includes additional information on severity and environmental factors. At ICF, functioning and disability are seen as a complex interaction between an individual's state of health and environmental and personal factors. This classification allows for the assessment of the degree of disability, although it is not a measurement tool. This applies to all people, regardless of their state of health. ICF emphasizes function, not condition or disease. It is designed to be appropriate for different cultures, ages and genders. ICF and ICD complement each other, therefore it is recommended to use both classification systems together.

16.4. Assessment of accessibility

16.4.1. Mapping WCAG to ICD and ICF

To identify the user's personal needs, it is necessary to select which success criteria are relevant to him or her. This can be done using a hospital report indicating a diagnosed disease (ICD code) or dysfunction (ICF code). Alternatively, the indication of the specific dysfunctions for which the website should be analysed can be done by the caregiver of the person with a disability or by the person himself. For each of the success criteria described in the WCAG, the related ICD and ICF codes have been mapped. Table 2 shows an example for criteria 1.1.1 Non-text Content.

Table 2

Example of guideline mapping

Success Criterion	Conformance Level	ICD-10	ICF
1.1.1 Non-text Content	A	H52.0, H52.1, H52.2, H52.3, H52.4 H53.0, H53.1, H53.3, H53.4, H54, H54.0, H54.1, H54.2, H54.3, H54.4, H54.5, H54.6, H54.7, H59, H59.0, H59.8, H59.9, H90, H91, H93.0, H93.1, H93.2, H93.8, H93.9	b210, b2100, b2101, b2102, b2103, b2108, b2109, b230, b2300, b2301,b2302, b2303, b2304, b2400, b2408, b2409

16.4.2. Personal web content accessibility factor

The personalized assessment takes into account only the relevant success criteria for the selected user dysfunctions. The *Success Criteria Threshold* (*SCT*) threshold of a success criterion, the number of reached and unreached occurrences of a criterion will be used to determine the factor. The final measure of the accessibility of a website in relation to a given dysfunction is assessed according to strict rules. If *SCT* percentage of occurrences of a given success criterion is not met, the component obtained from this criterion is zero, otherwise the *Web Content Accessibility Factor* (*WCAF*) is calculated according to the formula (1).

$$WCAF = \frac{\sum_{j=1}^{n} \begin{cases} f_l & when \ s_j = 0 \\ \dfrac{a_j}{s_j} f_l & when \ s_j > 0 \end{cases}}{\sum_{k=1}^{n} f_l} \tag{1}$$

where:

f_l – factor for the success criterion level (A – 3, AA – 2, AAA – 1),

a_j – sum of cases where a success criterion is reached,

s_j – sum of all cases where the success criterion applies

n – number of success criteria analysed.

For A level, the highest multiplier value is proposed, as this level deals with the removal of the most significant barriers that prevent the use of the functionality offered by the website. The next levels received decreasing values. If a guideline is not applicable (i.e. $s_j = 0$, e.g. provision of video audio description, on non-video pages), the criterion is scored with the maximum value (3, 2 or 1, depending on its level).

16.5. Evaluation and discussion

16.5.1 Methodology

The study was designed to experimentally validate the feasibility of using automated website accessibility tools to determine the adaptation of a website to specific impairments. The experiment consisted of collecting data from *www.pacjent.gov.pl* using pre-selected tools. Due to the proposed final factor of accessibility assessment, tools were selected to include information on passed and failed success criteria in the

reports. These were: *Axe core* (version 4.2.3-alpha) and *IBM Equal Access Accessibility Checker* (version 3.1.8). These studies did not involve users, so the results were grouped according to disability groups. Based on mapping WCAG to ICD and ICF, and considering data showing the percentage of specific dysfunctions among adults in the United States of America, collected in 2016 (a sample of 458,881 people) [11], obtained results were categorized into groups of disabilities including:

a) All dysfunctions,

b) Mobility dysfunctions,

c) Cognitive disorders (memory, attention, thinking, language),

d) Disorders related to independent living (intellectual, decision-making),

e) Hearing disorders (deafness, hearing impairment),

f) Vision disability (blindness, colour blindness),

g) Reading disabilities,

h) Disorders resulted in epilepsy.

In addition, three values for the SCT parameter were also used: 100%, 90% and 80%. The SCT parameter defines the limits of the percentage of implemented instances of a given guideline relative to all possible instances of its application. The reason for examining a threshold of less than 100% is to provide an assessment of a site where a particular guideline has been omitted in a few cases, e.g. by an oversight of the developers. Values of 100%, 90%, 80% were chosen experimentally. Then, one value was selected to look at the WCAF values for different dysfunction groups.

16.5.2. Discussion of results

Table 3 shows the number of passed and failed success criteria for the selected web site. The information contained in the reports of the automated audit tools, differs depending on the tool used. In particular, this is the case for the level of detail for certain success criteria (e.g. treating each character in the content independently).

Table 3

Results of guideline application detection at *www.pacjent.gov.pl*

Success Criterion	IBM Checker		AxeCore		Manual audit	
	Passes	Fails	Passes	Fails	Passes	Fails
1.1.1	1450	2	15	0	14	14
1.3.1	1659	3	36	0	107	4

Success Criterion	IBM Checker		AxeCore		Manual audit	
	Passes	Fails	Passes	Fails	Passes	Fails
1.3.2	646	0	0	0	1	0
1.3.3	574	0	0	0	0	0
1.3.5	1	0	1	0	1	0
1.4.1	56	0	0	0	1	0
1.4.3	721	2	120	2	49	1
1.4.4	55	0	0	0	0	0
1.4.5	0	0	0	0	10	0
1.4.10	0	0	0	0	0	0
1.4.11	0	0	0	0	212	0
1.4.12	0	0	7	0	6	0
1.4.13	0	0	0	0	0	0
2.1.1	12	0	0	0	0	0
2.2.2	35	0	0	0	0	0
2.4.1	296	4	1	0	0	0
2.4.2	2	0	1	0	2	0
2.4.4	99	0	69	0	92	3
2.4.6	23	1	0	0	0	1
2.4.7	26	0	0	1	0	1
2.4.10	0	0	0	0	3	2
2.5.3	6	1	0	0	0	1
3.1.1	1	0	2	0	2	0
3.1.2	3	0	2	0	0	0
3.2.2	5	0	0	0	0	0
3.3.2	3	0	1	0	4	0
4.1.1	21	1	26	1	9	3
4.1.2	78	2	129	2	142	4

Figure 1 shows the combined results for all separated disability groups. This means that all success criteria contained in the WCAG 2.1 document were taken into account. In the graph it can be seen that as the SCT parameter decreases the results increase, this is the expected result. A value of 100% means that there can be no omission of a possible success criterion. Lower values (90% and 80%) mean that, despite the occurrence of minor faults (no application of the expected success criterion), the criterion is taken into account when calculating the WCAF. The similar results obtained for 80% and 90% led to the decision to drop the analyses for the 80% value later in the study.
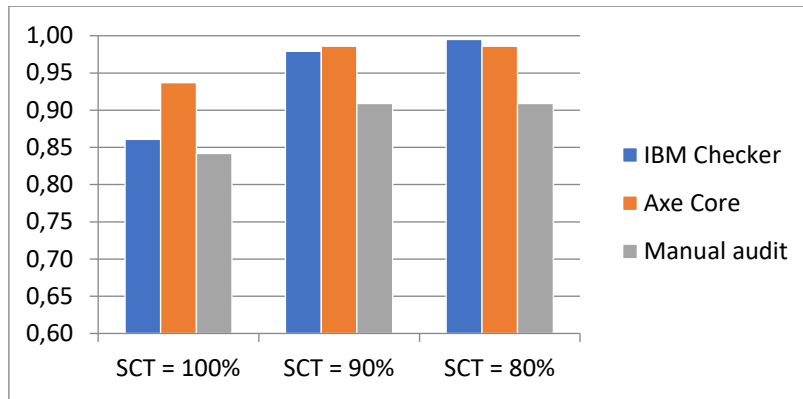
Fig. 1. Value of WCAF for all success criteria depending on SCT
Rys. 1. Wartość WCAF dla wszystkich kryteriów sukcesu w zależności od SCT

A significant difference can be seen between the results obtained using the IBM Checker tool and the manual audit. The difference reaches up to 0.2 of the WCAF. The Axe Core tool gives results similar to those of the manual audit for SCT = 100%, and more similar to the first tool for SCT = 90%. Then, the results were collected together according to the previously defined disability groups and the value of the SCT parameter. Figure 2 illustrates the values obtained for SCT = 100% and Figure 3 for SCT = 90%.
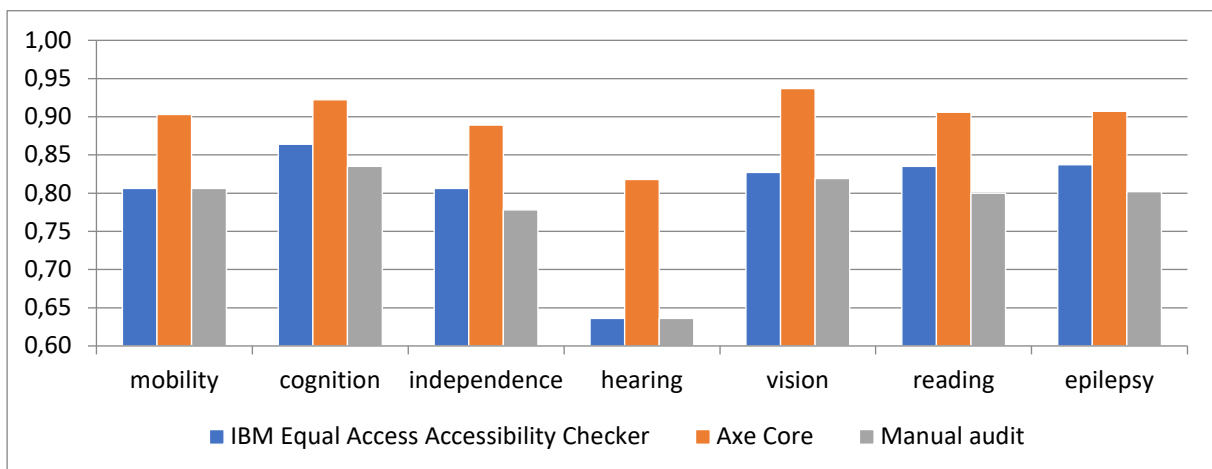

Fig. 2. Value of WCAF for different dysfunction groups (SCT=100%)
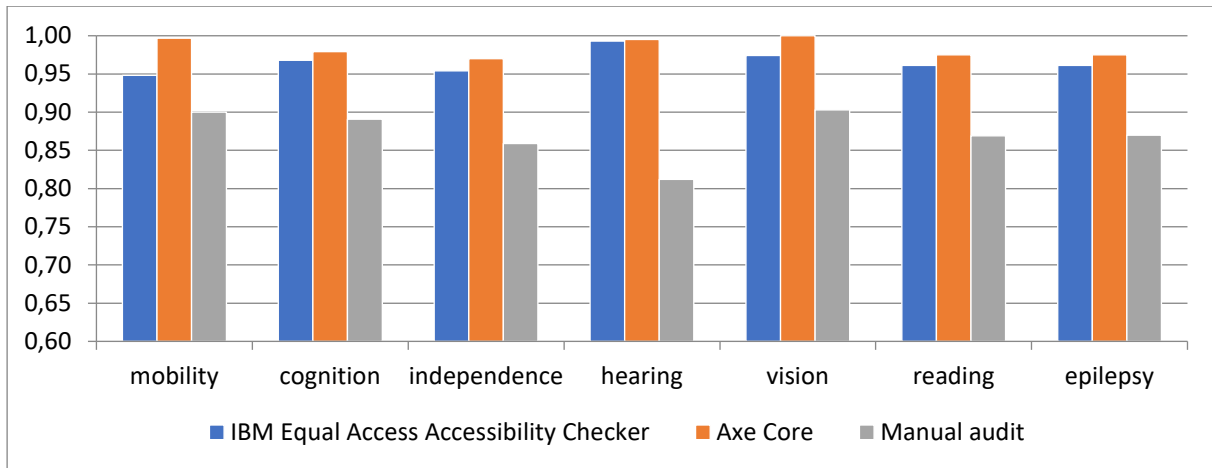Rys. 2. Wartość WCAF dla różnych grup dysfunkcji (SCT=100%)

Fig. 3. Value of WCAF for different dysfunction groups (SCT=90%)
Rys. 3. Wartość WCAF dla różnych grup dysfunkcji (SCT=90%)

Although the determined WCAF values are different for the disability groups, as in the summary chart, the correlations between the audit methods are similar. The best value of the r-Pearson correlation coefficient was calculated for the AxeCore tool and the manual audit: 0.972 (SCT = 100%). The results obtained with the AxeCore tool are characterized by high values, which is particularly noticeable for SCT = 100%. This is a result of many small elements of the website (e.g. individual characters) being recognised as correct, and are therefore a very high percentage of all elements verified. IBM Equal Access Accessibility Checker gave results similar to manual audits for SCT = 100%, and the results w0ere similar to those of the AxeCore tool for SCT = 90%. The WCAF for manual audits has always been the lowest, which may mean that they were the most rigorous, although certainly the most time-consuming.

16.6. Conclusions

In the study, we described how to make a personalized assessment of website accessibility. First, we chose people with special needs as the target group. The main government patient website (*www.pacjent.gov.pl*) was chosen as the source material. It was then assumed that all guidelines defined in the WCAG do not need to be taken into account for a personalized assessment. A description of the user's personal deficits given in the form of a list according to the ICD or ICF can be used to select guidelines. However, it should be noted that the ICF seems to be more appropriate as it relates directly to functioning and disability. In the next step, a method for calculating the accessibility index is proposed in order to present the assessment numerically. Finally,

the WCAF values for the different disability groups and the two SCT threshold values were calculated. Although we did not involve users, we showed that, depending on personal needs, using mainly the ICF to WCAG mapping, we are able to select which guidelines should be assessed.

An observation resulting from the research is that automated testing does not give a complete view of a page's accessibility due to the number of cases requiring contextual assessment of elements. However, it is a quick and easy way to verify whether a page will be accessible at all to a person with special needs. A site evaluated positively by automatic tools may therefore meet the basic criteria, breaking down the most difficult barriers for people with impairments, but a high automatic audit score does not ensure a comfortable use of the site, for which an expert audit is needed. Thus, tools allowing automatic web accessibility audits can be used for initial verification, but cannot be fully relied upon, due to the different ways of validation and the incomplete coverage of verification of success criteria.

Bibliography

1. A. Arch. Web accessibility for older users. *Proceedings of the 2009 International Cross-Disciplinary Conference on Web Accessibility* (W4A) – W4A '09, ACM Press (2009) 1–6.
2. S. Schmutz, A. Sonderegger, J. Sauer. Implementing recommendations from web accessibility guidelines. Human Factors: *The Journal of the Human Factors and Ergonomics Society* (2016), 58(4):611–629.
3. S.L. Henry, S. Abou-Zahra, J. Brewer. The role of accessibility in a universal web. *Proceedings of the 11th Web for All Conference on – W4A '14*. ACM Press (2014) 1–4.
4. International Organization for Standardization, ISO 9241-11:2018 Ergonomics of human-system interaction – part 11: Usability: Definitions and concepts, https://www.iso.org/standard/63500.html, [access: 30.01.2023].
5. T. Frazão, C. Duarte. Comparing accessibility evaluation plug-ins. *Proceedings of the 17th International Web for All Conference*. ACM (2020) 1–11.
6. J. Brewer. Web accessibility highlights and trends. *Proceedings of the international cross-disciplinary workshop on Web accessibility – W4A*. ACM Press (2004) 51–55.
7. D. Sloan, A. Heath, F. Hamilton, B. Kelly, H. Petrie, L. Phipps. Contextual web accessibility – maximizing the benefit of accessibility guidelines. *Proceedings of the 2006 international cross-disciplinary workshop on Web accessibility (W4A) Building the mobile web: rediscovering accessibility? – W4A*, ACM Press (2006) 121–131.

8. M. Vigo, J. Brown, V. Conway. Benchmarking web accessibility evaluation tools. *Proceedings of the 10th International Cross-Disciplinary Conference on Web Accessibility – W4A '13,* ACM Press (2013) 1–10.

9. R. Calvo, F. Seyedarabi, A. Savva. Beyond web content accessibility guidelines. *Proceedings of the 7th International Conference on Software Development and Technologies for Enhancing Accessibility and Fighting Infoexclusion*, ACM (2016) 77–84.

10. World WideWeb Consortium. Web Content Accessibility Guidelines (WCAG) 2.1. https://www.w3.org/TR/WCAG21/ [access: 30.01.2023].

11. G. Brajnik. A comparative test of web accessibility evaluation methods. *Proceedings of the 10th international ACM SIGACCESS conference on Computers and accessibility – Assets '08*, ACM Press (2008) 113–120.

12. L. Keen S. Abou-Zahra, N. Steenhout. Selecting web accessibility evaluation tools, https://www.w3.org/wai/test-evaluate/tools/selecting/. [access: 03.07.2021].

13. G. Brajnik, A. Mulas, C. Pitton. Effects of sampling methods on web accessibility evaluations. *Proceedings of the 9th international ACM SIGACCESS conference on Computers and accessibility – Assets '07*, ACM Press (2007) 59–66.

14. M. Cooper, Q. Limbourg, C. Mariage. Integrating universal design into a global approach for managing very large web sites, http://ui4all.ics.forth.gr/ui4all-99/cooper.pdf. [access: 30.01.2023].

15. C. Power, A. Freire, H. Petrie, David Swallow. Guidelines are only half of the story. *Proceedings of the SIGCHI Conference on Human Factors in Computing Systems*. ACM (2012) 433–442.

16. M. Vigo, G. Brajnik. Automatic web accessibility metrics: Where we are and where we can go. *Interacting with Computers* (2011) 23(2):137–155.

17. World Health Organization. International Statistical Classification of Diseases and Related Health Problems 10th Revision. https://icd.who.int/browse10/2019/en [access: 22.03.2023]

18. World Health Organization. ICF. International classification of functioning, disability and health. https://icd.who.int/dev11/l-icf/en [access: 22.03.2023]

19. C. Okoro, N. Hollis, A. Cyrus, S. Griffin-Blake. Prevalence of disabilities and health care access by disability status and type among adults – united states, 2016. *Morbidity and Mortality Weekly Report* (2018) 67(32):882–887.

20. World Wide Web Consortium. Essential Components of Web Accessibility. https://www.w3.org/WAI/fundamentals/components/ [access: 10.01.2023].

21. World Wide Web Consortium. User Agent Accessibility Guidelines (UAAG) Overview. https://www.w3.org/WAI/standards-guidelines/uaag/ [access: 10.01.2023].

22. World Wide Web Consortium. Authoring Tool Accessibility Guidelines (ATAG) Overview. https://www.w3.org/WAI/standards-guidelines/atag/ [access: 10.01.2023].

23. World Wide Web Consortium. W3C Process Document. https://www.w3.org/2004/02/Process-20040205/tr.html [access: 10.01.2023].

24. World Wide Web Consortium. Web Content Accessibility Guidelines (WCAG) 2.2. https://www.w3.org/TR/WCAG22/ [access: 10.01.2023].

25. World Wide Web Consortium. WCAG-EM Report Tool. https://www.w3.org/WAI/eval/report-tool/ [access: 10.01.2023].

26. World Wide Web Consortium. Web Accessibility Evaluation Tools List. https://www.w3.org/WAI/ER/tools/ [access: 10.01.2023].

PERSONALIZED ASSESSMENT OF WEB CONTENT ACCESSIBILITY FOR PEOPLE WITH SPECIAL NEEDS

Abstract

In the study, we described how to make a personalized assessment of website accessibility. First, we chose people with special needs as the target group. The main government patient website (*www.pacjent.gov.pl*) was chosen as the source material. It was then assumed that all guidelines defined in the WCAG do not need to be taken into account for a personalized assessment. A description of the user's personal deficits given in the form of a list according to the ICD or ICF can be used to select guidelines. However, it should be noted that the ICF seems to be more appropriate as it relates directly to functioning and disability. In the next step, a method for calculating the accessibility index is proposed in order to present the assessment numerically. Finally, the WCAF values for the different disability groups and the two SCT threshold values were calculated. Although we did not involve users, we showed that, depending on personal needs, using mainly the ICF to WCAG mapping, we are able to select which guidelines should be assessed.

Keywords: accessibility, assessment, personalization, web

POSTĘPY W ONKOLOGII OBLICZENIOWEJ I SPERSONALIZOWANEJ MEDYCYNIE
TOM 3
PRZEKRACZAJĄC GRANICE, ŁĄCZĄC NAUKĘ

Streszczenie

Trzeci tom serii *Postępy w Onkologii Obliczeniowej i Spersonalizowanej Medycynie* poświęcony jest eksploracji najnowszych badań i praktycznych rozwiązań w ramach Priorytetowego Obszaru Badawczego 1 (POB1) Politechniki Śląskiej. W 16 rozdziałach zaprezentowano wyniki innowacyjnych badań konsorcjum naukowców, studentów i współpracujących partnerów ze środowiska akademickiego oraz społeczno--gospodarczego, które najczęściej powstały w odpowiedzi na praktyczne potrzeby lekarzy i biologów.

W monografii poruszono zagadnienia z następujących obszarów:

a) Bioinformatyka – w tym obrazowanie biomedyczne (kwantyzacja obrazów histopatologicznych barwionych H&E; analiza przeżywalności komórek bakteryjnych za pomocą mikroskopii konfokalnej), badania związane z rakiem (ekspresja cytokin w raku jelita grubego; ewolucja klonów i mutacje somatyczne w nowotworach), nowe narzędzia do przetwarzania i analizy danych (system stratyfikacji pacjentów z dystrofią mięśniową; symulator danych z sekwencjonowania DNA; mapowanie długich odczytów oxford nanopore), wspierające proces rehabilitacji (analiza dostępności mobilnych aplikacji i stron rehabilitacyjnych; gry wspomagające rehabilitację) oraz inne zastosowania (efekt proliferacji przy ekspozycji na pole elektromagnetyczne).

b) Modelowanie numeryczne (analiza procesu nagrzewania tkanki biologicznej i jej uszkodzeń termicznych; modelowanie układu mięśniowo-szkieletowego).

c) Inżynieria biomateriałów (synteza biodegradowalnego i bioresorbowalnego rusztowania naczyń krwionośnych).

d) Zdrowie publiczne (badania epidemiologiczne dengi i duru brzusznego).

Wydanie niniejszej publikacji ma na celu propagowanie najnowszych osiągnięć i metod obliczeniowych w środowisku naukowym. Idee i rozwiązania przedstawione w tej serii mogą być przydatne do stworzenia nowych narzędzi diagnostycznych, przełomowych metod leczenia i zaawansowanych terapii. Te innowacje mogą pomóc podmiotom świadczącym opiekę zdrowotną, ostatecznie prowadząc do lepszej jakości życia pacjentów.

Politechnika Śląska, jako jedna z polskich uczelni, uzyskała status uczelni badawczej i rozpoczęła realizację programu, mającego na celu wzrost jej doskonałości naukowej i międzynarodowego znaczenia. Monografia wydawana jest w ramach programu Inicjatywa Doskonałości – Uczelnia Badawcza.

The third book in the series continues to report recent research in the area of computational oncology and personalized medicine, being the topic of the **Priority Research Area #1 (POB1)** of the **Silesian University of Technology**. The chapters are the result of the close collaboration of SUT researchers and their academic and socio-economic partners. This volume chapters include research related to cancer research, epidemiology, medical diagnostics, bioinformatics, image analysis, tissue and biomaterial engineering, rehabilitation, in silico medicine & modelling.

The editorial team believe that the new ideas and applications presented within the series would lead to the implementation of new diagnostic tools, drugs, or therapies to assist clinicians in their practice and eventually would lead to an increase in life quality.

Series: Excellence Initiative - Research University

Silesian
University
of Technology

RESEARCH
UNIVERSITY
EXCELLENCE INITIATIVE